Optimization of Piezoresistive Cantilevers for Static and Dynamic Sensing Applications

A Dissertation
Presented to
The Academic Faculty

By

Kianoush Naeli

In Partial Fulfillment
Of the Requirements for the Degree
Doctor of Philosophy in the
School of Electrical and Computer Engineering

Georgia Institute of Technology

May, 2009

Optimization of Piezoresistive Cantilevers for Static and Dynamic Sensing Applications

Approved by:

Dr. Oliver Brand, Advisor
School of electrical and Computer Engineering
Georgia Institute of Technology

Dr. Mark G. Allen
School of electrical and Computer Engineering
Georgia Institute of Technology

Dr. F. Levent Degertekin
School of electrical and Computer Engineering
Georgia Institute of Technology

Dr. Ali Adibi
School of electrical and Computer Engineering
Georgia Institute of Technology

Dr. Lawrence A. Bottomley
School of Chemistry and Biochemistry
Georgia Institute of Technology

Date Approved: March 23, 2009

To my wonderful family,
To the loving memory of my grandfather

ACKNOWLEDGMENTS

I would like to express my sincere gratitude to my advisor, Prof. Oliver Brand. Working with Prof. Brand, in my opinion, is the best thing that a PhD student can wish for. He perfectly understands the character of his students. He believes in his students; and he provides the best conditions for blossoming of intellectual qualities and creative thinking. Professor Brand highly values creativity and integrity. When presented with a new idea, he is humble enough to think about the subject twice, but at the same time, he is quick to find and remind the flaws.

I would like to thank my dissertation defense committee members, Prof. Mark Allen, Prof. Levent Degertekin, Prof. Lawrence Bottomley, and Prof. Ali Adibi, for the helpful discussions and their invaluable feedbacks in shaping and finalizing this thesis. In particular, I would like to express my gratitude to Prof. Degertekin and Prof. Allen, and the members of their research groups, for their supports in the device fabrication and obtaining the measurement data using their labs facilities.

I shall express my great thankfulness to the “then-” undergraduate student assistants who helped me with the characterization of resonant cantilevers, namely, Ankit Shah, Ariel Brown, Sinan Sutcu, Sadegh Mohammadi, and Alexander Santiago. Also, the mutual respect, the support and the spirit of cooperation among my graduate student fellows in Prof. Brand’s research group, past and present, made my years as a PhD student even more memorable. My salute to these great individuals: Jae Hyeong Seo, Kemal Safak

Demirci, Luke Beardslee, Robert Sunier, Stefan Schild, Juan Cesaretti, Thomas Schweizer, Prateek Tandon, and Albert Byun.

A major motivation for this thesis originated from a nano-jet characterization effort. I shall thank my colleagues in that project, Jungchul Lee, Nisarga Naik and Hanif Hunter, as well as Profs. Ari Glezer and William King for providing the lab facilities and support.

I had the privilege of not only benefiting from the excellent support provided by the MiRC cleanroom, but also working behind the scene in the cleanroom for a period of time. I must express my best regards to the director of MiRC, Prof. James Meindl and Dr. Kevin Martin, as well as Mr. Gary Spinner, the restless manager of the cleanroom. Also, I shall thank the dedicated cleanroom staff members, especially my good friend, Mr. Tran-Vinh Nguyen.

TABLE OF CONTENTS

LIST OF TABLES

LIST OF FIGURES

LIST OF ABBREVIATIONS

AC	Alternating Current
AFM	Atomic Force Microscopy
AU	Arbitrary Unit
CMOS	Complementary Metal Oxide Semiconductor
DC	Direct Current
DI Water	Deionized Water
DRIE	Deep Reactive Ion Etching
ECOM	Environmental Effect Cancellation with Overtone and Effective Mass
FEM	Finite Element Method
Epi	Epitaxially Grown Crystal
Eq.	Equation
HB	Hard-Bake
HP	Hotplate
HWA	Hot Wire Anemometry
ICP	Inductively Coupled Plasma
Log	Logarithmic
MRFM	Magnetic Resonance Force Microscopy
PECVD	Plasma Enhanced Chemical Vapor Depostion
PIV	Particle Image Velocimetry
PSD	Position Sensitive Detection
Q	Quality Factor

Q-factor	Quality Factor
QCM	Quartz Crystal Micro-Balance
RIE	Reactive Ion Etching
SAW	Surface Acoustic Wave
SB	Soft-Bake
SC	Stress Concentrating; Stress Concentration
SEM	Scanning Electron Microscopy
SHO	Simple Harmonic Oscillator
SLT	Simple Loop Topology
SNR	Signal to Noise Power Ratio
SOI	Silicon on Insulator
STM	Scanning Tunneling Microscopy
TED	Thermoelastic Damping
TLT	Twisted Loop Topology
TSMR	Thickness Shear Mode Resonator
UV	Ultra-Violet

SUMMARY

The presented work aims to optimize the performance of piezoresistive cantilevers in cases where the output signal originates either from a static deflection of the cantilever or from the dynamic (resonance) characteristic of the beam. While the presented optimizations for the static mode specifically targets the force sensitivity of piezoresistive cantilevers, the results and findings for the dynamic mode can be used for improving the resonance quality of rectangular cantilevers in general, regardless of the implemented sensing schemes.

Based on a new stress concentration technique, which utilizes silicon beams and wires embedded in the cantilever, the force sensitivity of the cantilever is increased up to 8 fold with only about a 15% decrease in the cantilever stiffness. Moreover, the developed stress-concentrating cantilevers show almost the same resonance characteristic as conventional cantilevers. Through simulation and measurement, the effect of the stress concentrating elements on the force sensitivity and stiffness of cantilevers is studied and it is found that decreasing the size of these elements results in an improved sensitivity.

The focus of the second part of the present work is to provide guidelines for designing rectangular silicon cantilever beams to achieve maximum quality factors for the fundamental and higher flexural resonance at atmospheric pressure. The applied methodology is based on experimental data acquisition of resonance characteristics of silicon cantilevers, combined with modification of analytical damping models to match

the measurement data. To this end, rectangular silicon cantilever beams with thicknesses of 5, 7, 8, 11 and 17 μm and lengths and widths ranging from 70 to 1050 μm and 80 to 230 μm, respectively, have been fabricated and tested. To better describe the experimental data, modified models for air damping have been developed. Moreover, to better understand the damping mechanisms in a resonant cantilever system, analytical models have been developed to describe the cantilever effective mass in any flexural resonance mode. To be able to extract reliable Q-factor data for low signal-to-noise ratios, a new iterative curve fitting technique is developed and implemented, which is applicable even for cases where the noise and signal powers are equal.

To address the challenge of frequency drift in (mass-sensitive) resonant sensors, and especially cantilever-based devices, the last part of the research deals with a novel compensation technique to cancel the unwanted environmental effects (e.g., temperature and humidity). This technique is based on exploring the resonance frequency difference of two flexural modes. Experimental data show improvements in temperature and humidity coefficients of frequency from -19.5 to 0.2 $ppm^{\circ}C^{-1}$ and from 0.7 to -0.03 $ppm\%RH^{-1}$, respectively.

To apply the compensation technique, the cantilever-based resonator must be tuned in two distinct frequency overtones. Thus, the last part of the work is aimed on techniques to enhance or suppress the vibration amplitude in desired overtones, either by optimizing the location of piezoresistive detectors, or by selectively actuating the cantilever.

CHAPTER 1

INTRODUCTION

A fundamental part of every sensor is the transducer, which converts the measurand of interest into an interpretable output signal. One of the most prominent transducers in the micro-realm is the piezoresistive cantilever, which translates information from the mechanical into the electrical domain, e.g. the amount of force exerted on the cantilever into a resistance change or the amount of mass added to the cantilever into a resonance frequency change. As the title of this thesis suggests, this research focuses on both aspects, i.e. the application of piezoresistive cantilevers in static and dynamic sensing. In other words, the presented work aims to optimize the performance of piezoresistive cantilevers in cases where the output signal is either DC (e.g., strain gauges) or an AC (e.g., resonant sensors) signal. While the presented research for the static mode specifically targets piezoresistive cantilevers, the optimization results and findings for the dynamic mode can be extended to cantilevers with other sensing schemes.

This thesis can be virtually divided in two parts: while the majority of Chapter 3 is about the static behavior of cantilevers, the discussions in Chapter 4 to Chapter 10 are dedicated to resonant cantilevers only. As an introduction to the field of cantilever-based microsensors, Chapter 2 highlights the fundamentals of cantilever sensors as well as the governing equations and principles of piezoresistive cantilevers. In the subsequent chapters, the presented research has been based on design, simulation, micro-fabrication, and characterization efforts.

The focus of Chapter 3 is on modifying piezoresistive cantilever designs for static-mode force sensing. To this end, a new technique utilizing stress concentration in cantilevers is introduced. Using a new fabrication method, stress concentrating beams and wires are embedded in the cantilevers. This way the force sensitivity of the cantilevers is significantly increased without any substantial decrease in the cantilever stiffness.

Chapter 4 presents a new iterative curve fitting technique as a robust tool in interpreting the transfer characteristics of resonant cantilevers. The significant advantage of this technique is its accuracy in calculating the quality factor of resonators. The presented method is especially useful in eliminating the effect of noise, even for cases in which the output signal to noise power ratio is as small as one.

Through modeling and characterization efforts, Chapters 5, 6, and 7 target the damping of resonant cantilevers in air in both fundamental and higher flexural modes. As a result, guidelines for optimization of the cantilever geometry with respect to the achievable Q-factor in air are established. As part of this study, Chapter 6 presents how a resonant cantilever can be modeled as a simple spring-mass system not only in the fundamental mode, but also in any flexural mode.

A critical challenge for resonant (mass) sensors is to distinguish resonance frequency variations caused by changes of the measurand (e.g., binding of molecules) from unintended frequency changes due to environmental effects (e.g., temperature and humidity). In Chapter 8, a novel technique for cancellation of environmental effects is

presented. This technique is based on monitoring the effective mass in two resonance modes. The presented method is applicable not only for resonant cantilevers, but also for any type of resonator as long as the described requirements are satisfied.

To improve the selectivity of a resonant cantilever to a desired flexural mode, the focus of Chapter 9 is on different schemes for enhancement and suppression of the excitation and detection of particular resonance overtones. The findings in this chapter can be potentially used for the closed-loop operation of cantilevers in higher flexural modes, or for an efficient implementation of the compensation technique presented in Chapter 8.

Finally, the focus of the research presented in Chapter 10 is on the effect of holes and trenches in the cantilever surface on its performance.

It is important to note how the terms “mode” and “overtone” are used throughout this work. A mechanical structure can resonate in different classes of *modes* (or simply, modes), e.g., flexural, torsional, or longitudinal modes. Each class of modes consists of *overtones*, which correspond to the eigenvalues of the general solution for the governing resonance equation of that particular mode (e.g., flexural mode). In special cases, e.g., vibrations of a string, the resonance overtones are actually harmonics of the fundamental mode, with their resonance frequency related to the fundamental frequency through integer ratios. For a resonant cantilever in flexural mode, however, the overtone frequencies are not integer harmonics of the fundamental resonance frequency. This issue is explained in more details in Chapter 2.

CHAPTER 2

CANTILEVER SENSORS

A single supported beam, known as a cantilever, is a basic mechanical structure with well described strain and bending characteristics [1]. These two aspects, strain and bending, are the bases of most cantilever applications in static sensing. Moreover, a cantilever can be described as a second-order system with distinct resonance characteristics determined by the cantilever mass and spring constant as well as by the ambient conditions [2]. Therefore, any changes in these parameters will be reflected as a variation in the resonance characteristics. This characteristic makes the cantilever a prominent choice for dynamic sensing applications [3-7].

In this chapter, first a brief overview of different cantilever sensor schemes is introduced; then the basic equations of the cantilever deflection and vibration are presented. Next, the characteristics of a cantilever-based system, as a second-order system, are summarized. Finally, a concise description of piezoresistive cantilever sensors, including their sensing principle and applications, is presented.

2.1 Sensing Techniques Using Cantilevers

Extensively used as building blocks in civil and aeronautical structures, cantilevers were first introduced in the sensors realm as strain gauges [8, 9]. Despite earlier applications as microphones [10], pressure sensors [11], and accelerometers [12, 13], it was the invention of the atomic force microscopy (AFM) [14] that gave a robust commercial momentum to

cantilever-based sensors. Also, it was upon the development of AFM that the potential of the cantilever as a dynamic sensor was explored [14-17].

Regardless of the sensing method (static or dynamic), cantilever sensors can be categorized based on the employed detection scheme. The main detection schemes are listed as optical, piezoresistive, piezoelectric, electrostatic, tunneling, and thermal. The rest of this section introduces these schemes. Piezoresistive cantilevers will be reintroduced in more detail in Section 2.4.

2.1.1 Optical Cantilever

Not long after the invention of AFM, optical cantilevers were first introduced [15]. The basic operation principle of this type of cantilever lies in optical reflection from the back surface of the beam, while the front surface interacts with the sample [5, 18-23]. The earlier optical detection schemes were based on laser interferometry [15, 16], in which the resonance characteristic is extracted from the interference patterns between a reference light beam and the one reflected from the cantilever's back surface. Soon after the introduction of optical cantilevers, the less complex scheme of position-sensitive detection (PSD) was developed [24, 25]. In a PSD scheme, a laser beam is emitted to the cantilever back surface at an angle; depending on the bending of the cantilever, the reflected laser beam travels at a peculiar angle; thus the cantilever deflection can be measured down to nano-scales. In this application, the cantilever functions only as a light-reflecting ultra-soft spring, often called an "optical lever" [25].

Optical cantilevers are highly sensitive to such an extent that, for example, when implemented in the magnetic resonance force microscopy (MRFM) [26], a single electron spin can be detected [27]. Besides the high sensitivity, another advantage of this type of cantilever is its relative ease of fabrication, which is due to the omission of any needs for electrical connections to the cantilever. Optical cantilevers have been primarily made of tungsten wires [16, 24], silicon [28-31], silicon nitride [32-34], and polymers [35-37].

2.1.2 Piezoresistive Cantilever

Bending a cantilever beam introduces directional stress, which will cause a resistance change if applied to a resistor. This quality, the dependence of electrical resistivity on stress, is called piezoresistance. Crystals, both metals and semiconductors, show piezoresistance [38-40], but while in metals the change of resistance is mainly a result of the geometrical variation [39, 41], in semiconductors the piezoresistance originates from a change of the band-gap energy [42, 43].

In a piezoresistive cantilever the detecting resistors, called piezoresistors, are placed at potentially high-stress points of the cantilever beam; as long as the cantilever deflection is negligible compared to its length, the resistance of piezoresistors changes linearly with the deflection [44]. The considerable advantages of this scheme are the implementation of the detection mechanism within the cantilever [45, 46], CMOS integration capability [6, 47], and the possibility of making large cantilever arrays [48, 49]. A limiting factor in this detection scheme is the presence of Johnson and Hooge noise with the resistors [50]. This type of cantilever is introduced in more detail in Section 2.4.

2.1.3 Piezoelectric Cantilever

Piezoelectric cantilevers are used in a variety of applications, including accelerometers [13, 51], mass sensors [52-55], mass flow sensors [56], chemical sensors [57], scanning tunneling microscopy (STM) [58], and AFM [59-61]. The detection mechanism in this type of cantilever is based on the generation of an electric field resulting from the introduction of stress (e.g., by bending) to single or multiple layers of piezoelectric materials such as ZnO and PZT. Whereas in the first three cited applications the cantilever is operating in the static mode, resonating piezoelectric cantilevers are extensively used in AFM.

2.1.4 Electrostatic Cantilever

By forming a capacitor between the cantilever surface and a fixed plate (i.e., counter electrode), the cantilever deflection can be measured as a capacitance change [62-65]. With this approach, not only can the static deflections be detected, but also in the dynamic mode, the resonance characteristic of the capacitive cantilever can be used as a sensing measure. A resonating cantilever, when used in the capacitive configuration, generates a periodic capacitance change. When implemented in an LC circuit, the cantilever resonance results in a frequency modulation. Hence, variations of the cantilever resonance frequency can be detected by demodulating the output signal [66].

2.1.5 Tunneling Cantilever

The very first AFM was in fact a modification of the existing scanning tunneling microscopy systems [14]. In this scheme, a tunneling tip is placed at nano-scale

proximity of the cantilever surface that has a conductive coating. The dependence of the tunneling current I on the gap g between the metallic electrodes is described as [67, 68]

$$I \propto Ve^{-a\sqrt{\Phi g}} \qquad (2.1)$$

where V is the bias voltage, Φ is the height of tunneling barrier, and $a = 1.025\ \text{Å}^{-0.5}\text{eV}^{-0.5}$ is a conversion factor. When the sample is scanned, the cantilever deflects, thus causing a change in the gap between the tunneling tip and the coated surface on the cantilever. Hence, the tunneling current changes in proportion to the deflection of the cantilever tip [14]. Besides for the AFM application, tunneling cantilevers have been used in accelerometers [69] and infrared sensors [69].

2.1.6 Thermal Cantilever

Unlike the mentioned cantilever detection schemes, beam bending is not the working principle of a thermal cantilever; rather the beam acts as a heat conduction path for a thermal probe [70, 71]. Thermal interaction of the scanning probe with the surface can be utilized in a voltage generation scheme as in thermocouples [72], or it can result in a thermal resistance variation, which in turn changes the electrical resistance of the detector [73]. Thermal cantilevers have been used in thermal imaging [72], data storage [71, 73, 74], and nano-topographical imaging [75, 76].

The pros and cons of the different detection schemes are summarized in Table 2.1.

Table 2.1. Overview of cantilever detection schemes.

Detection scheme	Pros	Cons
Optical	• No need for electrical connection to cantilever • Ease of fabrication with capability of making ultra thin beams • Linear response • Highly sensitive • Reliability; Highly commercialized	• Needs external optical detection unit • Needs calibration upon change of medium (e.g. liquid, gas) • Unsuitable for high opacity, or high turbidity media • Parallel scanning of an array of cantilever is challenging • Limited to bandwidth of PSD
Piezoresistive	• Implementation of detection mechanism inside cantilever • CMOS integration • Can be used in any medium • Large dynamic range • Reliability; Well commercialized • Implementation in large arrays	• Needs a piezoresistive layer to be implemented over structural layer • Thermal power dissipation in piezoresistors and thermal drift • Generated heat can cause erratic beam deflection • Associated noise of resistors
Piezoelectric	• Self-generating, Self-sensing	• DC leakage current makes static applications challenging • Small output signal
Electrostatic	• CMOS compatible • Large dynamic range	• Needs calibration upon change of dielectric constant of medium • Unsuitable in electrically conductive media • Variation of dielectric constant of different parts of scanned sample should be taken into account. • Non-linear response
Tunneling	• Highly sensitive	• Non-linear response • Limited dynamic range • Needs extra tunneling tip mounted over cantilever
Thermal	• Highly sensitive • No (out of plane) bending is required • CMOS compatible	• Thermal power dissipation • Can alter scanned sample properties • Needs calibration upon change of medium • No dynamic application reported • Variation of thermal conductivity of different parts of the scanned sample should be taken into account.

2.2 Physics of Cantilevers

In this section the basic equations of cantilever beam deflection in both static and dynamic modes are briefly reviewed. The beam is assumed to be homogenous with uniform cross section. Also, for simplicity, the Poisson ratio is assumed to be negligible. First, to interpret the characteristics of systems utilizing cantilevers, the characteristics of second-order systems are briefly reviewed.

2.2.1 Second-Order Systems

The motion of a cantilever resonator, as a lumped mass-spring system, can be described by the differential equation of a second-order system with constant coefficients [2]:

$$m\frac{d^2y}{dt^2} + B\frac{dy}{dt} + ky = F(\Omega t), \tag{2.2}$$

where *y(t)* is the displacement of the lumped mass *m*, *k* is the spring constant, *B* is the velocity-related damping coefficient, and *F* is the excitation force applied on the lumped mass with an angular velocity of Ω. From the properties of the second-order system, the natural resonance frequency f_0 is calculated:

$$f_0 = \frac{\omega_o}{2\pi} = \frac{1}{2\pi}\sqrt{\frac{k}{m}}, \tag{2.3}$$

where ω_o is the natural angular velocity (radial resonance frequency) of the system.

The quality factor (*Q* or Q-factor) of a damped system is defined as [77]

$$Q = 2\pi\frac{\text{stored vibration energy}}{\text{dissipated energy per cycle}}. \tag{2.4}$$

In a second-order electrical system, the definition in Eq. (2.4) can be described in terms of the real and imaginary parts of impedance [78]:

$$Q = \frac{\mathrm{Im}(Z)}{\mathrm{Re}(Z)}. \tag{2.5}$$

A second-order mechanical system is analogous to an electrical system by corresponding F and dy/dt to voltage V and current I, respectively. This way, Q is calculated as

$$Q = \frac{m\omega_o}{B} = \frac{k}{B\omega_o} = \frac{\sqrt{km}}{B}. \tag{2.6}$$

The free vibration resonance angular velocity $\omega_{\max}$ is given by [2]

$$\omega_{\max} = \omega_o \sqrt{1 - \frac{1}{4Q^2}}. \tag{2.7}$$

Excited by a sinusoidal force F, the vibration amplitude will be [2]

$$y(t) = \frac{\beta}{k}|F|\sin(\Omega t - \theta), \tag{2.8}$$

where $|F|$ is the maximum amplitude of the applied force, β is the magnification factor

$$\beta = \frac{1}{\sqrt{(1 - \frac{\Omega^2}{\omega_o^2})^2 + (\frac{1}{Q}\frac{\Omega}{\omega_o})^2}}, \tag{2.9a}$$

and θ is the phase angle expressed as

$$\theta = \tan^{-1}\left(\frac{\Omega/\omega_o}{Q(1 - \Omega^2/\omega_o^2)}\right). \tag{2.9b}$$

The forced vibration resonance angular velocity Ω_o is given by

$$\Omega_o = \omega_o \sqrt{1 - \frac{1}{2Q^2}}. \tag{2.10}$$

In the case of weak damping, or alternatively large Q, the resonance frequency can be closely approximated by Eq. (2.3); in other words, $\Omega_o = \omega_o$ and $\omega_{\max} = \omega_o$.

The most common way to measure the Q-factor of a resonator is based on the half-power bandwidth Δf_{-3dB} in the resonance transfer function [79]:

$$Q = \frac{f_o}{\Delta f_{-3dB}}. \qquad (2.11)$$

Other techniques of measuring the Q-factor are discussed in more detail in the next chapter.

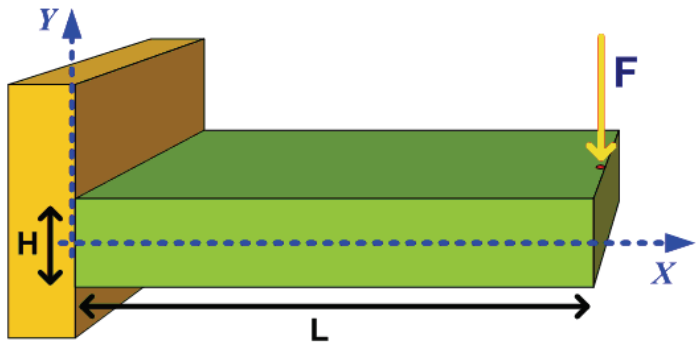

Figure 2.1. Schematic of a cantilever with length *L* and thickness *H*, with respect to coordinates *X* and *Y*, before being deflected by a point force *F* applied on the tip.

2.2.2 Cantilever Bending (Static)

The cantilever bending *y* as the result of applying a point force *F* on the beam free end (i.e., the tip – see Figure 2.1) is described at a point *x* along the cantilever length as [80]

$$y(x) = \frac{FL}{2EI} x^2 \left(1 - \frac{x}{3L}\right), \qquad (2.12)$$

where *E* is the Young's modulus, *I* is the moment of inertia, and *L* is the beam length. Equation (2.12) is valid as long as the beam deflection is negligible compared to its length (i.e., y << L). Regarding Eq. (2.12), the cantilever spring constant, i.e., the ratio of force to deflection on the cantilever tip, can be calculated as

$$k = \frac{F}{y(L)} = \frac{3EI}{L^3}. \tag{2.13}$$

In general, if the force is exerted at an arbitrary point x_f on the cantilever, the bending will be [81]

$$y(x) = \frac{FL}{2EI} \times \begin{cases} \frac{x_f}{L} x^2 (1 - \frac{x}{3x_f}) & x \le x_f \\ 2\frac{x_f^2}{L}(\frac{x_f}{3} + \frac{x - x_f}{2}) & x_f \le x \le L \end{cases}. \tag{2.14}$$

The moment of inertia for a rectangular cantilever beam is given as [1]

$$I = \frac{1}{12} W H^3, \tag{2.15}$$

where W and H are the width and length of the cantilever.

The induced longitudinal stress on the cantilever is calculated as [1]

$$\sigma_x = z\frac{E}{\rho}, \tag{2.16}$$

where z is the distance from the beam neutral axis, and ρ is the beam radius of curvature. For a point force F applied at the point x_f on a single-layer rectangular cantilever, the stress is

$$\sigma_x = \begin{cases} \frac{12z(x_f - x)}{H^3 W} F & x \le x_f \\ 0 & x_f \le x \le L \end{cases}. \tag{2.17}$$

From Eq. (2.16) it can be seen that the maximum stress occurs on the cantilever surface. Also, from Eq. (2.17), the stress magnitude is the highest at the cantilever clamped end, and linearly decreases toward the tip. When a point force is applied at the tip, the magnitude of the longitudinal stress at point x is

$$\sigma_x = \frac{12z(L-x)}{H^3 W} F \,. \tag{2.18}$$

In a single-layer rectangular cantilever, where the neutral axis is located at the center of the beam, the maximum stress at point x is ($z = H/2$)

$$\sigma_x = \frac{6(L-x)}{H^2 W} F \,. \tag{2.19}$$

On the other hand, considering Eqs. (2.13), (2.15), and (2.18), the induced stress resulting from a deflection $\Delta y = y(L)$ at the tip is

$$\sigma_x = \frac{3E(L-x)z}{L^3} \Delta y \,, \tag{2.20}$$

and the maximum stress at point x is ($z = H/2$)

$$\sigma_x = \frac{3}{2} \frac{EH(L-x)}{L^3} \Delta y \,. \tag{2.21}$$

In assessing the performance of a cantilever in force sensing applications, an important figure is the cantilever's force spectral density $S_F(f)$, which is defined as the Fourier transform of the autocorrelation function of the fluctuating (time dependent) effective force on the cantilever tip [82]. The "force noise spectral density" is given by $(S_F(f))^{0.5}$ (unit: N/Hz$^{1/2}$), and the total root mean square force noise is the integral of force noise spectral density over the measurement bandwidth. In some literature the force noise spectral density is also called force sensitivity [82, 83]. Ideally, the noise performance of the cantilever is limited to the sensor's thermomechanical noise [84, 85]; in this case $S_F(f)$ is calculated as (lumped-mass model)

$$S_F = 4k_B TB = 4k_B Tk / \left(2\pi Q f_0\right), \tag{2.22}$$

where k_B and T are the Boltzmann constant and temperature, respectively. As mentioned in Section 2.2.1, k, f_0, Q, and B are the cantilever's spring constant, resonance frequency, quality factor, and damping coefficient, respectively.

2.2.3 Cantilever Vibration (Dynamic)

The equation of cantilever motion for flexural vibrations of an undamped system is given by [86]

$$EI\frac{\partial^4 y(x,t)}{\partial x^4}+\rho A\frac{\partial^2 y(x,t)}{\partial t^2}=0\,, \tag{2.23}$$

where ρ is the mass density and A is the cross-sectional area. Equation (2.23) is solved by assuming the possibility of separation of time and space:

$$y(x,t)=y(x)e^{i\omega_n t}\,, \tag{2.24}$$

where ω_n is the angular resonance frequency of the n^{th} overtone (flexural mode). With the above assumption, the differential equation for the spatial coordinates based on Eq. (2.23) can be written as

$$EI\frac{\partial^4 y(x)}{\partial x^4}-\rho A\omega_n^2 y(x)=0\,. \tag{2.25}$$

For a cantilever (clamped-free beam), the boundary conditions are as follows:

at the clamped end ($x = 0$):

$$y(0)=0,\quad \left.\frac{\partial y}{\partial x}\right|_{x=0}=0\,, \tag{2.25a}$$

and at the free end ($x = L$):

$$\left.\frac{\partial^2 y}{\partial x^2}\right|_{x=L}=0,\quad \left.\frac{\partial^3 y}{\partial x^3}\right|_{x=L}=0\,. \tag{2.25b}$$

The deflection y, i.e., the vibration amplitude, along the beam is

$$y(x) = c_1(\cos\frac{\lambda_n}{L}x - \cosh\frac{\lambda_n}{L}x) + c_2(\sin\frac{\lambda_n}{L}x - \sinh\frac{\lambda_n}{L}x) \tag{2.26}$$

with

$$\lambda_n^4 = \frac{\rho A \omega_n^2 L^4}{EI}, \quad \cos\lambda_n \times \cosh\lambda_n = -1 \tag{2.26a}$$

and

$$\begin{aligned} c_1 &= \frac{y(L)}{2}, \\ c_2 &= -\frac{\cos(\lambda_n) + \cosh(\lambda_n)}{\sin(\lambda_n) + \sinh(\lambda_n)} \times c_1 \ . \end{aligned} \tag{2.26b}$$

Hence, from Eqs. (2.15) and (2.26a), the resonance frequency of a rectangular cantilever beam is calculated as

$$f_n = \frac{\omega_n}{2\pi} = \frac{\lambda_n^2}{2\pi\sqrt{12}}\frac{H}{L^2}\sqrt{\frac{E}{\rho}} \ . \tag{2.27}$$

For a simple rectangular cantilever beam, the values of λ_n are as follows:

$\lambda_1 = 1.875$, $\lambda_2 = 4.694$, $\lambda_3 = 7.855$, $\lambda_4 = 10.996$, and for $n > 4$: $\lambda_n \approx (n - ½)\pi$.

2.3 Piezoresistive Cantilever Sensors

In this section, after a brief introduction to the piezoresistance effect, the sensing applications of piezoresistive cantilevers are reviewed. The section is concluded by referring to a special application, i.e., using piezoresistive cantilevers for the characterization of nano/micro-jets.

2.3.1 Piezoresistance Effect

As briefly mentioned before, piezoresistance is a characteristic of conductive and semi-conductive materials, attributed to the change of the electrical resistance with an applied stress (strain). The phenomenon of the resistance change of metallic wires with elastic strain has been investigated since the mid-19th century, after the pioneering works of Thomson[1] [87, 88] followed by, particularly, Bridgman's works on the piezoresistance measurements of polycrystalline materials [38, 89]. In the mid-20th century, after the theoretical modeling of the energy level structure in diamond crystals (e.g., silicon and diamond), it was predicted that the energy gap between the valence and conduction bands would increase with the decrease of the atomic spacing and, therefore, with pressure [90, 91]. This prediction was confirmed by observation of the resistance change of p-n junctions with pressure in germanium [92], and especially by Smith's work on the piezoresistance effect in germanium and silicon [40]. Being the dominant material in the semiconductor industry, silicon has been comprehensively studied as a prominent piezoresistive material [42, 43, 93-96]. Also, besides crystalline silicon, the piezoresistive properties of other microelectronic materials have been exploited and characterized, such as poly-Si [97, 98], GaAs [99-101], GaN [102], SiC [103], poly-C [104, 105], and amorphous materials [106, 107]. In addition, with the development of non-conventional micro-fabrication techniques, the piezoresistance effect in carbon nanotubes [108] and thin metal films [41] has been recently investigated. These materials are demonstrated to be viable alternatives in piezoresistive detection [109-111].

[1] Also known as Lord Kelvin

The change of resistance with strain is partly due to geometrical changes in the deformed body and partly due to physical changes within the material itself. Together these two effects are described by the strain gauge factor γ [112]:

$$\gamma \equiv \frac{\Delta R/R_o}{\Delta \varepsilon} = (1+2\nu) + \frac{\Delta \rho/\rho_o}{\Delta \varepsilon}, \qquad (2.28)$$

where R_o is the initial resistance, $\Delta R=R-R_o$ is the resistance change resulting from the strain change $\Delta\varepsilon$, ν is the Poisson's ratio, and ρ_o and $\Delta\rho$ are the electrical resistivity and the change of resistivity resulting from $\Delta\varepsilon$, respectively. Whereas the first term on the right-hand side of Eq. (2.28) is the dominant factor in metals, the piezoresistance of semiconductors is overwhelmingly determined by the second term. When an isotropic monocrystalline semiconductor is subjected to stress, its resistivity ρ becomes a symmetric second-rank tensor. For small stresses, the partial change of each element of the resistivity tensor can be approximated from a linear relationship with the stress via the fourth-rank tensor π of piezoresistance coefficients [40, 43]:

$$\frac{\Delta \rho_{ij}}{\rho_o} = \sum_{k,l} \pi_{ijkl} \sigma_{kl} \,. \qquad (2.29)$$

Here, σ_{kl} is the stress tensor, which implies that the resistance change depends on the orientation of the stress too. In cubic materials (e.g., Si), the resistivity is a scalar ρ_o, and π can be simplified to a six-element column matrix [40, 80]. Moreover, for relatively long and narrow resistors, the expression for the resistance change can be simplified by casting the piezoresistance matrix into only two coefficients. These coefficients represent the piezoresistance when the stress is oriented either in parallel, π_l [113], or perpendicular, π_t [114, 115], to the electrical current flow direction:

$$\frac{\Delta R}{R} = \frac{\Delta \rho}{\rho_o} = \pi_l \sigma_l + \pi_t \sigma_t , \qquad (2.30)$$

where σ_l and σ_t are, respectively, the longitudinal and transverse components of the stress with respect to the current direction. The piezoresistance coefficients, particularly in silicon, depend not only on the direction of the applied stress, but also on the operating temperature as well as the material doping [93, 116]. To reduce the effect of local temperature variations on the measured resistance change, i.e., to have a first-order temperature compensation, the piezoresistors are usually arranged in a Wheatstone bridge configuration [117, 118].

To apply Eq. (2.30) in a piezoresistive cantilever, the piezoresistor must experience a considerable net compressive (tensile) stress. To meet this requirement, the piezoresistive cantilever can be formed by stacking two distinct lateral layers, namely, structural and transducer layers. In this way, each layer experiences a net stress opposite in direction to the other layer; hence, the compressive and tensile stresses across the cantilever beam do not cancel out each other in that layer.

2.3.2 Piezoresistive Cantilever Applications

Because of their self-sensing characteristic and CMOS integrability, piezoresistive cantilevers have been successfully commercialized, especially in applications such as accelerometers (Sensonor [119], Endevco [120]), AFM probes (Piezolever® from Park Scientific [121, 122]), and sensing modules (Cantion [123]).

Piezoresistive cantilevers have been used either in the direct measurement of force/stress and their associates such as acceleration, deflection, and bending, or in the measurement of general cantilever properties such as resonance frequency and mass via a piezoresistive detection scheme. This section summarizes the applications of these measurement approaches.

A. Force sensing - static mode

Inspired by the available strain gauges [8], the first application of semiconductor piezoresistive cantilevers as force sensors was in microphones [10]. In the early piezo-resistive sensors, the cantilever consisted of two layers of semiconductor attached together with an insulating cement to form a bimorph unit, where each layer would sense a net stress opposite in direction [10, 113]. Besides the microphone application, bimorph piezoresistive cantilevers were used in accelerometers [124], displacement, force and torque sensors [113], and as pressure sensors in intracardiac catheters, the first reported biomedical application of silicon piezoresistance [11]. Later on, with the development of semiconductor technology, the bimorph approach was replaced with designs based on diffused piezoresistors [114, 125]. The first batch-fabricated silicon accelerometers were presented in the late 1970s, at the onset of integrated-circuit technology [12]. Eventually, the invention of AFM opened a new horizon for the piezoresistive cantilever application [45].

As presented by Eq. (2.19), for a given applied force on the cantilever tip, the induced stress increases with decreasing cantilever thickness. In contrast, from Eq. (2.21), for a

given tip deflection, the induced stress increases with increasing cantilever thickness. Therefore, for the direct force sensing applications, e.g., in force, torque, pressure sensors or accelerometers, the piezoresistive cantilever is desired to be thinner. In the topography applications, e.g., AFM, there are two main approaches [59]: 1) contact imaging, when the cantilever is operated in the repulsive atomic force region and its deflection is sensed; 2) non-contact imaging, when the cantilever is operated in the attractive atomic force region and the force is sensed directly. In non-contact imaging, too, the piezoresistive cantilever is desired to be as thin as possible. In contact imaging, however, there is a trade-off between the piezoresistive cantilever sensitivity, which increases with the cantilever thickness, and performing a non-destructive measurement. Here, a thicker piezoresistive cantilever has a greater sensitivity, but also a greater stiffness (see Eq. (2.13)); hence, despite the intended gain in sensitivity, applying thicker cantilevers can potentially damage the specimen.

The thinnest cantilever reported is an optical cantilever with a thickness of 12 nm [31]; however, reaching such small thicknesses is not trivial in piezoresistive cantilevers because a piezoresistive cantilever needs at least two separate layers for an efficient stress detection. As mentioned before, these layers are either formed by employing the bimorph configuration or by using different doped regions. In the latter case, despite the undertaken efforts [126, 127], it is practically impossible to scale down the thickness to the limit and still maintain separate doped regions. Hence, the alternative approach in minimizing the thickness of a piezoresistive cantilever is to adopt the bimorph configuration in a way that the nano-scale transducer layer can be attached to or built

over the structural layer. Adopting this approach, e.g., by using epitaxially grown p-doped silicon over an n-doped region, piezoresistive cantilevers as thin as 100 nm are fabricated [82, 128], with force resolutions in the atto-Newton scale at room temperature. The same approach has been applied to InAs/AlGaSb heterostructures to fabricate 300 nm thick III-V piezoresistive cantilevers [129].

To boost the sensitivity, besides decreasing the cantilever thickness, the piezoresistive coefficients can be improved. As mentioned before, the conventional methods in improving the piezoresistance effect are to change the dopant concentration and to reduce the operation temperature. Moreover, the most recent method is to shrink the piezoresistive layer to the nano-scale domain, where 2-D and 1-D quantum effects in the piezoresistive material also contribute to improving the piezoresistance of the thinned layers [130], or nanowires [131].

Finally, utilizing the principle of stress concentration (SC) [1] is another unique approach in increasing the sensitivity of piezoresistive cantilevers [132-134]. In this approach, the strain energy of the beam is concentrated on the locations that the piezoresistors are placed; hence, for a given force, the output signal increases. This topic is revisited in Chapter 3.

B. Force sensing - dynamic mode

A resonant force gauge converts an externally applied force into a shift of resonance frequency [135]. In the non-contact scanning mode in AFM, when the tip-sample

proximity z is within the range of the van der Waals and electrostatic forces (both represented by a net force F), the force gradient of the tip-sample interaction $\Delta k = \partial F / \partial z$ alters the effective spring constant [136], and, according to Eq. (2.3), it changes the resonance frequency of the cantilever. Depending on the extent of the resonance frequency shift, therefore, the amplitude of the applied force can be calculated. This method is applicable not only to the piezoresistive cantilevers [49, 121] but also to the other detection schemes [15].

C. Surface stress sensing

A difference in surface stress at an interface on a plate results in bending toward the side experiencing the higher tension. This deflection was first formulated by Stoney [137]. A more generally used equation relates the radius of curvature R to the surface stress difference $\Delta\sigma$ [138, 139]:

$$\Delta\sigma = \frac{E}{(1-\nu)}\frac{t^2}{6R} \tag{2.31}$$

where t is the thickness of the plate, E is the effective Young's modulus, and ν the Poisson ratio. This concept can be used in cantilever sensors: Upon binding ligands to receptors, which are covering only one side of a cantilever, the cantilever bends and hence experiences a volume stress. Applying this technique, optical cantilevers have been repeatedly used in environmental [140] and chemical-biological sensing applications [5, 7, 21, 23, 141]. Piezoresistive cantilevers also have shown promising results in this application [142-145], especially when the beams are made from polymeric structures [109, 110].

D. Mass sensing

Based on Eq. (2.3), which describes the resonance frequency of a second-order system, it can be derived that

$$\frac{df}{f} = -\frac{1}{2}\left(\frac{dm}{m} - \frac{dk}{k}\right). \qquad (2.32)$$

Hence, assuming no variations in the spring constant (i.e., $dk = 0$), a mass change dm will result in a frequency shift df. This concept has long been in use for chemical detection [146]: Upon interaction of the targeted analyte with a proper coating on the resonator surface, the total mass of the resonator changes. Therefore, the resonance frequency stabilizes at a new value. Although first used to determine the spring constant of cantilevers [147], this technique in conjunction with cantilevers has formed a very reliable sensing method [3, 148-150], especially when the detection mechanism is integrated with the sensor by means of the piezoresistive scheme [6, 140, 151-153].

Cantilever mass sensors benefit from two distinct advantages over other resonant mass sensors (e.g., QCM, TSMR and SAW [154, 155]), namely, higher sensitivity and the possibility of implementation in arrays. The smaller mass of the cantilevers ensures the advantage of higher sensitivity, while the smaller size of the cantilevers makes it possible to implement arrays of cantilevers in a limited area, especially when the read out is integrated with the sensors, as in the case of piezoresistive cantilevers [49]. For resonant sensors, the ultimate reported mass detection sensitivity is in the ranges of zeptogram [156, 157] and attogram [158], while the mass sensitivity of piezoresistive cantilevers typically is in the picogram range [6, 151, 159].

The quality factor, Q, is an important parameter in resonant cantilever sensors for both mass sensing and force sensing applications. To have a clearly detectable frequency shift, the new resonance frequency should be completely distinguishable from any previous resonance traces at that frequency (see Figure 2.2). The minimum detectable frequency shift Δf can be described in proportion to the resonator half-power bandwidth Δf_{-3dB},

$$\Delta f = r\Delta f_{-3dB}, \tag{2.33}$$

where r defines the proportionality ratio; hence, using Eq. (2.11), it can be derived that the resonator's frequency resolution is inversely proportional to Q

$$\frac{\Delta f}{f} = \frac{r}{Q}. \tag{2.34}$$

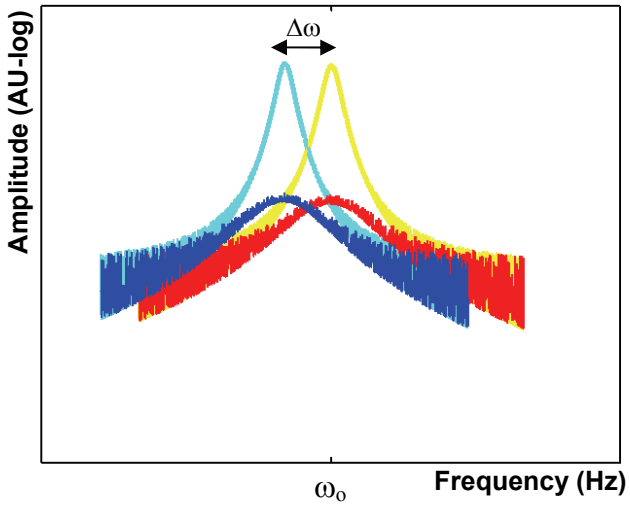

Figure 2.2. Shift in resonance frequency as the result of mass change: Δω, the shift in resonance frequency due to a mass change, is more apparent in the resonator with a higher Q, i.e. the one with sharper peaks.

In other words, it is ultimately desirable to have the resonance spectrum in the shape of an extremely confined peak at the resonance frequency (i.e., a Dirac's Delta function). This spectral characteristic becomes even more desirable after considering the effect of

noise on the variation of resonance peak. In practice, based on the definition of the quality factor, a higher level of sharpness in the resonance spectrum is achieved with a higher Q. Hence, it is an objective to optimize the cantilever geometry to obtain the maximum quality factor in the resonance mode of interest. This objective is pursued in this work and discussed in more details in Chapter 5.

2.3.3 Special Application: Micro/Nano-Jet Characterization

Conventional metrology techniques in the characterization of liquid flows, in particular jet streams, are mainly the particle image velocimetry (PIV) [160-162] and the hot-wire anemometry (HWA) [163, 164]; however, when the jet diameter is shrunk to 10 μm and less, the accuracy of these conventional techniques is questionable. In the micron and submicron jet domains, not only is the laser wavelength in PIV comparable or larger than the jet diameter, but also the tracing particles [160] can clog the jet nozzle. On the other hand, the existing hot-wire anemometers, even when miniaturized [164], are still larger than the micro/nano jet columns, so they cannot be fully immersed into the jet stream, especially in the liquid flows.

Utilizing piezoresistive sensors is another approach for measuring the flow characteristic [165-167]. Although, unlike in PIV, placing a cantilever in front of the jet will disturb the flow stream (i.e., it is an intrusive diagnostic investigation), a piezoresistive cantilever, because of its integrated read-out mechanism, is a viable alternative for characterizing jet flows in the micro/nano domains [168]. Since the liquid and gaseous jet can dramatically change the temperature along the cantilever, the measurement will be more reliable if the

piezoresistors are implemented in a Wheatstone bridge to have first-order temperature compensation.

Figure 2.3 shows a transverse scan profile of a piezoresistive cantilever over a liquid jet steam ejected from a 10 μm×10 μm square nozzle at a pressure of 3.8MPa across the cantilever with a speed of 0.7 μm/s [168]. The jet impinges on the cantilever at 50 μm distance from the beam free end. The distance between nozzle and cantilever is approximately 480 μm. The employed cantilever has a deflection sensitivity of 1.01 mV/μm at 1V bias.

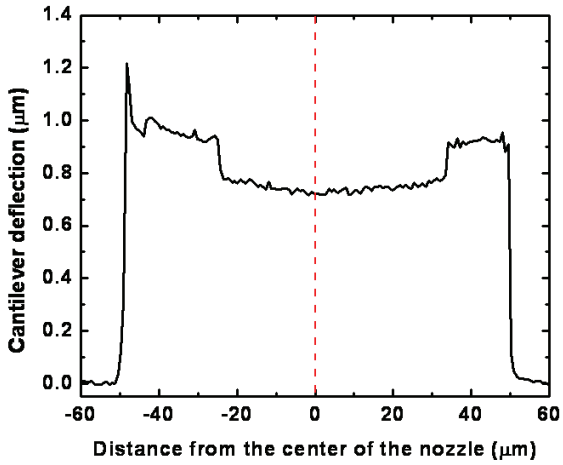

Figure 2.3. Transverse scan of a piezoresistive cantilever over liquid jet [168].

A major criterion in selecting a piezoresistive cantilever for the micro-jet metrology is the force sensitivity of the cantilever. The jet velocity v is proportional to the impingement force on the cantilever, F, [169]:

$$v = \sqrt{\frac{F}{C_m A_{jet} \rho}}, \tag{2.35}$$

where A_{jet} is the size of the impingement area, ρ is the fluid density, and C_m is a correction factor that accounts for the portion of the total momentum that is transferred to the cantilever (ideally C_m = 1, when the total jet momentum is transferred to the cantilever). Using Eq. (2.17), F is extracted based on the measured stress and the impingement location. In Eq. (2.30) the amount of resistance change corresponds to the induced stress given by Eq. (2.17). In practice, the stress calculation is usually bypassed and the cantilevers are calibrated by recording the force gauge factor, i.e., the resistance change versus the applied force. The force preferably should be applied at the same spot as the jet impingement location; otherwise, using Eq. (2.14), the force gauge factor should be corrected.

As mentioned before, a common approach to improve the force sensitivity of a cantilever is to thin the beam, i.e., to reduce its spring constant. In this case, however, reducing the beam stiffness results in delicate devices that are not suitable for harsh-environment testing, e.g., interaction with the jet streams. Moreover, for a given force, a smaller spring constant means a larger deflection, thus potentially operating the device in its nonlinear region. Also, after the jet impingement, the presence of the surrounding liquid layer [168] can affect the sensitivity of ultra-soft cantilevers. To address these issues, a new type of cantilever, highly sensitive yet stiff enough, is introduced in Chapter 3.

CHAPTER 3

STRESS CONCENTRATING CANTILEVER

The focus of this chapter is on modifying piezoresistive cantilevers for an optimum force sensing in static mode. To this end, a new technique in utilizing the stress concentration in cantilevers is introduced. In general, the force sensitivity of a piezoresistive cantilever can be described by 3 partial sensitivity terms associated to the transduction of a) S_1: force F to deflection z, b) S_2: deflection to stress σ, and c) S_3: stress to relative resistance change dR/R,

$$S = \frac{dz}{dF} \times \frac{d\sigma}{dz} \times \frac{dR/R}{d\sigma} = S_1 \times S_2 \times S_3 \ . \tag{3.1}$$

S_3 depends only on the piezoresistive coefficients and the piezoresistors arrangement [43]. In a simple cantilever beam subjected to a transverse point force F, as described in Chapter 2 by Eq. (2.17), the longitudinal stress is given [81]

$$\sigma_x = \begin{cases} \dfrac{12z(x_f - x)}{H^3 W} F & x \le x_f \\ 0 & x_f \le x \le L \end{cases}, \tag{3.2}$$

where L, W, and H are the cantilever length, width, and thickness, respectively, and x_f is the location of the force exertion point on the beam. Inside the cantilever, z represents the distance from the neutral axis ($z \le H/2$). Based on Eq. (3.2) the maximum longitudinal stress occurs on the surface (i.e., $z = \pm H/2$) and its magnitude increases toward the clamped edge of the beam (i.e., $x = 0$). In general, according to Eq. (2.16) from Chapter 2, the maximum longitudinal stress is inversely proportional to the radius of bending curvature [1]. In other words, with a point force applied on the cantilever tip, the maximum induced stress increases by decreasing the beam stiffness [81]. In

piezoresistive cantilevers the conventional approach in improving the force sensitivity is to reduce the stiffness by making the beams thinner, i.e., increasing S_1 [128]; however, despite the effectiveness of this approach, the resulting reduction of the resonance frequency overshadows the sensor performance. Moreover, decreasing the beam stiffness may increase the fragility of the force sensor to survive harsh-environment operations [170]. Finally, for a given force, a smaller cantilever stiffness amounts to a larger deflection, potentially causing a nonlinear sensing characteristic by driving the cantilever into its nonlinear bending region.

In a piezoresistive cantilever, however, instead of increasing the stress through the entire beam volume, it is possible to concentrate the strain energy only in fractions of the beam that the sensing elements are located; in other words, increasing S_2 without decreasing the overall thickness of the beam. The two approaches previously reported in this regard are either to make the cantilever locally thinner in the piezoresistors region [1, 132, 133], or to etch holes through the beam next to the piezoresistors [171]. The disadvantage of the former approach is the decrease of the cantilever stiffness, while the latter approach does not significantly improve the sensitivity.

The proposed design in this chapter combines both approaches by concentrating stress through fully suspended beams on the cantilever surface. In the presented scheme, the sensitivity S_2 is increased without sacrificing S_1.

3.1 Theory of Stress Concentrating Cantilevers

As mentioned in Chapter 2, in a simple cantilever beam, a flexural bending introduces a longitudinal stress σ_x along the beam, which is defined by

$$\sigma_x = \frac{zE}{\rho}, \tag{3.3}$$

where ρ is the radius of bending curvature, E the Young's modulus, and z the distance from the neutral axis. Equation (3.3) indicates that the absolute magnitude of the stress σ_x increases linearly with distance z form the beam neutral axis, thus the maximum stress appears on the cantilever surface. Hence, it is desirable to place the stress sensing elements at a location as far as possible from the neutral axis. We call such location the sensing surface. Alternatively, the same objective can be accomplished by driving the neutral axis away from the sensing surface. This goal is achieved in this work by forming a void underneath the sensing area. The void is extended across the beam and it is asymmetrical to the neutral axis by being closer to the sensing surface (see Figure 3.1). By using such a configuration not only is the neutral axis pushed away form the sensing surface, but also the presence of the void results in a stress concentration in the adjacent areas. Referring to Eq. (3.3), applying the proposed approach affects both z and ρ in such a way that leads to further increase of σ_x. Figure 3.1 illustrates the effect of void location on the neutral axis position. When the void is centered with respect to the beam thickness, the neutral axis stays at the same level as for the rest of the cantilever (Figure 3.1(a)). By placing the void closer to one surface, the neutral axis moves toward the opposite surface (Figure 3.1(b)). In the extreme case, the void is at an infinitesimal distance from the top surface and can be considered as a notch. In this case, the neutral

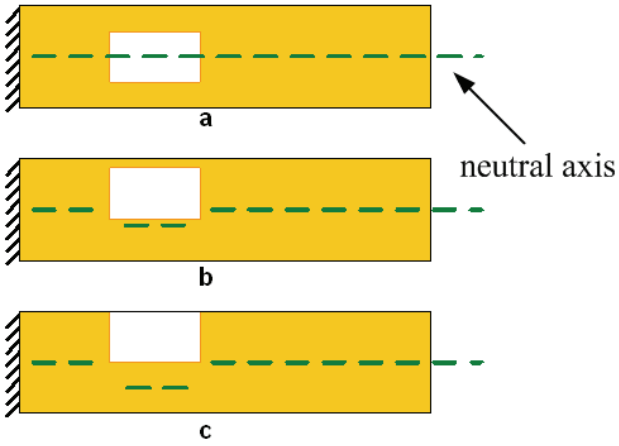

Figure 3.1. Illustration of the stress concentration principle on the cross section of three cantilevers with: a) symmetrical void, b) asymmetrical void, and c) the ultimate asymmetry in the void positioning.

axis is in its maximum recession and located at the center of the under-notch section of the beam (Figure 3.1(c)).

A general schematic of stress concentrating (SC) cantilevers is shown in Figure 3.2. In this diagram, a series of parallel beams has bridged the cantilever notch, next to the clamped end. We simply refer to these parallel beams as SC beams, and the cantilever that utilizes SC beams as SC cantilever. In this work, applying the term SC beam refers to a class of stress concentrating elements that includes both beams and wires. In the rest of

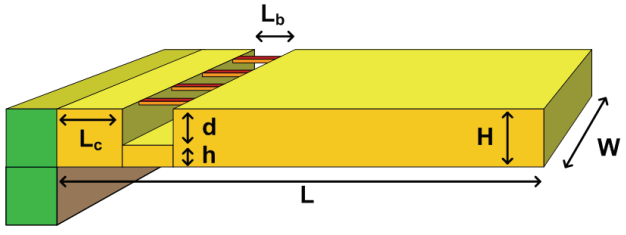

Figure 3.2. Schematic of a stress concentrating (SC) cantilever; the SC beams are suspended over the notch near the clamped end. The support is highlighted in green.

this chapter the effectiveness of the proposed cantilever scheme is examined through both simulation and measurement.

In the finite element simulations, performed with COMSOL Multiphysics 3.3, the cantilever length L, width W, and thickness H are 350, 70 and 20 μm, respectively, unless stated. In these simulations, the structural material of the cantilevers is considered to be only crystalline silicon with density, modulus of elasticity and Poisson's ratio of $\rho = 2329$ kg/m^3, E = 170 GPa, and $\nu = 0.064$, respectively. The finite element simulations are performed using tetrahedral meshing elements with a linear solver in the COMSOL module of 3-D Structural Mechanics. As a boundary condition, the clamped end of the cantilever experiences no movement. The cantilever bending is simulated by applying a line-force on the lower edge of the free end of beam. For simplicity in the calculations, the notch is assumed to have a rectangular geometry with perpendicular sidewalls and it is characterized by three parameters, namely, the notch depth d, the notch length L_b, and the notch distance from the cantilever clamped end, L_c (see Figure 3.2). Figure 3.3 shows an example of the applied meshing in the simulation. A plot of simulation result for the induced stress along a typical SC cantilever and the SC beams is presented in Figure 3.4.

The advantage of the proposed stress concentration technique is illustrated in Figure 3.5, in which the normalized simulated cantilever stiffness and the average longitudinal stress acting on the SC beam are depicted as functions of the normalized notch depth. In the corresponding finite element simulations, the length, width and thickness of the SC beams are L_b = 10 μm, W_b = 2.5 μm, and H_b = 0.5 μm, respectively. The SC beams are

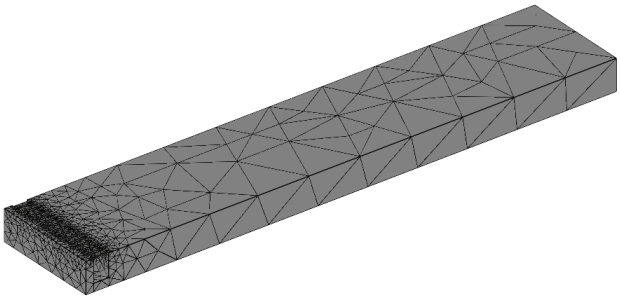

Figure 3.3. Example of meshing used in finite element simulations.

located at L_c = 5 μm from the clamped edge of the cantilever. The spacing between adjacent SC beams is 2.5 μm. The cantilever is deflected by applying a constant point force, F = 1 mN, on its free end (tip). The calculated cantilever stiffness and the stress acting on the SC beams are normalized to the corresponding values for a solid cantilever (i.e., a conventional cantilever with no notch), which has the same thickness of 20 μm. For both cantilever types (i.e., SC and solid cantilevers), the maximum longitudinal stress is monitored at 10 μm distance from the clamped edge, coinciding with the middle of

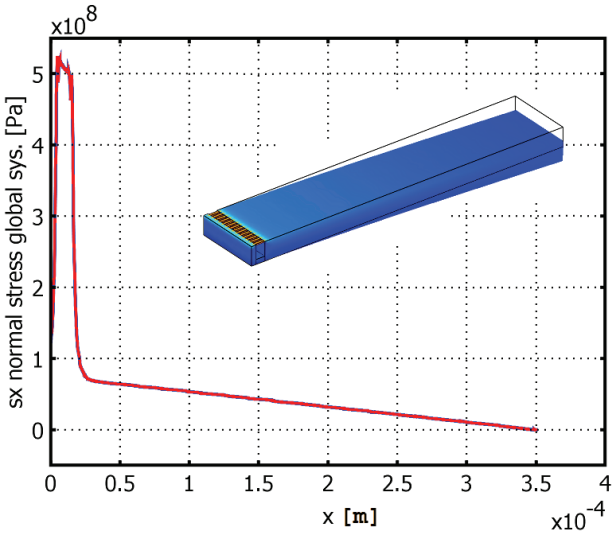

Figure 3.4. Plot of longitudinal stress σ_x, induced on the surface of cantilever and SC beam, versus the distance from the clamped edge. Inset shows the distribution of σ_x for simulated cantilever deflection.

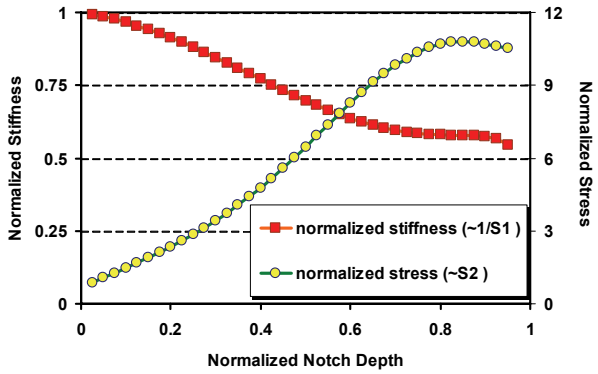

Figure 3.5. Normalized simulated average stress acting on SC elements and cantilever stiffness as a function of normalized notch depth d/H for 1 mN force applied on the tip. The thickness of the SC beams is 2.5% of the cantilever thickness (H = 20 μm).

the SC beams. This point is where the stress acting on an SC beam is equal to the average of stress acting over the entire length of the SC beam. Based on the simulation results, the induced stress in the SC cantilever is considerably larger than the corresponding value in the solid cantilever, provided h, i.e., the remaining thickness under the notch, is not smaller than the thickness of the SC beams. This gain comes at the price of a less than 50% decrease in stiffness. This advantage is also shown in Figure 3.6, in which the normalized longitudinal stress and stiffness of the same SC cantilevers are plotted as

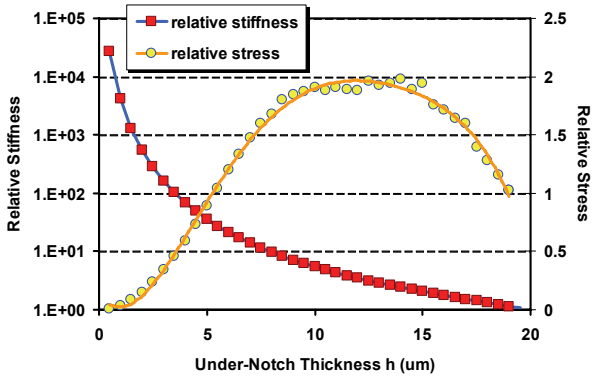

Figure 3.6. Ratios of the simulate stiffness (rectangles) and longitudinal stress (circles) in a 20 μm-thick SC cantilever to the corresponding values in a solid cantilever with the thickness of h (see Figure 3.2) as a function of h. A constant force of 1 mN is applied on the tip.

functions of the under-notch thickness h. Both cantilever types have the same length and width as in the previous case, but here, stress and stiffness are normalized with respect to the corresponding values for a solid cantilever with a thickness equal to the under-notch thickness in the SC cantilever (h). As shown in Figure 3.6, as long as h is larger than 5 μm, the SC cantilever experiences a larger stress compared to the solid cantilever. Also, despite comparatively smaller stress in the SC cantilever with $h < 5$ μm, the stiffness of the SC cantilevers is significantly larger than that of the solid cantilevers.

The remainder of this section concentrates on the variation of stiffness and induced stress in an SC cantilever with respect to three sets of parameters: a) the notch depth and length, b) the SC beam dimensions, and c) the cantilever dimensions. Here, the term stiffness refers to the cantilever spring constant when a constant point force is applied on its tip, and the term stress refers to the maximum longitudinal stress induced at the middle of the SC beam length.

3.1.1 Notch Effect

The simulated effects of the notch location L_c and its length L_b (i.e., the SC beams length) are summarized in Figure 3.7. The notch depth is considered to be constant and equal to 15 μm. The SC beams thickness, width, and spacing are 1, 2.5, and 2.5 μm, respectively. The simulation results indicate that a closer proximity of the notch to the clamped edge, i.e., a smaller L_c, would cause a larger induced longitudinal stress in the SC beams, but also a smaller cantilever spring constant. On the other hand, when the notch length L_b increases, both stress and stiffness will decrease. However, as shown in Figure 3.7, the

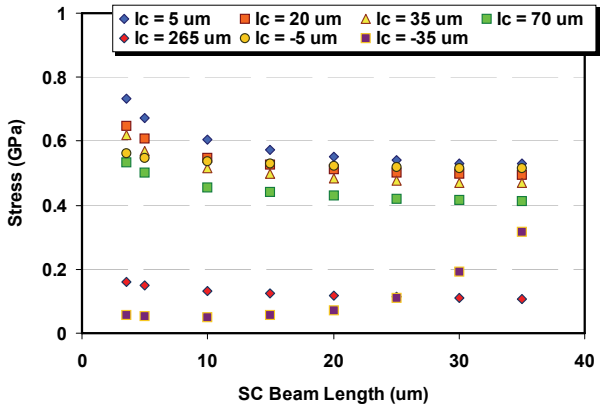

(a)

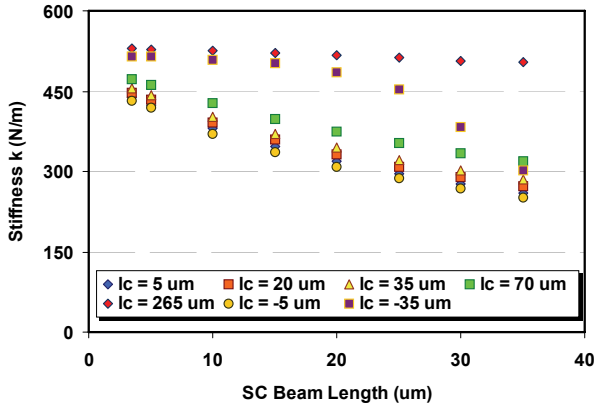

(b)

Figure 3.7. Simulation results for (a) induced longitudinal stress and (b) cantilever stiffness for different notch locations L_c and notch lengths (i.e., SC beam lengths) L_b. The cantilever length, width and thickness are 350, 70, and 20 μm, respectively.

influence of L_b on the stress is less pronounced for longer SC beams. Also the simulation data presented in Figure 3.7 shows that when placing the notch slightly before the clamped edge of cantilever ($L_c < 0$), the compromise in stress is insignificant. This characteristic can be advantageous compared to regular cantilevers in cases that the clamped edge cannot be well-defined due to fabrication inaccuracy. In the corresponding simulations, as a boundary condition the cantilever has no movement at the clamped edge; however, for the case that L_c is negative, the movement of the cantilever is fixed

not only at distance L_c from the support edge, but also along the extension of the cantilever that rests over the support, between L_c and the support edge (see Figure 3.8). Overall, to optimize the force sensitivity, i.e., to maximize the amount of induced stress for a constant force, the notch must be short in length and positioned as close as possible to the cantilever clamped end.

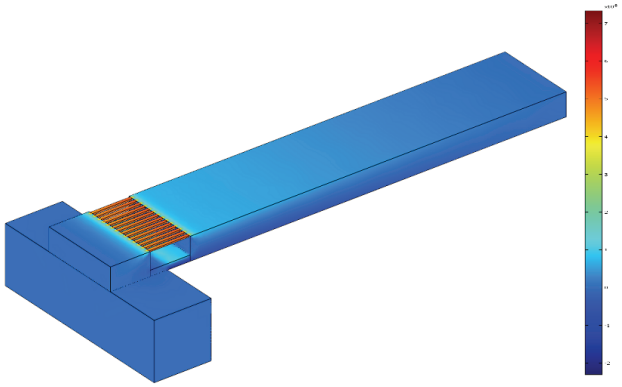

Figure 3.8. Example of a simulation case with a negative L_c (L_c = -15 μm). The color bar shows the intensity of longitudinal stress σ_x across the SC cantilever. The cantilever length, width and thickness are 350, 70, and 20 μm, respectively.

The effect of the notch depth d is revisited in Figure 3.9. Increasing the notch depth, as previously shown in Figure 3.5, has a profound effect in increasing the stress; in contrast, increasing the notch length, as observed in Figure 3.7, does not significantly affect the amount of induced stress for longer SC beams. As shown in Figures 3.7 and 3.9, for different notch depths and notch locations, increasing the notch length causes an almost linear decrease in the cantilever stiffness.

3.1.2 SC Beam Effect

In addition to the effect of the SC beams length on stress and stiffness, which is previously discussed as the effect of the notch length, the SC beams contribution can be

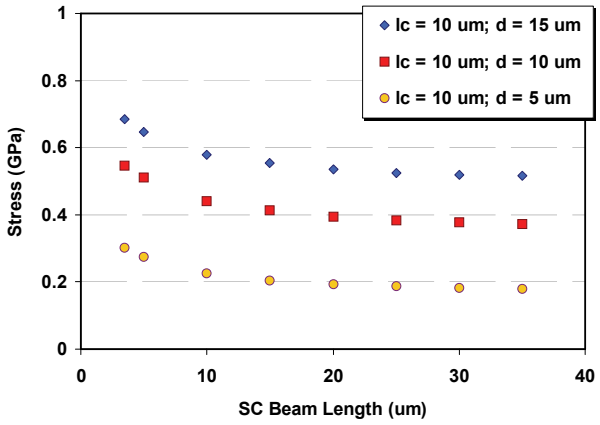

(a)

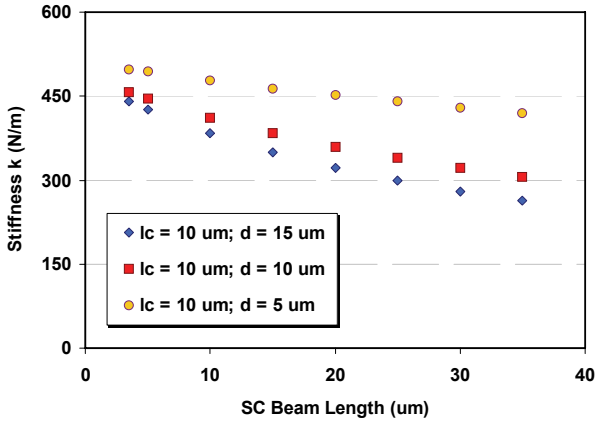

(b)

Figure 3.9. Simulation results for (a) induced longitudinal stress and (b) cantilever stiffness for different notch depths *d* and notch lengths (i.e., SC beam lengths) L_b. The cantilever length, width and thickness are 350, 70, and 20 μm, respectively.

investigated in more aspects including the effect of the SC beams thickness, width, count and arrangement. According to the simulation results, the SC beams arrangement has a small influence on the average stress and stiffness; hence, the effects of SC beams width and count can be summarized together as the effect of SC beams net width.

As depicted in Figure 3.10, reducing the SC beams thickness leads to a considerable decrease in the cantilever stiffness, but an exponential increase in stress. In the

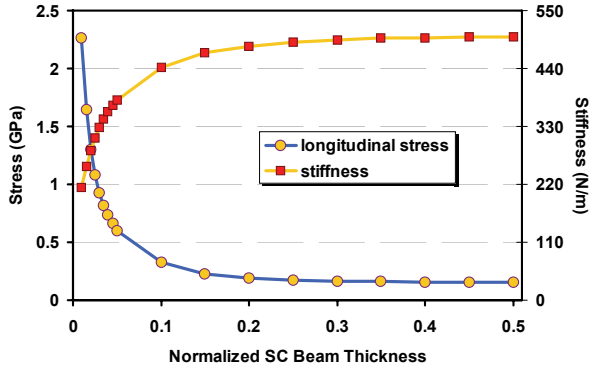

Figure 3.10. Variation of stiffness (squares) and longitudinal stress (circles) versus SC beams thickness in an SC cantilever. The thickness of SC beams is normalized to the cantilever thickness H = 20 μm. The number of SC beams considered in the simulation is 14.

corresponding simulations d, L_b, and L_c are 15, 10 and 5 μm, respectively. The SC beams width and spacing are 2.5 μm. The cantilever thickness is 20 μm, as before. Also observed in Figure 3.10, the thickness of the SC beams will be significantly more influential if it is less than 10% of the cantilever thickness. In other words, to maximize the stress enhancement, the SC beams should be as thin as possible; however, this advantage comes at the price of a considerable reduction in the cantilever stiffness.

Similarly, reducing the number of SC beams, i.e., reducing the net width of the SC beams, will cause an increase in the induced stress but a decrease in the stiffness. Cantilevers with identical dimensions but different numbers of SC beams are compared in Figure 3.11. In the corresponding simulations, the SC beams specifications are the same as in the case for Figure 3.10, with the SC beams thickness being equal to 1 μm.

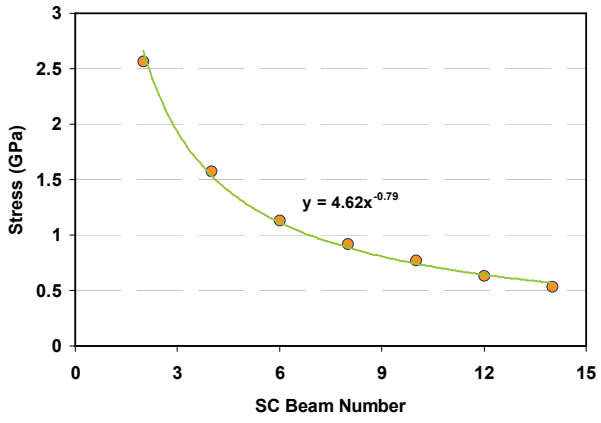

(a)

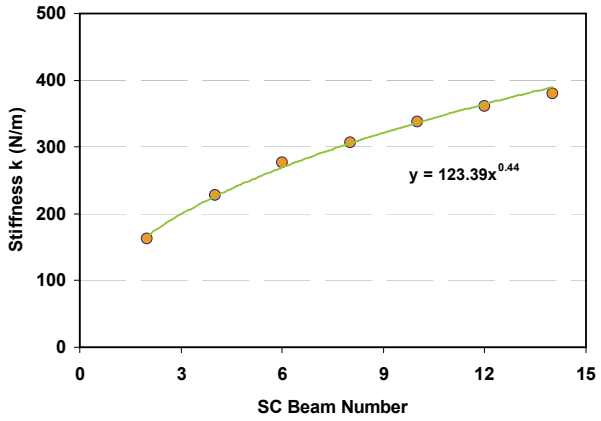

(b)

Figure 3.11. Simulated variation of (a) longitudinal stress and (b) stiffness versus the number of SC beams in SC cantilevers. The cantilever length, width and thickness are 350, 70, and 20 μm, respectively.

3.1.3 Cantilever Dimensions Effect

In this section the effect of cantilever dimensional parameters, i.e., length *L*, width *W*, and thickness *H*, in both solid and SC cantilevers are compared. To this end, the simulation results for the maximum stress at half length of the SC beams are compared with the corresponding results for a conventional solid cantilever beam at exactly the same longitudinal location. Also, the validity of simulation results for the solid cantilever is

checked with analytical predictions. As expressed by Eq. (3.2), for a given force F applied on the cantilever tip, the maximum induced longitudinal stress σ_x at a distance x from the clamped edge of a solid cantilever is obtained by

$$\sigma_x = \frac{6(L-x)}{H^2 W} F \,. \tag{3.4}$$

For the same loading condition, the cantilever stiffness (spring constant) k is defined with respect to Eqs. (2.13) and (2.15):

$$k = \frac{1}{4} EW \left(\frac{H}{L} \right)^3 , \tag{3.5}$$

where E is the modulus of elasticity.

A. Effect of cantilever width

In the corresponding simulations for both types of cantilevers the values of L and H are 350 and 20 μm, respectively. The SC beams are 10 μm long, 1 μm thick, and 2.5 μm wide. They are located at 5 μm from the clamped edge (L_c = 5 μm) and equally spaced from each other with 2.5 μm gap in between. The study of the effect of cantilever's width is conducted with changing W in 10 μm increments; in a way that each increment is accompanied by introducing two additional SC beams. For both cantilevers the stress is observed at 10 μm from the clamped edge, i.e., at the half length of the SC beams, while a force of 1 mN magnitude is applied on the cantilever tip. Simulation results of solid cantilevers are in agreement with Eq. (3.4), which shows that in a solid cantilever the amount of induced stress is inversely proportional to W. The same trend is recognized in Figure 3.12 for SC cantilevers, but with an 8 times larger stress magnitude.

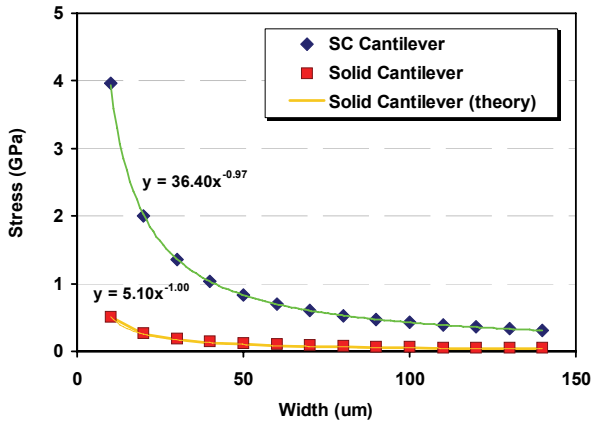

(a)

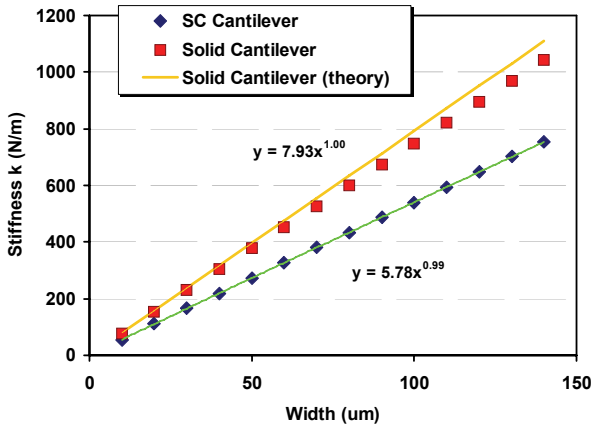

(b)

Figure 3.12. Effect of cantilever width on (a) longitudinal stress and (b) stiffness in SC cantilevers (diamonds) and solid cantilevers (squares) for an applied force of 1 mN on the cantilever tip. The cantilever length and thickness are 350, and 20 μm, respectively.

B. Effect of cantilever thickness

Equation (3.4) shows that for a solid cantilever, thickness is the most effective dimensional parameter in inducing a longitudinal stress. In the corresponding simulations the cantilevers are scaled vertically in 5 μm steps, in such a way that the thickness ratio of the SC beams to the cantilever remains constant at 5%. Also, the ratio of the notch depth to the cantilever thickness is maintained at 75%. The width, length and location of

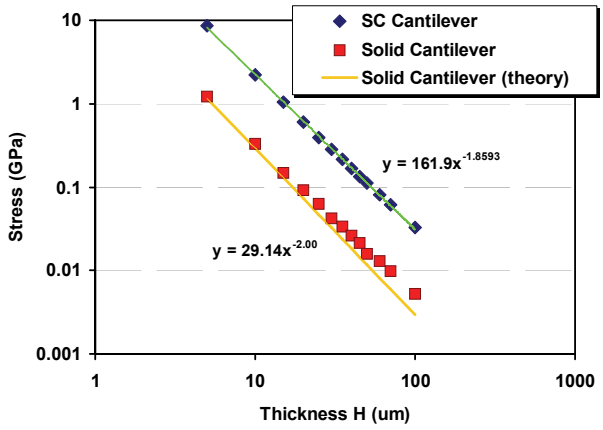

(a)

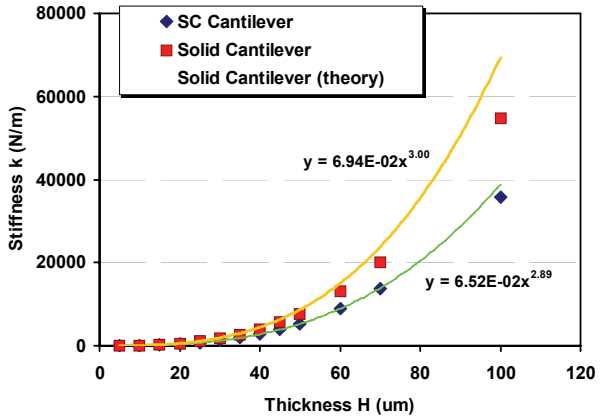

(b)

Figure 3.13. Effect of cantilever thickness on (a) longitudinal stress and (b) stiffness in SC cantilevers (diamonds) and solid cantilevers (squares) for an applied force of 1 mN on the cantilever tip. The cantilever length and width are 350, and 70 μm, respectively.

SC beams are the same as in the previous case, while both types of cantilevers are 350 μm long and 70 μm wide. As depicted in Figure 3.13, the variation of stress in both cantilevers closely follows the trend predicted by Eq. (3.4), while the SC cantilever experiences about an order of magnitude larger stress than the solid cantilever. The small discrepancy observed between the analytical and simulation results in Figure 3.13 is

because of simplifying assumptions made in the analytical derivation, where the thickness of the cantilever beam is assumed to be negligible compared to its length.

C. Effect of cantilever length

According to Eq. (3.4), in a solid cantilever σ_x is directly proportional to the cantilever length. The induced stress in an SC cantilever can be compared to a solid cantilever in two ways: depending on whether the SC beams length is maintained constant or scaled with the cantilever length, two sets of simulations can be performed. In the first set, the SC beams length L_b and their location L_c are constant. In the second set, L_b and L_c are changed in proportion to the cantilever length L, so that the ratios of L/L_b and L/L_c are maintained constant. In the corresponding simulations, the SC beams are 1 μm thick, 2.5 μm wide, and they are spaced equally with gaps of 2.5 μm. In the first set of simulations, the beams are 10 μm long and located 5 μm from the cantilever clamped edge. In the second set, the ratios are fixed at $L_b/L = 2/70$ and $L_c/L = 1/70$, e.g., for a 350 μm long cantilever, the SC beams are 10 μm long and located 5 μm from the clamped edge. In both sets of simulations, the maximum longitudinal stress at half length of the SC beams is recorded and compared to the corresponding stress value in a solid cantilever, observed at the exact same longitudinal location. Results of the first simulation set, presented in Figure 3.14, indicate that not only increasing the cantilever length leads to an increase in the induced stress, but also there is an additional enhancement when the length ratio of SC beams to the cantilever is reduced. This effect, which has been mentioned before for the case of the notch length, results in a larger slope of stress versus cantilever length. On the other hand, in the second set of simulation, in which the length of SC beams is scaled

with the cantilever, both types of cantilevers follow similar trends (see Figure 3.15). Similar to Figure 3.13, for the case of solid cantilevers, a slight discrepancy is observed in Figure 3.15 between the simulation and analytical results, which has been associated with the simplifying assumption made in the analytical derivation.

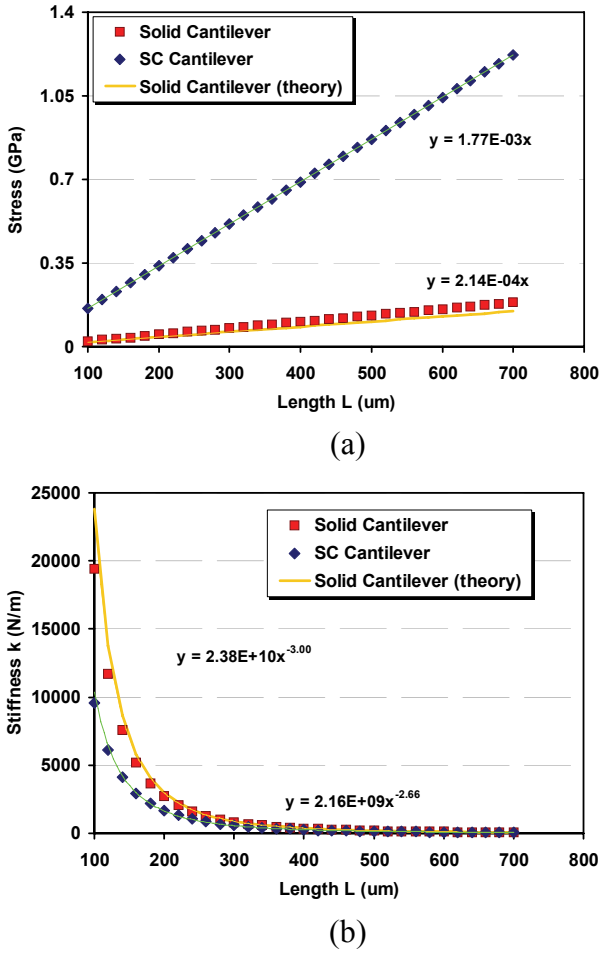

Figure 3.14. Effect of cantilever length on (a) longitudinal stress and (b) stiffness in SC cantilevers (diamonds) and solid cantilevers (squares) for an applied force of 1 mN on the cantilever tip. The location of notch and the SC beams length are invariable. The cantilever width and thickness are 70, and 20 μm, respectively.

Overall, based on the simulation results presented in this section, the influence of cantilever dimensions is the same for both solid and SC cantilevers, but accounting for different amounts of stiffness and normalized longitudinal stress.

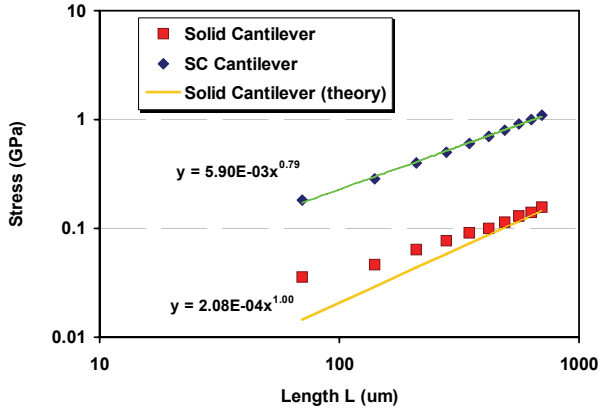

(a)

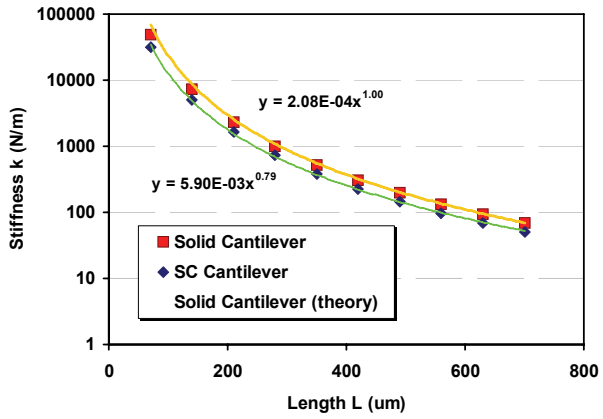

(b)

Figure 3.15. Effect of cantilever length on (a) longitudinal stress and (b) stiffness in SC cantilevers (diamonds) and solid cantilevers (squares) for an applied force of 1 mN on the cantilever tip. The notch location and SC beam length vary in proportion to the cantilever length. The cantilever width and thickness are 70, and 20 μm, respectively.

3.2 Fabrication

The cantilevers are fabricated utilizing bulk micromachining techniques. Using multi-layer wafers as the starting material, e.g. silicon on insulator (SOI) or epitaxially grown (Epi) silicon wafers, the doping regions, metal lines, and eventually, the cantilevers' geometry are defined on the device layer, while the cantilevers are prepared for the final

release after the back side patterning and etching the handle layer [47, 172]. To provide higher piezoresistive coefficients, the doping of the piezoresistors is chosen as p-type, which necessitates using n-doped device layers. In Epi wafers, the combination of the n-doped device layer and p-doped handle layer provides the possibility of using the electrochemical etch-stop technique to form a silicon membrane on the wafer surface [173]. The thickness of this membrane, which is the same as the intended thickness of cantilevers, is defined by the thickness of the device layer. A brief overview of the cantilever fabrication is presented in Figure 3.16. The complete cantilever fabrication process flow is presented in Appendix A.

Utilizing a new process module right after defining the doped regions, embedded clamped-clamped stress concentrating beams and wires, with dimensions down to the submicron domain, are fabricated (see Figure 3.17). This process module can be performed using UV lithography (e.g., i-line at 365 nm) and requires only a single mask; as a result, the beams and wires can be batch-fabricated on a wafer-level scale. The fabrication of the SC elements starts with a thermal oxidation of the wafer surface, followed by pattering parallel openings on the oxide layer in <110> direction. Then, using an inductively coupled plasma (ICP), the oxide layer and the underlying silicon are etched to form shallow trenches in the device layer (with a silicon etch depth of less than 1.2 μm). Next, another thermal oxide layer is grown to conformally cover the sidewalls and bottom of the etched trenches. The purpose of growing the latter oxide layer is to protect the silicon bars in between the trenches during the forthcoming etching steps. The

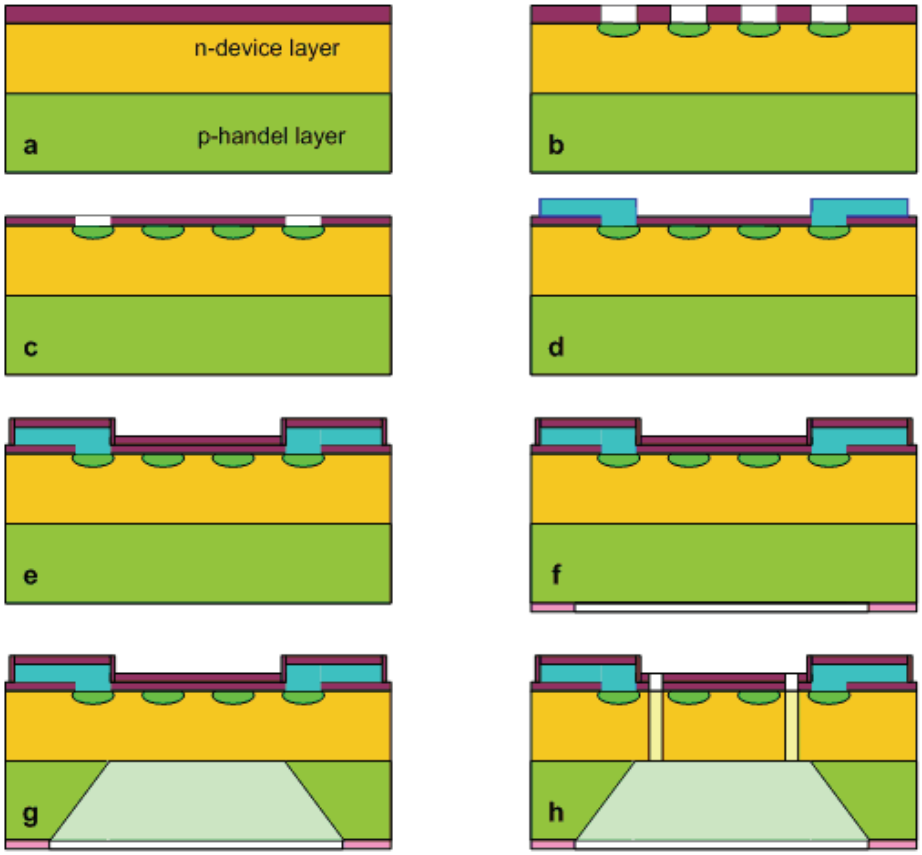

Figure 3.16. General process flow for fabrication of cantilevers using bi-layer silicon wafers, e.g., SOI and Epi wafers: (a) cross section of a bi-layer wafer with an oxide layer on top; (b) doping of desired regions using the oxide layer as a mask; (c) removal of doping mask and deposition of insulation layer, followed by opening windows for electrical contacts; (d) deposition, patterning and sintering the metal layer; (e) deposition of passivation layer, PECVD SiO_2; (f) deposition of KOH masking layers (PECVD SiN_x and SiO_2) on the wafer back-side, and subsequent patterning; (g) Backside anisotropic etching in KOH solution; (h) release of final structure by front-side dry etching.

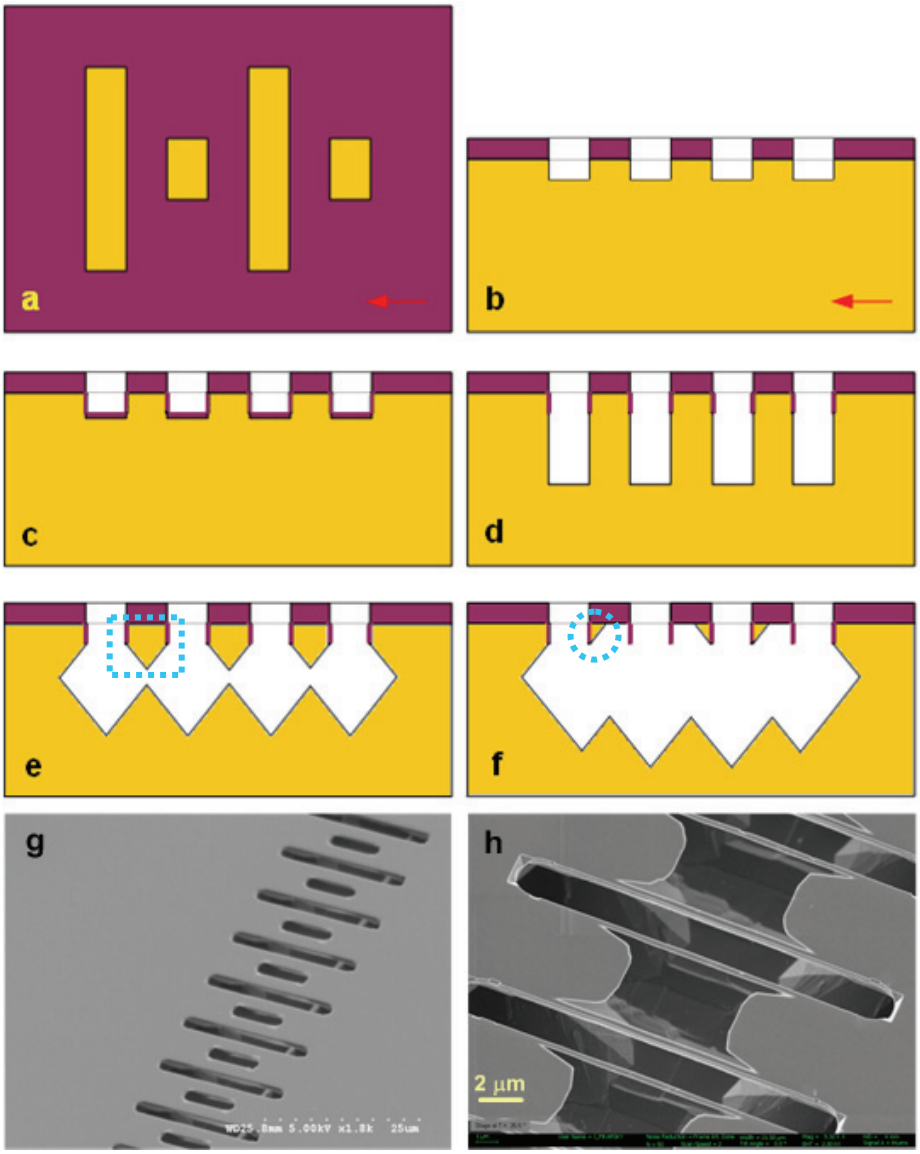

Figure 3.17. Single mask fabrication process flow for SC elements: (a) top-view of mask layout for trench etching; cross-sections after (b) etching shallow trenches, (c) covering sidewalls and bottom of the trenches with thermal oxide; (d) deepening the trenches using deep reactive ion etching (DRIE), without any significant decrease in the sidewall oxide thickness, (e) releasing the beams (highlighted with the rectangle) by immersing the sample in 6 molar KOH solution, (f) additional anisotropic etching, inverting the etch profile and releasing nanowires (highlighted with the circle) inside the clad oxide layer; (g&h) SEM micrographs of released SC beams and nanowires, respectively, after removing the clad oxide in HF.

SC beams and wires are constructed within these bars; hence, the dimensions of the bars (trenches), determine the final dimensions of the beams and wires.

In the next step, using reactive ion etching, the oxide layer on the bottom of the trenches is removed. Then, using the Bosch® process in an ICP system, the trenches are further deepened into silicon, while no significant decrease is observed in the thickness of protecting oxide on the sidewalls. At this point, a portion of the sidewall, indicated in Figure 3.18 with d_1, is covered with oxide, while over the remaining portion, indicated with d_2, the bare silicon is exposed. Finally, to release the SC elements, the wafer is immersed in a 6-molar KOH solution at 30 ºC for approximately 60 minutes. The etching time depends on the spacing G between adjacent trenches as well as the targeted shape of the SC elements, i.e., the shape of either a beam or wire.

To have a successful beam release, the following requirement must be fulfilled:

$$G \le d_2/\sqrt{2}\,. \qquad (3.6)$$

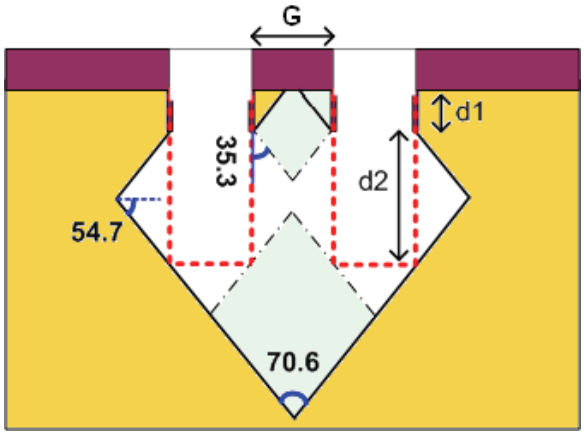

Figure 3.18. Etching profile of the released SC beams and wires. To release the wires, the pale colored (torquise) areas are removed after the extended etching.

By extending the etching time, the etched profile inverts and prismatic wire strands form in place of the beams. The cross sections of the released wires are triangular. A wire would be released only if

$$d_1 \le G/\sqrt{2}\,. \qquad (3.7)$$

The widths of the two perpendicular facets of the released wire are d_1 and $d_1/\sqrt{2}$ (see Figure 3.18). To successfully release the wires as clamped-clamped structures, the length of adjacent trenches must be unequal (see Figure 3.17(a)). This way, at the expense of detachment and sacrificing the wire along the shorter trench, the wire along the longer trench will be released attached to the substrate at both ends. Figure 3.19 shows the excursion angle at the clamped end of a released wire, which is approximately 14.5˚. As a rule of thumb, based on geometrical analyses on the captured micrographs, it is discovered that the difference in the length of adjacent trenches, when placed symmetrically, needs to be at least about 8 times larger than the spacing between the two trenches. However, since the etching process is time-dependent, a prolonged immersion can result in a complete loss of the wires. Also, when releasing beams and wires with the

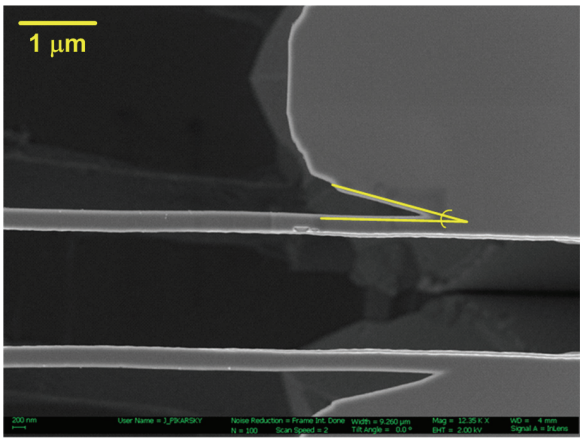

Figure 3.19. Excursion angle on a released wire.

presented technique, because of the anisotropic etching characteristics, the notch floor is not even (see Figure 3.20).

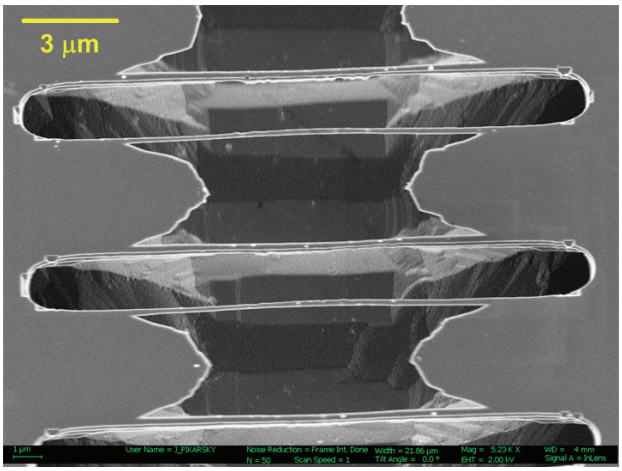

Figure 3.20. SEM picture of the uneven trench floor morphology; the released wires are suspended over the trench (notch).

In the fabricated cantilevers, after the deposition of an extra passivation oxide layer over the metal lines, the released beams and wires were covered with a 0.8 µm-thick oxide layer. Figure 3.21 shows an SEM micrograph of a fabricated device, with the SC

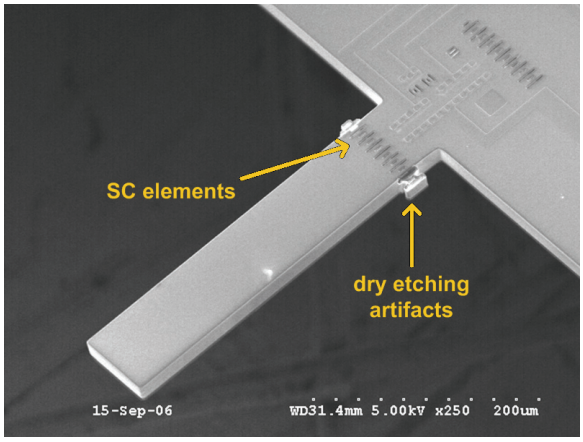

Figure 3.21. SEM micrograph of a fabricated SC cantilever; the SC elements (covered by the clad oxide) are suspended over the notch, 25 µm from the clamped edge.

elements suspended over the notch and covered by a clad oxide layer. Because of variations in the thickness of the handle wafer, the clamped edge of the cantilever did not coincide exactly with the edge of the back-side-etched cavity; instead, the cantilevers were supported by a silicon rim of the same thickness, providing about 8-20 μm spacing between the edges of the cantilever and the cavity (see Figure 3.22).

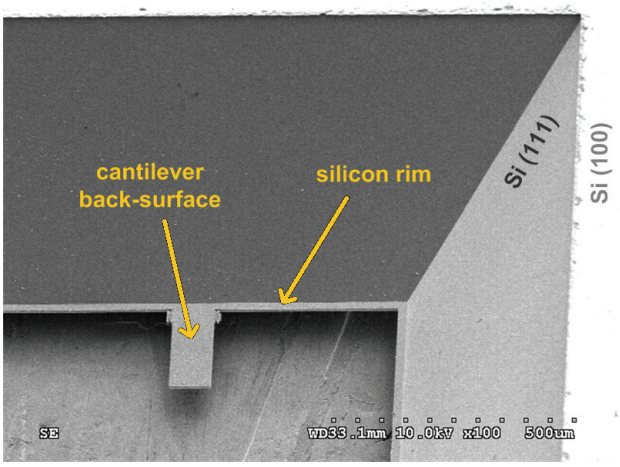

Figure 3.22. SEM picture of a back-side etched cavity showing the back-surface of an SC cantilever and the silicon rim.

3.3 Measurements and Discussion

3.3.1 Static Characteristics

Using a Berkovich tip in a Hysitron TriboIndenter®, different preset forces were applied on the free end of the cantilever and the resulting deflections were recorded with sub-nanometer precision. Meanwhile, the resistance change in the piezoresistors was measured by a Keithley 2400 Sourcemeter®. By adjusting the current, the dissipated power in the piezoresistors was set at 15 ± 5 μW.

In the first set of measurements, the effect of the SC beam thickness has been investigated. As shown before in Figure 3.10, decreasing the thickness of the SC element results in an increase of the induced longitudinal stress. Hence, it is expected that a cantilever utilizing wires instead of beams as SC elements shows a higher sensitivity for a given force. In this regard, Figure 3.23 compares the force sensitivity and the spring constant of three SC cantilevers and a solid cantilever. The specifications of the measured cantilevers are summarized in Table 3.1. As for the stress concentrating elements, two of the compared SC cantilevers have wires with submicron cross-sections, and the third one has thicker SC beams. The cantilever with a thinner wire is associated with a higher resistance. Figure 3.23 shows that for the thinner SC elements the sensitivity is higher but, at the same time, the stiffness is slightly smaller. Since in the cantilevers presented in Figure 3.23 only a fraction of the measured resistance is aligned with the longitudinal stress (see Figure 3.24(a)), in cantilevers with thicker SC elements a smaller fraction of the overall resistance of the piezoresistor experiences the concentrated stress, and hence,

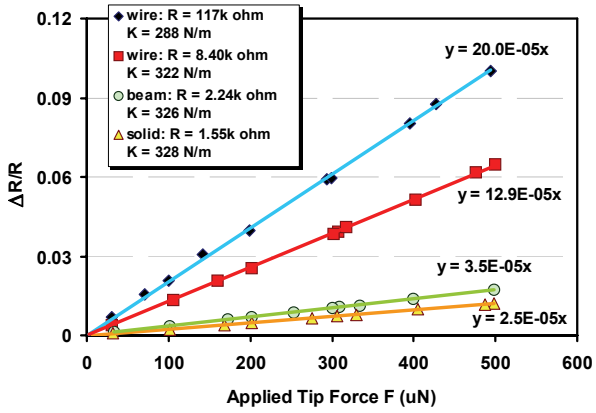

Figure 3.23. Relative resistance change as a function of the applied tip force for a solid cantilever (triangles), cantilevers with stress-concentrating silicon wires with resistance R = 8.4 kΩ (squares) and R = 117 kΩ (diamonds), and a cantilever with stress-concentrating beam (circles).

Table 3.1. Specifications of cantilevers in Figure 3.23.

Cantilever length L	350 μm
Cantilever width W	70 μm
Cantilever thickness H	17 μm
Notch location L_c	25 - 30 μm
Average notch depth d	~ 10 μm
SC beam thickness (sidewall)	~ 0.8 μm
SC beam length L_b	~ 6 μm
SC beam width	2.5 μm
SC wire width	< 0.5 μm
SC beams number	14
SC wires number	20

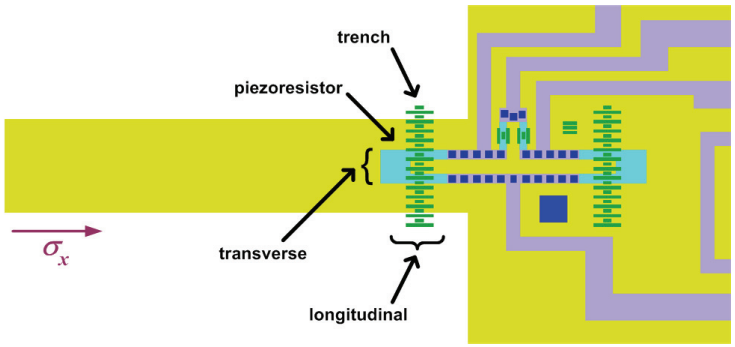

(a)

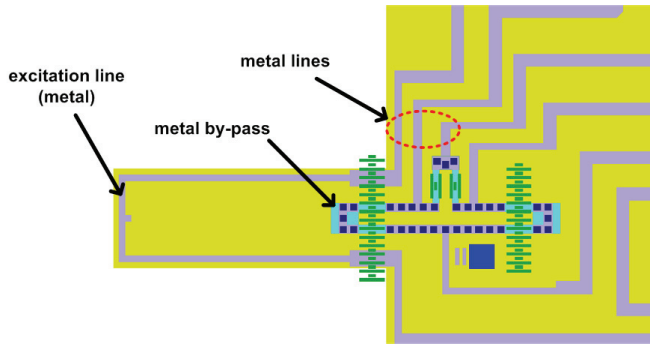

(b)

Figure 3.24. Layout of two SC cantilevers: (a) transverse fraction of piezoresistor, unlike longitudinal fraction, is not aligned with longitudinal stress σ_x; (b) transverse fraction of piezoresistor is by-passed (short-circuited) using metal line.

compared to a device with thinner SC elements, the sensitivity is further reduced. This issue is an additional reason for the large difference between the measured sensitivity of cantilevers with wires and the one with beams in Figure 3.23. The force sensitivity of the SC cantilever with thinner wires (R = 117 kΩ) is 5.7 times larger than the sensitivity of the SC cantilever with beams. On the other hand, the force sensitivity of the same SC cantilever with wires (R = 117 kΩ) is 8.0 times larger than that of the solid cantilever, which is consistent with the simulation results presented in Figure 3.5 for $d/H = 0.55$, in spite of the fact that the silicon wires are covered by the clad oxide layer. It must be noted that since in the fabricated cantilevers the resistors are placed in a Wheatstone bridge configuration, the measured resistance change of a single resistor is in fact affected by the other three resistors as well. However, the data shown in Figure 3.23 represents the resistance change of the single piezoresistor that is subjected to stress, whereas the effect of the other three resistors, which are not undergoing a stress change, is excluded. To this end, the resistance change of the single piezoresistor is extracted from the measured data using a ratio that is calculated based on the measured resistances between every two nodes on the Wheatstone bridge.

Also, it is observed in Figure 3.23 that the reduction in the SC cantilevers stiffness, compared to the solid cantilever, is less than what has been predicted by the simulation. This issue can be attributed to the presence of the cavity rim, which results in a decrease of the solid cantilever's stiffness; in contrast, the stiffness of the SC cantilevers, as an advantage of this type of cantilevers, is less affected by non-idealities on the clamped end.

As indicated in Figure 3.6, based on the simulation results the force sensitivity of the SC cantilevers improves with increasing the *d*/*H* ratio. The validity of this prediction is confirmed by the measurement results depicted in Figure 3.25. To have a fair comparison between SC cantilevers with different *d*/*H* ratios, in Figure 3.25 the simulated piezoresistor values are adjusted to include the effect of the unstressed fraction of the resistors. For this reason, the simulation is not in a complete agreement with the data shown in Figure 3.6. In addition, the discrepancy between the simulation and measurement can also be associated with the presence of dry etching artifacts on the sidewalls of the notch (see Figure 3.21), an uneven trench floor, the difference between the actual and simulated thickness of the SC elements, as well as the difference between the actual and assumed piezoresistive coefficients. The piezoresistive coefficient is a function of doping [93], and in this case, the simulated doping concentration (performed by SSUPREM3) is about 2 x 10^{18} cm^{-3}, which may not the same as the actual doping concentration.

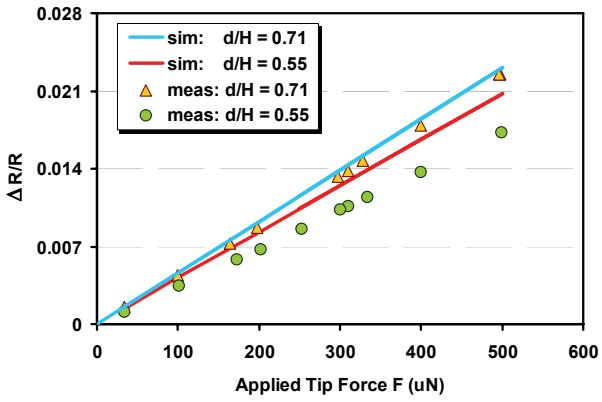

Figure 3.25. Measured (symbols) and simulated (solid lines) relative resistance change as a function of applied tip force for *d*/*H* ratios of 0.55 and 0.71 in cantilevers with stress-concentrating beams.

The focus of rest of this section will be only on SC cantilevers utilizing beams as stress concentrating elements. The measured cantilevers are 12 μm thick, with SC beams located at L_c = 8.5 μm from the cantilever edge. The SC beams are 1.0 μm thick (on the sidewall) and the notch is about 6.0 μm deep. Each SC cantilever has 23 SC beams unless mentioned. Also, by short-circuiting with a metal line, the effect of the unstressed fraction of the resistors canceled (see Figure 3.24(b)). The reason for confining the investigation only to the SC beams and not the SC wires is the fact that the cross sectional area of the fabricated wires, unlike the beams, were less uniform across the wafer, therefore, a fair comparison between many different devices was not possible.

An investigation of the effect of the SC cantilever length on the force sensitivity is presented in Figure 3.26. In this comparison all the measured cantilevers are 82 μm wide. As it has been shown for a solid cantilever by Eq. (3.4), the amount of induced longitudinal stress at a given point x would increase with the increase of cantilever length with a constant tip force. The same trend has been also observed in the simulation results for SC cantilevers (see Figure 3.14). In practice, for a given force, a larger amount of induced stress at point x corresponds to a higher force sensitivity of the cantilever. Therefore, if the piezoresistors are located at a fixed distance from the cantilever clamped edge, a larger resistance change for a given force corresponds to a larger force sensitivity. In this respect, the variation of force sensitivity with length, shown in Figure 3.26, follows the same linear pattern as predicted by simulation, presented in Figure 3.14; thus the measurement results are qualitatively in agreement with the simulation.

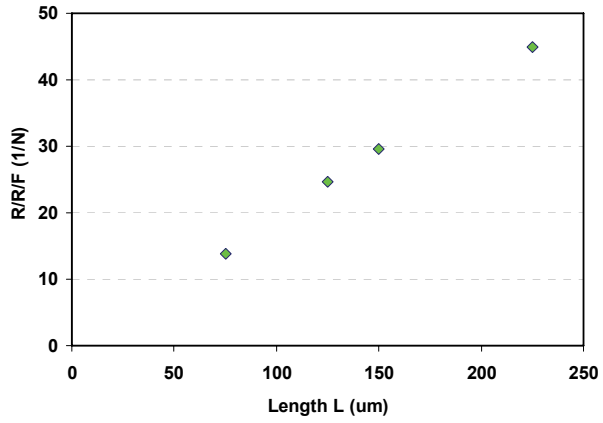

(a)

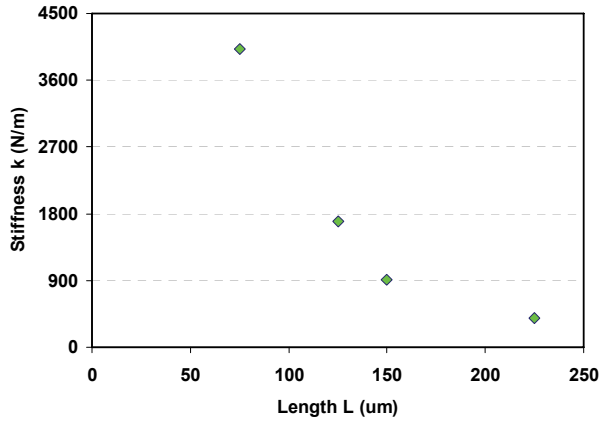

(b)

Figure 3.26. Measured effect of cantilever length on (a) force sensitivity and (b) stiffness in SC cantilevers. The location of notch and the SC beams length are invariable. All cantilevers are 12 μm thick and 82 μm wide.

The effect of cantilever width on the measured force sensitivity is shown in Figure 3.27(a), which also compares the sensitivity of solid versus SC cantilevers. In this comparison the cantilever lengths are equal L = 450 μm, while the only variable parameter is the cantilever width. The measurement results presented in Figure 3.27(a) indicate that for a constant tip force, the amount of induced stress in the piezoresistors in both SC and solid cantilevers is inversely proportional to the cantilever width. This

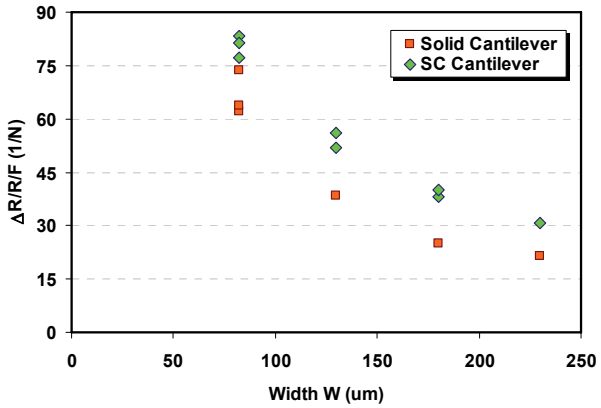

(a)

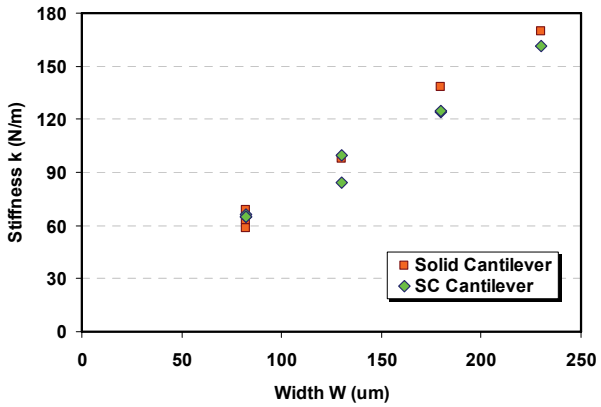

(b)

Figure 3.27. Measured effect of cantilever width on (a) force sensitivity and (b) stiffness in SC cantilevers (diamonds) and solid cantilevers (squares). All cantilevers are 450 μm long and 12 μm thick.

observation is in agreement with the analytical prediction of Eq. (3.4) and the simulation results depicted in Figure 3.12. On the other hand, as shown in Figure 3.27(b), despite variation of the cantilever width, the stiffness plots of the SC cantilevers closely follows the plots of solid cantilevers.

The effect of the SC beam length on the measured force sensitivity and stiffness are shown in Figures 3.28(a) and 3.28(b), with all the measured cantilevers being 450 μm

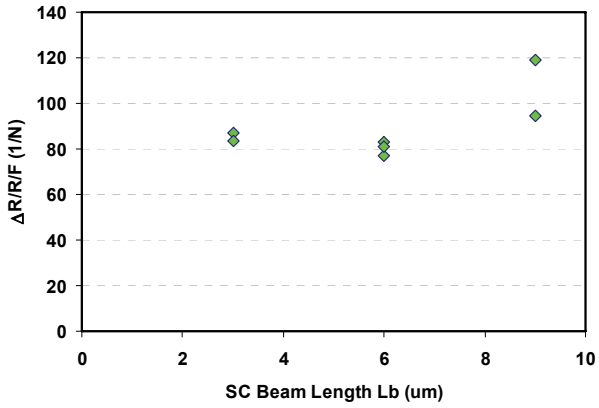

(a)

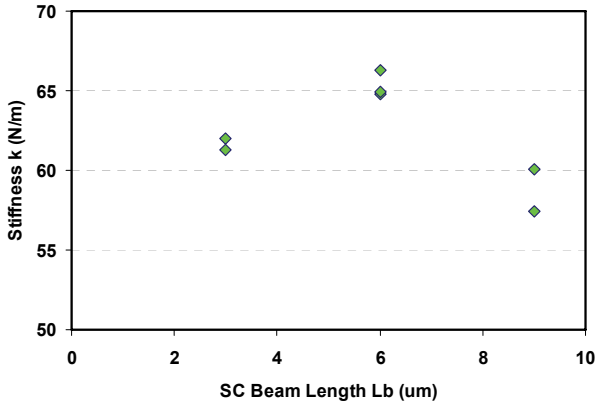

(b)

Figure 3.28. Effect of SC beams length on (a) force sensitivity and (b) stiffness in SC cantilevers. All cantilevers are 450 μm long, 82 μm wide, and 12 μm thick.

long and 82 μm wide. Compared to Figures 3.7 and 3.9, the measurement data shown in Figure 3.28(a) are not consistent with the simulation: while the cantilevers with 3 μm-long SC beams are only slightly superior in force sensitivity over the cantilevers with 6 μm-long SC beams, unexpectedly the highest sensitivity is observed for the cantilevers with the longest SC beams, i.e., the 9 μm-long beams. The difference between the simulation and measurement results can be explained by reviewing the fabrication process of the SC beams: we have observed that the parts around the middle of an SC

beam release faster than the parts closer to the clamped ends (see Figure 3.20); hence, when most of a 9 μm-long beam is well released, the 3 μm-long beam is still comparably thick, whereas the thickness of the 6 μm-long beam is between the other two. As a result, the force sensitivity trend shown in Figure 3.28(a) emerges as a trade off between the effect of SC beam thickness and the effect of SC beam length. Unlike the force sensitivity, the measured cantilever stiffness data (shown in Figure 3.28(b)) are in agreement with the simulation results (see Figures 3.7 and 3.9), except for cantilevers with 6 μm-long SC beams. The reason for such deviation is not clear; however, it is speculated that variations in the cantilever thickness might play a role.

Finally, from the simulation results (see Figure 3.11) it is expected that decreasing the number of SC beams causes an increase in the force sensitivity (i.e., induced stress). This speculation is confirmed by the measurement results presented in Table 3.2, in which the force sensitivity of two identical SC cantilevers, but one with 12 SC beams and the other one with 23 SC beams, are compared. In addition to the previously mentioned specifications, both cantilevers are 450 μm long and 82 μm wide. The SC beams in both cantilevers are identical and 6 μm long.

Table 3.2. Effect of number of SC beams on the force sensitivity.

Beams number	Force sensitivity $\Delta R/R/F$ ($1/\mu N$)
23	$81.2\ 10^{-6}$
12	$110\ 10^{-6}$

3.3.2 Noise Considerations

Noise in a piezoresistive cantilever originates from both electrical and mechanical domains [50, 85, 174, 175]. In this regard, the main determining factor in both domains is the damping of the system, which is represented by an electrical resistance R in the electrical domain, and a mechanical damping coefficient B in the mechanical domain.

The power spectral density of electrical noise, S_v, for a piezoresistor is determined by the Flicker noise for lower frequencies f [176],

$$S_v(f) \propto \frac{1}{f}, \tag{3.8}$$

and the Johnson noise for higher frequencies [177],

$$S_v(f) = 4KTR, \tag{3.9}$$

where K is Boltzmann's constant and T is the temperature of the resistor.

As mentioned before, both simulation and measurement results suggest that thinning the stress concentrating elements will increase the force sensitivity of SC cantilevers. However, for a given length, when a piezoresistor is realized through a thinner and narrower beam, its electrical resistance will be larger [178]:

$$R \propto \frac{L_b}{H_b W_b}, \tag{3.10}$$

and thus the associated Johnson noise will increase. As a result, optimizing the piezoresistors (i.e., the SC elements) will always involve a compromise between sensitivity and resolution of the SC cantilevers.

Previously it was observed in Figure 3.23 that the force sensitivity of an SC cantilever utilizing submicron silicon wires could be 8 times larger than the force sensitivity of a similar solid cantilever. However, since the measured resistance in the SC cantilever is considerably larger than the resistance in the solid cantilever, at any given temperature the noise spectral density of the SC cantilever also would be larger. The noise spectral densities of the same two previously mentioned SC and solid cantilevers (in Figure 3.23) are compared in Figure 3.29. The data presented in this figure are acquired using an SRS Digital Spectrum Analyzer 780, with a minimum resolution of about -165 dBm. Since during the noise measurement the devices were not completely isolated from the outside environment, at certain frequencies similar ambient induced parasitic spikes are measured in addition to the actual cantilever noise. For the data shown in Figure 3.29, unlike in Figure 3.23, the contribution of single piezoresistors is not extracted; rather, Figure 3.29 shows the measured resistance between the two nodes of the Wheatstone bridge that are

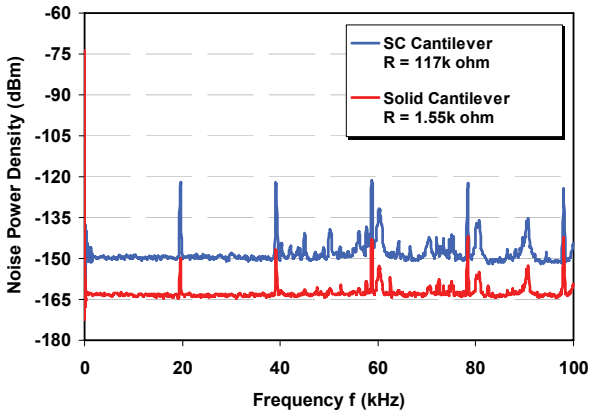

Figure 3.29. Noise power spectra of an SC cantilever (blue) and a solid cantilever (red). The repeated periodic spikes are the results of ambient noise. The minimum resolution of the spectrum analyzer is about -165 dBm. Both cantilevers are 350 μm long, 70 μm wide, and 17 μm thick.

connected to the same piezoresistors represented in Figure 3.23. In this configuration the

piezoresistor is in parallel with the rest of the bridge; hence, the effective resistance, which emerges in Eq. (3.9), is slightly smaller than the actual resistance of the piezoresistor shown in Figure 3.23.

The spectral density of thermomechanical noise of a resonant cantilever beam, for force per unit length of beam, is calculated as [85]

$$S_n(f) = \frac{4KTm^* f_n}{QL^2}, \tag{3.11}$$

where m^* is the effective mass of cantilever, f_n is the resonance frequency of the beam in the n^{th} overtone (mode), and Q is the resonance quality factor. As mentioned in Chapter 2, a resonant cantilever at the fundamental resonance mode ($f_n = f_1$) can be considered as a second order system, in which the mechanical damping coefficient is defined by Eq. (2.6):

$$B = 2\pi \frac{m^* f_1}{Q}. \tag{3.12}$$

With f_1 given as

$$f_1 = \frac{1}{2\pi}\sqrt{\frac{k}{m}}, \tag{3.13}$$

the mechanical damping coefficient will be calculated as

$$B = 2\pi \frac{\sqrt{m^* k}}{Q}. \tag{3.14}$$

Replacing Eq. (3.12) in Eq. (3.11) would define the noise spectral density in a term similar to the Johnson noise in Eq. (3.9):

$$S_n(f) = 4KT \frac{B}{2\pi L^2}. \tag{3.15}$$

Therefore, to compare the thermomechanical noise spectral densities of an SC cantilever with a solid cantilever, both having the same length and operating temperature, we need to compare the mechanical damping coefficients of the two cantilevers. As indicated by Eq. (3.14), the mechanical damping coefficients of two cantilevers can be compared in terms of the effective mass, spring constant, and quality factor of each cantilever.

To optimize the force sensitivity of an SC cantilever, as mentioned before, the notch should be short in length and positioned as close as possible to the clamped end. In forming a notch, the cantilever mass loss would be insignificant when the notch is comparably short. On the other hand, in a resonant cantilever the vibration amplitude in the proximity of the clamped end, where the notch would be located, is negligible. Therefore, the kinetic energy associated with the removed mass in an SC cantilever, while forming the notch, is negligible and as the result, the contribution of the removed mass in the effective mass of cantilever can be ignored. In other words, for approximately the same resonance mode shapes, the amount of effective mass considered in Eq. (3.14) is almost equal for both SC and solid cantilevers. Nevertheless this statement may not be valid if the notch depth is closely comparable to the cantilever thickness. In this case, the resonance mode shapes of SC and solid cantilevers could be different and to have an accurate comparison, the effective mass of the SC cantilever should be calculated based on the exact vibration amplitude along the beam.

Besides the effective mass, according to Eq. (3.14), the other two parameters that define B are the cantilever spring constant and quality factor. The presented measurement results

in this work indicate that the spring constant of the SC and solid cantilevers, with the same geometrical dimensions and the reported notch specifications, are almost equal.

To perform a comparison of the quality factors, the resonance characteristics of two SC cantilevers and one solid cantilever are measured (see Figure 3.30). The length, width and thickness of all cantilevers are 450, 82, and 12 µm, respectively. The SC beams are 3 and 9 µm long. All other specifications of the SC beams and cantilevers are the same as before (Table 3.1). The measurement results are summarized in Table 3.3. Since the implemented Wheatstone bridges on the cantilever are not completely balanced, the cantilevers show different offsets in the output voltage, which are visible as different off-resonance power magnitudes in Figure 3.30. Confirmed by the measurement results, it has been expected that the SC and solid cantilevers resonate at very close frequencies:

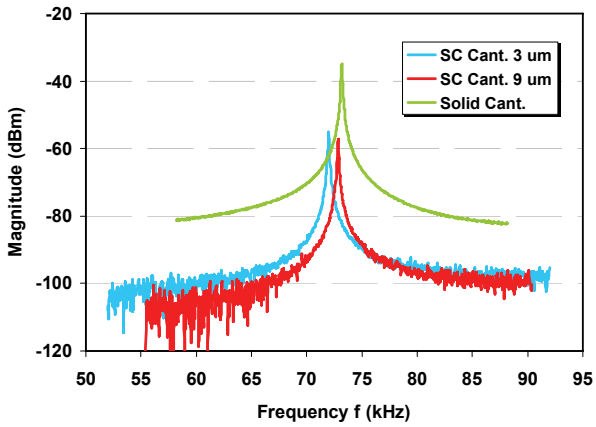

Figure 3.30. Resonance spectra of two SC cantilevers with SC beam length L_b = 3 µm (blue) and 9 µm (red) and a solid cantilever (green). All cantilevers are 450 µm long, 82 µm wide, and 12 µm thick.

Table 3.3. Resonance characteristics of measured SC and solid cantilevers.

Type	Resonance frequency f (kHz)	Quality factor
Solid cantilever	73.175	740
SC cantilever (L_b = 3 μm)	71.983	704
SC cantilever (L_b = 9 μm)	72.842	695

The effective masses and the spring constants in both SC and solid cantilevers are estimated to be equal, thus according to Eq. (3.13) the resonance frequency must be approximately equal too. Also observed in Table 3.3, the quality factor of both cantilevers are closely comparable. Therefore, since the effective masses and the spring constants in both cantilevers are almost equal and the quality factors are close, based on Eq. (3.14) the mechanical damping coefficients for both cantilevers are approximately the same. In other words, the thermomechanical noise density of both cantilevers is almost the same.

The dynamic behavior of SC cantilevers is further investigated in Chapter 10.

***

In this chapter a new technique in utilizing the stress concentration in piezoresistive cantilever force sensors is introduced and verified through simulation and experiment. Introducing a new fabrication process module, embedded stress concentrating silicon wires and beams are fabricated and implemented in cantilevers. By using these structures as piezoresistors and concentrating stress through such piezoresistors, the force sensitivity of cantilevers is increased without noticeably sacrificing the stiffness,

resonance frequency, and quality factor. The performed finite element simulation results are confirmed by experiment data and indicate that in an SC cantilever the amount of induced stress for a given force, i.e., the force sensitivity of the cantilever, not only follows the same relationship with geometrical dimensions as in a solid (conventional) cantilever, but also increases by decreasing the thickness of the stress concentrating elements (e.g., beams or wires). This advantage comes at the expense of a small decrease in the spring constant, compared to solid cantilevers. As an example, the measurement results of SC cantilevers with embedded stress concentrating wires show an up to 8.0 times increase in force sensitivity at the price of only a 15% reduction in stiffness. On the other hand, in designing SC cantilevers, special attention must be paid to the noise characteristic of the device. While the thermomechanical noise of both solid and SC cantilever types are closely comparable, using a long and thin stress concentrating element can result in an increased Johnson (thermal) electrical noise, hence, deteriorating the force resolution of the cantilever sensor.

CHAPTER 4

CALCULATION OF Q-FACTOR BY ITERATIVE CURVE FITTING

As expressed before by Eq. (2.4), the quality factor (Q or Q-factor) of a resonant system provides a measure for the ratio of the stored and lost energy in that system. The Q-factor of a mechanical system can provide information about loss mechanisms in the system, e.g., viscous damping, support loss, and thermoelastic loss [179-181]. In an electronic oscillator, the Q-factor provides valuable information about the Ohmic loss in the system [182]. In a microwave resonator, the Q-factor can reveal information about the structural material with respect to its dielectric permittivity, magnetic permeability and surface impedance [183-187].

From this chapter forward the focus of the thesis will be on the dynamic behavior of cantilevers, with an emphasis on magnetically excited piezoresistive cantilevers. To have a valid assessment of the performance of a resonant cantilever, it is imperative to acquire reliable data about the resonance frequency and the Q-factor of the resonator. To this end, this chapter is aimed to provide an accurate method for measuring the quality factor of simple harmonic resonators based on their magnitude transfer characteristic. The goal of introducing this method is to overcome the effect of noise in interpretation of the measurement results. This method can be especially useful when no specific data is available about the measurement noise, except the assumption that the noise spectral density is constant over the measured bandwidth.

4.1 Simple Harmonic Oscillators

The frequency transfer function of every resonator can be considered as a product of transfer functions of multiple "simple harmonic oscillators (SHO)," each representing a resonance mode of the system. A simple harmonic oscillator is in fact a second order system, which its time-dependent characteristic equation is the same as Eq. (2.2) [188]:

$$a\frac{d^2S_o}{dt^2}+b\frac{dS_o}{dt}+cS_o=S_i(2\pi ft) \tag{4.1}$$

where S_o is the output signal magnitude, f is the frequency of the excitation signal S_i, and a, b and c are constant coefficients. For a resonant cantilever beam, as mentioned in section 2.2.1, the coefficients a, b, and c are the cantilever effective mass m, damping coefficient B, spring constant k, respectively. Hence, similar to Eq. (2.8), at a given excitation frequency f (i.e., $f = \Omega/2\pi$), the output signal S_o is calculated in the time domain as

$$S_o(t)=\frac{\beta(f)}{c}|S_i|\sin\big(2\pi ft-\theta(f)\big), \tag{4.2}$$

where $|S_i|$ is the amplitude of the excitation signal, β is the magnification factor,

$$\beta(f)=\frac{1}{\sqrt{(1-\frac{f^2}{f_r^2})^2+(\frac{1}{Q}\frac{f}{f_r})^2}}, \tag{4.3}$$

and θ is the phase angle,

$$\theta(f)=\tan^{-1}\left(\frac{f/f_r}{Q(1-f^2/f_r^2)}\right). \tag{4.4}$$

In close proximity to the resonance frequency, i.e., $f \approx f_r$, the magnification factor can be approximated by a Lorentzian curve:

$$\beta(f) \approx \frac{1}{\sqrt{4(1-\frac{f}{f_r})^2 + (\frac{1}{Q})^2}}. \qquad (4.5)$$

4.2 Common Methods in Extraction of Q-Factor

The Q-factor of a resonator can be calculated from the magnitude, phase, or complex transfer characteristics of the resonance [189-193]. Petersan and Anlage have provided a comprehensive comparison between the different methods [189]. The focus of this chapter, however, is to calculate the Q-factor based on the magnitude transfer characteristic of the resonator, i.e., based on the magnification factor β described by Eq. (4.3). Widely used methods in this regard are the 3-dB method and the least-square fit method.

In the 3-dB method, the frequency of the maximum magnitude is considered as the resonance frequency f_r, according to Eq. (4.3), and the difference between the half power frequencies, where the signal magnitude (amplitude) is $1/\sqrt{2}$ of the maximum magnitude, defines the half power bandwidth $\Delta f_{3\text{-}dB}$. The Q-factor is then calculated as [79]

$$Q = \frac{f_r}{\Delta f_{3-dB}}. \qquad (4.6)$$

In the least-square fit method, the measured magnitude transfer function is fitted to either an SHO transfer function given by Eq. (4.3), or to a Lorentzian curve given by Eq. (4.5). A non-linear least-square fit is iterated with respect to f and Q until the fitted curve shows the minimal chi-square [189, 194].

Besides the mentioned approaches, Eq. (4.2) can be used to establish two other less common methods for calculating the Q-factor. In the first method the Q-factor is extracted based on the ratio of transfer characteristic magnitudes at the resonance frequency and a considerable lower frequency. This ratio, by combining Eqs. (4.2) and (4.3), is given as

$$Q = \frac{\beta(f = f_r)}{\beta(f \approx 0)}. \tag{4.7}$$

In applying this method one should be careful about the effect of 1/*f* noise [176]. In the second method the Q-factor is extracted from the slope of the phase angle. Here, by differentiating Eq. (4.4) with respect to *f*, the quality factor is calculated at the resonance frequency:

$$Q = \frac{f_r}{2}\left|\frac{d\theta}{df}\right|_{f=f_r}. \tag{4.8}$$

4.3 Noise in Measurement Set-up

Presence of both noise and cross-talk signals can affect the measurement result. However, the focus of this chapter is on the effect of noise, i.e., interfering signals that have zero mean and zero correlation to the input signal. The presence of noise in a measurement set-up is illustrated in Figure 4.1. For an electromechanical resonator, for example, the input signal S_i is accompanied with thermomechanical noise [85] N_{th} and also with N_i, the noise generated due to variations in S_i itself. Since S_i, typically generated by a network analyzer, has a uniform power spectral density over the measurement sweeping bandwidth, any other input signal with a uniform spectral density can be represented as a

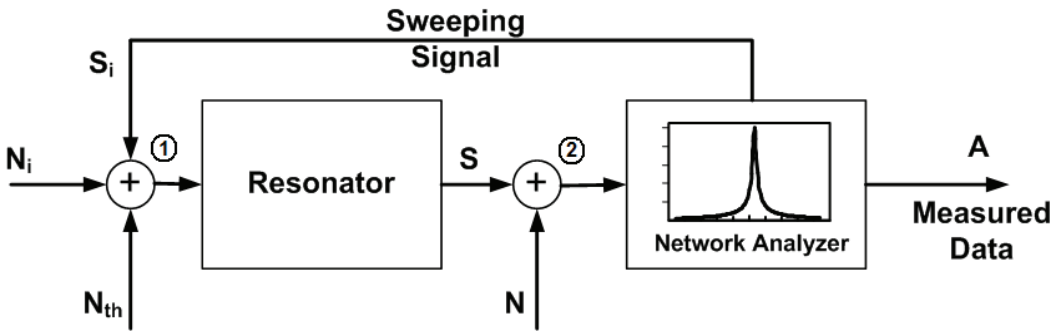

Figure 4.1. Schematic of the measurement set-up, including the resonator and network analyzer, with the corresponding signal and noise inputs marked. At node 1: S_i is the input signal from the network analyzer, N_i and N_{th} are the noises associated with the input signal and the ambience (e.g., thermomechanical noise), respectively. At node 2: S is the resonator output signal and N is the intermediate stage noise. The measured output signal is A.

fraction of S_i; hence, if the input noises, at node 1 in Figure 4.1, have uniform power spectral densities in the measurement bandwidth, they can be simply considered altogether as a part of the input signal S_i without affecting the Q-factor of the measured data $A(f)$. In fact, using noise as the input signal is an established method in examining the mechanical properties of cantilever resonators [195].

In contrast to the input noise, the measurement result is highly susceptible to noise introduced at the intermediate stages, i.e., at node 2 in Figure 4.1. This noise appears in the read-out stage, e.g., in the sensors and the interface circuitry, and its power spectral density is independent of the transfer characteristic of the resonator, thus potentially can contribute to erroneous data interpretation. Through the rest of this chapter, the intermediate stage noise is simply referred as noise.

In the following sections an iterative curve-fitting method is introduced to eliminate the effect of noise introduced at intermediate stages when extracting the Q-factor from the measured magnitude data. This method is especially useful when no specific data is available about the measurement noise.

4.4 Iterative Curve Fitting Method

As mentioned previously, a well established technique for measuring the resonance characteristic of a system is to fit the measured magnitude spectrum with the transfer function of an SHO (or a Lorentzian curve). However, with the presence of noise at the intermediate stages, the measured output power spectral density will not be solely defined by the resonance characteristic of the system; instead, with a reasonable assumption that signal and noise are statistically independent, the power spectral density of the measured signal $G_A(f)$ is [196]

$$G_A(f) = G_S(f) + G_N(f), \tag{4.9}$$

where $G_s(f)$ and $G_N(f)$ are the power spectral densities of the SHO signal and noise, respectively. By integrating both sides of Eq. (4.9) over the measurement bandwidth W, the measured signal power P_A is calculated as:

$$P_A = P_S + P_N, \tag{4.10}$$

where P_S and P_N are the signal and noise power, respectively. In a network analyzer the power spectral density of the measured signal over the minimum resolution bandwidth is approximated to be constant. Ideally, the minimum resolution bandwidth is equal to an infinitesimal frequency change df. In practice, however, the minimum resolution

bandwidth B_{mr} is a finite number, by which Eq. (4.9) gives the average power at a swept (measured) frequency f_j as

$$G_A(f_j)B_{mr} = G_S(f_j)B_{mr} + G_N(f_j)B_{mr}\,. \tag{4.11}$$

In a transfer characteristic measurement set-up the load impedance is not a function of frequency (e.g., it has a constant impedance of 50 Ω or 75 Ω); hence, for a load impedance normalized to unity, the average signal power is proportional to the square of the signal amplitude for every measured frequency:

$$G_A(f_j)B_{mr} = A^2(f_j)\,. \tag{4.12}$$

As the result, with respect to Eq. (4.11), the measured signal magnitude at a frequency f_j can be expressed as the sum of the square magnitudes of the SHO signal, S, and the noise, N:

$$A^2(f_j) = S^2(f_j) + N^2(f_j)\,. \tag{4.13}$$

When the noise power spectral density is constant over the measurement frequency span W, e.g., as in the case of white noise, the square of noise magnitude can be described as

$$N^2(f_j) = N^2 = P_N/W\,, \tag{4.14}$$

where the load impedance is again normalized to unity. In this case Eq. (4.13) simplifies to

$$A^2(f_j) = S^2(f_j) + N^2\,, \tag{4.15}$$

or

$$A(f_j) = \sqrt{S^2(f_j) + N^2}\,. \tag{4.16}$$

If N^2 is equal to zero, the measured transfer characteristic perfectly matches the resonance transfer characteristic of an SHO signal with magnitude $S_f(f)$. It is important to notice that

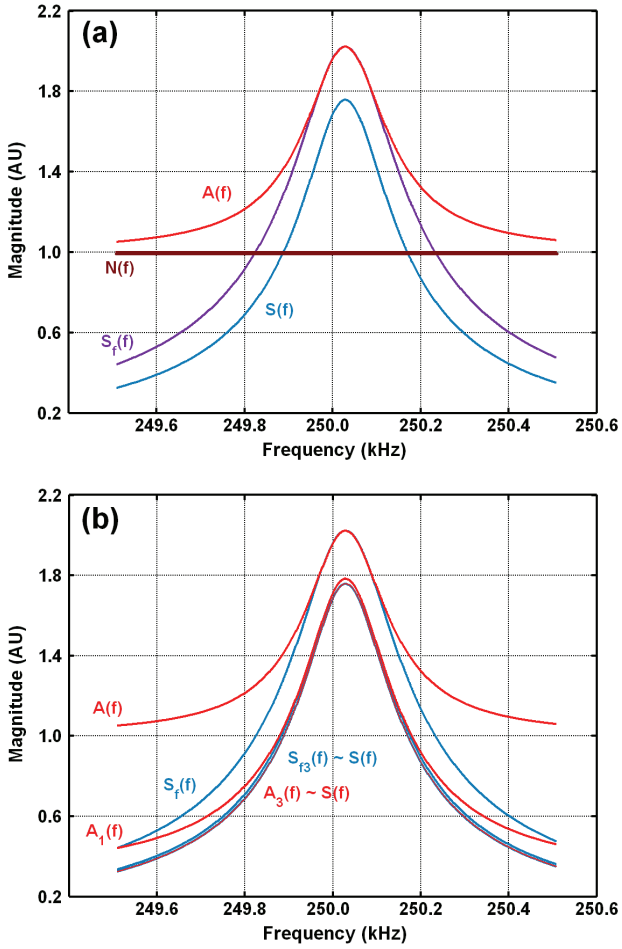

Figure 4.2. (a) The magnitude of the measured signal amplitude $A(f)$ compared to the contributing SHO transfer function $S(f)$, the initial least-square curve fit $S_f(f)$, and root-mean-square (rms) noise $N(f)$, (b) illustration of the proposed iterative procedure for step-by-step elimination of the noise effect, with intermediate signals $A_k(f)$ and $S_{fk}(f)$ of the k^{th} iteration step are marked. In both graphs the signal amplitude is shown in linear scale. In the presented data, the signal-to-noise ratio at the resonance frequency, i.e., $S^2(f_r)/N^2$, is 3.0; also, the extracted Q-factor based on $S_f(f)$ is 1074, while the actual resonance Q-factor, which is extracted based on $S(f)$, is 1280.

in contrast to the actual SHO transfer characteristic of the system $S(f)$, which is unknown, $S_f(f)$ is the transfer characteristic that is obtained by curve fitting to the measured signal $A(f)$ (see Figure 4.2). When N^2 is negligible, the difference between $A(f)$ and $S_f(f)$ at frequencies considerably far from the resonance frequency will be negligible too. On the

other hand, if N^2 is not negligible, $A(f)$ will not follow the transfer characteristic of an SHO, thus $S_f(f)$, as an SHO transfer function, will overlap with $A(f)$ only around the maximum magnitude, i.e., at the resonance frequency (see Figure 4.2),

$$A^2(f_r) = S_f^2(f_r). \tag{4.17}$$

For a reasonable measurement bandwidth, in which the magnitude transfer function of an SHO can also be described by a Lorentzian curve, moving away from the resonance frequency results in reduction of $S_f^2(f)$, while $A^2(f)$ settles around at the noise power level. In a measurement frequency span, therefore, the maximum difference between $A^2(f)$ and $S_f^2(f)$ occurs at frequency f_i, the farthest frequency from the resonance frequency, with the spectral power difference N_1^2 calculated as

$$N_1^2 = A^2(f_i) - S_f^2(f_i). \tag{4.18}$$

It can be shown that $N_1^2 \le N^2$ if it is possible to show that $S_f^2(f_i) > S^2(f_i)$. The latter statement is true, because S_f is associated with a smaller Q-factor and a larger maximum magnitude: The Q-factor associated with S_f would be same as the actual Q-factor of the system if N^2 was negligible, but since a power P_N across the spectra is uniformly added to the signal power, the Q-factor of the fitted signal S_f becomes smaller than the actual Q-factor of the system. Hence, considering Eq. (4.3), $S_f^2(f_i)/S_f^2(f_r) > S^2(f_i)/S^2(f_r)$. But according to Eqs. (4.15) and (4.17) $S_f^2(f_r) > S^2(f_r)$, thus $S_f^2(f_i) > S^2(f_i)$. This conclusion is also illustrated in Figure 4.2(a).

In the next step, the effect of noise on the measured signal is reduced by eliminating the contribution of N_1^2. Therefore, the modified measured signal is defined as

$$A_1^2(f_j) = A^2(f_j) - N_1^2 \ , \tag{4.19}$$

and with respect to Eq. (4.15),

$$A_1^2(f_j) = S^2(f_j) + N^2 - N_1^2 \, . \tag{4.20}$$

The modified amplitude can be fitted by a new SHO curve, $S_{f1}(f)$. Similar to Eq. (4.18), the maximum difference N_2 is calculated by

$$N_2^2 = A_1^2(f_i) - S_{f1}^2(f_i) \, . \tag{4.21}$$

It can be shown that $N_2^2 \le N^2 - N_1^2$, i.e., $S_{f1}(f_i) > S(f_i)$, with an explanation similar to what was mentioned earlier for $N_1^2 \le N^2$.

By repeating the procedure of modifying the measured signal, the partial noise power in the k^{th} iteration step is calculated as

$$N_{k+1}^2 = A_k^2(f_i) - S_{fk}^2(f_i) \, , \tag{4.22}$$

where $A_k^2(f_j)$ can be expanded with respect to Eq. (4.15) as

$$A_k^2(f_j) = S^2(f_j) + N^2 - \sum_{p=1}^{k} N_p^2 \, . \tag{4.23}$$

This procedure can be is iterated until the m^{th} step, in which

$$N^2 \approx \sum_{k=1}^{m} N_k^2 \, ; \tag{4.24}$$

At this point, the modified measured transfer characteristic is almost identical to the actual SHO transfer characteristic:

$$A_m^2(f_j) = S^2(f_j) + N^2 - \sum_{k=1}^{m} N_k^2 \approx S^2(f_j) \, . \tag{4.25}$$

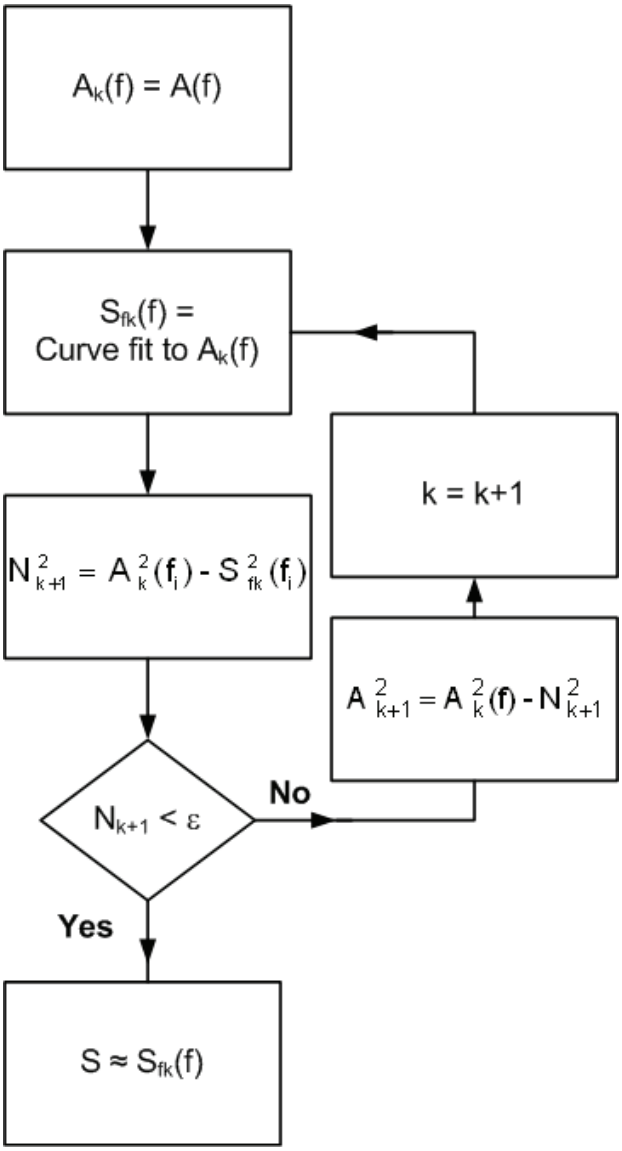

Figure 4.3. Flowchart of proposed iterative curve fitting method.

In other words, at the final step (i.e., the m^{th} step) not only $S_{fm}(f_j)$ is the same as $S(f_j)$, but also it closely fits to $A_m(f_j)$ because $A_m(f_j)$ has become the same as an SHO transfer characteristic itself. The latter statement provides the criterion for finding the final iteration step:

$$N_{m+1}^2 = A_m^2(f_i) - S_{fm}^2(f_i) \approx 0 \qquad (4.26)$$

Figure 4.3 shows the flowchart of proposed method.

To examine the convergence of this method, the explanation mentioned for $N_1^2 \le N^2$ can be generalized to the n^{th} iteration step with respect to Eq. (4.23):

$$N_{n+1}^2 \le N^2 - \sum_{k=1}^{n} N_k^2 ,$$

or alternatively,

$$N^2 \ge \sum_{k=1}^{n} N_k^2 ;$$

since N^2 is constant in the measured data, for $n >> 1$ the partial noise power N_n^2 must approaches zero, thus the presented method is always converging.

With this technique, based on the measured magnitude of the resonator transfer characteristic, the effect of noise in extraction of Q-factor can be eliminated without any pre-existing knowledge of the noise spectral density, except the assumption that the noise spectral density is constant over the measured bandwidth. For simplicity, in the following sections the proposed method is referred to as the iterative fitting method.

4.5 Experiment

As an example of simple harmonic oscillators, the fundamental flexural resonance mode of a rectangular silicon cantilever beam with length, width and thickness of 225, 106 and 11 μm, respectively, is measured and characterized. The cantilever resonance is exited at $f_r \approx 250$ kHz by passing an alternating current with amplitude of 2.0 mA along the beam perimeter in presence of a static magnetic field, at room temperature and atmospheric pressure. Piezoresistors in a Wheatstone bridge configuration, implemented near the clamped edge of cantilevers, are used to transduce the cantilever mechanical vibrations into electric signals. A complete description of the excitation and detection schemes used in the cantilevers is presented in Chapter 5. The data is acquired using an Agilent 4395A Network Analyzer (50 Ω load impedance), with frequency sweeping span W and averaging bandwidth of 1 kHz and 100 Hz, respectively. The captured spectrum consists of 801 data points. To improve the symmetry of the captured transfer characteristics, the largest magnitude, which occurs around the resonance frequency, is recorded as the 401st data point. To change the signal-to-noise power ratio in the measured spectrum, the flux density of the excitation magnetic field is changed from 25 to 3750 Gauss. To diversify the measured noise sources (e.g., night-time versus day-time activity noises), the measurements were performed in different time periods of day.

A schematic of the measurement set-up is shown in Figure 4.1. In calculating the SNR, the absolute noise level is obtained based on the noise power spectral density of the minimal static magnetic field (during the same measurement time period), while the signal level is calculated based on the maximum moving average of the power magnitude

in the captured spectrum, according to Eq. (4.15). In each iteration of the procedure explained in section 4.4, the Q-factor and the resonance frequency f_r are calculated by a nonlinear least-square fit of the measured magnitude transfer characteristic to an SHO transfer function.

4.6 Results and Discussion

A series of measured magnitude transfer characteristics for different signal-to-noise ratios are shown in Figure 4.4. Since the transfer characteristics shown in Figure 4.4 are captured with insignificant time lapses, the noise spectral density is almost equal for all the shown data.

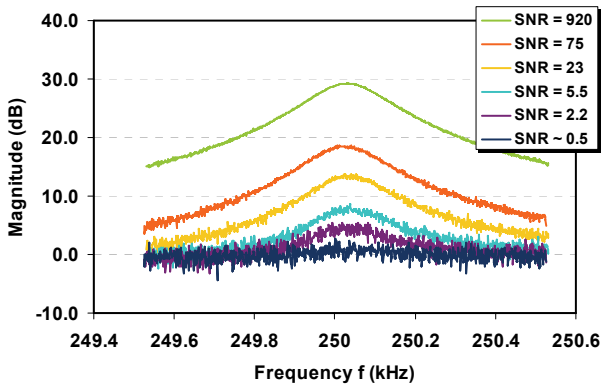

Figure 4.4. Measured resonance characteristics (magnitude) for different signal powers. The corresponding measurements are performed with minimum sequential time delay to prevent possible variations in the noise power density. (The presented magnitudes are in dB, with the noise power set as reference.)

In this work the Q-factors of measured transfer characteristics are calculated based on three methods: (a) half-power bandwidth (i.e., the 3-dB method), (b) single least-square fit to an SHO transfer function, and (c) iterative least-square fit as presented in this chapter. In implementing the iterative fitting method, due to fluctuation of the noise

spectral density (see Figure 4.5), the initial signal power, i.e., $A_k^2(f_i)$ in Eq. (4.22), is calculated by averaging the power of the first few data points of $A_k(f)$. Figure 4.6 compares the calculated Q-factor values for different signal-to-noise ratios. Each data point in this figure represents an average of repeated measurements with the same SNR, with the number of measurement repetition starting at 5 and increasing up to 20 for the data with larger standard deviation. In Figure 4.6, the bars on each side of the data points are equal to the standard deviation of the calculated Q-factor for the corresponding SNR. As shown in Figure 4.6, the chosen method has no significant effect on the value of extracted Q-factor as long as the SNR is larger than 20. Also, it is observed that for a larger SNR, the standard deviation is smaller. On the other hand, for signal-to-noise ratios smaller than 10, there is a clear difference between the calculated Q-factors. The Q-factor calculated based on the half-power bandwidth (if it is possible to find such a bandwidth− see Figure 4.5), shows the largest deviation from the actual Q-factor number, while the result of a single least-square fit appears modestly better. However, the most precise results, even down to an SNR of 1, are calculated using the proposed iterative fitting method. Overall, as it is observed in Figure 4.6, for an SNR larger than unity the calculated Q-factor with iterative fitting method undergoes less than 5% variation, which appears in a noticeable contrast to the errors associated with the other two methods in the same SNR range.

The basic assumption in the presented method is that the noise spectral density is constant over the measurement bandwidth. Such assumption may be held valid if the measurement bandwidth is relatively small. However, as mentioned before, the noise spectral density

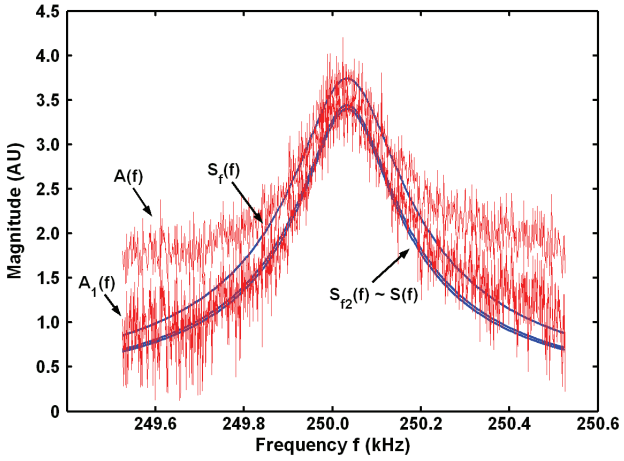

Figure 4.5. Implementation of the proposed iterative fitting method on an actual measured signal $A(f)$. Because of magnitude fluctuations, the partial noise power N_{k+1}^2 is calculated by considering the average of squares of the first 10 data points of $A_k(f)$. In this graph, the signal-to-noise ratio is 3.5, and the magnitude is in linear scale.

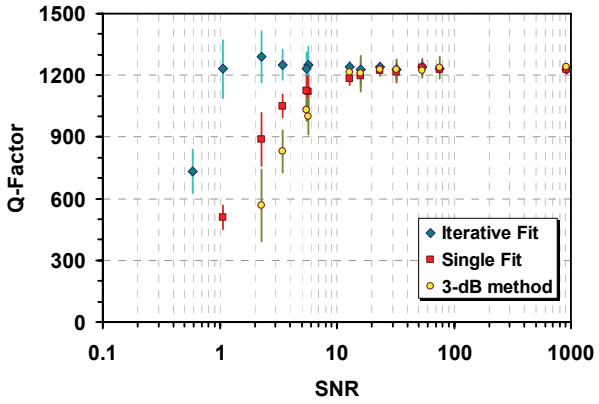

Figure 4.6. Q-factor as a function of SNR, extracted from the measurement data by using the two conventional methods, i.e., single least-square curve fit (square) and the 3-dB bandwidth methods (circle), and also the proposed iterative fitting method (diamond). No meaningful Q-factor data were obtain with the 3-dB bandwidth method for SNR smaller than 2, and with the single fit method for SNR smaller than 1.

may exhibit fluctuations around a constant average. If the signal power becomes comparable to these fluctuations, the accuracy of calculation will decline, as it is reflected by higher standard deviations in Figure 4.6. In the extreme case, when the signal power is smaller than the fluctuations, the presented method will be flawed. For this reason, a considerable drop in the extracted Q-factor values can be observed in Figure 4.6 for the SNR smaller than unity.

***

In the work presented in this chapter, the Q-factors extracted based on the 3-dB and the least-square curve fit methods are found to be inaccurate when the signal-to-noise ratio is less than 20. For a small SNR, it may not be even possible to clearly detect a half-power bandwidth on the resonator's magnitude transfer characteristic. To overcome the noise effect, a new iterative method is proposed and successfully tested. In this method, first the magnitude transfer characteristic of the resonator is fitted to the transfer function of an SHO (or a Lorentzian curve), then after calculating the power difference between the measured signal and the fitted curve, the measurement data is refined. By iterating this sequence, the noise effect is significantly eliminated from the measured data, to such an extent that for a tested cantilever resonator, the error in the Q-factor calculation is reduced to less than 5% for an SNR of unity. The applicability of the iterative method in canceling the effect of noise is confirmed by proving that the presented method converges to a unique solution for a given SHO transfer function. Although the resonance quality factors are extracted from SHO transfer characteristics, in general, for the purpose

of noise elimination, the presented iterative method can be applied to any transfer function as long as the convergence criterion is met; i.e., as long as unique solutions exist for the transfer functions of interest (e.g., Lorentzian, Gaussian, and etc.). The proposed method is especially useful in interpreting the measurement data when obtaining specific data about noise is not possible, either because of the special measurement set-up or because of the considerable time laps between the measurements.

CHAPTER 5

Q-FACTOR IN FUNDAMENTAL FLEXURAL MODE

As mentioned earlier in Chapter 2, resonant cantilever sensors have been used in a variety of chemical and biochemical sensing applications [3, 6, 140, 149, 153]. The operation principle in most of these sensors is based on the detection of a resonance frequency shift as a result of interaction with the targeted subject [7, 111, 146, 147]. An important parameter in this detection scheme is the quality factor of the resonator: a larger quality factor results in better frequency stability and consequently better sensing resolution [197, 198]. Also, in force detection techniques with cantilevers, e.g., in atomic force microscopy (AFM) and magnetic resonance force microscopy (MRFM), the thermomechanical noise of cantilever sensors is reduced by increasing the Q-factor [85, 199, 200].

For a simple resonator, higher Q-factors can be obtained either by improving the quality of the resonator structural material [201] or by optimizing the resonator shape to decrease the energy loss of the system. For a simple micro-cantilever beam resonating in air, since the choice of material is usually limited to what is commonly provided in micro-fabrication technology, e.g., silicon, silicon nitride and silicon oxide, the effect of cantilever's geometrical dimensions on the Q-factor becomes an attractive subject to study. In this regard, the focus of this chapter is on the fundamental flexural resonance mode of rectangular silicon cantilever beams resonating in air. The goal of this chapter is

to find the optimum dimensions for such cantilevers to achieve maximum Q-factors in the fundamental flexural mode.

5.1 Damping Mechanisms in a Resonant Cantilever

As described by Eq. (2.4), the quality factor is a measure of energy loss in a system. As long as the stored energy is constant, the higher quality factor means the lower energy dissipation per cycle. The quality factor of a cantilever resonating in air can be attributed to two main loss mechanisms, extrinsic and intrinsic. The extrinsic loss is due to interactions with the surrounding medium, e.g., viscous losses [202-204] and acoustic radiation [205, 206]. The intrinsic loss is due to interactions within the cantilever structure or with its support structure, e.g., support loss [207], thermoelastic loss (TED) [208-210], volume loss [179, 204], and surface loss [84, 179, 180]. The total energy dissipation in a system is calculated by adding the energy dissipation of each individual loss mechanism. Hence, for a given resonance frequency, the quality factor of the system is obtained from the quality factors attributed to each individual loss mechanism Q_{indiv},

$$\frac{1}{Q} = \sum \frac{1}{Q_{indiv}} = \frac{1}{Q_{air}} + \frac{1}{Q_{clamp}} + \frac{1}{Q_{TED}} + \frac{1}{Q_{vol}} + \frac{1}{Q_{surf}} \quad . \tag{5.1}$$

The individual Q-factors Q_{indiv} are calculated as if there is no other loss mechanism except the investigated one, e.g. air, support (clamp), thermoelastic, volume, or surface loss. For cantilevers resonating at atmospheric pressure, the dominant damping mechanism is the viscous (air) damping [180, 202]; on the other hand, in vacuum, where the resonators generally have significantly larger Q-factors, the support loss becomes more dominant when decreasing the cantilevers length [84, 180, 211]. In the next sections,

the three main damping mechanisms for a resonant cantilever, the air damping, support loss and thermoelastic damping (TED), are reviewed.

5.1.1 Air (Viscous) Damping

To analytically describe the air damping of a transversely resonating cantilever, three major approaches are proposed in the literature [212-214]. All these approaches rely on analytically well-known solutions for the viscous damping of basic solid bodies, which are derived from the Navier-Stokes equation and the continuity equation for incompressible fluids [215]

$$\frac{\partial \mathbf{u}}{\partial t} + (\mathbf{u}.\nabla)\mathbf{u} = -\frac{1}{\rho_o}\nabla P + \frac{\eta}{\rho_o}\Delta \mathbf{u}\,, \tag{5.2}$$

$$\nabla \cdot \mathbf{u} = 0\,, \tag{5.3}$$

where $\mathbf{u}(x,y,z,t)$ is the velocity field of the medium, P is the medium pressure, η and ρ_o are the dynamic viscosity and the density of the medium, respectively.

In the first analytical approach, the air damping of the cantilever is approximated by the viscous damping of a plate that undergoes a steady motion in the normal direction to the surface [212, 216]. In the second approach the beam is visualized as a single or a string of coherently resonating spheres, and based on the damping of each sphere, the total damping is calculated [202, 213, 217-221]. In the last approach, the beam vibration is described based on the vibration of a cylinder in a viscous medium [214, 222, 223]. In most of the models derived based on these approaches, a general assumption is to have a flow with a small Reynolds number. The Reynolds number R_e for a resonating beam is defined as [214]

$$R_e = \frac{\rho_o \omega}{4\eta} W^2 \tag{5.4}$$

where W is the width of the beam and ω is the angular resonance velocity. The requirement for a small Reynolds number implies that there are possibly less accurate predictions for higher resonance frequencies or for wider cantilevers.

Regardless of the chosen approach, the medium-exerted drag force F_d on the cantilever beam can be descried by two components, the dissipative and inertial [202, 217, 223]:

$$F_d = d_1 \frac{\partial y(x,t)}{\partial t} + d_2 \frac{\partial^2 y(x,t)}{\partial t^2}, \tag{5.5}$$

where $y(x,t)$ is the cantilever deflection, and d_1 and d_2 are the dissipative and inertial coefficients of the drag force, respectively. The dissipative component of the drag force causes an energy loss in the resonant system, while the inertial component accounts for an extra force applied on the mass of medium that resonates with the beam. Often in the study of damping, especially in the earlier works, the inertial component of the drag force has been ignored [204, 212]. Equation (5.5) can be combined with Eq. (2.23) to describe the damped vibration of resonant cantilever beams:

$$EI \frac{\partial^4 y(x,t)}{\partial x^4} + d_1 \frac{\partial y(x,t)}{\partial t} + \left(\rho_b A + d_2\right) \frac{\partial^2 y(x,t)}{\partial t^2} = 0, \tag{5.6}$$

where ρ_b and A are the cantilever mass density and cross section area, respectively, I is the moment of inertia and E is the modulus of elasticity. The general solution for Eq. (5.6) has the form of

$$y(x,t) = y(x) T_n(\omega) e^{i\omega_n t}, \tag{5.7}$$

where ω_n is the angular resonance frequency of the n^{th} overtone (mode) and $T_n(\omega)$ is a frequency dependant function, given by [224]

$$T_n(\omega) \propto \frac{1}{\sqrt{(\frac{\omega^2}{\omega_n^2}-1)^2+(\frac{1}{Q_n}\frac{\omega}{\omega_n})^2}}, \tag{5.8}$$

which describes the transfer characteristic of a simple harmonic oscillator (see Eq. (2.9a)).

In calculating the air damping, the first aforementioned analytical approach only accounts for the continuous movement of the cantilever through the medium (steady flow), while this model neglects the presence of resonant flows. This shortcoming is addressed in the other two approaches. In the second approach, i.e. the string of spheres model, the stream-line around the cantilever beam can be considered the same as a stream-line around a sphere when the Reynolds number is fairly small (R_e < 1) [202, 219]. An analytical expression for the oscillatory motion of a sphere in a viscous fluid has been derived by Landau *et al.* [215], based on which Blom *et al.* [202] have calculated the Q-factor of an oscillating beam in a viscous medium. In Blom's model, the whole cantilever beam is approximated with a single sphere, whose radius is obtained by curve fitting the experimental results. Hosaka *et al.* [219] have expanded the analytical expression of this model by considering the entire cantilever structure as a string of identical spheres. The diameter of each sphere is equal to the width of the beam. According to this model, the quality factor associated with the air damping Q_{air} is calculated as

$$Q_{air} = \frac{\rho_b H W^2 \omega_n}{3\pi\eta W + \frac{3}{4}\pi W^2\sqrt{2\rho_a\eta\omega_n}}, \tag{5.9}$$

where ρ_a is the density of air and H is the thickness of the beam. This model, however, does not include the effect of the drag force on the areas of the beam that the spheres do not cover. This issue is addressed by empirically calculating an effective sphere radius based on the measurement data [220, 225].

The third approach, applying the vibration solution of a resonating cylinder instead of a string of spheres, can alleviate the issue of incomplete coverage of spheres over the beam structure. The analytical solution of the Navier-Stokes equation for oscillation of a cylinder in a viscous medium is well-known [223, 226]. Sader [214] and Kirstein *et al*. [223] approximated the damping of a resonating cantilever with that of an infinitely long cylinder. In Sader's model, the assumptions are that the length of the beam L greatly exceeds the width W, and also the width greatly exceeds the beam thickness H. The accuracy of this model is improved by using a complex frequency dependent correction factor[214].

5.1.2 Support Loss

For a cantilever with an infinite width (a two-dimensional, 2-D, assumption) and with the cantilever-support considered as a semi-infinite large elastic body, the damping due to elastic energy radiation to the support from the cantilever is proportional to the cube of thickness to length ratio [211] $(H/L)^3$. Hence, the quality factor of a resonator enduring only the support loss, Q_{clamp}, is estimated as

$$Q_{clamp} = \kappa(\frac{L}{H})^3 \ , \qquad (5.10)$$

where κ is a coefficient calculated as κ = 0.34 [153], 2.17 [84, 219] or 2.081 [211]. In practice, the support usually does not have the exact shape assumed in the 2-D theoretical derivations. In a special case, when the support is a plate as thin as the cantilever beam [207, 227], the deteriorated quality factor is proportional to *L*/*H*.

5.1.3 Thermoelastic Damping (TED)

In the absence of the air damping and support loss, one of the most influential loss mechanism is the thermoelastic damping [84, 209]. The basic analytical calculations for TED in resonant structures, especially beams in flexural mode, are derived by Zener[208]. In Zener's model the thermoelastic quality factor of an isotropic homogenous beam resonating in the fundamental flexural mode, Q_{TED}, is approximated by

$$Q_{TED} = \frac{\rho_b C_p}{E\alpha^2 T_o} \frac{1+(\omega_1 \tau_Z)^2}{\omega_1 \tau_Z}, \qquad (5.11)$$

with

$$\tau_Z = \frac{\rho_b C_p H^2}{\pi^2 \kappa_{th}},$$

where C_p is specific heat capacity, α is the linear thermal expansion coefficient, T_o is the equilibrium temperature, and κ_{th} is thermal conductivity. Although Zener's model provides a good estimate of Q_{TED} for a resonating cantilever beam at the fundamental flexural mode, a better accuracy especially for more complicated structures, e.g., laminated beams, requires a more complex modeling [228].

In this chapter, the goal is to optimize the cantilever dimensions in order to maximize the Q-factor of the fundamental flexural resonance mode in air, and establish design

guidelines for cantilever-based resonators. To this end, the relationships between the Q-factor and the cantilever length, width and thickness are studied by measuring transfer characteristic of various rectangular silicon cantilever resonators, and by comparing the experimental data to analytical derivation. As an eminent result, accurate models for air damping are extracted.

5.2 Theory of Air Damping in Fundamental Resonance Mode

In this work, despite the mathematical elegance of Sader's model, it is chosen to use the more physically comprehensible approach of the string of spheres as a backbone for modeling the Q-factor of resonating cantilevers in the fundamental flexural mode. It can be seen from Eq. (5.9) that the Q-factor is almost independent of the beam width if

$$\frac{3}{4}\pi W^2\sqrt{2\rho_a\eta\omega_n} >> 3\pi\eta W ,$$

which defines the following requirement for the resonance frequency of the beam:

$$f_n >> \frac{1}{2\pi}\frac{8\eta}{\rho_a W^2} . \qquad (5.12)$$

Therefore, for micro-cantilever beams with a width of larger than 100 μm, to satisfy the condition of Eq. (5.12) at the room temperature (see Table 5.1), the required resonance frequency should be larger than 20 kHz, i.e., typically at least 10 times larger than the right-side of Eq. (5.12). The flexural resonance frequency of a cantilever beam is given by[188]

$$f_n = \frac{\omega_n}{2\pi} = \frac{\lambda_n^2}{2\pi\sqrt{12}}\frac{H}{L^2}\sqrt{\frac{E}{\rho_b}} , \qquad (5.13)$$

Table 5.1. Material properties of silicon and air.

	Quantity	Symbol	value
Air (T_o = 27 ˚C)	Density [202] [kg.m^{-3}]	ρ_a	1.18
	Dynamic Viscosity [202] [Pa.s]	η	18.6×10^{-6}
Silicon	Density [43] [kg.m^{-3}]	ρ_b	2330
	Specific Heat Capacity [84] [J.kg^{-1}.K^{-1}]	C_p	700
	Modulus of Elasticity [43] <110> [GPa]	E	169
	Linear Thermal Expansion Coefficient [84] [K^{-1}]	α	2.6×10^{-6}
	Thermal Conductivity [43] [W.m^{-1}.K^{-1}]	κ_{TH}	156

where λ_n is the flexural mode identifier constant with $\lambda_1 = 1.875$. By placing Eq. (5.13) in Eq. (5.9), provided the condition of Eq. (5.12) is satisfied, a simplified expression for Q_{air} is obtained:

$$Q_{air} = \frac{2}{3}\frac{\lambda_n}{\pi}\left(\frac{\rho_b^3 E}{3\rho_a^2\eta^2}\right)^{\frac{1}{4}}\frac{\sqrt{H^3}}{L}. \qquad (5.14)$$

Equation (5.14) is a function of the cantilever geometry through the ratio χ defined as

$$\chi = \frac{L}{\sqrt{H^3}}, \qquad (5.15)$$

and also is a function of the material properties of the beam as well as the ambient conditions through the coefficient ε

$$\varepsilon = \frac{3}{2}\frac{\pi}{\lambda_n}\left(\frac{3\rho_a^2\eta^2}{\rho_b^3 E}\right)^{1/4}. \qquad (5.16)$$

Hence, Q_{air} can be simply described by a reciprocal relationship with χ :

$$\frac{1}{Q_{air}} = \varepsilon\chi \,. \tag{5.17}$$

Revisiting Eq. (5.10), Q_{clamp} can also be expressed as a function of χ:

$$Q_{clamp} = \kappa H^{3/2}\chi^3 \tag{5.18}$$

Using Eqs. (5.1), (5.17) and (5.18), the combined quality factor Q can be calculated as

$$\frac{1}{Q} = \frac{1}{Q_{clamp}} + \frac{1}{Q_{air}} = \varepsilon\chi + \kappa^{-1}H^{-3/2}\chi^{-3} \,. \tag{5.19}$$

The maximum Q is found at the optimum χ_{opt}:

$$\chi_{opt} = \frac{1}{\sqrt[4]{\frac{\varepsilon\kappa}{3}H^{3/2}}} \,. \tag{5.20}$$

In other words, for a simplified case that the loss mechanism is dominated by only the air damping and support loss, the maximum Q-factor is obtained when the beam length and thickness fulfill the ratio:

$$\frac{L}{H^{9/8}} = \sqrt[4]{\frac{3}{\varepsilon\kappa}} \,. \tag{5.21}$$

The accuracy of this calculation can be improved by including the effect of thermoelastic damping. For a simple rectangular beam resonating at the fundamental flexural mode, Q_{TED} is approximated by Eq. (5.11), which can be rearranged with respect to χ after applying Eq. (5.13):

$$Q_{TED} = \frac{\rho_b C_p}{E\alpha^2 T_o}\frac{1+(\beta\chi^{-2})^2}{\beta\chi^{-2}}, \tag{5.22}$$

where β is

$$\beta = \frac{\rho_b C_p}{\kappa_{th}}\left(\frac{\lambda_1}{\pi}\right)^2\sqrt{\frac{E}{12\rho}} \,. \tag{5.23}$$

Using Eqs. (5.1), (5.17), (5.18) and (5.22), the combined quality factor Q can be written as

$$\frac{1}{Q}=\frac{1}{Q_{clamp}}+\frac{1}{Q_{air}}+\frac{1}{Q_{TED}}=\varepsilon\chi+\kappa^{-1}H^{-3/2}\chi^{-3}+\frac{E\alpha^2T_o}{\rho_bC_p}\frac{\beta\chi^{-2}}{1+(\beta\chi^{-2})^2}. \quad (5.24)$$

Hence for the independent variable χ, the maximum Q occurs when

$$\varepsilon-3\kappa^{-1}H^{-3/2}\chi^{-4}-\frac{2E\alpha^2T_o\beta}{\rho_bC_p}\frac{1-(\beta\chi^{-2})^2}{(1+\beta^2\chi^{-4})^2}\chi^{-3}=0. \quad (5.25)$$

Using the analytical expression of Eq. (5.24), variations of Q^{-1} with χ for beams with thicknesses of 5, 10 and 20 μm are calculated and depicted in Figure 5.1(a). The required

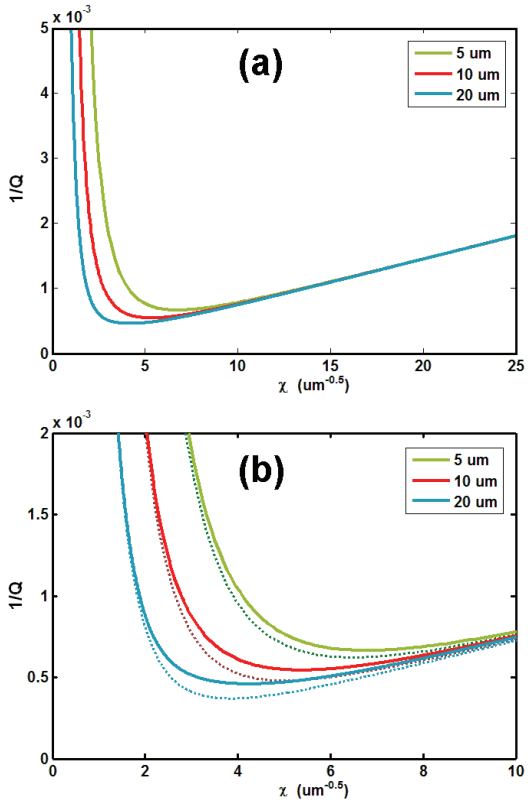

Figure 5.1. (a) Plots of Q^{-1} versus $\chi = L/H^{1.5}$ for cantilevers with thicknesses of 5, 10 and 20 μm, calculated from Eq. (5.24), (b) close-up of the region of maximum Q comparing the model described by Eq. (5.24) (solid lines) with the model described by Eq. (5.19) that excludes TED (dotted lines).

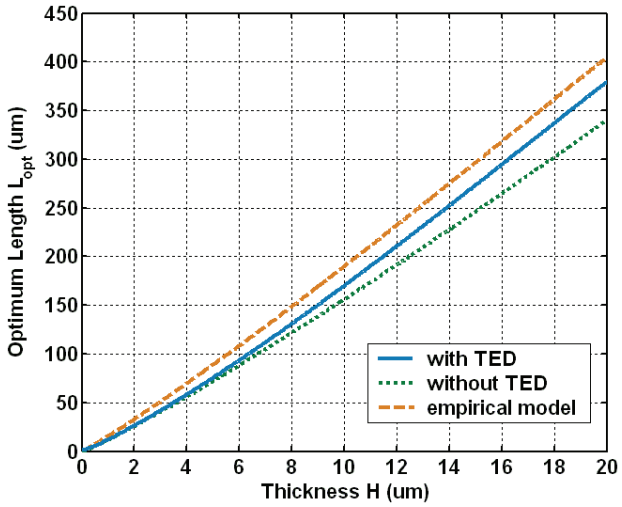

Figure 5.2. Optimum length of cantilever versus cantilever thickness for achieving maximum Q-factor; the calculation represented by the solid line, based on Eq.(5.25), includes the three dominant damping mechanisms, i.e., the air damping, support loss and TED, while the calculation of dotted line, based on Eq. (5.20), excludes TED. The dashed line calculation, which also includes the three dominant damping mechanisms, is based on an empirically adjusted model that is described by Eq. (5.30) with an exponent of support loss $p = 2.7$.

parameters for plotting Figure 5.1(a) are summarized in Table 5.1, based on which, ε and β are calculated as 7.2×10^{-8} $m^{0.5}$ and 9.33×10^{6} m^{-1}, respectively. Here, the assumed coefficient for the support loss is [84, 211] $\kappa = 2.1$. As depicted in Figure 5.1(b), including Q_{TED} in Eq. (5.24) only slightly changes the value of minimum Q^{-1} and the location of the optimum χ. The same observation can be made in Figure 5.2, which shows the optimum calculated length L_{opt} versus the cantilever thickness. In general, as seen in Figure 5.1(a), the Q-factor is limited by the support loss for smaller χ, and by the air damping for larger χ. Equation (5.25) indicates, as shown in Figure 5.1(a), that increasing the cantilever thickness will monotonically increase the maximum Q-factor; but since in this model the effect of other damping mechanisms is ignored, e.g.,

especially air friction on the sidewalls, increasing the thickness beyond a limit can no longer be helpful in achieving larger Q-factors.

5.3 Measurement

Rectangular silicon cantilever beams with lengths and widths ranging from 70 to 1050 μm and 80 to 230 μm, respectively, have been tested (see Figure 5.3). The cantilevers were fabricated using epitaxial silicon wafers with an n-type device layer and a p-type handle layer. The device layer thickness ultimately defined the cantilever thickness. The handle layer was about 525 μm thick. The beams were released by a combination of

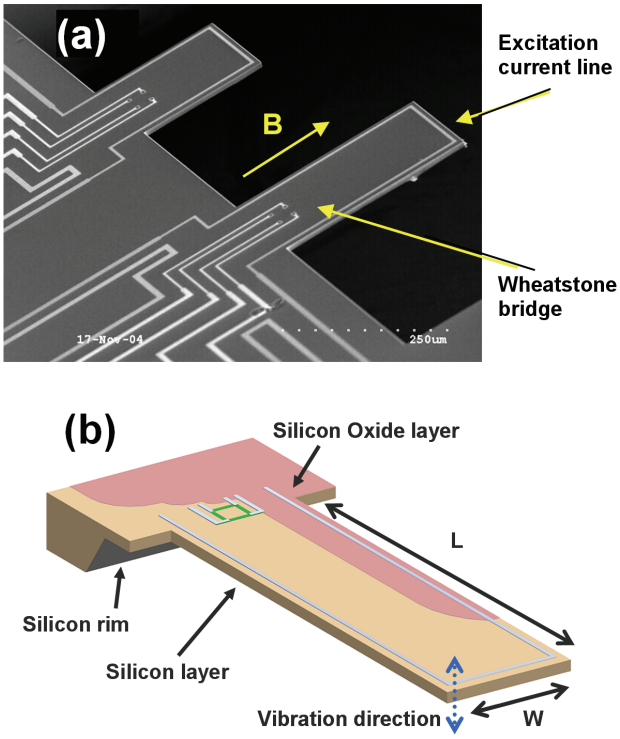

Figure 5.3. (a) SEM micrograph of fabricated silicon cantilevers showing the current route along the beam perimeter for excitation of beam vibrations in the presence of a static magnetic flux B; a Wheatstone bridge is located close to the clamped edge to sense the beam deflections. (b) Schematic of a typical cantilever.

back-side anisotropic wet etching, using an electrochemical etch-stop technique, and front-side dry etching to define the lateral geometries along the [110] directions. Depending on the thickness of device layer, the fabricated cantilevers had final silicon thicknesses of 5, 7, 8, 11 and 17 μm, covered with an approximately 0.8 μm thick PECVD silicon dioxide layer. As mentioned in Chapter 3, it must be pointed out that due to variations in the thickness of the handle wafers, the clamped edge of the cantilevers was not exactly coinciding with the edge of the back-side etched cavity; instead, the cantilevers were supported by a silicon rim of the same thickness, 5 to 20 μm long for different wafers (see Figure 5.3).

Flexural cantilever vibrations are electro-magnetically excited: in the presence of a static magnetic flux B in the cantilever length direction, an excitation force is exerted on the cantilever by passing an alternating current through a metal loop along the perimeter of the cantilever (see Figure 5.3). In the measurement set up, the cantilevers were at least 525 μm away from the closest parallel surface. The flexural beam vibrations are sensed on-chip by a piezoresistive Wheatstone bridge located near the clamped-edge of the beam. To have comparable results, it was imperative to keep the resonance amplitude of cantilever confined within the linear bending region of the beam; to this end, depending on the stiffness of the cantilever, the amplitude of excitation current was in the range of 3–20 mA, and the magnetic flux density was between 0.1-0.6 T. The transfer characteristics of the resonant cantilevers were recorded by an Agilent Network Analyzer 4395A. Figure 5.4 shows an amplitude and phase spectrum of a sample device. All measurements were performed at 30 ± 5 ºC. For each data point presented in the

following section, at least eight transfer characteristics were recorded, and after fitting the data to the amplitude transfer characteristic of a second-order system, using the iterative method presented in Chapter 4, the extracted resonance frequencies and Q-factors were averaged. For the presented data, the maximum relative standard deviation for the Q-factor is less than 3.3%.

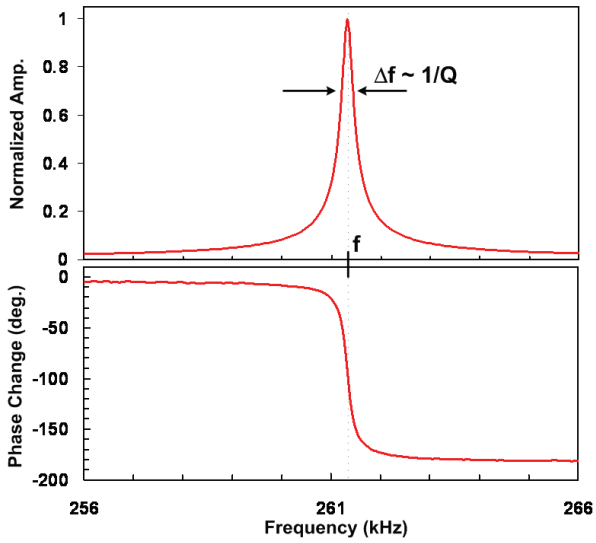

Figure 5.4. Measured amplitude and phase transfer characteristic of a silicon cantilever beam resonator with L, W, and H of 225 , 82 and 11 μm, respectively, around the fundamental flexural resonance frequency.

5.4 Results and Discussion

In this section, first the measurement results for different cantilevers are presented and compared with the previously presented analytical predictions. Next, using correction factors, Eq. (5.24) is adjusted to have the best agreement with the measurement results.

The dependence of the Q-factor on the cantilever length is shown in Figure 5.5. In this plot, the width and thickness of the measured cantilevers are 130 and 11 μm, respectively.

Two distinct regions can be recognized: in the first region, for a cantilever length smaller than 200 μm, the Q-factor increases with increasing length, whereas in the second region (L > 200 μm), the Q-factor decreases with an increase in length. From Eq. (5.24) it is known that the dominant damping mechanisms are the air damping and support loss; hence, the two regions in Figure 5.5 can be each attributed to one of these damping mechanisms. In the first region, where the length is smaller than 200 μm, i.e., χ is smaller than 5 $\mu m^{-0.5}$, damping is dominated by the support loss. In the second region, for χ larger than 7 $\mu m^{-0.5}$, the air damping is dominant.

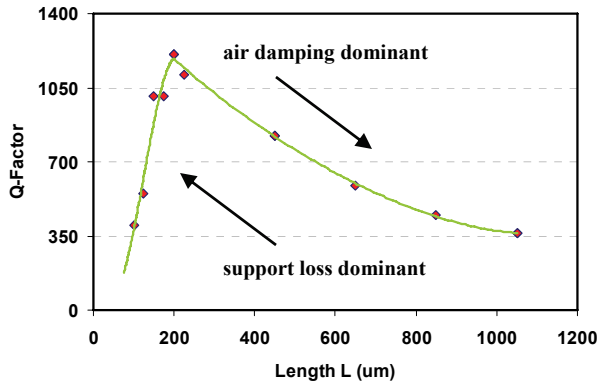

Figure 5.5. Q-factor as a function of length for cantilevers with width and thickness of 130 and 11 μm, respectively. The solid line is a guide to the eye only.

To investigate the dependence of the Q-factor on χ, data from all measured cantilevers with different W, L and H, are gathered in Figure 5.6, where Q^{-1} is plotted versus χ. It is observed that the Q-factors of beams with different dimensions not only follow similar trends, but also overlap for larger χ values. This behavior has been predicted by Eq. (5.24), as shown in Figure 5.1. Equation (5.24) indicates that for larger χ, where the air damping is the dominant loss mechanism, Q^{-1} increases linearly with χ following a slope

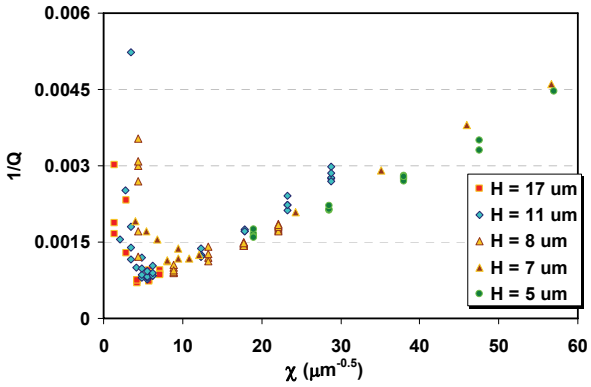

Figure 5.6. Plot of measured Q^{-1} versus $\chi = L/H^{1.5}$ for cantilevers with thicknesses of 5, 7, 8, 11 and 17 μm. Although not marked in the graph, the widths of the measured cantilevers are not necessarily equal.

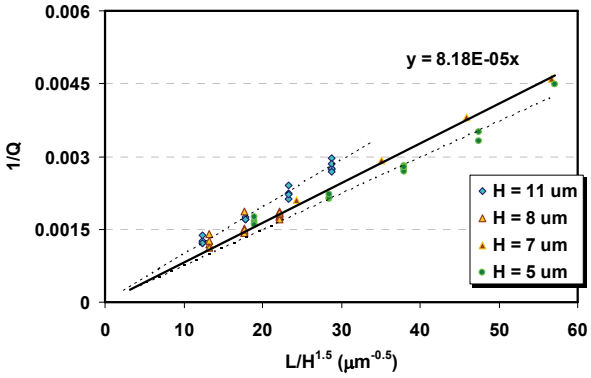

(a)

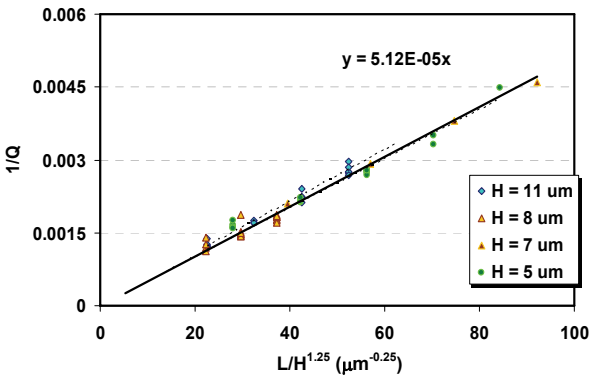

(b)

Figure 5.7. Inverse of Q-factor Q^{-1} as a function of: (a) $L/H^{1.5}$ and (b) $L/H^{1.25}$. The exhibited Q-factors belong to cantilever resonators enduring the air damping as the dominant loss mechanism

given by the coefficient of air damping ε. Therefore, an empirical value for ε can be obtained by a linear regression for all data with $\chi > 12$ $\mu m^{-0.5}$, yielding $\varepsilon_{ipm} = 8.2\times 10^{-5}$ $\mu m^{0.5}$ (see Figure 5.7(a)). Since the calculated air damping factor from Eq. (5.16) is 7.2×10^{-8} $m^{0.5}$ (i.e., $\varepsilon = 7.2\times 10^{-5}$ $\mu m^{0.5}$) for the conditions given in Table 5.1, a correction factor of $c_1 = 1.14$ can be introduced in Eq. (5.17) to describe the measured results:

$$Q_{air}^{-1} = c_1 \varepsilon \chi = 1.14 \times \frac{3}{2}\frac{\pi}{\lambda_n}\left(\frac{3\rho_a^2\eta^2}{\rho_b^3 E}\right)^{1/4}\chi . \qquad (5.26)$$

Generally, the energy loss in the region dominated by the air damping is larger than what is predicted by Eq. (5.14), i.e., by approximating the beam as a string of spheres. A potential explanation for this observation can be attributed to the influence of the beam thickness on the energy loss as the result of, for example, air friction on the beam sidewalls. This explanation is supported by the fact that the measured slope ε for equally thick cantilevers slightly increases by increasing the thickness (see Figure 5.7(a)). In fact, based on the measured data for the air damping dominated region, i.e., χ larger than 12 $\mu m^{-0.5}$, it is found that all the Q^{-1} data points, regardless of the cantilever thickness, will follow almost identical slopes if they are plotted versus $L/H^{1.25}$, i.e., $H^{0.25}\chi$ (see Figure 5.7(b)). In this case, the air damping coefficient, extracted from the slope of experimental data, is about 1.6×10^{-6} $m^{0.25}$ (i.e., 5.1×10^{-5} $\mu m^{0.25}$):

$$Q_{air}^{-1} = 1.6\times 10^{-6} H^{0.25}\chi . \qquad (5.27)$$

It must be noted that this coefficient is extracted from the data of the fundamental flexural resonance of silicon cantilevers in air and at a temperature of 30±5 ºC.

For $\chi < 15\ \mu m^{-0.5}$ (see Figure 5.6), unlike in the air damping dominated region, Q^{-1} sharply depends on the device thickness and width. While the thickness dependence is theoretically predicted (as depicted in Figure 5.1), the dependence of the Q-factor on W is left unexplained by the basic theory discussed earlier. The width dependence of the Q-factor is further investigated in Figure 5.8, which compares the measured Q-factors versus the width of cantilevers with $H = 11\ \mu m$ and shows that for longer cantilevers (i.e., larger χ values) the Q-factor becomes almost independent of the width; however, when L is smaller (e.g. shorter than 250 μm) the wider beams have noticeably smaller Q-factors. The variation of the Q-factor with W is also shown in Figure 5.9, for cantilevers with a fixed length of 400 μm but different thicknesses of 5, 8, and 17 μm. In this figure, the Q-factor variation with width is only observed for cantilevers with χ smaller than $15\ \mu m^{-0.5}$, i.e., for 17 μm-thick cantilevers.

Revisiting the theoretical derivations for the air damping expression in Eq. (5.14), the associated energy loss has become independent of W when the requirement described by Eq. (5.12) is fulfilled. To examine the validity of this simplification, the Q-factors of 11 μm-thick cantilevers as a function of their fundamental resonance frequency are plotted in Figure 5.10. Noting that from Eq. (5.13) the resonance frequency is independent of the cantilever width, as observed in Figure 5.10, the width dependence is more pronounced for the Q-factors of cantilevers with higher resonance frequencies. However, cantilevers with higher resonance frequency even better satisfy the condition of Eq. (5.12); hence, the simplification made in deriving Eq. (5.20) is valid, and the width variations must be due to another loss mechanism. By comparing the results of Figures 5.8–5.10 and

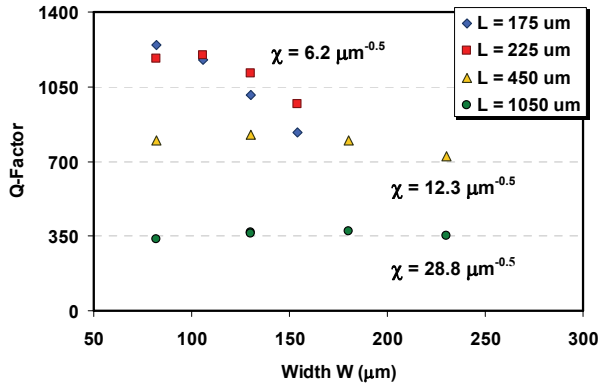

Figure 5.8. Q-factor as a function of the cantilever width for different lengths; the cantilever thickness is 11 μm.

considering the observation that the width dependence is more noticeable in the support loss dominated region, i.e., for smaller lengths, we conclude that using the Q_{clamp} expression of Eq. (5.18) does not give accurate results for smaller L/H ratios; in fact, Q_{clamp} increases by decreasing the width. Although this observation has been predicted by other theoretical models[227], the 2-D support loss model of Eq. (5.18) still provides the best overall approximation for the measurement data. Also, since the maximum Q-factor for different cantilever widths occurs at almost identical χ values, as shown in Figure 5.6,

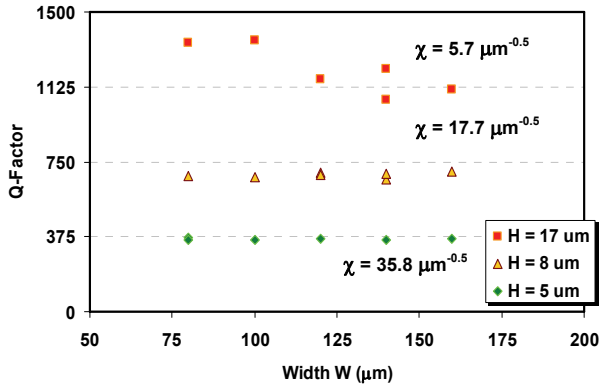

Figure 5.9. Q-factor as a function of width W for cantilevers with a fixed length L = 400 μm but different thicknesses of 5, 8, and 17 μm.

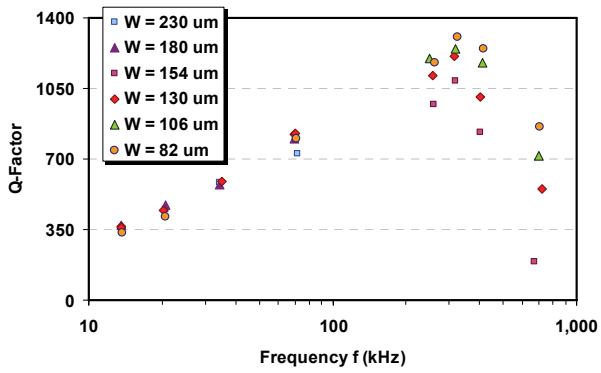

Figure 5.10. Q-factor as a function of the fundamental flexural resonance frequency for 11 μm-thick cantilevers with different widths ranging from 82 to 230 μm.

Eq. (5.18) can still be helpful in determining the optimum cantilever geometry, despite of its shortcoming in including the effect of width. On the other hand, since the fabricated cantilevers are not ideal beams, which must be clamped on a straight semi-infinite sidewall as assumed in the derivation of Eq. (5.18), Q_{clamp} may not be exactly proportional to $(L/H)^3$, but to an L/H ratio with a different exponent[207]. This statement becomes more viable when considering the effect of the silicon rim between the clamped end of the cantilever and the supporting sidewall. To account for this effect, Q_{clamp} can be expressed in a more general form of

$$Q_{clamp} = \kappa H^{p/2} \chi^p . \qquad (5.28)$$

For ideal boundary conditions, i.e., perfect support, the exponent p is 3, while by increasing the length of support rim, a smaller p can give a more accurate expression. By replacing the air damping and support loss terms in Eq. (5.24) with Eqs. (5.26) and (5.28), the Q-factor of resonating cantilevers is obtained as

$$Q^{-1} = 1.14 \times \frac{3}{2}\frac{\pi}{\lambda_n}\left(\frac{3\rho_a^2\eta^2}{\rho_b^3 E}\right)^{1/4}\chi + \kappa^{-1}H^{-p/2}\chi^{-p} + \frac{E\alpha^2 T_o}{\rho_b C_p}\frac{\beta\chi^{-2}}{1+(\beta\chi^{-2})^2}. \tag{5.29}$$

On the other hand, using the empirically adjusted expression for air damping from Eq. (5.27), a better agreement with the measurement results of resonant silicon cantilever at a temperature of 30 ± 5 ºC can be obtained:

$$Q^{-1} = 1.6 \times 10^{-6} H^{0.25}\chi + \kappa^{-1}H^{-p/2}\chi^{-p} + \frac{E\alpha^2 T_o}{\rho_b C_p}\frac{\beta\chi^{-2}}{1+(\beta\chi^{-2})^2}. \tag{5.30}$$

The effect of the support loss exponent p is further investigated in Figure 5.11, where the Q-factors of cantilevers with thickness and width of 11 and 130 μm, respectively, are compared with the empirical model of Eq. (5.30). In this figure the measured cantilevers have a silicon rim, approximately 8 μm long. As observed in Figure 5.11, a support loss exponent of p = 2.7 provides the best estimate for the Q-factor of the cantilevers in the

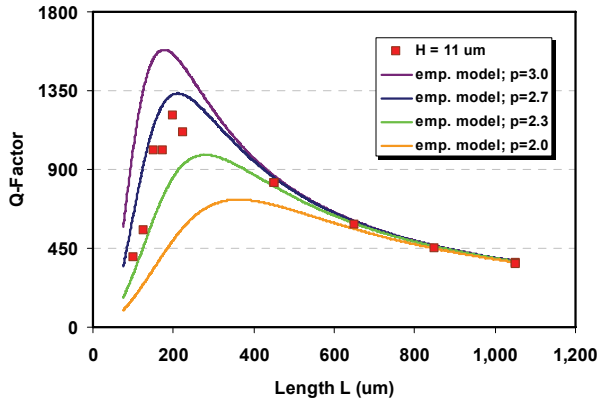

Figure 5.11. Comparison of measured and calculated Q-factor data for different support loss exponents p; the cantilever thickness and width are 11 and 130 μm, respectively. The Q-factor calculation is based on the empirical model described by Eq. (5.30).

support loss dominated region, i.e., $L < 400$ μm. When evaluating the quality of the empirical model of Eq. (5.30), it must be noted that the calculated maximum Q-factor is expected to be larger than the measured data because Eq. (5.30) neglects possible additional damping mechanisms, e.g., the volume loss and the air friction, as well as the effect of ambient conditions, e.g., temperature. Moreover, the influence of the silicon oxide layer covering the cantilever (~ 0.8 μm) and also the effect of small variations in the thickness of fabricated beams are not considered in the calculation. Finally, the influence of the cantilever width is also not included in Eq. (5.30). It should be emphasized that unlike the absolute value of the calculated Q-factor, the optimum calculated length L_{opt} does not vary significantly with the empirical and theoretical values of $p = 2.7$ and 3 (where $L_{opt} = 210$ and 176 μm, respectively).

A comparison of different models for describing the Q-factor versus the resonance frequency f is presented in Figures 5.12 and 5.13. Figure 5.12 summarizes the Q-factor data for 140 μm wide cantilevers with thickness of 5, 8 and 17 μm, and compares them to the calculated data based on the combined effects of support loss using Eq. (5.28) with $p = 2.7$, TED using Eq. (5.22), and three different air damping models: (A) the corrected analytical air damping model described by Eq. (5.29); (B) the well-known analytical air damping model proposed by Sader[214]; and (C) the empirical model of air damping according to Eq. (5.30). Overall, model C, based on Eq. (5.30), best describes the experimental data (see Figure 12(c)). This observation becomes even more evident in Figure 5.13, where the results obtained from the three models are compared closely together and to the measurement data of cantilevers with width and thickness of 130 and

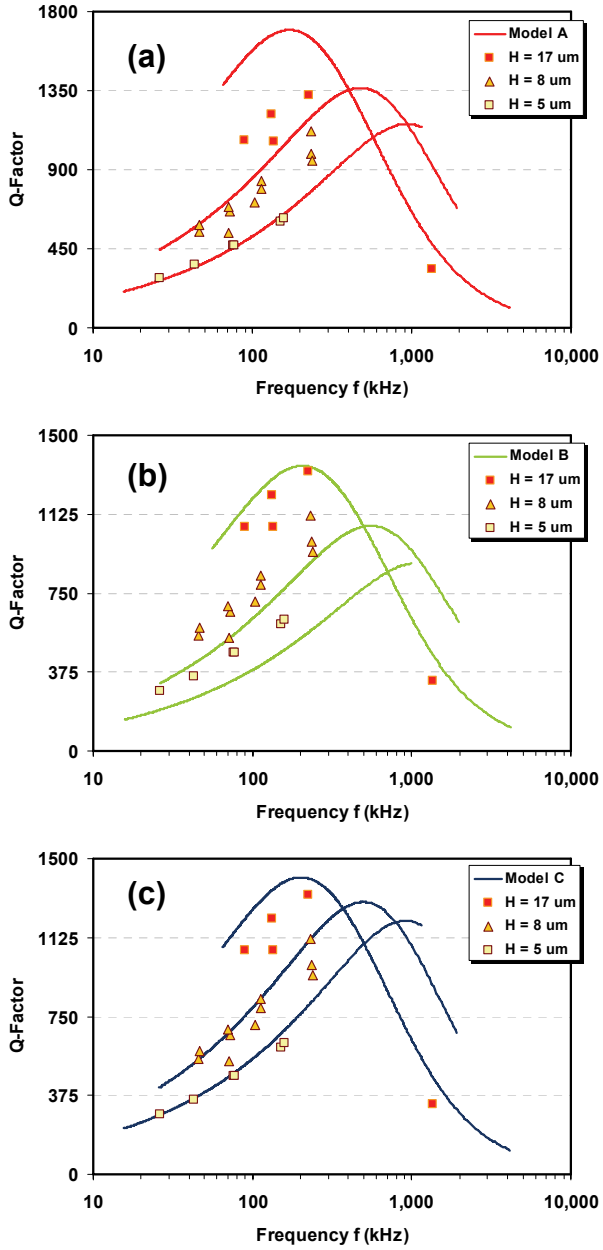

Figure 5.12. Q-factor as a function of resonance frequency for 140 μm-wide cantilevers. The measured data is compared with the following models: (a) model A, the proposed analytical model of Eq. (5.29), (b) model B, in which the air damping is described by Sader's analytical model [213], and (c) model C, the proposed empirical model of Eq. (5.30). The x-axis indicates the corresponding fundamental flexural resonance frequency.

11 μm, respectively. For lower resonance frequencies (i.e., longer cantilevers), model C perfectly matches the measurement data, while the two other models closely follow the data trend. However, for higher frequency (i.e., shorter cantilevers), there is a frequency gap between the measurement and calculations. Since in Figure 5.11 the result of model C has exhibited an acceptable match with the experimental data for the shorter cantilevers, the presence of the frequency gap in Figure 5.13 is believed to be associated with the discrepancy between the calculated and measured frequencies in the shorter cantilevers. An explanation for this effect is referred to the increasing significance of non-ideal boundary conditions (e.g., the presence of silicon rim and non-ideal clamped edge) for shorter beams.

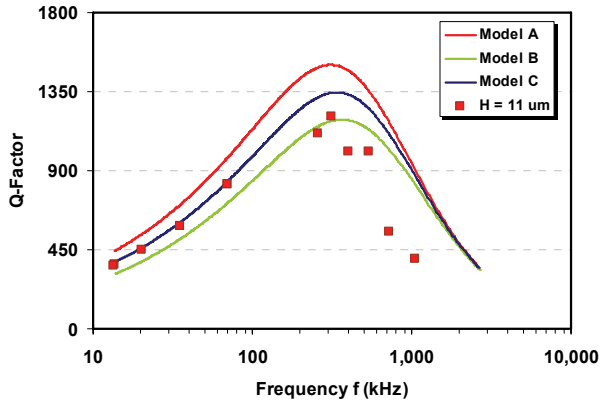

Figure 5.13. Q-factor as a function of resonance frequency for cantilevers with thickness and width of 11 and 130 μm, respectively. The measured data is compared with the results of previously mentioned models A, B, and C. The x-axis indicates the corresponding fundamental flexural resonance frequency.

The presence of resonant modes in close frequency proximity (coupled peaks) is another factor that can undermine the analytical predictions. It is well-known that the presence of multiple peaks in a close vicinity results in reduction of the Q-factor[179]. This effect can

be observed in Figure 5.14, which demonstrates two examples of significant aberration of the measured Q-factors from the analytical prediction for cantilevers with lengths of 100 and 150 μm. In this figure, the cantilevers width and thickness are 11 and 82 μm, respectively. The analytical calculation is based on Eq. (5.30) with a support loss exponent p = 2.75. In all presented plots in this work, the data-points associated with coupled peaks are omitted unless they are explicitly marked.

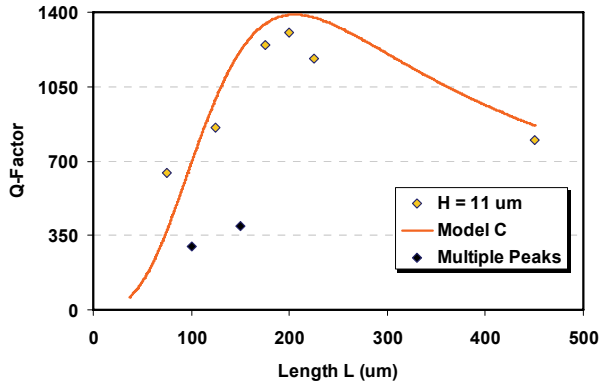

Figure 5.14. Reduced Q-factors for two cases of cantilevers with lengths of 100 and 150 μm (dark diamonds) due to occurrence of multiple peaks in a close frequency proximity (coupled peaks); the thickness and width of the cantilevers in this graph are 11 and 82 μm, respectively. The solid line shows the Q-factor calculation based on Eq. (5.30).

Finally, the optimal cantilever geometry for achieving the maximum Q-factor, given by Eq. (5.25) can be revised by including the fit parameter as in Eqs. (5.29) or (5.30). Similar to Eq. (5.25), the optimal χ can be calculated by finding the minimum Q^{-1} in Eq. (5.30). Based on this calculation, for p = 2.7, the optimal length, as a function of thickness, is presented with a dashed line in Figure 5.2. The required parameters for plotting Figure 5.2 are summarized in Table 5.1. It is observed that using the empirically adjusted model only slightly affects the predicted optimal cantilever length for a given

thickness; therefore, Figure 5.2 can be used as a simple look-up graph to find the cantilever dimension for maximizing the Q-factor of the fundamental flexural resonance mode.

***

In this chapter by combining analytical derivations and experimental results, two models are developed to estimate the optimum dimensions of resonant rectangular cantilever beams for achieving maximum quality factor in air at the fundamental resonance. For silicon cantilevers with thicknesses between 5 to 17 μm, it has been calculated that the reciprocal of Q-factor is linearly proportional to $L/H^{1.5}$ if this ratio is larger than 15 $\mu m^{-0.5}$. This behavior indicates that the air damping is the dominant loss mechanism for cantilevers with such length to thickness ratios; however, a close examination of the measured quality factors of these cantilevers shows that they exhibit almost identical quality factors if they share the same ratio of $L/H^{1.25}$, or in other words, the air damping seems to be proportional to $L/H^{1.25}$. Also, it has been shown that the effect of cantilever width may be neglected in analytical calculations, and the measurement results of cantilevers with large $L/H^{1.5}$ confirm this assumption. In contrast, with the support loss being a major contributor to the damping, in short cantilevers (i.e., $L/H^{1.5} < 15\ \mu m^{-0.5}$) the Q-factor becomes a strong function of the cantilever width. Nevertheless, it is observed that the maximum measured Q-factor of cantilevers with different widths but same thickness occurs almost at the same length. Moreover, it is recognized that the support loss equation must be adjusted to include the effect of imperfectness on the cantilever

support (i.e., the clamped edge) when compared to the ideal boundary condition. Combining the corrected equations of air damping and support loss with the well-known Zener approximation for TED has made it possible in this chapter to calculate the optimum lengths of resonant cantilevers with given thicknesses to achieve the maximum achievable quality factor for the fundamental flexural resonance mode in air.

CHAPTER 6

EFFECTIVE MASS IN FLEXURAL VIBRATIONS

The goal of this chapter is to provide a theoretical model for estimating the effective mass and spring constant of a cantilever resonating in flexural modes. To establish such a model, first, using beam theory, the conditions for statically bending a beam to resemble the flexural mode shapes are explored. Next, a cantilever resonating in the n^{th} overtone is modeled as a system with n degrees of freedom, which consists of n coupled single mass-spring systems. The presented model is used in Chapter 7 to evaluate the damping of cantilevers resonating in flexural modes.

6.1 Flexural Vibration of a Cantilever Beam

As mentioned in Chapter 2, the undamped vibration of a homogenous cantilever in the n^{th} flexural resonance mode can be described by

$$y(x,t) = y(x)e^{i\omega_n t}. \tag{6.1}$$

The vibration amplitude $y(x)$ is calculated as [2, 229]

$$y(x) = c_1(\cos\frac{\lambda_n}{L}x - \cosh\frac{\lambda_n}{L}x) + c_2(\sin\frac{\lambda_n}{L}x - \sinh\frac{\lambda_n}{L}x) \tag{6.2}$$

with

$$\lambda_n^4 = \frac{\rho A\omega_n^2 L^4}{EI}, \quad \cos\lambda_n \times \cosh\lambda_n = -1 \tag{6.2a}$$

and

$$c_1 = \frac{y(L)}{2},$$
$$c_2 = -\frac{\cos(\lambda_n)+\cosh(\lambda_n)}{\sin(\lambda_n)+\sinh(\lambda_n)} \times c_1 = \frac{\sin(\lambda_n)-\sinh(\lambda_n)}{\cos(\lambda_n)+\cosh(\lambda_n)} \times c_1 \ . \quad (6.2b)$$

The kinetic energy K of a particle is defined by [230]

$$K = \frac{1}{2} m v^2 , \quad (6.3)$$

where m and v are the mass and velocity of the particle, respectively. A vibrating beam can be considered as a series individual particles; hence, its kinetic energy is given by [175]:

$$K = \frac{1}{2} \int_0^L \rho A \left(\frac{\partial y}{\partial t}\right)^2 dx , \quad (6.4)$$

where A and ρ are the beam cross section and density, respectively, and L is the beam length. For a cantilever resonating in a flexural mode, the velocity of any single point of the beam can be calculated with respect to Eq. (6.1):

$$\frac{\partial y(x,t)}{\partial t} = i\omega_n y(x) e^{i\omega_n t} , \quad (6.5)$$

assuming that no part of the beam undergoes a shear movement (i.e., the cantilever thickness is negligible compared to the length). Therefore, with respect to Eq. (6.4), the maximum kinetic energy of the entire beam in the n^{th} flexural mode can be calculated as

$$K = \frac{\omega_n^2}{2} \int_0^L \rho A y^2(x) dx . \quad (6.6)$$

It must be noted that for the derivation of Eq. (6.6) the damping of system is considered to be negligible; hence, the contribution of resonance modes other than the n^{th} flexural mode can be ignored. In a homogeneous cantilever beam with uniform cross section, Eq. (6.6) can be simplified to

$$K = \frac{1}{2}\frac{m\omega_n^2}{L}\int_0^L y^2(x)dx\,. \qquad (6.7)$$

In Appendix C it is shown that for all flexural modes the amount of integral in Eq. (6.7) is

$$\int_0^L y^2(x)dx = \tfrac{1}{4}Ly^2(L)\,. \qquad (6.8)$$

where, $y^2(L)$ is the vibration amplitude of the cantilever tip (free end) . Hence, Eq. (6.7) for all flexural modes can be simplified to

$$K = \frac{1}{2}\left(\frac{m}{4}\omega_n^2 y^2(L)\right). \qquad (6.9)$$

A cantilever beam can be considered as a single point-mass resonator, which vibrates at the same amplitude as the cantilever tip. In this case, according to Eqs. (6.3) and (6.5), the maximum kinetic energy of the point-mass resonator will be

$$K = \frac{1}{2}\left(m^*\omega_n^2 y^2(L)\right), \qquad (6.10)$$

where m^* is the effective resonator's mass corresponding to the total actual mass of cantilever when concentrated on the tip. (For simplicity we refer to it as the tip point-mass.) To have a valid correspondence between the single point-mass resonator and the resonant cantilever, the kinetic energies of the both systems must be equal; hence, with respect to Eqs. (6.9) and (6.10):

$$m^* = \tfrac{1}{4}m\,. \qquad (6.11)$$

In other words, for all flexural vibration modes the effective mass of a cantilever, if considered as a point-mass on the tip, is a quarter of the actual mass. For the fundamental flexural mode this ratio will be examined further in section 6.3.1.

6.2 Imitating Flexural Mode Shapes with Static Beam Bending

The flexural vibration amplitude of a cantilever can be resembled by statically bending the beam. It must be noted that such a resemblance is in fact an approximation since the governing equations for static and dynamic beam deflection, despite close similarity, are not identical. In other words, revisiting Eq. (2.23), the deflection of a resonant cantilever beam is caused by a distributed inertial force:

$$\frac{\partial^2}{\partial x^2}\left(EI\frac{\partial^2 y(x,t)}{\partial x^2}\right) = -\rho A\frac{\partial^2 y(x,t)}{\partial t^2}, \tag{6.12}$$

while the static bending of a beam is caused by discrete point forces. For example, when the cantilever is deflected by a force applied on the tip ($x = L$) the deflection along the beam is described as [1]

$$EI\frac{\partial^2 y(x)}{\partial x^2} = M = F(L-x), \tag{6.13}$$

where M is the bending moment.

A cantilever resonating in the n^{th} flexural mode (i.e., the n^{th} flexural overtone) has n-1 nodes (regardless of the clamped end) and n antinodes. Therefore, to imitate the vibration mode shape, at least n different point forces are needed. Here we assume that each of the point forces is applied on an antinode. The fairness of this assumption is examined later by comparing the modeled beam deflection with the theoretical flexural vibration amplitude. Also with this assumption there will be always a point force applied on the cantilever tip in any flexural overtone. The proposed force arrangement along the beam is illustrated in Figure 6.1.

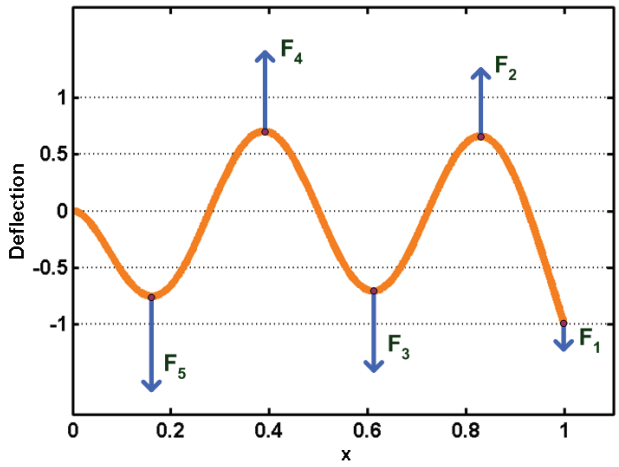

Figure 6.1. Configuration of independent point forces applied on antinodes in the 5th flexural mode. The size of point force vectors are in proportion to the ratios given in Table 6.2.

In Chapter 2 the bending of cantilever due to a point force was expressed by Eq. (2.14). Based on the same equation, the cantilever deflection y_j at a point x on the cantilever, as the result of applying a force F_j at the point x_j, can be expressed in a more general form:

$$y_j(x) = \frac{F_j L}{2EI} \times \begin{cases} p_j x^2 (1 - \frac{x}{3p_j L}) & \frac{x}{L} \le p_j \\ p_j^2 L \, (x - \frac{p_j L}{3}) & p_j \le \frac{x}{L} \end{cases}, \qquad (6.14)$$

where $p_j = x_j/L$ is the ratio between the location of applied force (x_j) and the cantilever length. (For example $p_j = 1$ when the force is applied on the cantilever tip.) Using the superposition principle [81], the overall deflection of the cantilever beam as the result of applying multiple point forces can be calculated as

$$y(x) = \sum_{j=1} y_j(x). \qquad (6.15)$$

Equation (6.15) can be used in resembling the bending of a cantilever to the deflection of a flexural mode shape. In this regard the overall deflection is described as

$$y(x) = \sum_{j=1} \beta_j \overline{y_j}(x) , \tag{6.16}$$

where the point force applied on the cantilever tip is counted as $j = 1$ and β_j is the ratio between the force applied at point x_j and the tip force ($\beta_j = F_j/F_1$). In Eq. (6.16), $\overline{y_j}(x)$ is the deflection caused by the unit point force $F_u = F_1$ applied at x_j. For calculating the net deflection Y_i of the beam at the point x_i where the point force F_i is applied, Eq. (6.16) can be further simplified:

$$Y_i = y(x_i) = \frac{L^3 F_u}{2EI} \sum_{j=1} \alpha_{ij} \beta_j , \tag{6.17}$$

where i indicates the point of interest, as i is equal to 1 on the cantilever tip and increases by moving toward the clamped end, and α_{ij} is

$$\alpha_{ij} = \begin{cases} p_i^2 (p_j - \frac{p_i}{3}) & j \le i \\ \\ p_j^2 (p_i - \frac{p_j}{3}) & i \le j \end{cases} . \tag{6.17a}$$

In other words, α_{ij} is an element of the symmetrical $n \times n$ matrix **C**:

$$\mathbf{C} = \begin{bmatrix} 2p_1^3/3 & p_2^2(p_1 - p_2/3) & \dots & p_n^2(p_1 - p_n/3) \\ p_2^2(p_1 - p_2/3) & 2p_2^3/3 & \dots & p_n^2(p_2 - p_n/3) \\ \dots & \dots & \dots & \dots \\ p_n^2(p_1 - p_n/3) & p_n^2(p_2 - p_n/3) & \dots & 2p_n^3/3 \end{bmatrix}, \tag{6.17b}$$

and Eq. (6.16) can be described by:

$$\begin{bmatrix} Y_1 \\ Y_2 \\ \dots \\ Y_n \end{bmatrix} = \frac{L^3 F_u}{2EI} \begin{bmatrix} 2p_1^3/3 & p_2^2(p_1 - p_2/3) & \dots & p_n^2(p_1 - p_n/3) \\ p_2^2(p_1 - p_2/3) & 2p_2^3/3 & \dots & p_n^2(p_2 - p_n/3) \\ \dots & \dots & \dots & \dots \\ p_n^2(p_1 - p_n/3) & p_n^2(p_2 - p_n/3) & \dots & 2p_n^3/3 \end{bmatrix} \begin{bmatrix} \beta_1 \\ \beta_2 \\ \dots \\ \beta_n \end{bmatrix} . \tag{6.17c}$$

The force ratios β_j can be obtained by solving Eq. (6.16) for the zero deflection (i.e., $y(x) = 0$) in x corresponding to node locations, while from Eq. (6.2) the node locations can be calculated. The node (and antinode) locations, normalized with respect to the cantilever length, are summarized in Table 6.1 for the first 6 flexural modes, based on which the β_j ratios are calculated and presented in Table 6.2. Using Eqs. (6.16) and (6.2), the resemblance of the static and dynamic deflection of a cantilever beam are compared in Figure 6.2. As it can be observed, the resembled static deflection closely follows the vibration amplitude. This statement becomes even more evident by comparing the deflection at the antinodes for the first 6 flexural modes as presented in Table 6.3; hence, the earlier assumption of applying the point forces on the antinodes is valid.

6.3 Effective Mass in Flexural Vibration Modes

As expressed with Eq. (6.11), for all flexural modes the corresponding mass of a cantilever beam, when considered as a single point-mass on the cantilever tip, is a quarter of the actual mass. The tip point-mass is also known as the effective mass of the fundamental mode [231]. Nevertheless, we will show that for the other overtones the resonant beam can be characterized with more than one point-mass. In this perspective, a beam resonating in the n^{th} overtone can be considered as a system of n coupled lumped mass-spring subsystems. In other words, a resonant beam in the n^{th} overtone can be considered as a system with n degrees of freedom, which consists of n coupled point-masses subsystems each located on an antinode (i.e., the same locations that the point forces should be applied to imitate the vibration deflection as shown in Figure 6.3). In

Table 6.1. Normalized location x/L of nodes z_j and antinodes p_j in flexural modes.

	1st mode	2nd mode	3rd mode	4th mode	5th mode	6th mode
z_1	–	0.784	0.868	0.906	0.927	0.940
z_2	–	–	0.504	0.644	0.723	0.774
z_3	–	–	–	0.358	0.500	0.591
z_4	–	–	–	–	0.279	0.409
z_5	–	–	–	–	–	0.228

	1st mode	2nd mode	3rd mode	4th mode	5th mode	6th mode
p_1	1	1	1	1	1	1
p_2	–	0.471	0.692	0.780	0.829	0.860
p_3	–	–	0.291	0.501	0.611	0.682
p_4	–	–	–	0.208	0.389	0.500
p_5	–	–	–	–	0.162	0.318
p_6	–	–	–	–	–	0.132

Table 6.2. Force ratio β_j in flexural modes.

	1st mode	2nd mode	3rd mode	4th mode	5th mode	6th mode
β_1	1	1	1	1	1	1
β_2	–	-3.266	-2.541	-2.578	-2.575	-2.576
β_3	–	–	3.683	3.090	3.119	3.118
β_4	–	–	–	-3.660	-3.056	-3.088
β_5	–	–	–	–	3.655	3.059
β_6	–	–	–	–	–	-3.661

Table 6.3. Normalized deflection amplitude at antinodes r_{j1} (with respect to the tip deflection) in flexural modes (*fl.*) versus the resembled static bending (*st.*).

	1st mode		2nd mode		3rd mode		4th mode		5th mode		6th mode	
	fl.	*st.*	*fl.*	*st.*	*fl.*	*st.*	*fl.*	*st.*	*fl.*	*st.*	*fl.*	*st.*
r_{11}	1	1	1	1	1	1	1	1	1	1	1	1
r_{21}	–	–	-0.720	-0.715	-0.659	-0.648	-0.661	-0.650	-0.661	-0.650	-0.661	-0.651
r_{31}	–	–	–	–	0.758	0.762	0.707	0.704	0.709	0.705	0.709	0.705
r_{41}	–	–	–	–	–	–	-0.756	-0.761	-0.705	-0.700	-0.707	-0.703
r_{51}	–	–	–	–	–	–	–	–	0.756	0.761	0.705	0.702
r_{61}	–	–	–	–	–	–	–	–	–	–	-0.756	-0.762

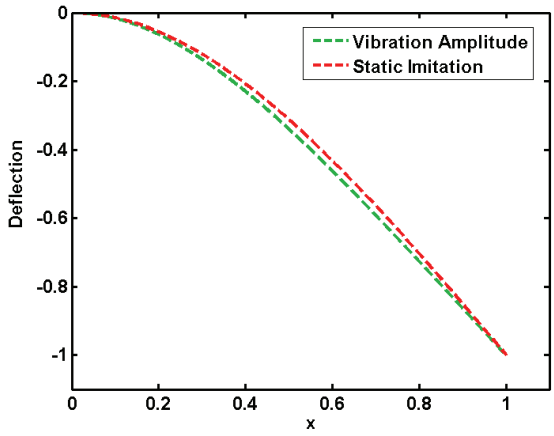

(a)

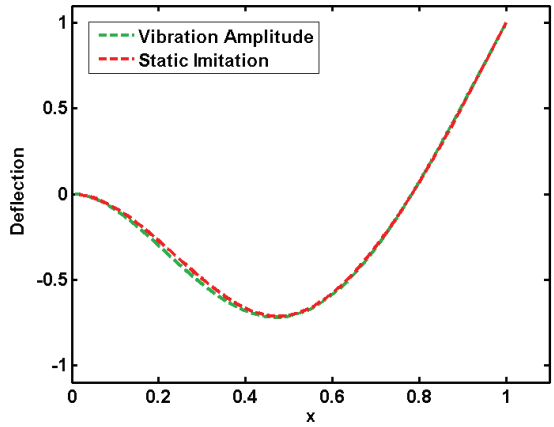

(b)

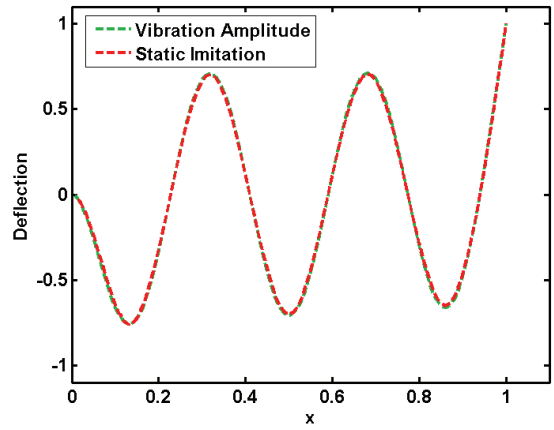

(c)

Figure 6.2. Static deflection imitation (red lines) versus flexural mode shapes (green lines) of a 1-dimensional cantilever in (a) fundamental flexural mode, (b) second flexural mode, (c) 6^{th} flexural mode. The deflections are normalized.

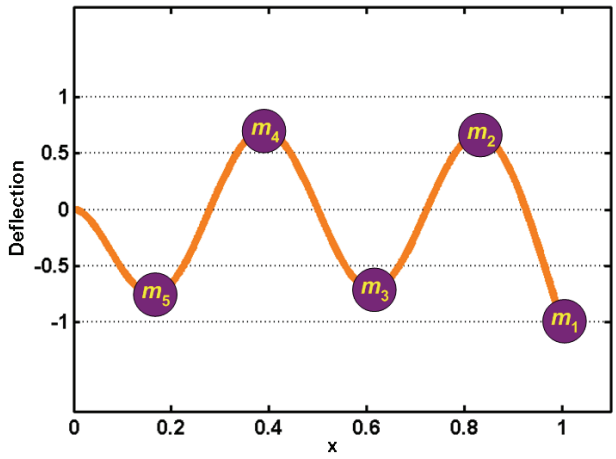

Figure 6.3. Cantilever resonating in the 5th flexural mode as a system of 5 point-masses, each located on an antinode.

this system the defining equations for an undamped free vibration have the general form of [2]

$$\mathbf{M}\ddot{\mathbf{Y}} + \mathbf{S}\mathbf{Y} = \mathbf{0}, \tag{6.18}$$

where **S** is the stiffness matrix, **M** is the mass matrix:

$$\mathbf{M} = \begin{bmatrix} m_1 & 0 & \dots & 0 \\ 0 & m_2 & \dots & 0 \\ \dots & \dots & \dots & \dots \\ 0 & 0 & \dots & m_n \end{bmatrix},$$

and **Y** is the displacement vector with

$$\mathbf{Y} = \mathbf{\Phi}_n e^{i\omega_n t}, \tag{6.19}$$

in which $\mathbf{\Phi}_n$ represents the corresponding vector of antinode amplitudes based on Eq. (6.1):

$$\mathbf{\Phi}_n = \begin{bmatrix} y(x_1) \\ y(x_2) \\ \cdots \\ y(x_n) \end{bmatrix} = \begin{bmatrix} Y_1 \\ Y_2 \\ \cdots \\ Y_n \end{bmatrix}, \tag{6.19a}$$

where $y(x_j)$ is the vibration amplitude of the j^{th} point-mass located at x_j from the beam free end (i.e., $y(x_1) = Y_1$ is the amount of deflection on the cantilever tip).

For a cantilever resonating in the n^{th} flexural mode there are two conditions in determining the point-mass m_j. The first condition comes from the characteristic equation for the resonance frequency [2]:

$$(\mathbf{S} - \omega_n^2 \mathbf{M})\mathbf{\Phi}_n = 0. \tag{6.20}$$

Expanding Eq. (6.20) for the j^{th} point-mass gives:

$$m_j \omega_n^2 = \sum_{k=1}^{n} s_{jk} r_{kj}, \tag{6.21}$$

where r_{kj} defines the ratio between the vibration amplitudes of the k^{th} and j^{th} point-masses:

$$r_{kj} = \frac{Y_k}{Y_j}. \tag{6.22}$$

It is worth mentioning that the right-hand side of Eq. (6.21) is the effective spring constant at the point j in the coupled system:

$$k_j = \sum_{k=1}^{n} s_{jk} r_{kj}. \tag{6.23}$$

Since at any resonance overtone all point-masses vibrate at the same frequency, using Eq. (6.21) the point-masses relationship can be described by

$$\frac{m_j}{m_l} = \frac{\sum_{k=1}^{n} s_{jk} r_{kj}}{\sum_{k=1}^{n} s_{lk} r_{kl}} . \qquad (6.24)$$

The second condition in determining the point-mass m_j is imposed by the total effective mass of a resonant cantilever. In this regard, the maximum kinetic energy of a single mass-spring subsystem resonating at point j is calculated with respect to Eqs. (6.3), (6.5) and (6.19):

$$K_j = \frac{1}{2} m_j \omega_n^2 Y_j^2 . \qquad (6.25)$$

Hence, the maximum total kinetic energy of the system is described by

$$K = \sum_{j=1} K_j = \frac{1}{2} \omega_n^2 \sum_{j=1} m_j Y_j^2 .$$

On the other hand, the maximum kinetic energy of the resonant cantilever is described by Eq. (6.9); therefore, the maximum total kinetic energy of the system must be

$$K = \frac{1}{2} \omega_n^2 \sum_{j=1} m_j Y_j^2 = \frac{1}{2} (\frac{1}{4} m \omega_n^2 Y_1^2) , \qquad (6.26)$$

where $Y_1 = y(L)$. Thus, with the notation of Eq. (6.22), the second condition in determining the point-masses is defined by

$$\sum_{j=1} m_j r_{j1}^2 = \frac{1}{4} m . \qquad (6.27)$$

6.3.1 Effective Mass in the Fundamental Flexural Resonance Mode

The static imitation of the first flexural resonance mode can be obtained by a simple cantilever bending as the result of applying a point force on the tip. In this case the matrix

S has only one element which is equal to the static spring constant of the beam described by Eq. (2.13):

$$s_{11} = k = \frac{3EI}{L^3}. \tag{6.28}$$

As expressed by Eqs. (6.11) and (6.27), the effective mass of a resonant cantilever, when the entire mass a considered to be on the tip point, is exactly one quarter of the actual cantilever mass. On the other hand, the resonance frequency of a mass-spring system is given by Eq. (2.3), therefore, the fundamental flexural resonance frequency is calculated as

$$f_1 = \frac{1}{2\pi}\sqrt{\frac{k}{0.25m}}. \tag{6.29}$$

Equation (6.29) can be simplified after replacing k from Eq. (6.28), I from Eq. (2.15) for a rectangular cantilever beam, and expressing the actual mass m based on the cantilever density ρ:

$$f_1 = \frac{1}{2\pi}\frac{H}{L^2}\sqrt{\frac{E}{\rho}}. \tag{6.30}$$

However, according to Eq. (2.27):

$$f_1 = \frac{\lambda_1^2}{2\pi\sqrt{12}}\frac{H}{L^2}\sqrt{\frac{E}{\rho}} = \frac{1.0149}{2\pi}\frac{H}{L^2}\sqrt{\frac{E}{\rho}}. \tag{6.31}$$

In other words, for the fundamental flexural mode, it seems that the ratio of effective mass to the total mass is equal to 0.24 instead of the expected ratio of 0.25. To explain the origin of this discrepancy, one must point out the difference between the dynamic and static deflection of a beam. Figure 6.2(a) shows the normalized deflection profile of a cantilever beam with uniform cross-section when the beam is deflected by a tip point

force (dashed red line) and when it is vibrating in the fundamental flexural mode (dashed green line). As observed, along the length of the beam the deflection due to a point force is slightly smaller than the vibration amplitude, which results in a slightly smaller kinetic energy, and hence, a smaller effective mass ratio.

The 0.24 ratio has a special value in characterization of AFM cantilever probes [218, 232], as with this ratio the static spring constant of a cantilever can be calculated based on its resonance frequency.

6.3.2 Effective Mass in All Flexural Resonance Modes

Similar to the case of the fundamental mode, the proposed vibration amplitude imitation can be used to calculate the stiffness matrix elements s_{jk} of a flexural overtone. Nevertheless, also similar to the previous case, the slight mismatch between the static model and the flexural vibration amplitude can result in a small discrepancy between the actual and calculated effective masses.

The stiffness matrix **S** describes the ratio between displacements and the applied forces; therefore, with respect to Eqs. (6.17), for the static imitation of all flexural resonance modes (including the fundamental mode) the stiffness matrix can be described as

$$\mathbf{S} = \frac{2EI}{L^3}\mathbf{C}^{-1}. \qquad (6.32)$$

Substituting the corresponding stiffness matrix elements in Eq. (6.24) reveals the relationship between every two point-masses in a given resonance overtone, which together with the condition described by Eq. (6.27) will lead to finding the exact ratios of

point-masses in the flexural mode of interest. Calculated with this approach, the effective point-mass ratios – with respect to the actual mass – in the first 6 flexural modes are listed in Table 6.4.

Table 6.4. Effective point-mass ratios in flexural modes.

	1st mode	2nd mode	3rd mode	4th mode	5th mode	6th mode
m_1	0.25	0.075	0.046	0.033	0.026	0.021
m_2	–	0.338	0.177	0.128	0.099	0.081
m_3	–	–	0.222	0.143	0.112	0.092
m_4	–	–	–	0.157	0.110	0.091
m_5	–	–	–	–	0.122	0.090
m_6	–	–	–	–	–	0.100

It is interesting to note that the sum of all point-masses converges to half of the actual mass as the overtone number increases. In the extreme case, when the overtone number is reaching infinity, i.e., $n \to \infty$, the sum of all point-masses will be

$$\sum_{j=1}^{\infty} m_j = \frac{1}{2} m \,. \tag{6.33}$$

This can be explained as follows: when the resonance overtone approaches infinity, each infinitesimal segment of the cantilever is quantized into a node and an antinode, which are corresponding to the two quantized energy states of high (at antinode) and zero (at node). Therefore, the entire cantilever beam becomes a long chain of quantized masses equally distributed on the nodes and antinodes (see Figure 6.4). Since the kinetic energy of each quantized segment is defined by the energy associated with the antinode, the effective mass of each quantized segment is equal to the mass located on the antinode. In other words, the effective point-mass in each segment is equal to the half of the actual

mass of the segment. Thus the total mass located on the antinodes is half of the cantilever's actual mass, as expressed by Eq. (6.33).

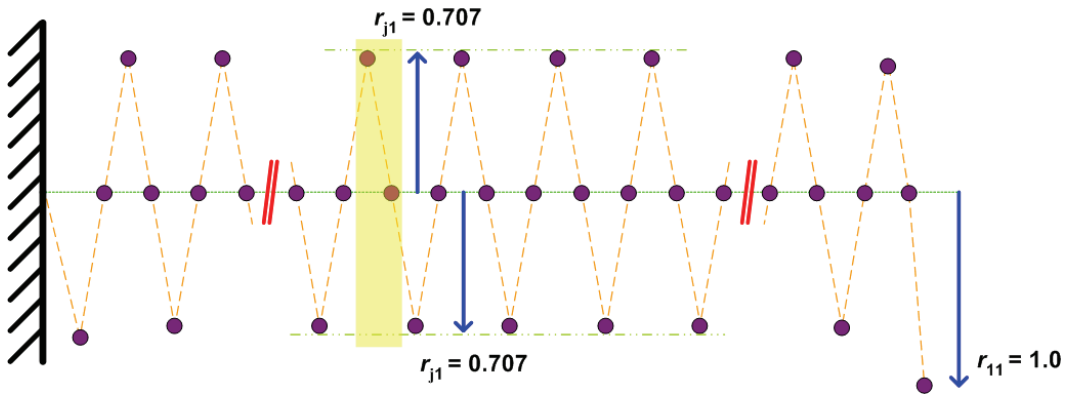

Figure 6.4. Quantization of a resonant cantilever into nodes and antinodes in the n^{th} flexural mode, where $n \to \infty$. The highlighted area shows a quantized segment, consisting of a node and an antinode.

The validity of this conclusion can be confirmed by investigating the vibration amplitude at antinodes. To this end, according to Eq. (6.27), the relationship between the sum of point-masses located on the antinodes and the cantilever mass is defined as:

$$\sum_{j=1}^{\infty} m_j r_{j1}^2 = \frac{1}{4} m \,. \qquad (6.34)$$

On the other hand, in higher overtones the mode shape of a resonant cantilever approaches a sinusoidal shape (except for the points that are very close to both ends) [229]; hence, for $n \to \infty$ the amplitude of antinodes can be considered to be equal − with the exception of the tip amplitude, which can be used as the reference. In other words, the coefficients r_{j1} for $j > 1$ have the same value for all antinodes, thus

$$m_1 + r_{j1}^2 \sum_{j=2}^{\infty} m_j = \frac{1}{4} m \,. \tag{6.35}$$

where $r_{11} = 1$ based on the definition expressed by Eq. (6.22). Since on an infinitely quantized cantilever each single point-mass is negligible in comparison to the total mass of the cantilever, the contribution of m_1, the point-mass on the tip, can be ignored:

$$r_{j1}^2 \sum_{j=2}^{\infty} m_j = \frac{1}{4} m \,. \tag{6.36}$$

The same argument can be stated for Eq. (6.33). Therefore, for overtones approaching the infinity, Eq. (6.36) together with Eq. (6.33) can be used to define the vibration amplitude of antinodes (for $j > 1$, which are normalized with respect to the tip amplitude):

$$r_{j1} = \frac{1}{\sqrt{2}} \,. \tag{6.37}$$

Since the result of Eq. (6.37) is consistent with the theory [229] and calculation (e.g., see r_{j1} for the center antinodes in higher flexural modes in Table 6.3), the assumption made for deriving Eq. (6.33) is valid.

In Figure 6.5(a) the total point-mass ratios of each overtone (i.e., the sum of individual point-mass ratios in that overtone) are depicted versus the corresponding flexural mode overtone. As discussed before, by increasing the overtone number the total mass ratio approaches 0.5. Investigating the change of total point-mass ratios in every two consecutive overtones reveals, as shown in Figure 6.5(b), that the largest increase in the amount of total point-mass ratio occurs for the 2nd flexural mode. This overtone shows a 65% increase with a total point-mass ratio of 0.413 compared to the 0.25 ratio in the fundamental mode. However, the increment rate sharply drops after the 2nd overtone, to

such an extent that the amount of total point mass-ratio in the 6th overtone is barely 1% more than the same ratio in the 5th overtone.

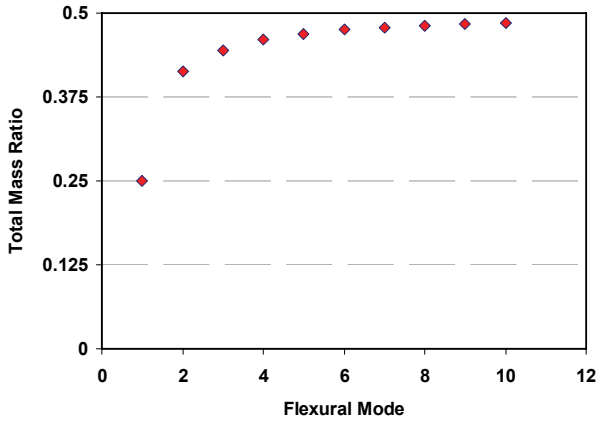

(a)

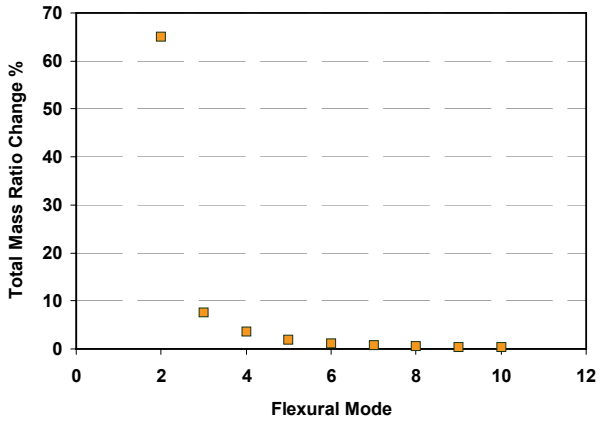

(b)

Figure 6.5. (a) The total point mass ratio in the first 10 flexural modes; (b) change in the total mass ratio in each flexural mode compared to the previous mode.

CHAPTER 7

Q-FACTOR IN FLEXURAL OVERTONES

In Chapter 5 the dependence of the Q-factor on the geometrical dimension of a cantilever in the fundamental flexural resonance mode was investigated and it was observed that the two major damping mechanisms are the air damping and support loss. In this chapter the measurement results for the same resonant cantilevers at higher flexural overtones are presented.

The variation of the Q-factor in different overtones can be studied in two aspects. In the first aspect the study focuses on the change of the Q-factor for different resonance overtones of the same cantilever; whereas the second aspect involves a comparative study of different cantilevers resonating in the same overtone. The latter approach is similar to the presented study in Chapter 5 for the fundamental flexural mode. This chapter covers both aspects; however, to grasp a better understating about damping in higher flexural modes, the chapter starts with a theoretical modeling of the slightly damped resonance of cantilevers.

7.1 Damping in Flexural Overtones

7.1.1 Effective Damping Coefficient of Resonant Cantilevers

The objective of this section is to find a system level model for the damping in a resonant cantilever system at any given flexural overtone. As mentioned in Chapter 6, a resonant cantilever in the n^{th} overtone (i.e., ω_n) can be considered as a system with n degrees of

freedom, consisting of n mass-spring subsystems which resonate at the same frequency. In this section, the damping associated with such system is investigated.

The deflection y_j in the j^{th} mass-spring subsystem is defined by a second order differential equation:

$$m_j \frac{d^2 y_j}{dt^2} + B_j \frac{dy_j}{dt} + k_i y_j = 0, \qquad (7.1)$$

where, as discussed in Chapter 6, m_j and k_j are the j^{th} point-mass and spring constant, respectively, and B_j represents the damping coefficient of the subsystem. When the second term in Eq. (7.1) is relatively small, i.e., the quality factor is large, as mentioned in Chapter 2 the damped and natural resonance frequencies of the subsystem will be almost equal; therefore the free vibration amplitude in the subsystem can be described in the time domain as [233]

$$y_j(t) = Y_j \, e^{\frac{\omega_n}{2Q_j}t} \cos(\omega_n t), \qquad (7.2)$$

where Y_j is the initial resonance amplitude of the point-mass m_j as described in Chapter 6. Since at any given overtone of a resonant cantilever system, the resonance of each subsystem damps no faster than the others, the quality factor of all subsystems must be identical and equal to the quality factor of the system:

$$Q_j = Q. \qquad (7.3)$$

With respect to Eq. (2.6), it can be deducted from Eq. (7.3) that the ratios of the damping coefficient to the point-mass in all subsystem are equal:

$$\frac{B_j}{m_j} = \frac{\omega_n}{Q}. \qquad (7.4)$$

Therefore, by measuring the Q-factor and resonance frequency of the cantilever and by calculating the amount of m_j as explained in Chapter 6, the damping coefficient of any subsystem in any resonance overtone can be extracted. The assumption here is that the medium has an insignificant effect on the inertial part of Eq. (7.1), i.e., m_j is defined only based on the cantilever mass and the resonance overtone.

The energy loss in each subsystem consists of two mechanisms: a) the energy that is dissipated out of the overall resonant cantilever system, b) the energy that is transferred to other subsystems within the resonant cantilever system. Since the net amount of energy transferred between the subsystems is zero, the total energy loss in the subsystems is equal to the dissipated energy in the resonant cantilever system.

The one-cycle energy loss L_j in the j^{th} subsystem is defined based on Eq. (7.1):

$$L_j = \int_o^T B_j (\frac{dy_j}{dt})^2 dt . \qquad (7.5)$$

If the subsystem is forced to resonate with an amplitude $y_j(t) = Y_j \cos(\omega t)$, the integral of Eq. (7.5) will be simplified to

$$L_j = \pi \omega_n B_j Y_j^2 . \qquad (7.6)$$

In a resonant system the maximum stored energy is equal to the maximum kinetic energy, while their relationship with the energy loss per cycle is expressed by the Q-factor through Eq. (2.4). Applying the same definition to each subsystem gives

$$L_j = \frac{2\pi}{Q} K_j , \qquad (7.7)$$

where K_j is the maximum kinetic energy of the j^{th} mass-spring subsystem defined by Eq. (6.25). If the Q-factor of the resonant cantilever at a given overtone is large enough to ignore the effect of other overtones on the vibration amplitudes, the total dissipated energy of the cantilever system in that overtone, as mentioned before, will be equal to the total energy loss of the subsystems in the same overtone:

$$L = \sum_{j=1} L_j = \sum_{j=1} \pi \omega_n^2 B_j Y_j^2 \qquad (7.8)$$

Also, as mentioned in Chapter 6, the same argument is valid for the kinetic energy of the system: according to Eq. (6.26) the total kinetic energy of the system can be considered as the kinetic energy of an effective mass on the tip point ($m^* = 0.25m$). Hence, the total energy loss of the resonant cantilever system in the n^{th} overtone is

$$\sum_{j=1} L_j = \frac{\pi}{Q}(\tfrac{1}{4} m \omega_n^2 Y_1^2) . \qquad (7.9)$$

Simplifying Eq. (7.9) with respect to Eq. (7.8) and the definition of Eq. (6.22) yields

$$\sum_{j=1} B_j r_{j1}^2 = \frac{\tfrac{1}{4} m \omega_n}{Q} . \qquad (7.10)$$

On the other hand, B^*, the effective damping coefficient of the resonant cantilever system when considered as a tip point mass-spring system, can be defined by Eq. (7.8):

$$B^* Y_1^2 = \sum_{j=1} B_j Y_j^2 , \qquad (7.11)$$

which with respect to Eq. (6.22) simplifies to

$$B^* = \sum_{j=1} B_j r_{j1}^2 . \qquad (7.12)$$

Therefore, considering Eqs. (7.10) and (7.12), the overall damping of a resonant cantilever at the n^{th} overtone can be modeled as the damping of resonating mass-spring system on the cantilever tip:

$$B^* = \frac{\frac{1}{4} m \omega_n}{Q}. \qquad (7.13)$$

Equation (7.13) can be very helpful in evaluating and comparing the damping coefficients (i.e., energy losses) in different overtones of a same resonant cantilever.

7.1.2 Damping Mechanisms in Flexural Overtones

As mentioned in Chapter 5, the energy loss in the fundamental flexural resonance mode of a cantilever can be associated with different mechanisms, among which the air damping and support loss are the most prominent ones. In the same way, the total energy loss at a given overtone also can be attributed to different loss mechanisms:

$$L = L_{air} + L_{clamp} + etc., \qquad (7.14)$$

where L_{air} and L_{clamp} are the viscous (air) and support (clamp) energy losses, which individually can be calculated by the same expression presented in Eq. (7.6). Thus the total energy loss can be calculated with respect to the model presented in Eq. (7.11):

$$L = \pi \omega_n B_{air} Y_1^2 + \pi \omega_n B_{clamp} Y_1^2 + etc. \qquad (7.15)$$

Therefore, the overall effective damping coefficient of the system can be described as:

$$B^* = B_{air} + B_{clamp} + B_{other}, \qquad (7.16)$$

where B_{other} represents the cumulative damping coefficient of other loss mechanisms besides the air damping and support loss. Combining Eqs. (7.13) and (7.16), the overall Q-factor of the system at any given overtone is

$$\frac{1}{Q} = \frac{1}{Q_{air}} + \frac{1}{Q_{clamp}} + \frac{1}{Q_{other}}, \qquad (7.17)$$

which has been also mentioned in Chapter 5.

7.2 Measurement Results and Discussion

The measurement results presented here are obtained from the same cantilevers investigated in Chapter 5 but at higher flexural resonance overtones. The measurement setup and data acquisition conditions are exactly the same as what has been mentioned in Chapter 5. Also, each data point presented in this chapter is an average of extracted Q-factors of at least 8 repeated resonance characteristic measurements for a single resonance mode of each cantilever. The associated relative standard deviation (statistical uncertainty) with each data point is less than 5%, otherwise the data is discarded.

7.2.1 Q-factor of Different Overtones for the Same Cantilevers

The focus of this section is on the change of Q-factor with different overtones for the same cantilever. The investigated cantilevers are 850 and 1050 μm long and have a thickness of 11 μm (i.e., according to the notation of Eq. (5.15), χ = 23.3 and 28.8 $\mu m^{-0.5}$). The widths of measured cantilevers are 82, 130, 180 and 230 μm. As mentioned in Chapter 5, the quality factor of cantilevers with such χ values in the fundamental flexural mode is overwhelmingly determined by the air damping and almost independent of the width. However, it is predicted that in higher flexural overtones the support loss becomes more influential since Q_{clamp} approximately changes inversely proportional to λ_n^2 [234] while Q_{air} approximately increases by λ_n (see Eq. (5.9)) [219].

On the other hand, it was observed in Chapter 5 that in the fundamental flexural mode the Q-factor would become a function of the cantilever width if the support loss was the dominant damping mechanism. Therefore, assuming that in higher flexural modes the two major damping mechanisms are still the air damping and support loss, the dependence (independence) of Q-factor on the cantilever width might indicate the support loss (air damping) as the dominant damping mechanism. To this end, in Figure 7.1 the measured Q-factors are depicted versus the resonance frequencies of the

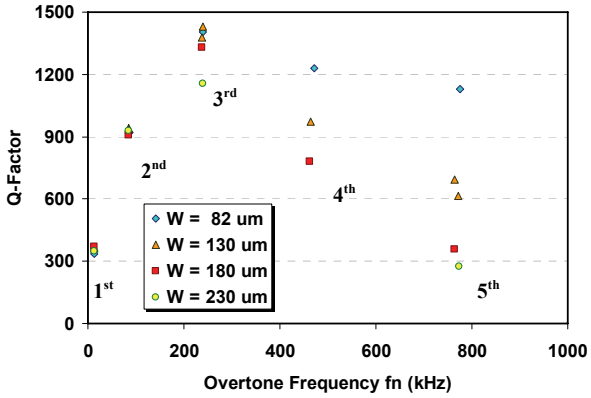

(a)

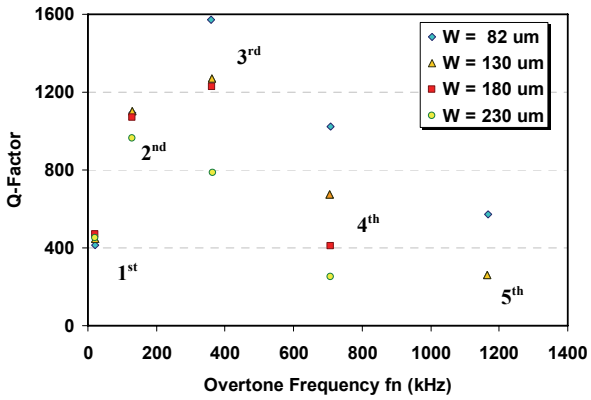

(b)

Figure 7.1. Q-factor as a function of the overtone resonance frequency for cantilevers with different width W ranging from 82 to 230 μm, and with (a) L = 1050 μm, and (b) L = 850 μm. All cantilevers are 11 μm thick.

overtones. It is observed that the Q-factor becomes a function of the width, starting from the second overtone for 850 μm-long cantilevers, but from the third overtone for 1050 μm-long cantilevers. Therefore, it may be conceived that at higher flexural modes the support loss becomes the dominant damping mechanism. In this regard, based on the theoretical support loss model proposed by Hao *et al.* [234], Q_{clamp} is calculated as

$$Q_{clamp} = C_{C-F}(\frac{c_1}{c_2\lambda_n})^2(\frac{L}{H})^3, \qquad (7.18)$$

where $C_{C\text{-}F}$ is 3.99, and the coefficients c_1 and c_2 are given by Eq. (2.26b) which result in the ratio of c_1/c_2 to be equal to -0.73, -1.02 and -1.00 for the fundamental, second and all higher flexural modes, respectively. However, depicting the calculated support loss as an inverse of Q_{clamp} (see Figure 7.2) reveals that the damping in the higher overtones significantly exceeds the theoretical prediction of Hao *et al*. The explanation for the observed discrepancy is not known to the author; but it is speculated that in higher flexural modes either Hao's theoretical model is less accurate in predicting the support loss, or there are other dominant damping mechanisms besides the support loss. On the other hand, the width-independent increase of Q-factor for the first two flexural modes in 1050 μm-long cantilevers indicates that the air damping is not only the dominant damping mechanism for these flexural modes, but also Q_{air} increases with the overtone number as expected by the theory [219]. Therefore, the decrease of the measured Q-factor in higher overtones indicates that the air damping is no longer a significant contributor to the energy loss in those overtones.

Using Eq. (7.13) the variation of the total damping coefficient B^* of the system for different flexural modes is traced in Figure 7.3, which shows that for both sets of

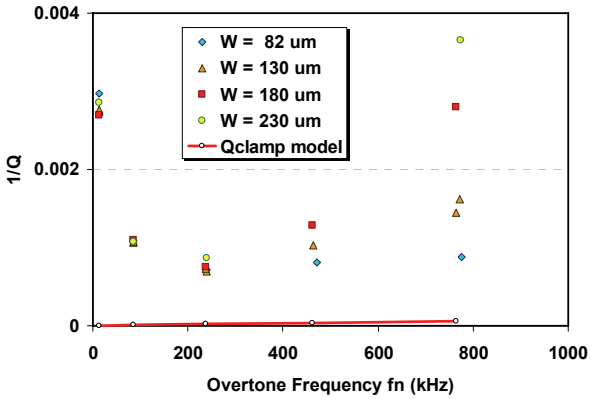

(a)

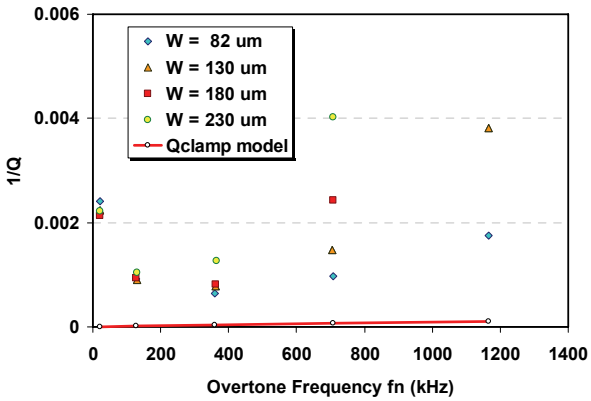

(b)

Figure 7.2. Measured $1/Q$ and calculated $1/Q_{clamp}$ in the first 5 flexural modes as functions of the overtone resonance frequency for cantilevers with different width W ranging from 82 to 230 μm, and (a) L = 1050 μm, (b) L = 850 μm. All cantilevers are 11 μm thick.

cantilevers the damping monotonically increases with the overtone number. This observation is made despite the fact that for both sets of cantilevers the Q-factors in the second overtone are larger than in the fundamental mode. In other words, for higher overtones with an increase in Q_{air} the air damping also increases, but the negative contribution of the air damping to Q_{air} is overshadowed by the increase of resonance frequency, as expressed by Eq. (7.13).

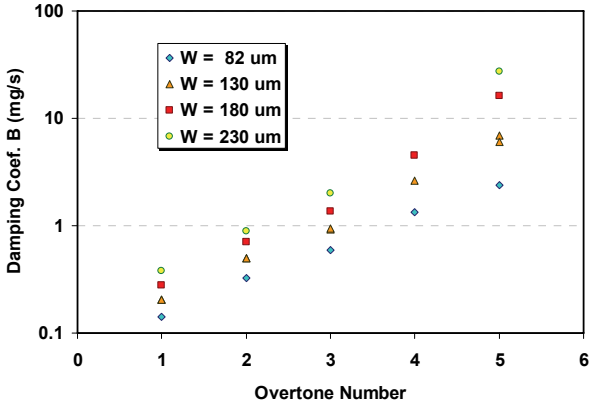

(a)

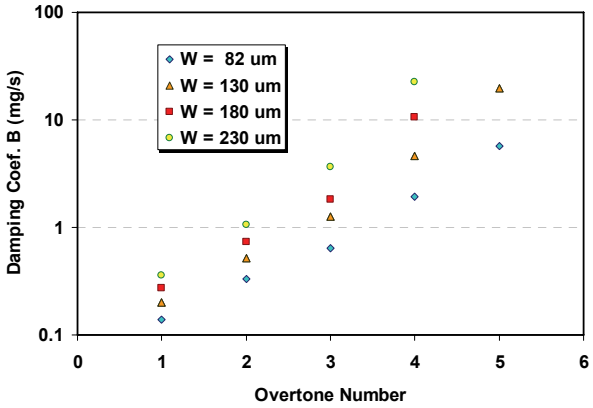

(b)

Figure 7.3. Variation of the effective damping coefficient versus the flexural mode (overtone) number for cantilevers with different width W ranging from 82 to 230 μm, and (a) L = 1050 μm, (b) L = 850 μm. Both cantilevers are 11 μm thick.

7.2.2 Q-factor of Different Cantilevers for the Same Overtones

Previously in Figure 5.6 the dependence of the Q-factor on χ for the fundamental flexural mode was shown. In a similar way, Q^{-1} is depicted as a function of χ in Figure 7.4 not only for the fundamental mode, but also for the second and third flexural modes. For acquiring the presented data, the same cantilevers are measured in different overtones, with the same dimensional specifications as described in Chapter 5. Because of the

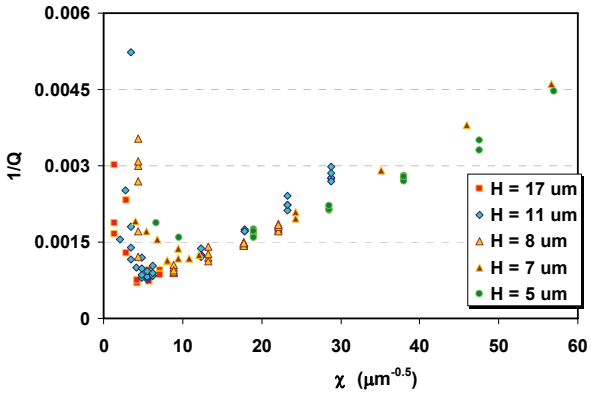

(a)

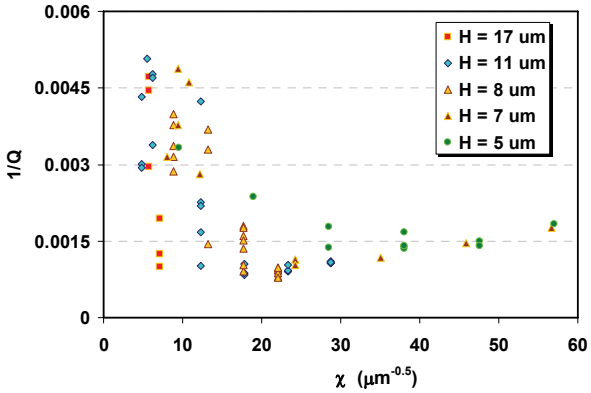

(b)

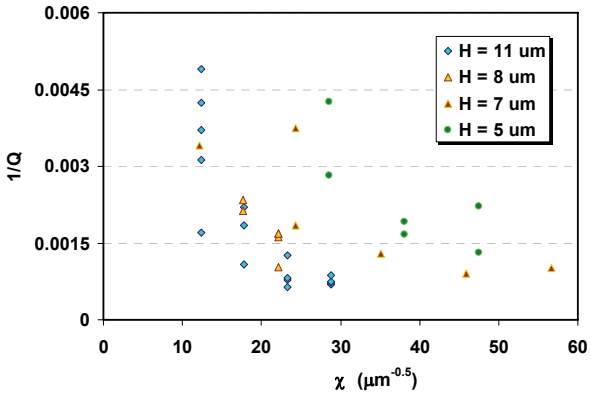

(c)

Figure 7.4. Plots of measured Q^{-1} versus $\chi = L/H^{1.5}$ for cantilevers with thicknesses of 5, 7, 8, 11 and 17 μm; (a) fundamental flexural mode – same as Figure 5.6, (b) second flexural mode, (c) third flexural mode. Although not marked in the graph, the widths of the presented cantilevers are not necessarily equal.

measurement limitations especially for higher overtones, no data for a number of cantilevers could be collected in those overtones. Also, data points associated with coupled peaks (see Chapter 5) are discarded in the presented graphs. It can be observed that the critical region, i.e., the region where the support loss is comparable or larger than the air damping, ends at $\chi = 14\ \mu m^{-0.5}$ for the fundamental flexural mode, while it extends to $\chi \approx 30\ \mu m^{-0.5}$ for the second overtone, whereas all the collected data for the third overtone ($\chi < 60\ \mu m^{-0.5}$) are in the critical region. In other words, as mentioned before, it seems that at higher overtones the support loss becomes the dominant damping mechanism.

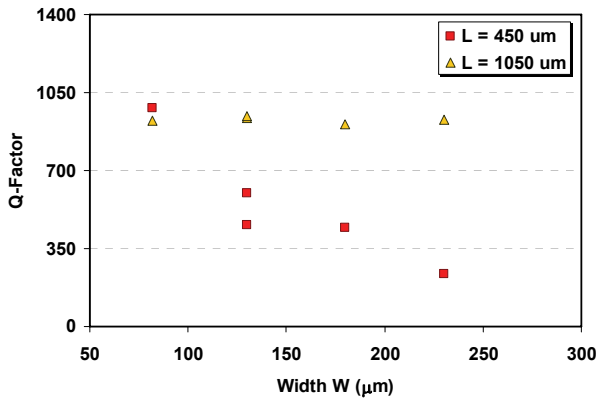

Figure 7.5. Q-factor in the second flexural mode as a function of the cantilever width for different lengths; the cantilever thickness is 11 μm.

Similar to the discussion in Chapter 5, the Q-factor becomes a function of the cantilever width in the critical region. Figure 7.5 compares the effect of the width on the Q-factor for two cantilever sets resonating in the second flexural mode, with both sets having the same thickness of 11 μm, but different lengths of 1050 versus 450 μm. As seen in the

graph, the Q-factors of 1050 μm-long cantilevers ($\chi = 28.8\ \mu m^{-0.5}$) are independent of the cantilever width, while the narrower 450 μm-long cantilevers ($\chi = 12.3\ \mu m^{-0.5}$) have the higher Q-factors.

The dependence of Q_{air} on the geometry of resonant cantilevers in the second overtone is shown in Figure 7.6, in which, similar to the graphs for the fundamental flexural mode (see Figure 5.7), data points from the air damping dominated region are plotted versus

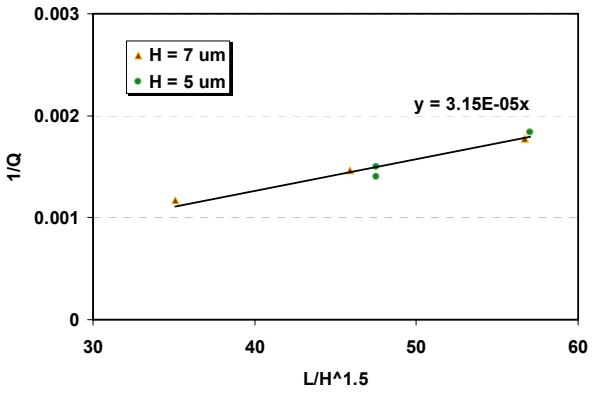

(a)

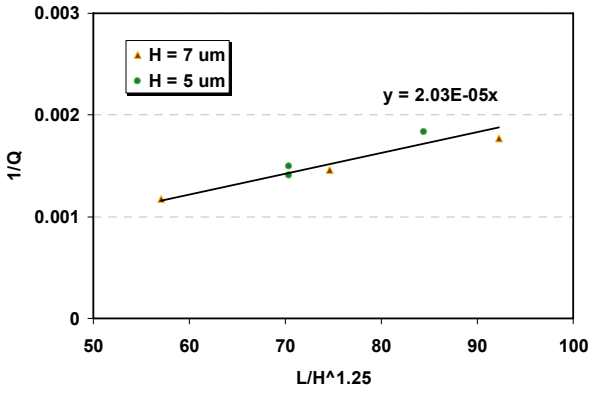

(b)

Figure 7.6. Inverse of Q-factor Q^{-1} in the second flexural mode as a function of: (a) $L/H^{1.5}$ and (b) $L/H^{1.25}$. The presented Q-factors belong to cantilever resonators enduring the air damping as the dominant loss mechanism.

$L/H^{1.5}$ and $L/H^{1.25}$. Applying a linear regression for the data that is plotted versus $L/H^{1.5}$ (see Figure 7.6(a)) yields an empirical air damping coefficient of $\varepsilon_{emp} = 3.15\times10^{-5}$ $\mu m^{0.5}$. In comparison with the corresponding coefficient for the fundamental mode, i.e., $\varepsilon_{emp} = 8.18\times10^{-5}$ $\mu m^{0.5}$, extracted in Chapter 5, the air damping coefficient is reduced by a factor of 2.5, while according to the model proposed by Hosaka *et al.* this factor is predicted to be approximately equal to $\lambda_2/\lambda_1 = 4.2$ (see Eq. (5.9)) [219]. In other words, the increase of Q_{air} in the second overtone is less than the theoretical prediction. Comparing Figures 5.7(b) and 7.6(b) shows that the empirical air damping coefficient for the data plotted versus $L/H^{1.25}$ is also decreased by a factor of 2.5 in the second flexural mode.

Figure 7.7 shows the variation of the Q-factor with the resonance frequency for the first three flexural modes. An interesting observation is that for all the measured cantilevers, the maximum Q-factors are found in a small frequency span of 200 to 400 kHz, regardless of the overtone number. This observation indicates that, at least for the first three flexural modes of resonant cantilevers within the investigated dimensions, the maximum achievable Q-factor is bound to an upper limit in frequency (i.e., $f < 400$ kHz). Similar to the discussion for the fundamental flexural mode, the decrease of Q-factor at higher and lower resonance frequency can be attributed to the dominance of support loss and air damping, respectively.

Finally, as depicted in Figure 7.7(c), the maximum measured Q-factor among all measured cantilevers regardless of the investigated overtone belongs to an 11 μm-thick cantilever with a length and width of 850 and 82 μm, respectively, which resonates at the

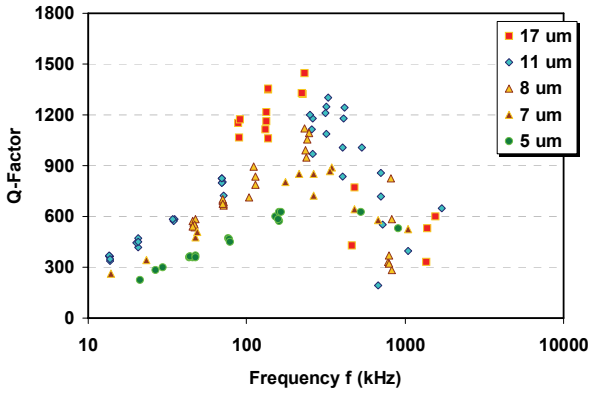

(a)

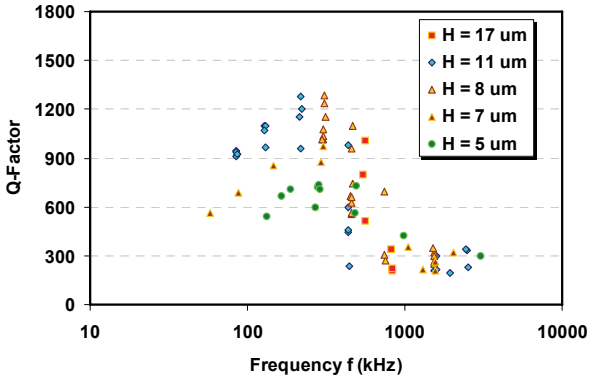

(b)

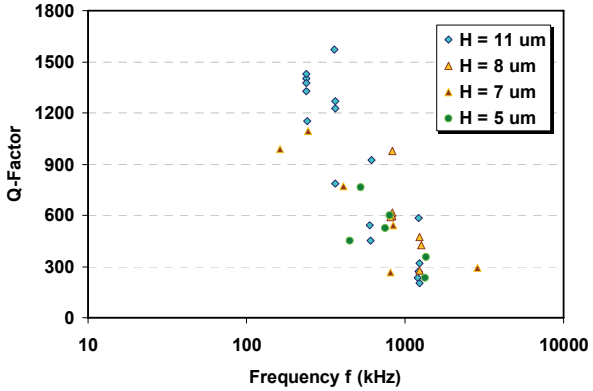

(c)

Figure 7.7. Q-factor versus resonance frequency for cantilevers with thickness of 5, 7, 8, 11 and 17 μm; (a) fundamental flexural mode (b) second flexural mode, (c) third flexural mode. Although not marked in the graph, the widths of the presented cantilevers are not necessarily equal.

third flexural mode with the measured Q-factor of 1574. Based on what is mentioned in this chapter, it is expected to reach even higher Q-factors by further decreasing the cantilever width.

7.3 Temperature Considerations

The measurement results presented in the previous section are obtained in a temperature range of 30 ± 5 ºC. Although the temperature span is small, it can be helpful to investigate the effect of temperature on the Q-factors and resonance frequencies of cantilevers. To this end, the resonance characteristics of a cantilever with length, width, and thickness of 1050, 130, and 11 μm has been captured in a temperature range form 10 to 70 ºC. The measurement was performed inside an ESPEC Environmental Chamber SH-241, with a relative humidity confined between 30 to 45%. To fit the measurement setup inside the chamber, and also to avoid any thermal influence form the setup, the excitation magnetic flux is generated by a permanent magnet instead of the previously used electromagnet.

Figure 7.8 presents plots of measured Q-factors versus temperature for the fundamental and the 5^{th} flexural modes. As observed in Figure 7.8(a), the influence of temperature on the Q-factor in the fundamental mode is negligible. However, as shown in Figure 7.8(b), in the 5^{th} mode the Q-factor dramatically increases by increasing the temperature. As a result, in general, trends of the Q-factor data for higher overtones must be interpreted with extra care since the observed variations may also be due to the temperature changes in addition to the cantilever dimension alterations. Also observed in Figure 7.8, for both

modes, the resonance frequency slightly decreases with an increase in the temperature. The latter observation is investigated in more details in Chapter 8.

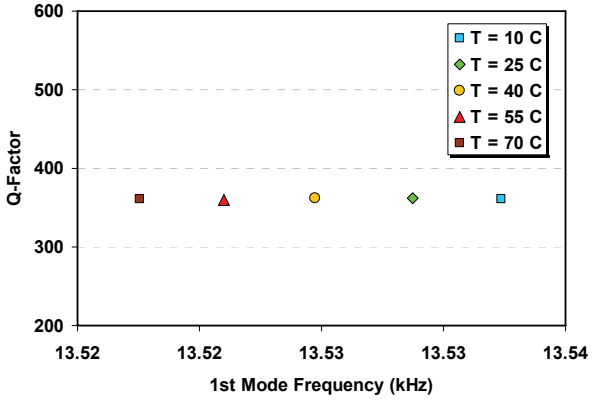

(a)

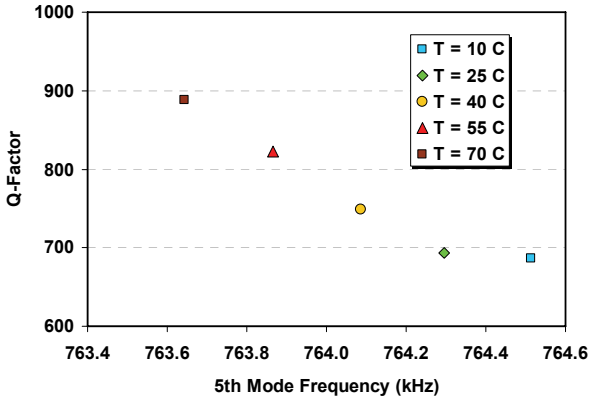

(b)

Figure 7.8. Plots of Q-factor versus resonance frequency for different temperatures; (a) fundamental flexural mode, (b) 5th flexural mode. The measured cantilever has a length, width, and thickness of 1050, 130, and 11 μm, respectively.

***

In this chapter, as a follow up to Chapter 5, the effect of cantilever dimensions on the Q-factor in flexural overtones was studied. Also, to have an accurate estimate of the

damping coefficient, based on the theoretical models given in Chapter 6, a model for the effective damping coefficient in every overtone was presented. The measurement results show that in higher flexural modes, similar to the fundamental mode, the dependence of Q-factor on cantilever geometry can be described by $\chi = L/H^{1.5}$; however, the critical region, in which the dominant damping mechanisms have equal influence, occurs at higher χ in the higher overtones. In other words, the Q-factors of cantilevers which have the air damping as the dominant loss mechanism in the fundamental flexural mode, initially increases in the second or third flexural modes, but eventually drops for higher modes. Also in this chapter the air damping and support loss were identified as dominant damping mechanisms for flexural overtones, although the cited theoretical models did not exactly match the measurement data. Finally, it was observed that a temperature variation can have a significant influence on the measured Q-factor, thus extra care must be applied in interpreting the trends of the Q-factor data in higher overtones.

CHAPTER 8

CANCELLATION OF ENVIRONMENTAL EFFECTS IN RESONANT MASS SENSORS

In study of the flexural resonance behavior of cantilevers in the previous chapters a major motivation has been to use the optimized resonators as mass sensors. As previously mentioned in Chapter 2, mass sensing with a resonant sensor was first demonstrated using quartz crystal microbalances (QCM) [146], which was based on the concept that a change in the resonant sensor's mass causes a change in resonance frequency [235]. Facilitated by the development of microfabrication technologies, this concept has been successfully implemented in other bulk acoustic wave resonators [236], as well as in surface acoustic wave sensors [237] and resonant cantilevers [6, 52, 238-240]. These mass sensors are especially used for (bio-) chemical detection, in which the mass change is typically caused by adsorption or absorption of target analytes to a sensitive layer coating the resonator.

One of the major challenges in resonant mass-sensing is to distinguish between frequency variations caused by a mass change and frequency variations caused by environmental changes, e.g., temperature, viscosity, or humidity. For example, in the previous chapter, in Figure 7.8, it was shown that a temperature increase would result in reduction of the cantilever resonance frequency. This observation can be explained by the well known phenomenon that a temperature change causes variations of the resonator's elastic modulus and/or dimensions [241]. On the other hand, changes in the ambient humidity

and viscosity alter the viscous damping of the resonant system and also cause resonance frequency drift [148, 241].

In this chapter a novel technique is presented to cancel the effect of environmental parameters, e.g., temperature and humidity, in resonant mass sensors, in general, and in resonant cantilevers, in particular. Utilizing a single resonator, the **e**nvironmental **c**ancellation is achieved by monitoring a pair of resonant **o**vertones and the effective sensed **m**ass in those overtones (ECOM: environmental effect cancellation with overtone and mass). As an eminent advantage the presented technique eliminates any need for previously measured look-up tables or fitting the measurement data.

8.1 A Brief Review of Temperature Compensation Techniques

To compensate the frequency drifts caused by ambient variations − temperature fluctuations in particular − one of the widely investigated approaches is to utilize another resonator as a reference [242-244]. In this approach, the sensing resonator, which is coated with the sensitive layer, and the uncoated reference resonator operate under the same environmental conditions. With the assumption that any environmental parameter affecting the resonance behavior will cause the same frequency drift in both sensing and reference resonators, the induced frequency change by an added mass can be extracted by subtracting the frequency changes of the two resonators. The drawback of this method originates from the aforementioned assumption that both resonators have exactly the same mechanical properties or at least respond similarly to environmental changes. In practice, however, no two resonators have exactly identical mechanical properties, even if

they are fabricated in the same batch process; consequently, their resonance frequencies and their responses to varying environmental parameters may not be same. Overall, this approach can be helpful in estimating the frequency change by a mass-uptake, but it cannot provide a complete solution.

Several other approaches in minimizing the temperature-induced resonance frequency variation include active frequency control with a co-integrated temperature sensor [242, 245] or feedback loop [246], passive temperature compensation using the stress induced by thin films [247-249], and selection of structural materials that are less sensitive to temperature [250]. When using a co-integrated temperature sensor, it is mandatory to establish a reproducible relationship between temperature and resonance frequency change. Here, a major challenge is that the temperature coefficient of the resonance frequency varies from one resonator to another, thus requiring a calibration for each sensor. Also, the required circuitry for precise sensing of temperature may increase the complexity and cost of overall sensing system. Finally, this approach only compensates the temperature effect, but leaves other contributing effects, e.g., humidity, uncompensated. On the other hand, passive approaches utilizing thin-film-induced stresses are highly dependent on the packaging, the adopted resonant structure, and the quality of the selected thin film. Finally, finding an absolutely temperature insensitive material is not trivial, and integrating such material with existing microfabrication technologies includes challenges, both in terms of feasibility and cost.

Another approach in compensating the temperature effect is to study the variation of different resonance modes [251-253] or overtones [254]. Here, a relationship between the temperature and frequency changes of different overtones or modes is established; hence, the same resonant mass sensor also acts as a thermometer. For such a sensor, with the help of a look-up table or calibrated coefficients, temperature-induced frequency changes can be eliminated. However, the main drawback of this approach is the need for such look-up tables or coefficients.

This chapter describes a new technique for cancellation of environmental parameters in resonant mass sensing based on monitoring the overtones of partially coated resonators. Like the aforementioned mode-based compensation approaches, an essential part of this technique is also based on comparing the frequency changes of different overtones. However, as an advantage, this technique obliterates any needs for pre-measured temperature-frequency look-up tables. In fact, the aim of the presented technique is to eliminate any environmental-related frequency dependence only by aid of a single resonator. The applicability of the presented technique is tested on a cantilever resonator and the results show excellent agreement with the theoretical predictions.

8.2 Theory of ECOM

In this section, first the frequency dependence on variations in mass and environmental parameters is described. Next, a special class of resonators is identified, whose normalized frequency change caused by environmental parameters is independent of the

resonance overtone. The technique presented in this chapter (ECOM) is aimed at such resonators.

8.2.1 General Theory

For all mechanical resonators, according to Rayleigh's quotient method, the resonance frequency, f, is determined by the ratio of the potential energy U and the inertial part of the kinetic energy K_E [188, 255]:

$$f = \frac{1}{2\pi}\sqrt{\frac{U}{K_E}}, \tag{8.1}$$

where K_E is expressed by the kinetic energy K as follows:

$$K_E = \frac{K}{(2\pi f)^2}.$$

Therefore, variations in K_E and U will reflect as a change of the resonance frequency Δf, which for small variations is calculated as

$$\frac{\Delta f}{f} = -\frac{1}{2}\left(\frac{\Delta K_E}{K_E} - \frac{\Delta U}{U}\right). \tag{8.2}$$

For a mass-spring system, whenever variations of the vibration amplitude can be neglected,

Eq. (8.2) simplifies to

$$\frac{\Delta f}{f} = -\frac{1}{2}\left(\frac{\Delta m^*}{m^*} - \frac{\Delta k^*}{k^*}\right), \tag{8.3}$$

where m^* and k^* are the effective mass and spring constant, respectively. In a resonant mass sensor used for (bio-)chemical sensing, the detection is accomplished by binding of target molecules to the surface of the resonator [3, 47], which results in an effective mass

change Δm^*. As long as the effect of the added mass on the potential energy can be neglected, i.e., k^* does not change with Δm^*, the change of the resonance frequency can be described as a function of the independent parameter mass m and also environmental parameters, e.g., temperature T, relative humidity RH, etc.:

$$\frac{\Delta f}{f} = \frac{\Delta f(m)}{f} + \frac{\Delta f(T, RH, etc.)}{f}, \tag{8.4}$$

and with respect to Eq. (8.3),

$$\frac{\Delta f}{f} = -\frac{1}{2}\frac{\Delta m^*}{m^*} + \frac{\Delta f(T, RH, etc.)}{f}. \tag{8.5}$$

The second term in Eq. (8.5) emerges because of variation of the potential energy, i.e., the effective spring constant, with environmental parameters. Without mass change, the resonance frequency variation will only depend on environmental parameters. The influence of these parameters on the resonance frequency is caused by changes in the resonator's material properties and/or geometry. In general, the normalized frequency changes of overtones in a resonator due to environmental changes are not identical; however, in a special class of resonators (e.g., the flexural modes of homogeneous cantilever beams) the overtone frequencies are related to each other through constant coefficients. In these resonators, the resonance frequency f_i of the i^{th} overtone is described as

$$f_i = \lambda_i^2 \, \mathbf{F}(E, \rho, l_{x,y,z}), \tag{8.6}$$

where λ_i is the overtone constant and **F** is a function of the resonator geometry $l_{x,y,z}$, and the material properties, i.e., Young's modulus E, Poisson ratio ν and density ρ. For this class of resonators, in case of environmental variation, the change of the resonator geometry and material properties will be same for all overtones; therefore, the change of

F will be same for all overtones. Hence, the resonance frequency change Δf_i of the i^{th} overtone can be described as

$$\Delta f_i = \lambda_i^2 \Delta \mathbf{F}, \tag{8.7}$$

where $\Delta\mathbf{F}$ is an overtone-independent change of **F**. As the result, the overtone dependence, i.e., λ_i, vanishes after normalizing Δf_i with the overtone frequency f_i from Eq. (8.6),

$$\frac{\Delta f_i}{f_i} = \frac{\Delta \mathbf{F}}{\mathbf{F}}. \tag{8.8}$$

Since all variables affecting **F** are in fact functions of environmental variables, Eq. (8.8) can be rewritten with respect to Eq. (8.5):

$$\frac{\Delta f_i(T, RH, etc.)}{f_i} = \frac{\Delta \mathbf{F}(T, RH, etc.)}{\mathbf{F}}. \tag{8.9}$$

To completely describe Eq. (8.5) for a given overtone frequency, the effect of any added mass in that overtone needs to be included. In a resonant mass sensor, the attached analyte mass Δm generally vibrates with different normalized amplitudes in different overtones, and thus its contributed effective mass, Δm^*, will be different in those overtones. In other words, if the actual mass change is Δm, the effective mass change in the i^{th} overtone is given by

$$\Delta m_i^* = \alpha_i \Delta m. \tag{8.10a}$$

where α_i is the effective mass coefficient and calculated only based on the mode-shape and the location of the added mass on the resonator surface. Likewise, the effective mass of the resonator can also be described based on its actual mass and the overtone by a coefficient ζ_i,

$$m_i^* = \zeta_i m. \tag{8.10b}$$

By applying Eqs. (8.9) and (8.10) in Eq. (8.5), the normalized frequency change of the i^{th} overtone $\Delta f_i/f_i$ is given by

$$\frac{\Delta f_i}{f_i} = -\frac{1}{2}\frac{\alpha_i}{\zeta_i}\frac{\Delta m}{m} + \frac{\Delta \mathrm{F}(T, RH, etc.)}{\mathrm{F}}. \tag{8.11}$$

Hence, by subtracting the normalized frequencies of two overtones i and j, it is possible to eliminate the effect of environmental parameter changes

$$\frac{\Delta f_i}{f_i} - \frac{\Delta f_j}{f_j} = -\frac{1}{2}\left(\frac{\alpha_i}{\zeta_i} - \frac{\alpha_j}{\zeta_j}\right)\frac{\Delta m}{m}, \tag{8.12a}$$

If the resonator has the same effective mass in all overtones, Eq. (8.12a) simplifies to

$$\frac{\Delta f_i}{f_i} - \frac{\Delta f_j}{f_j} = -\frac{1}{2}(\alpha_i - \alpha_j)\frac{\Delta m}{m^*}. \tag{8.12b}$$

As mentioned earlier, the conditions for establishing Eqs. (8.12) are: 1) the added mass must not change the potential energy of the system (i.e., no change in the resonator effective stiffness), and 2) the effective added mass must be different in the examined overtones.

8.2.2 Beam Resonators with Flexural Resonance Overtones

Beams undergoing flexural resonance are prominent examples of the resonators that fit the conditions described for Eqs. (8.12). For homogenous, clamped-free (i.e., cantilever) or clamped-clamped beams, when damping of the resonant system is negligible, f_i can by Eq. (2.27): [188]

$$f_i = \lambda_i^2 \frac{1}{2\pi\sqrt{12}}\frac{h}{L^2}\sqrt{\frac{E}{\rho}}, \tag{8.13}$$

where L and h are the beam length and thickness, respectively. Comparing Eq. (8.6) and Eq. (8.13), the function **F** of a beam in a flexural overtone becomes

$$\mathbf{F}(E,\rho,l_{x,y,z}) = \frac{1}{2\pi\sqrt{12}}\frac{h}{L^2}\sqrt{\frac{E}{\rho}}. \tag{8.14}$$

The focus of the rest of this chapter will be on cantilevers resonating in the flexural resonance modes as resonant mass sensors. To calculate the effective mass of a deposited layer on the cantilever surface, the resonator's kinetic energy need to be studied. As mentioned in Chapter 6, the maximum kinetic energy K of a thin homogenous cantilever beam with a uniform cross-section is given by [188] :

$$K = \frac{1}{2}\omega^2\frac{m}{L}\int_0^L y^2(x)dx, \tag{8.15}$$

where y is the vibration amplitude at point x along the beam, and m and ω are the beam actual mass and angular velocity, respectively. A particle with mass dm, which is attached at point x on the cantilever surface, increases the kinetic energy by dK

$$dK = \frac{\omega^2}{2}y^2(x)dm, \tag{8.16}$$

provided that the change in the resonance amplitude is negligible. If the attached particle does not contribute to the stiffness of the beam, i.e., to the potential energy, the principle of energy conservation requires the equality of the kinetic energy before and after attachment:

$$\frac{1}{2}\omega_f^2\frac{m}{L}\int_0^L y^2(x)dx + \frac{\omega_f^2}{2}y^2(x)dm = \frac{1}{2}\omega_i^2\frac{m}{L}\int_0^L y^2(x)dx, \tag{8.17}$$

where ω_i and ω_f are the angular velocities for the initial case (unattached mass) and final case (attached mass). Since for all flexural modes of a resonating cantilever beam the

integral value of Eq. (8.15) is equal to ¼ $L\,y^2(L)$ [175, 229] (see Appendix C), Eq. (8.17) can be rearranged as

$$dm\omega_f^2 y^2(x) = \frac{1}{4} m(\omega_i^2 - \omega_f^2) y^2(L). \tag{8.18}$$

Assuming ω_i and ω_f are almost identical, the resulting relative frequency change $d\omega/\omega$ due to the added mass dm at distance x is obtained as

$$\frac{d\omega}{\omega} = \frac{\omega_f - \omega_i}{\omega_i} = -\frac{1}{2}\frac{dm}{\frac{1}{4}m}\frac{y^2(x)}{y^2(L)}. \tag{8.19}$$

On the other hand, as discussed in Chapter 6, for all flexural vibration modes (overtones) the effective mass of a cantilever, if considered as a point-mass on the tip, is a quarter of the cantilever's actual mass:

$$m^* = \frac{1}{4} m. \tag{8.20}$$

Thus Eq. (8.19) becomes

$$\frac{d\omega}{\omega} = -\frac{1}{2}\frac{dm}{m^*}\left(\frac{y(x)}{y(L)}\right)^2. \tag{8.21}$$

The result of Eq. (8.21) is consistent with reported experimental results [256, 257]. With the same argument, the frequency change due to attachment of a continues sequence of discrete particles, e.g., deposition of a layer or sorption of target molecules into a sensitive film on surface of the resonator, can be described as

$$\frac{d\omega}{\omega} = -\frac{1}{2m^*}\int_a^b \left(\frac{y(x)}{y(L)}\right)^2 dm, \tag{8.22}$$

where a and b are, respectively, the starting and ending points of the layer coverage. Assuming a uniform mass loading between a and b with a total added mass of Δm, Eq. (8.22) simplifies to

$$\frac{d\omega}{\omega} = -\frac{\Delta m}{2m^*}\frac{1}{b-a}\int_a^b \left(\frac{y(x)}{y(L)}\right)^2 dx\,. \tag{8.23}$$

Hence, by comparing Eq. (8.11) and Eq. (8.23), the effective mass coefficient α_i in the i^{th} overtone is calculated as

$$\alpha_i = \frac{1}{b-a}\int_a^b \left(\frac{y(x)}{y(L)}\right)^2 dx\,. \tag{8.24}$$

Here, $\Delta m^* = \alpha_i.\Delta m$ is the effective mass of the added mass when considered as a lumped point mass on the beam tip (see Figure 8.1). It is important to note that when the added layer covers the entire cantilever, according to Eq. (8.24) α_i will have the same value of ¼ for all overtones. Hence, to have an effective temperature cancellation through Eqs. (8.12), the attached layer (i.e., the added mass) must only partially cover the cantilever surface.

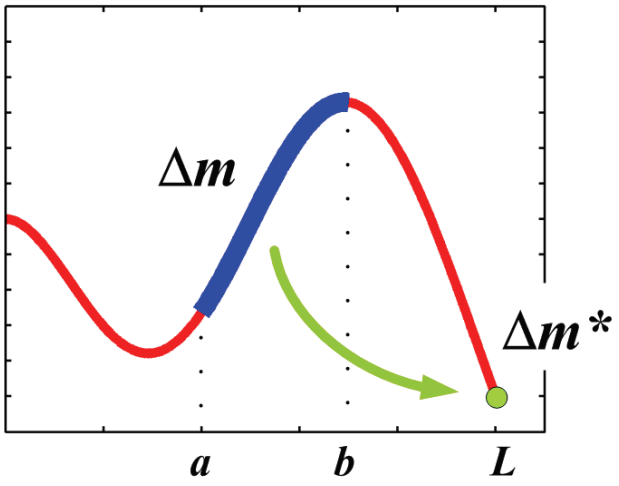

Figure 8.1. Schematic of the 3rd overtone mode-shape of a cantilever; Δm, the mass of the added layer, shown in thick blue, can be considered as a lumped effective mass Δm^* on the cantilever tip.

8.2.3 Technical Considerations

To apply the presented technique in a resonant cantilever mass sensor, the detection must be accomplished through binding of target analyte to a sensitive layer that partially covers the resonator surface. If the layer is uniformly deposited, it is a fair assumption that binding also takes place with a uniform rate across the layer. There are always at least two different flexural overtones of a resonant cantilever that exhibit different effective mass coefficients for a partially covering layer. Therefore, the requirement of Eqs. (8.12), i.e., having different α_i in different overtones, can be satisfied. However, addressing the second requirement, i.e., maintaining the same stiffness after binding, depends on the type of material or the location of binding on the cantilever surface. In other words, either the binding must have a negligible effect on the stiffness of the sensing layer, or the sensing layer must be placed at a location that causes a minimal contribution to the strain energy of the desired overtones. Such locations include areas on the cantilever surface that experience minimal stress in a flexural vibration. Finite element simulations results presented in Figure 8.2 indicate that in case of the fundamental and the 2^{nd} overtone, the final 20% portion of the cantilever length can satisfy this requirement. This portion of the cantilever length includes areas around the cantilever tip. In general, by approaching the cantilever tip the contribution of the sensing layer on the strain energy decreases. However, confining the sensing layer to a close proximity to the tip may not be a helpful approach; because in this case, the difference between the values of the effective mass coefficients in different overtones also becomes smaller; hence, the mass ratios in Eqs. (8.12) become smaller.

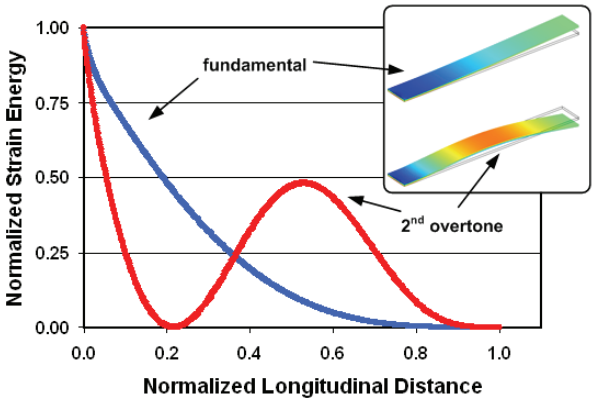

Figure 8.2. FEM simulation results for the longitudinal distributions of the normalized strain energy in a cantilever beam for the fundamental and 2nd flexural resonance modes; also for these vibration modes, the normal stress distributions are shown in the inset.

8.3 Experiments

Flexural resonance frequencies of a silicon cantilever with length, width and thickness of 1050, 130 and 11 μm, respectively, were investigated. The surface of the cantilever was covered with 0.8 μm silicon dioxide. The resonator vibration in air was electromagnetically exited by passing an alternating current along the perimeter of cantilever in the presence of a static magnetic field of 0.2 Tesla. The used measurement set-up was the same as the set-up described in Chapter 5 with the only exception that the magnetic field was generated by a permanent magnet block. In this set-up the transverse beam vibrations were sensed on chip by a piezoresistive Wheatstone bridge located at the clamped-end of the beam. The amplitude/phase transfer characteristics of the resonator were recorded by an Agilent Network Analyzer 4395A. Each data-point presented in this chapter is an average of at least 5 repeated measurements, with a maximum standard

deviation of 10 ppm. To improve the accuracy of the extracted resonance frequency, the measured transfer characteristic around each peak was fitted to an SHO transfer function, as described in Chapter 4. The ambient temperature and humidity were controlled with an ESPEC SH-241 environmental chamber, in which a part of the measurement set-up, including the resonant cantilever and the magnet block, were held.

The effect of mass loading was investigated by depositing a strip of SC1813 photoresist at approximately 90 μm from the cantilever free-end (Figure 8.3). For this location, according to Eq. (8.24), the effective mass coefficient α_1 is approximately 0.8. To evaporate the photoresist solvent, the sample was baked for 45 minutes at 100 ˚C in oven. Although identifying the photoresist mass has no influence in evaluating the validity of proposed technique, the actual mass of the photoresist layer was calculated by examining the frequency change at a constant temperature. At 10 ºC and for the fundamental flexural mode with α_1 = 0.8, according to Eqs. (8.23) and (8.20), the actual added mass is calculated as 0.095% of the actual cantilever mass, i.e., approximately 3.6 ng.

8.4 Results and Discussion

8.4.1 Temperature Effect

In the performed measurements, the initial temperature was 10 ºC. The influence of temperature was studied by increasing it to 70 ºC in 15 ºC steps, while the relative humidity was stabilized at 45%. The stability of temperature in the measured sample was

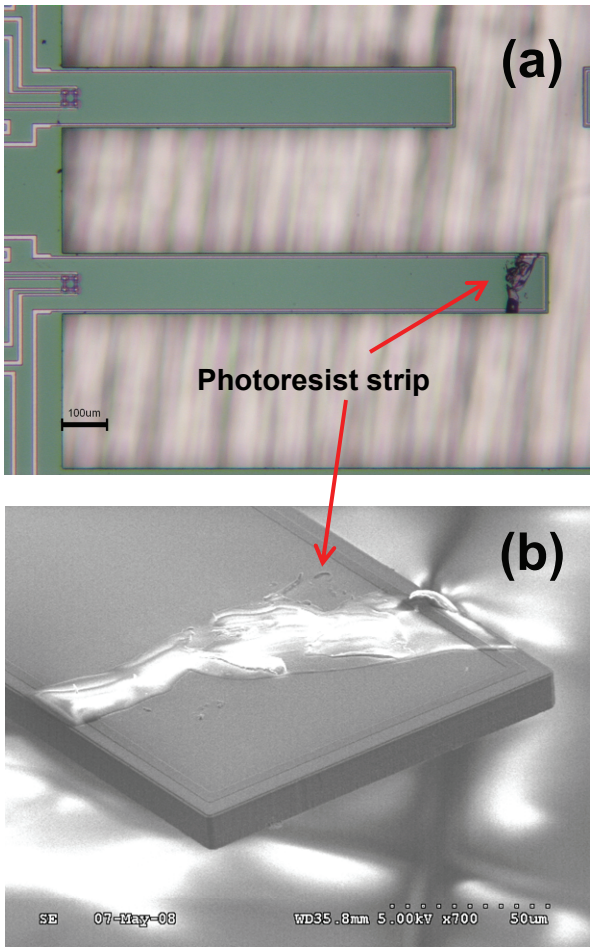

Figure 8.3. (a) Optical micrograph of magnetically excitable resonant cantilevers. The cantilever tested in this work is covered by a strip of photoresist about 90 μm from the tip. (b) SEM picture of the photoresist strip near the cantilever tip.

monitored by checking the (lack of) temperature-induced variations in a pair of reserved on-chip resistors. The resistance variations were measured with a Keithley 2400 Sourcemeter. Figure 8.4 plots the relative frequency change of both the unloaded and the loaded cantilever as a function of the temperature increase for different overtones; as expected from Eq. (8.14), the temperature-induced relative frequency changes ($\Delta f_n/f_n$) are coinciding and exhibit almost equal temperature coefficients, namely -18.8 ppm˚C^{-1} for the 2nd overtone. These results confirm that the measured cantilever beam can be

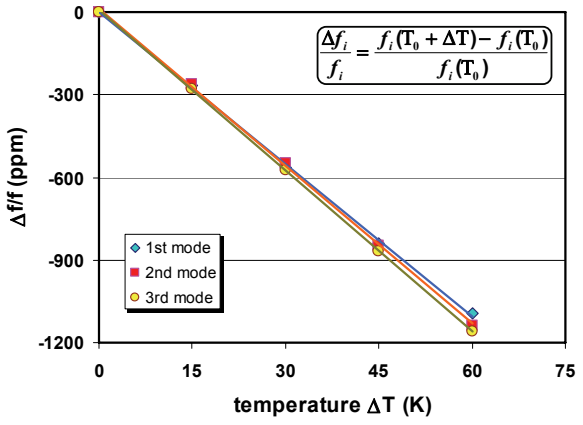

(a)

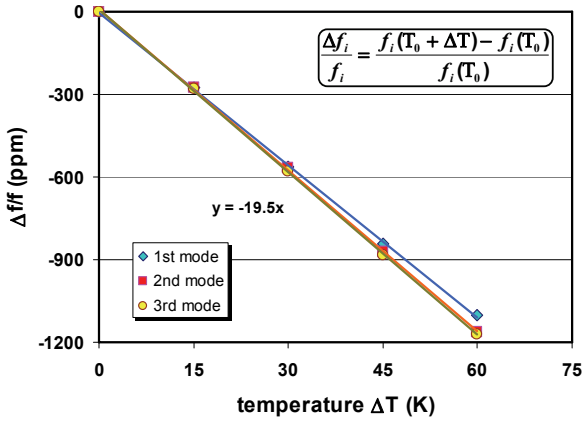

(b)

Figure 8.4. Relative frequency change $\Delta f/f$ of the first three flexural modes (fundamental, 2nd and 3rd overtones) for (a) the unloaded and (b) the loaded cantilever versus temperature change ΔT (reference temperature $T_0 = 10$ ˚C).

considered as a suitable example of resonators with the property presented in Eq. (8.9). Table 8.1 summarizes the measured absolute frequencies and quality factors of the unloaded cantilever for the first three overtones at the initial and final temperatures.

The combined effects of added mass and temperature on the resonance frequency are shown in Figure 8.5, which plots the relative frequency change of each overtone as a

Table 8.1. Measured resonance frequency and quality factor for the fundamental and the next two flexural resonance overtones of the unloaded cantilever beam at 10 ˚C and 70 ˚C. The theoretical values of the corresponding overtone constants are indicated by λ_i.

	λ_i	T = 10 ˚C		T = 70 ˚C	
		f (Hz)	Q-factor	f (Hz)	Q-factor
Fundamental mode	1.875	13,532.4	360.7	13,517.6	361.0
2nd overtone	4.694	84,874.3	946.5	84,777.8	999.1
3rd overtone	7.855	237,467	1378	237,192	1504

function of the temperature change. In this figure, the observed relative frequency change for $\Delta T = 0$ K, i.e., at the reference temperature of 10 ˚C, is only due to the effect of mass change. Increasing temperature affects the frequency with a similar trend as shown in Figure 8.4, and the frequency change in each overtone follows a trend parallel to the changes in other overtones; however, since the effective mass in each overtone is different, the overtone plots have different Y-intercepts. In other words, for a given temperature the relative frequency change of each overtone is different because the coefficients of effective mass in those overtones are different.

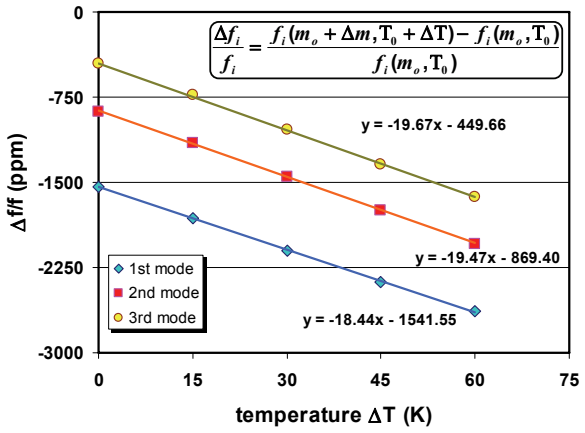

Figure 8.5. Relative frequency change $\Delta f/f$ of the first three flexural modes of cantilever as the result of a fixed mass change Δm, versus temperature change ΔT (reference temperature $T_0 = 10$ ˚C).

8.4.2 *Humidity Effect*

To investigate the effect of relative humidity, the temperature was kept constant at 55 ˚C, while the relative humidity was increased from 30% to 90% at 15% steps. For both loaded and unloaded cantilever, the effect of relative humidity on the relative frequency change of the overtones frequency is presented in Figure 8.6. Similar to the argument made for the temperature effects, the relative variations of overtone frequencies are coinciding and independent of the overtone number. However, the effect of humidity is

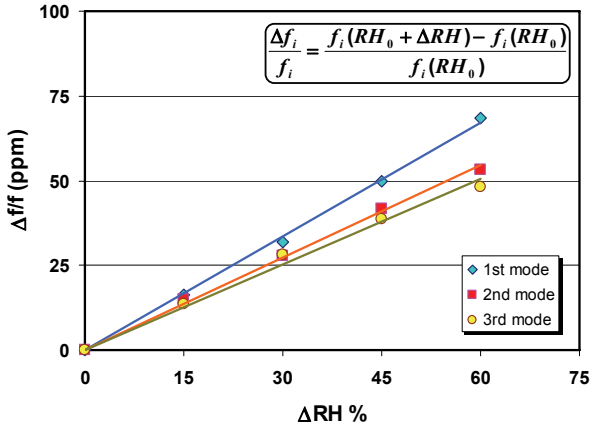

(a)

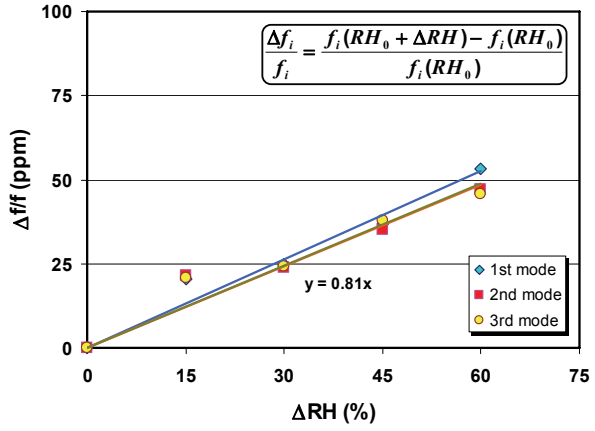

(b)

Figure 8.6. Relative frequency change $\Delta f/f$ of the flexural modes (fundamental, 2nd and 3rd overtones) for (a) the unloaded and (b) the loaded cantilever versus relative humidity change ΔRH (reference relative humidity RH_0 = 30%).

not as pronounced as the effect of temperature; for example the 2nd overtone has a humidity coefficient as low as 0.9 ppm-%RH^{-1}. For the loaded cantilever (see Figure 8.6(b)), none of the three overtones appears to follow the linear trend at the first 15% increase of relative humidity; nevertheless, for both loaded and unloaded cases, all data points are coinciding. The combined effects of mass loading and relative humidity changes on the resonance frequency are shown in Figure 8.7. Similar to the temperature case (see Figure 8.5), the plots of relative frequency change versus the relative humidity also follow parallel trends, but because of the dominating influence of the added mass, the slopes are more gradual, e.g., 0.7 ppm-%RH^{-1} for the 2nd overtone.

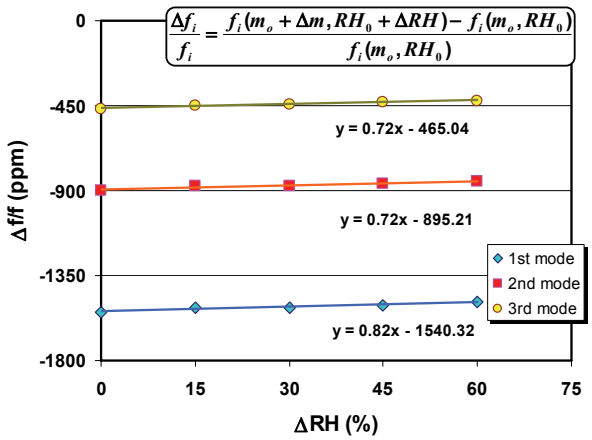

Figure 8.7. Relative frequency change $\Delta f/f$ of the first three flexural modes of cantilever as the result of a fixed mass change Δm, versus relative humidity change ΔRH (reference relative humidity RH_0 = 30%).

8.4.3 Environmental Effect Cancellation

As observed in Figure 8.5, for a given temperature, the added mass does not have the same effect for each of the overtone frequencies, but it follows the prediction of

Eq. (8.23). However, the variations of the relative resonance frequencies with temperature exhibit almost identical slopes. Hence, after subtracting the relative frequency changes of every two overtones according to Eq. (8.12b), the resulting plot, shown in Figure 8.8, is almost temperature independent. For example, the temperature coefficient of the 2nd overtone, as shown in Figure 8.5, is -19.5 ppm˚C^{-1}, but after applying Eq. (8.12b) on the measurement results of the 2nd and 3rd overtones, the temperature dependence changes to 0.2 ppm˚C^{-1}, an almost 2 orders of magnitude improvement.

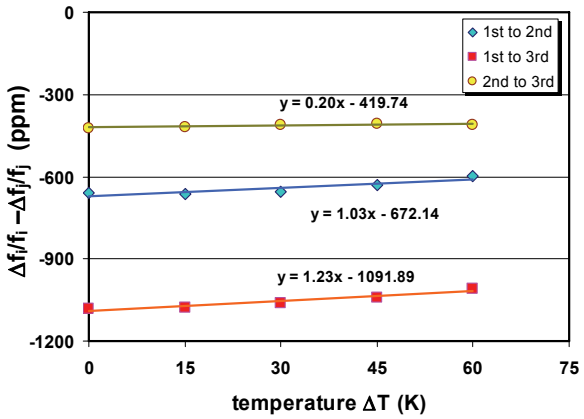

Figure 8.8. Cancellation of temperature dependence by evaluating the difference of relative frequency change $\Delta f/f$ of two overtones (based on the data from Figure 8.5).

Similarly, Figure 8.9 shows that by applying the result of Eq. (8.12b) the effect of humidity is canceled too. In this case, the humidity coefficient of the 2nd overtone is 0.7 ppm-%RH^{-1} (see Figure 8.7), but after applying the proposed technique on the results of the 2nd and 3rd overtones, the humidity dependence decreases to -0.03 ppm %RH^{-1} (see Figure 8.9), literally the level of measurement error (noise).

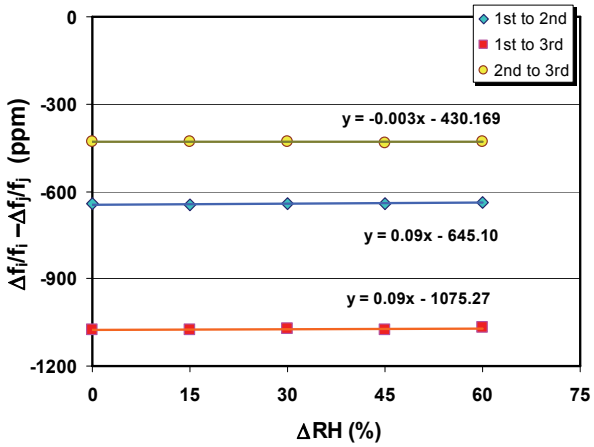

Figure 8.9. Cancellation of humidity dependence by evaluating the difference of relative frequency change $\Delta f/f$ of two overtones (based on the data presented in Figure 8.7).

Theoretically, applying Eq. (8.12b) shall result in a complete cancellation of temperature effects. However, as shown in Figures 8.4 and 8.6, the temperature coefficients of the overtones are not exactly the same, hence, the differences of the relative overtone frequency changes, shown in Figures 8.8 and 8.9, slightly vary with the temperature. The reason for the slight difference in the temperature coefficients of the overtones can be attributed to the facts that 1) the used cantilever is not an ideal beam with an ideal clamped-end boundary condition; in fact, because of fabrication limits, the thickness of the cantilever slightly varies along the beam, and also, the clamped-end of the beam is not attached to a solid straight wall, but to the upper rim of an etched cavity; 2) The vibration amplitude, especially in case of the fundamental flexural mode, can exceed the small amplitude assumption used in derivation of Eq. (8.13) – the maximum vibration amplitude of the beam was up to 35 μm; 3) The contribution of added mass on the resonator stiffness can cause a non-ideality and void the assumption made in deriving Eq. (8.4); and 4) as presented in Table 8.1, the resonance quality factor is not identical in

different overtones, hence, the relative frequency shift due to damping is not identical either.

Ideally, since the y-intercepts in Figures 8.8 and 8.9 are solely determined by the added effective mass, they must also have the same values for a given combination of overtones. However, as it is observed in these figures, the values of y-intercepts are slightly different. The main reason for this variation is the fact that the reference temperatures (and relative humidity) for the cases shown in Figures 8.8 and 8.9 are different. The reference temperatures in Figures 8.8 and 8.9 are 10 ˚C and 55 ˚C, respectively.

***

In this chapter, a novel technique for cancellation of environmental effects (e.g., temperature and relative humidity) on the resonance frequency of resonant mass sensors is introduced. After applying this technique in a resonant cantilever, the undesired resonance frequency shifts caused by environmental parameters, namely temperature and humidity, are suppressed by up to 2 orders of magnitude. To detect an added mass and meanwhile cancel the effect of environmental parameters, the presented technique needs only 4 frequency measurements; i.e., measuring the frequency of a pair of resonance overtones and comparing them with another pair measured before the potential variation in the mass. Hence, utilizing a single sensor, this technique obliterates any need for look-up tables, or the need for numerically adjusting the measurement results. The requirement for applying the presented technique are 1) the mass change must affect the examined

overtone frequencies with different ratios, and 2) the mass change must not alter the potential energy of the resonant system, i.e., it must have a minimal effect on the resonator stiffness. To fulfill the former requirement, the surface of the resonant mass sensor, e.g., a mass-sensitive (bio-) chemical sensor, must be partially covered with the sensing layer. To address the latter requirement, either the binding induced changes in the modulus of elasticity of the sensing layer must be negligible, or the sensing layer must be deposited on areas of resonator with minimal potential (strain) energy.

CHAPTER 9

OVERTONE-EMPHASIZED FLEXURAL RESONANCE

In Chapter 8 it was shown that unwanted effects of environmental parameters on the resonance frequency of cantilever sensors can be eliminated by simply monitoring the variation of normalized resonance frequencies in two different overtones. To do so, however, the detection scheme must be capable of tuning to the desired overtone. Usually resonant sensors are operated in a closed-loop configuration [258, 259], in which the oscillator normally locks on the largest output signal (e.g., the largest magnitude or phase-change). A conventional way to tune to the desired resonance frequency involves suppressing other resonance modes with electronic filters. Considering flexural resonance of a cantilever, however, the frequency separation between consecutive resonance overtones may not be large enough to avoid using high quality electronic filters. In fact for a given cantilever, the ratio $g_{i,j}$ between every two flexural resonance frequencies f_i and f_j is derived from Eq. (2.26a):

$$g_{i,j} = \frac{f_i}{f_j} = \left(\frac{\lambda_i}{\lambda_j} \right)^2 . \qquad (9.1)$$

Table 9.1 summarizes calculated ratios $g_{i+1,i}$ for consecutive flexural modes. The presented data imply that when the fundamental resonance frequency is small, the separation between the overtone frequencies will be small too, to such an extent that an efficient filtering may not be possible.

Another approach in selective tuning to an overtone is to use the cantilever itself as a mechanical filter. The focus of this chapter is on techniques to enhance or suppress the vibration amplitude in desired overtones, either by optimizing the location of piezoresistive detectors, or by selectively actuating the cantilever, similar to playing different notes on a string of the violin.

Table 9.1. Ratios of flexural resonance frequencies.

	$i=1$	$i=2$	$i=3$	$i=4$	$i>4$
$g_{i,1}$	1	6.27	17.55	34.39	$0.70 \times (2i - 1)^2$
$g_{i+1,i}$	6.27	2.80	1.96	1.65	$[(2i + 1)/(2i - 1)]^2$

9.1 Detection Enhancement and Suppression Techniques

9.1.1 Detection Enhancement by Optimization of Piezoresistive Bridge Location

When a cantilever is statically deflected by a point force, ideally the piezoresistive Wheatstone bridge must be implemented at the location that undergoes the maximum longitudinal stress, i.e., in the proximity of the cantilever clamped edge. Not only in the static mode, but also for all flexural resonance modes the clamped edge bears the maximum induced stress; because the radius of curvature is always minimal at the clamped edge as a result of applied boundary conditions, while according to Eq. (2.16) the longitudinal stress σ_x is inversely proportional to the radius of curvature ρ:

$$\sigma_x = z\frac{E}{\rho}. \tag{9.2}$$

Here E is the modulus of elasticity and z is the distance from the cantilever neutral axis. In general, for small deflections, the maxima and minima of longitudinal stress can be

found by investigating the second derivative of the flexural vibration amplitude $y(x)$, which is also inversely proportional to ρ [1]:

$$\frac{1}{\rho} = \frac{d^2 y}{dx^2}; \tag{9.3}$$

Solving Eqs. (9.2) and (9.3) together reveals that for flexural deflection $y(x)$ expressed by Eq. (2.26) the absolute longitudinal stress maximum is always on the clamped end (see Figure 9.1). In selective detection of overtones, however, the objective is to enhance the

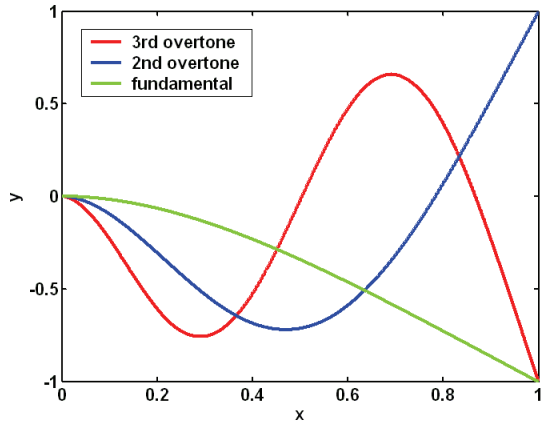

(a)

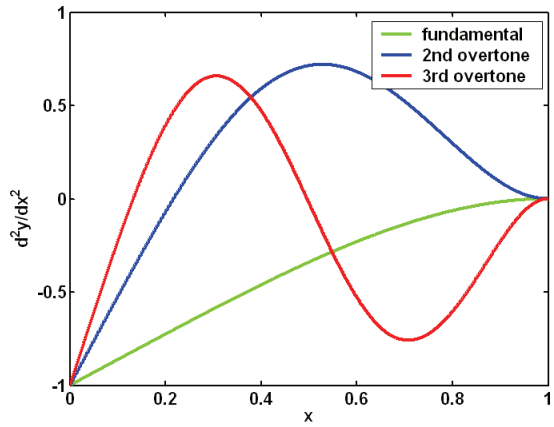

(b)

Figure 9.1. Normalized plots of (a) cantilever deflection y, and (b) d^2y/dx^2 along the cantilever length in the first three flexural modes.

detection of desired overtones. As shown in Figure 9.1, in a resonant cantilever for each flexural mode there is a location where the induced stress is locally maximized for that overtone; hence, by placing the piezoresistors on this location the detection selectivity for that particular overtone can be increased. Again, by solving Eqs. (9.2) and (9.3) together the exact location of local maxima for any flexural mode can be calculated. Applying this approach for the first three flexural modes, Table 9.2 summarizes locations of the longitudinal stress maxima, which are normalized with respect to the cantilever length. The presented data is also confirmed by finite element simulation results (see Figure 9.2).

Table 9.2. Normalized location of local longitudinal stress maxima.

Flexural mode	1	2	3
Normalized location	0	0.53	0.71

9.1.2 Detection Enhancement and Suppression by Optimization of Excitation Line

An advantage of magnetically actuated cantilevers is that the actuation force can be precisely exerted on selected locations, which are designated by excitation current lines passing over them. At these locations, as mentioned in Chapter 5, an out-of-plane force F is applied to the cantilever at the presence of a magnetic flux density B. This force (the Lorentz force) is calculated as [260]

$$F = IL_{exc} \times B, \tag{9.4}$$

where I is the current passing through an excitation line that has a length of L_{exc}. To excite the flexural resonance modes of a cantilever, the force direction must be normal to

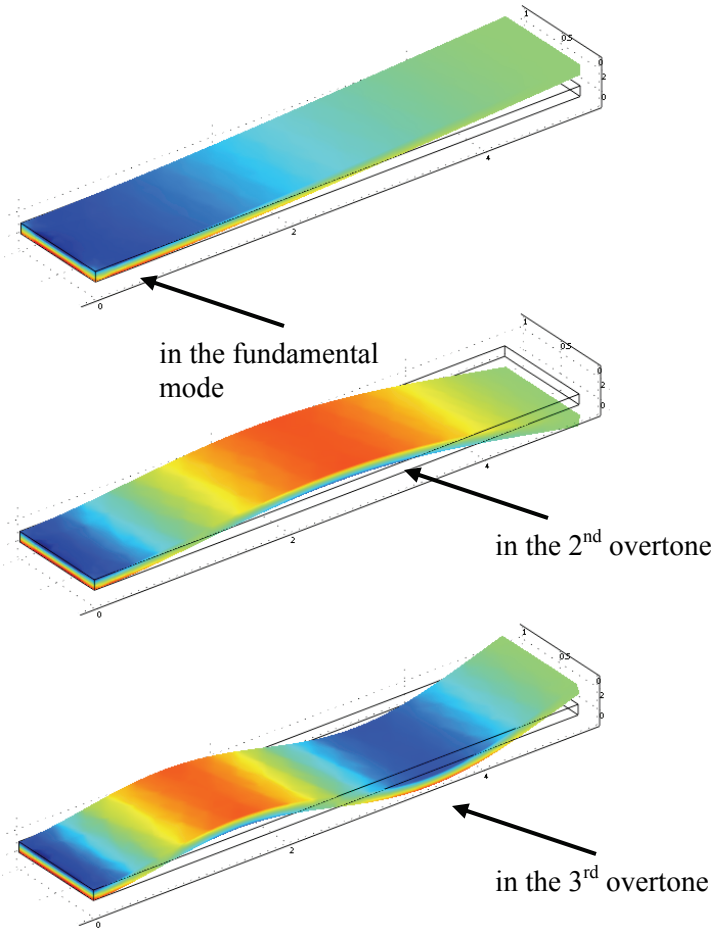

Figure 9.2. Simulation results for longitudinal stress σ_x in the first three flexural resonance modes of a cantilever.

the cantilever surface, which requires implementing a configuration as shown in Figure 5.3. In this configuration (see also Figure 9.3) the effective portion of the excitation line is only that section of the line that passes across the cantilever width (i.e., the transverse line), while the two parallel sections running along the cantilever length (i.e., the longitudinal lines) experience no force. Even if there was any force acting on the longitudinal lines, e.g., due to a change of the magnetic flux direction, the net out-of-plane force would be zero since the current directions in those lines are opposite.

Therefore, by changing the location of the transverse line along the beam it is possible to apply an excitation force at a desired location.

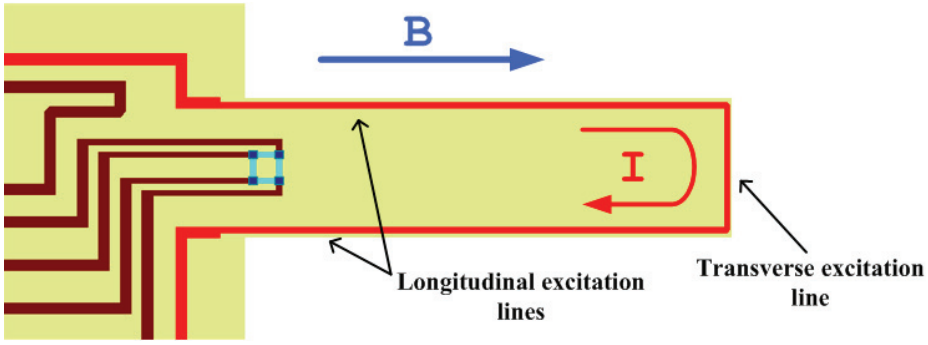

Figure 9.3. Implemented layout for the magnetic excitation. The blue arrow indicates the direction of the magnetic flux *B*. The alternating excitation current *I* passes through the red line.

A. Overtone suppression

As discussed in Chapter 6, the flexural mode shapes of a cantilever include peculiar points known as nodes and antinodes. While ideally the vibration amplitude at a node is zero, the cantilevers exhibits locally maximal vibration amplitudes at antinodes. The fundamental flexural mode shape does not have any nodes, yet its vibration amplitude at the cantilever clamped edge is zero, similar to all other modes.

Taking advantage from the fact that a given overtone has its own unique node location, it is possible to suppress that overtone by simply applying an excitation force at the corresponding node; in other words, suppression is imposed by forcing the cantilever to deflect at the locations where it naturally should have no deflection. This objective can be

achieved by positioning the transverse excitation at the nodes of the overtone to be suppressed.

B. Overtone enhancement

If applying a force at the node location can suppress an overtone, exerting excitation forces at the antinodes can enhance the overtone vibration. From Eq. (2.26) it is known that the maximum vibration amplitude is always at the cantilever tip; hence, positioning the transverse excitation line as close as possible to the tip is the best strategy for exciting all overtones. However, this excitation scheme will not be very helpful if the objective is to selectively excite an overtone. On the other hand, other than the absolute maximum amplitude at the tip, flexural overtones have local maximal amplitudes at the antinodes. Therefore, by implementing transverse excitation lines at the location of each antinode not only the desired overtone can be excited, but also as a result of using multiple excitation lines the vibration amplitude may be amplified.

To excite a flexural overtone, the applied forces on the adjacent antinodes must be opposite in direction. To this end, two topologies for the excitation lines can be defined, as shown in Figure 9.4: a) Simple loop topology (SLT), in which the net length of the excitation line on the farther antinode (i.e., the antinode closer to the tip) is larger, thus the farther antinode experiences a larger force; b) Twisted loop topology (TLT), in which by twisting the excitation loop the net length of the transverse line on the farther antinode is smaller, thus it experiences a smaller force. Although any ratio between the lengths of consecutive transverse excitation lines can be assumed, an efficient overtone tuning is

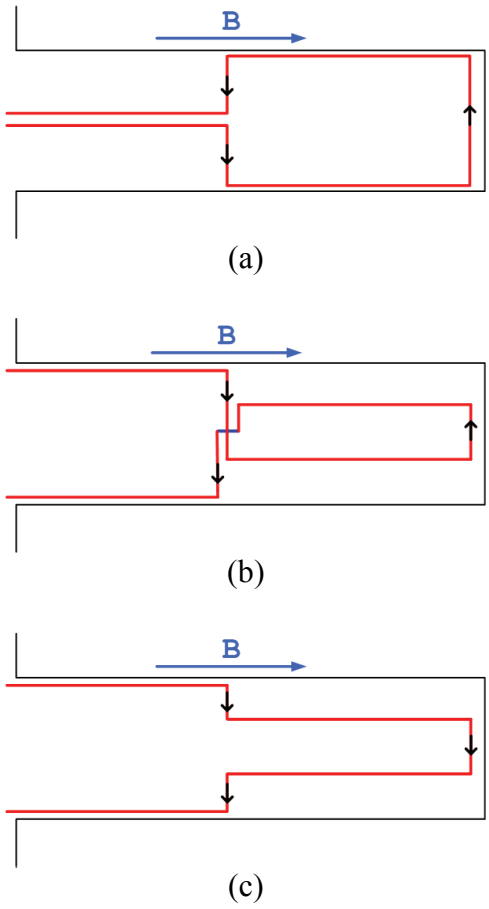

Figure 9.4. Excitation line schemes for applying force in opposite directions: (a) Simple loop topology (SLT), (b) Twisted loop topology (TLT). In the scheme shown in (c) the exerted out of plane forces are in the same directions. In this figure the black arrows indicate the relative direction of the current flow and the blue arrow indicates the direction of the magnetic flux *B*.

achieved by implementing the ratios presented in Table 6.2 in Chapter 6, i.e., by applying a unique force combination that causes the static deflection of the beam to be similar to the targeted flexural mode shape. Using the aforementioned ratios, the cantilever is forced to adapt to vibration amplitudes similar to the desired mode shape; hence, the vibration amplitudes of other overtones are suppressed, while the vibration of the desired flexural mode is enhanced. For example, in the second flexural mode the force ratio is calculated in Chapter 6 as $\beta_2 = -3.27$, which with respect to Eq. (9.4) gives

$$\frac{L_{ex2}}{L_{ex1}} = |\beta_2| = 3.27\,, \tag{9.5}$$

where L_{ex1} is the length of the shorter transverse excitation line, located in the proximity of the tip, and L_{ex2} is the total length of the transverse excitation lines located at the antinode at a normalized distance of p_2 = 0.47 from the clamped edge. Here, since a smaller force is applied on the farther antinode, TLT topology must be used. On the other hand, based on Figure 9.4(b) the relationship between the net lengths of the transverse excitation lines can be expressed as

$$L_{ex2} = L_W + L_{ex1}\,, \tag{9.6}$$

where L_W is the initial distance between the longitudinal excitation lines as shown in Figure 9.4(b). Therefore, by solving Eqs. (9.5) and (9.6) together, the calculated lengths of the excitation lines are

$$\begin{aligned} L_{ex1} &= 0.44 \times L_W \\ L_{ex2} &= 1.44 \times L_W \end{aligned}. \tag{9.7}$$

The efficiency of this approach is evaluated in the next section through the measurement.

To excite higher overtones, multiple combinations of SLT, TLT or both combined can be used. Some of the combined schemes are shown in Figure 9.5. In both TLT and SLT multiple combinations, the transverse excitation lines in the intermediate stages– but not the final stage– can assume arbitrary ratios. Nevertheless, in SLT combinations the excitation line in the final stage, i.e., the closest transverse line to the tip, is always longer than the transverse line in one stage before, while the opposite is true in TLT combinations.

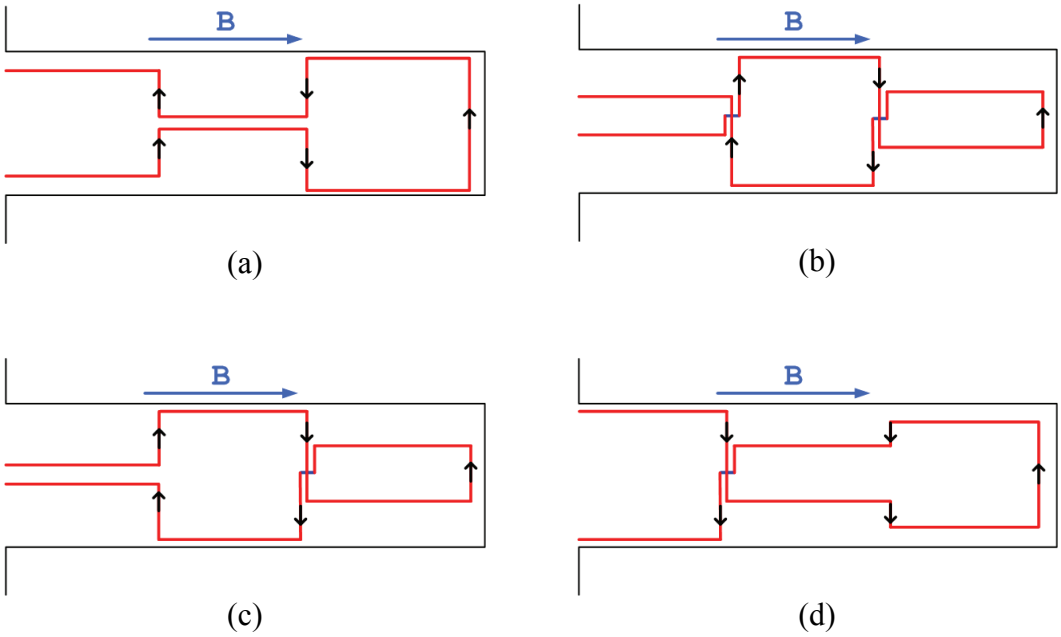

Figure 9.5. Combined schemes for anti-nodal actuation in the third flexural mode: (a) SLT-SLT combination, (b) TLT-TLT combination, (c) SLT-TLT combination, (d) TLT-SLT combination. It must be noted that in the TLT-SLT combination, unlike other combinations, the direction of current in the neighboring transverse excitation lines is not necessarily opposite. In this figure the black arrows indicate the relative direction of the current flow and the blue arrow indicates the direction of the magnetic flux *B*.

9.2 Experiments

The effectiveness of the proposed schemes has been tested using silicon cantilevers with the same length, width and thickness of 450, 130, and 7 μm, respectively, covered by a layer of PECVD oxide, approximately 0.8 μm thick. The cantilevers were fabricated according to the procedure described in Appendix A. The excitation lines have been realized with a single metal (aluminum) layer; therefore, whenever it was needed to cross two metal lines, e.g., in TLT cantilevers, the current line is tunneled through a diffused resistor in the substrate silicon. The width and thickness of the excitation lines have been 4 and 0.3 μm, respectively. The resonators were excited in the presence of static magnetic

flux densities B of 500 and 30 Gauss. All cantilevers were excited by applying a sinusoidal voltage waveform, with a peak-to-peak value of 2.1 V, to the excitation line. Depending on the resistance of the excitation line, however, the amplitude of passing current may not be the same for different devices. The cantilever vibration is detected by a piezoresistive Wheatstone bridge, which depending on the adopted scheme has been implemented either near the clamped end, or at the location of a local stress maximum (given in Table 9.2). The specifications of the Wheatstone bridge are presented in Table 9.3. Similar to the procedure described in Chapter 5, transfer functions of cantilever resonators have been captured with an Agilent Network Analyzer 4395A. All measurements were performed at 30 ± 5 ºC.

Table 9.3. Specifications of the Wheatstone bridge.

Single side resistance	≈ 800 Ω
Piezoresistor length	24 μm
Piezoresistor width	5 μm
Distance from geometrical center to the clamped edge (Regular cantilever)	20 μm

A complete summary of the characterized schemes is presented in Figure 9.6, where each design is labeled after its functionality: The first letter describes whether the design is intended for an overtone enhancement, marked with "E," or for suppression, marked with "S," whereas the label number represents the targeted flexural mode. For example E3-X is a design intended for the enchantment of the third flexural mode, while S2-Y is intended for suppression of the second flexural mode. Overall, the proposed schemes can also be characterized in three categories: 1) Schemes for optimized locations of the piezoresistive bridge; this category includes E2-A and E3-A. 2) Schemes for modified

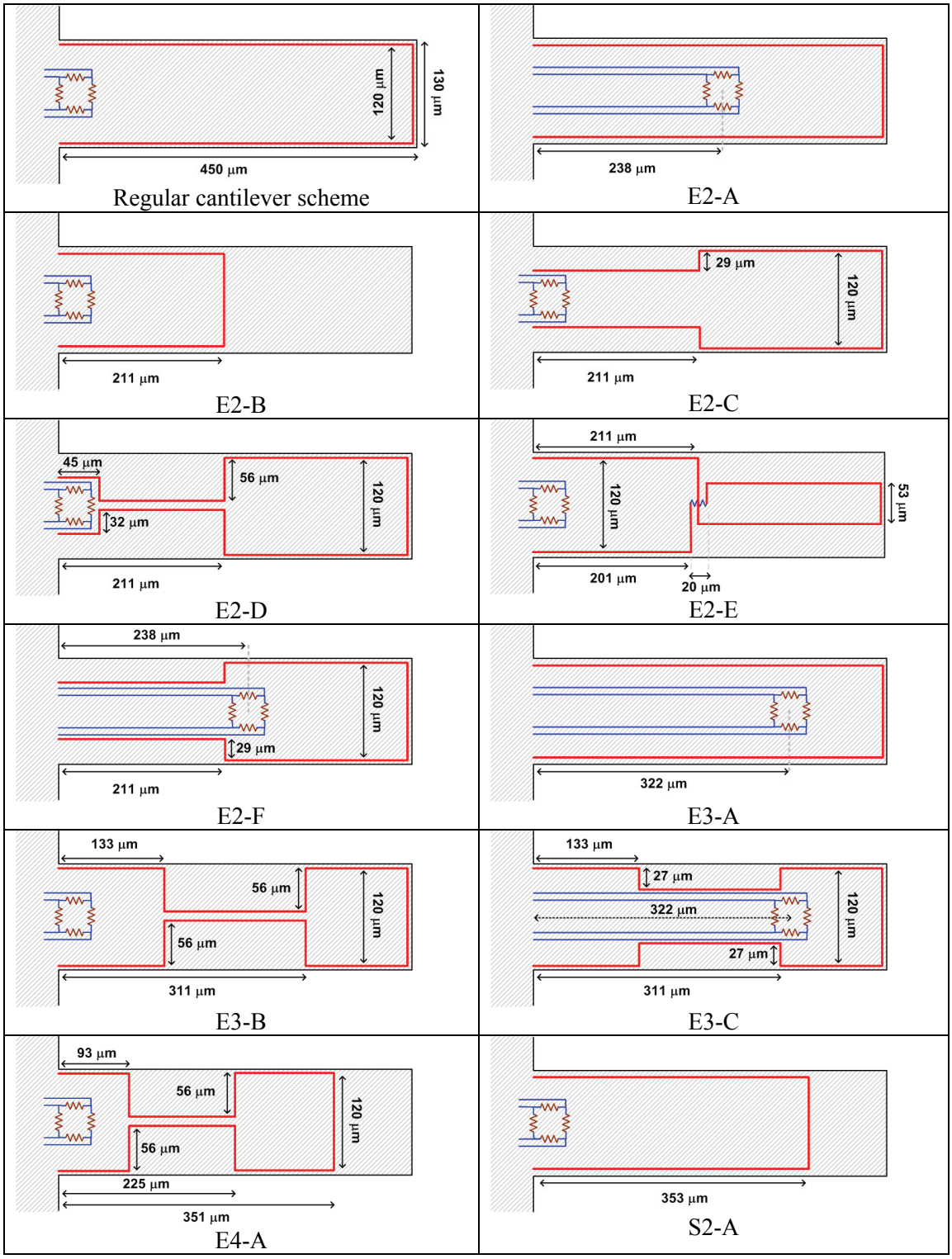

Figure 9.6. List of characterized overtone enhancement/suppression schemes.

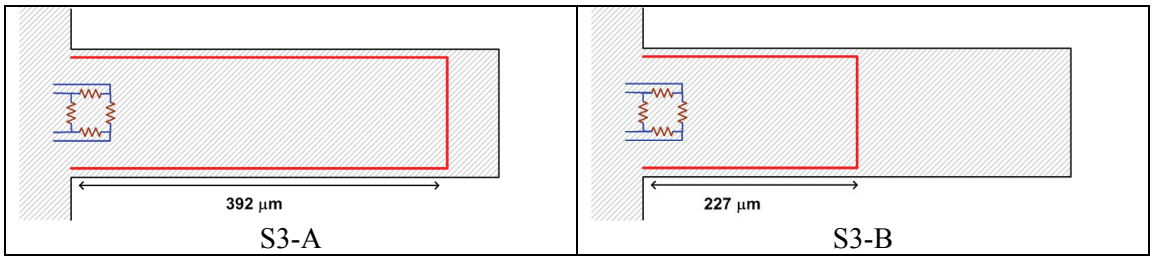

Figure 9.6. *continued.*

excitation line layouts; this category includes E2-B, E2-C, E2-D, E2-E, E3-B, E4-A, S2-A, S3-A, and S3-B. 3) Hybrid schemes, which are combinations of the previous two categories; this category includes E2-F and E3-C. As a reference for comparison, a cantilever with the same dimensions but with a regular design (labeled "Regular" in Figure 9.6) is characterized under the same conditions. Micrographs of some of the measured cantilevers are presented in Figure 9.7. The resonance frequencies and quality factors of the measured cantilevers are summarized in Table 9.4. It must be noted that by variations in patterning and positioning of the excitation line (in general, metal lines), the effective stiffness and mass of the cantilever may slightly change, resulting in small deviations in the resonance characteristics. However, this issue becomes insignificant when compared to the deviations caused by an imperfect fabrication process.

To have a fair comparison between the peak spectral magnitudes of different overtones, the effect of noise and cross-talk must be cancelled. To this end, the captured magnitude transfer characteristic at B = 30 Gauss can be considered as a measure of the power spectral density of noise and cross-talk, although even at such a small magnetic flux density still some resonance peaks are detectable. Nevertheless, here, it is possible to ignore the presence of resonance peak magnitudes at B = 30 Gauss; because if not buried

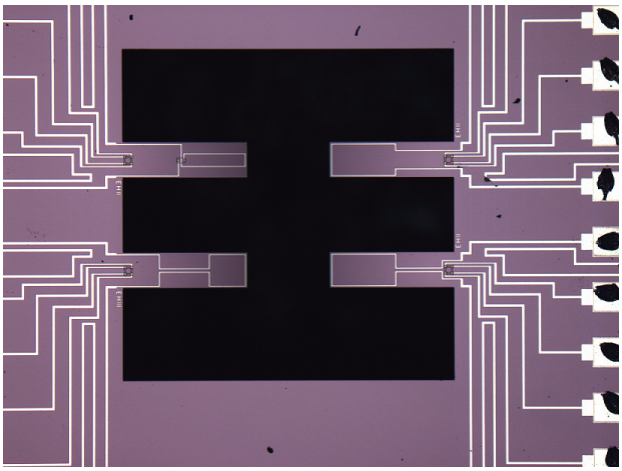

(a)

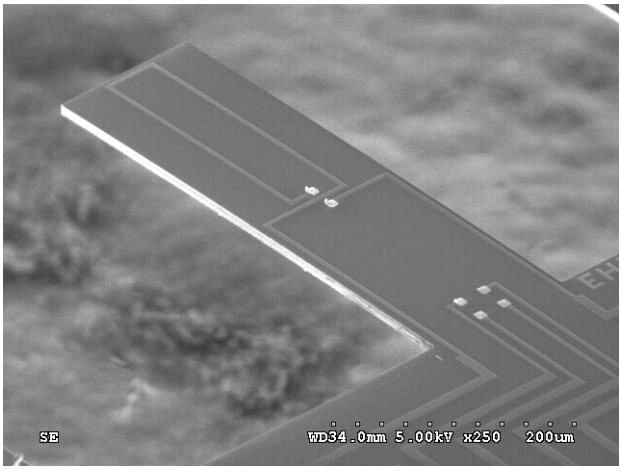

(b)

Figure 9.7. Characterized overtone-emphasized cantilevers: (a) Optical micrograph of (clockwise from top-right) E2-C, E2-D, E3-B, and E2-E; (b) Scanning electron microscopy picture of an E2-E cantilever.

under the noise power, the magnitude of these peaks will be negligible in comparison with the magnitude of resonance peaks at B = 500 Gauss. Hence, to eliminate the effect of noise and cross talk, the captured amplitude power – in linear scale – at B = 30 Gauss has been subtracted from the amplitude power at B = 500 Gauss. This procedure is illustrated in Figure 9.8, in which the effect of noise and cross-talk are removed from the magnitude spectrum of the Regular-type cantilever. The reason to choose B = 30 Gauss

as the reference, and not smaller values, is because B = 30 Gauss is approximately equal to the residual magnetic flux density of the measurement setup. Completely removing the residual flux density required a change in the setup, which would cause an alteration of the noise and cross-talk level.

Table 9.4. Resonance frequencies and Q-factors of measured cantilevers.

Type	1st flexural mode		2nd flexural mode		3rd flexural mode †		4th flexural mode ‡	
	f_1 (kHz)	Q	f_2 (kHz)	Q	f_3 (kHz)	Q	f_4 (kHz)	Q
E2-A	47.87	492	294.89	858	818.23	475	1594.20	193
E2-B	48.32	493	297.73	985	828.38	§	–	–
E2-C	48.07	507	298.11	872	833.63	320 *	–	–
E2-D	48.40	504	299.60	953	831.10	475	–	–
E2-E	48.06	531	295.56	945	822.28	450	–	–
E2-F	47.58	498	293.42	854	817.96	538	1589.80	211
E3-A	48.95	482	299.91	930	832.53	570	1621.17	221
E3-B	47.77	497	295.55	1008	821.74	501	–	–
E3-C	49.15	497	300.54	822	835.90	473	1632.30	248
E4-A	47.82	501	296.52	921	823.30	527	1601.26	149
S2-A	48.09	512	297.78	924	829.71	520	–	–
S3-A	48.66	508	302.68	949	838.45	464	–	–
S3-B	48.68	510	298.46	977	828.21	495	–	–
Regular	48.59	509	303.15	971	842.91	541	–	–

† Deteriorated Q-factor due to presence of multiple (coupled) peaks.
‡ For some devices the 4th mode signal was not detected.
§ Low signal to noise ratio.
* Presence of coupled peaks.

9.3 Results and Discussion

A comparison of the overtone enhancement devices is presented in Figure 9.9, in which the resonance peak magnitude in each flexural mode is normalized to the peak magnitude of fundamental mode for the same device. As observed in Figure 9.9, for the second flexural mode, the design based on a TLT excitation line, i.e., E2-E, has a significantly better selectivity. This result also indicates that the preceding theoretical calculation, presented in Chapter 6, is valid. The other schemes that show a good selectivity for the

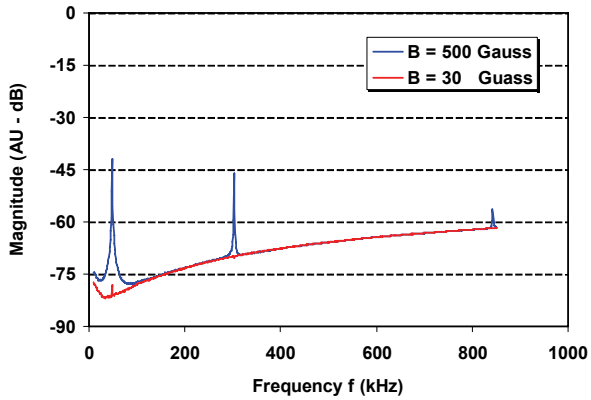

(a)

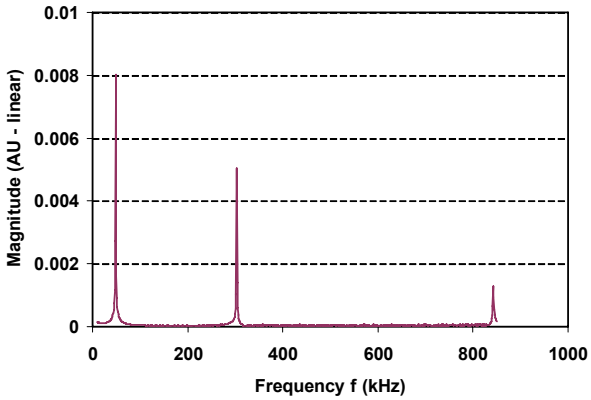

(b)

Figure 9.8. Elimination of noise and cross-talk: (a) captured frequency transfer characteristics of a Regular-type cantilever excited using a static flux density of 500 Gauss (blue) and 30 Gauss (red); (b) corrected transfer characteristic after eliminating the noise and cross talk powers.

second flexural mode are E2-F, E3-A, and E3-C. Contrary to the expectation, E2-A, i.e., the design with an enhanced location of the Wheatstone bridge for the second overtone, shows a poor selectivity between the first and second modes, while the location of the bridge on E3-A seems to undergo a considerable stress not only in the intended third mode, but also in all 3 other measured flexural modes.

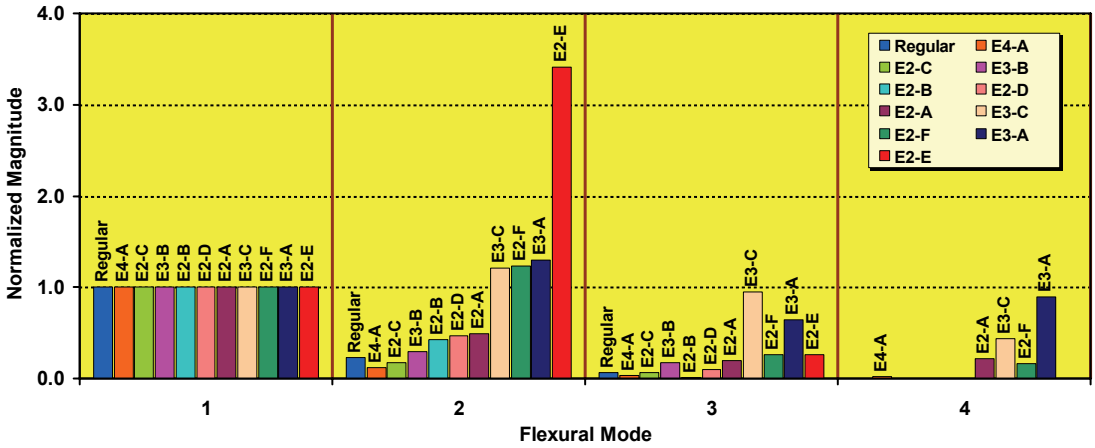

Figure 9.9. Normalized vibration amplitude in overtone enhancement cantilevers. The vibration magnitude of overtones for each device is normalized to the vibration amplitude of the fundamental resonance mode of the same device.

As shown in Figure 9.9, the best selectivity in the third flexural mode belongs to E3-C, i.e., the hybrid scheme for the third mode enhancement; however, for all schemes intended for the third mode enhancement, the peak magnitudes in the third mode are smaller than in the second mode. This observation implies that to have a good selectivity for the third mode, a more effective scheme must be applied, e.g., a scheme based on a TLT excitation line. This conclusion is emphasized by the fact that the least effective design for the third mode enhancement, i.e., E3-B, is based on an SLT-SLT excitation line. The same explanation can be offered for the poor performance of E4-A in the 4th flexural mode. E4-A is designed to enhance the selectivity to the 4th mode peak magnitude based on a multiple SLT excitation line. This device, unlike the characterized regular cantilever, can detect the 4th mode signal; however, using E4-A, the measured magnitude for the 4th overtone is smaller than the magnitudes of the three preceding flexural modes.

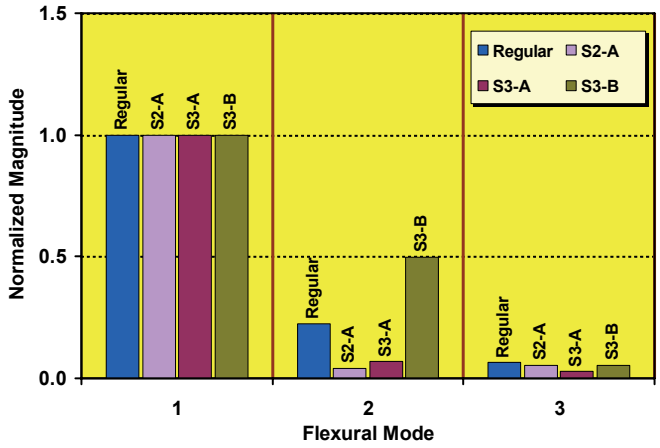

Figure 9.10. Normalized vibration amplitude in overtone suppression cantilevers. The vibration magnitude of overtones for each device is normalized to the vibration amplitude of the fundamental resonance mode of the same device.

Figure 9.10 presents a comparison of the overtone suppression devices, in which, similar to the previous figure, the resonance peak magnitude in each flexural mode is normalized to the peak magnitude of fundamental mode for the same device. In the second mode, as observed in Figure 9.10, S2-A (i.e., the design for the second mode suppression) has an acceptable performance in the targeted overtone. In the third mode, S3-A (i.e., the design with a suppression scheme based on forcing vibrations at the node that is closer to the tip) reduces the peak magnitude to less than half of the corresponding peak magnitude in the regular cantilever, while S3-B (i.e., the design with a suppression scheme based on forcing vibrations at the node that is closer to the clamped edge) has hardly reduced the peak magnitude of the third mode. It is worth noting that S3-B and E2-A have very similar designs, hence, they exhibit almost the same performance in the second flexural mode.

The absolute peak magnitude in each device depends not only on the flux density and excitation current, but also on parameters such as the quality of the implemented

piezoresistors and the perfectness of the Wheatstone bridge. In other words, comparing the absolute magnitudes among different designs is a subjective issue. Nevertheless, by normalizing the captured peak magnitudes – in linear scale – to the amplitude of the excitation current, different designs can be roughly compared. Such normalization is essential for comparing the performance of devices with highly resistive excitation line, e.g., E2-E. The typical resistance of the excitation lines in the characterized devices is measured to be in the range of 40 to 60 Ω. However, in E2-E, to resolve the metal line crossing, a part of the excitation line is tunneled via a diffused resistor in the substrate silicon, which has increased the resistance of the excitation line up to 770 Ω. Figure 9.11 compares the peak magnitudes of the measured devices, which are normalized not only to the excitation current of the same device, but also to the peak magnitude of the corresponding flexural mode in the regular cantilever. The data presented in Figure 9.11 is useful in comparing the absolute advantage of each design; for example, in the second

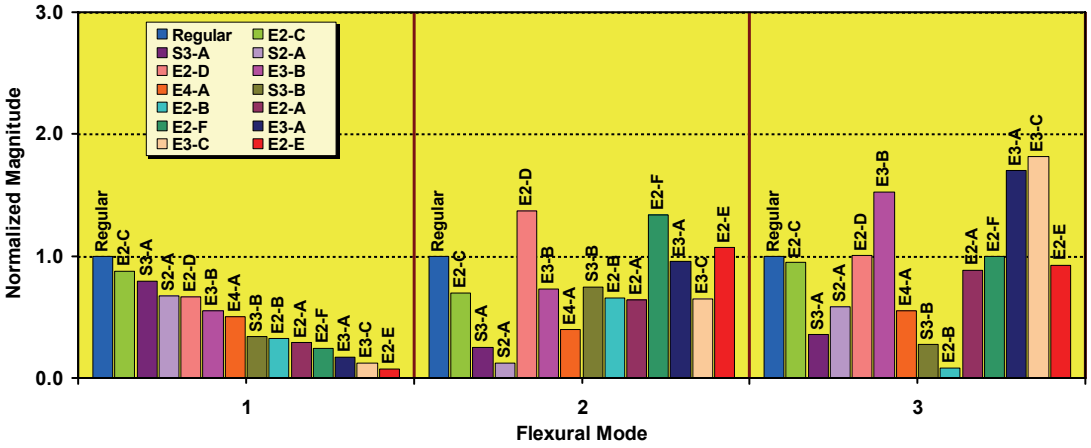

Figure 9.11. Normalized vibration amplitude in overtone-emphasized cantilevers. The vibration magnitude of overtones for each device is normalized to both a) the excitation current of the same cantilever and b) the vibration amplitude of the regular cantilever in the same overtone.

mode, E2-D, E2-E, E2-F, and S3-B exhibit absolute peak magnitudes higher than the regular cantilever, while in the third mode, for all cantilevers that are designed to enhance this mode, the resonance peak magnitudes are larger than the peak magnitude in the regular cantilever, as intended.

***

The focus of this chapter was on modifying the excitation and detection schemes on a regular rectangular cantilever to make it more (or less) sensitive to desired flexural modes; in other words, utilizing the cantilever resonator as an overtone filter. This study is aimed at applications such as the temperature compensation presented in Chapter 8, or closed-loop resonance of cantilevers in higher flexural modes. The chapter objective is achieved by optimizing the location of piezoresistive Wheatstone bridge, by modification of the excitation line pattern, or by a combination of both approaches. The presented measurement results indicate that a design with an excitation line based on the twisted loop topology has the best tuning selectivity in the second flexural mode, while the results from hybrid approaches in all investigated overtones were promising too.

CHAPTER 10

Q-FACTOR OF UNCONVENTIONAL RECTANGULAR CANTILEVERS

In Chapters 5 and 7 the dependence of the Q-factor on the cantilever geometry has been investigated. The proposed models and the performed measurements in these chapters, however, were in respect to rectangular cantilevers with a basic geometry. The focus of this chapter is again on rectangular cantilevers, but with some level of added structural complexity either by perforating the cantilever surface or forming a trench at the clamped end. The latter case is in fact a follow up to the study of resonance characteristics of stress concentrating cantilevers (SC cantilevers), which was presented in Chapter 3.

10.1 Quality Factor of Perforated Cantilevers

The effect of holes on the cantilever surface is studied among 10 different perforated cantilever designs, which are categorized in five classes each having single or double holes perforation. A complete list of the characterized cantilevers is presented in Figure 10.1. The cantilevers are 450 μm long, 130 μm wide and 11 μm thick. Each opening is 40×40 μm^2. The cantilevers are actuated and characterized with a similar procedure that has been used for regular shape cantilevers in Chapter 5, with the output signal being measured over a Wheatstone bridge at the clamped end of the cantilever. Figure 10.2 presents micrographs of some of the tested cantilevers.

In the first studied category of the perforated cantilevers, i.e., Class A, single or double hole openings are centered at 420 μm from the clamped end. This way the holes are as

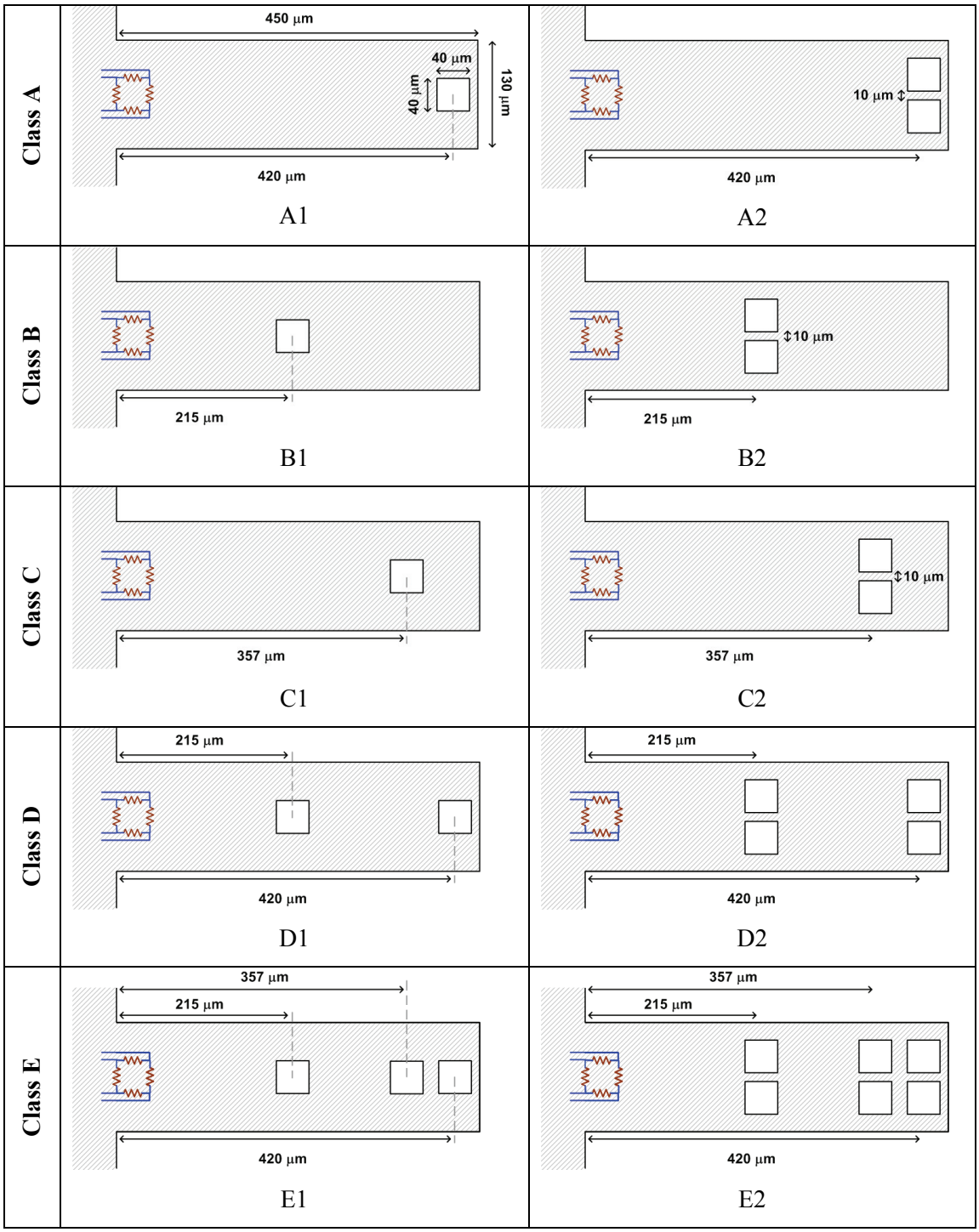

Figure 10.1.Complete list of characterized perforated cantilevers.

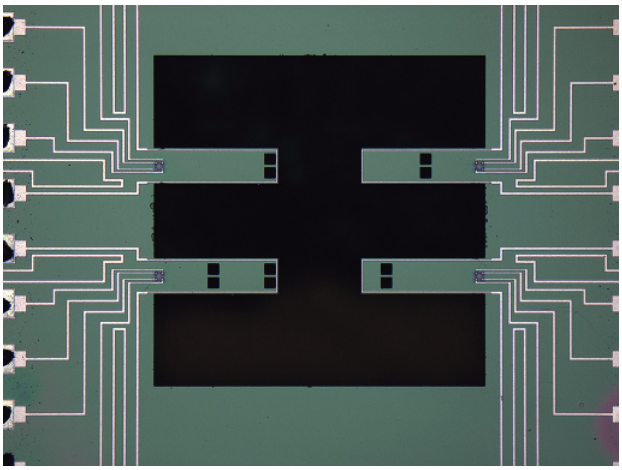

(a)

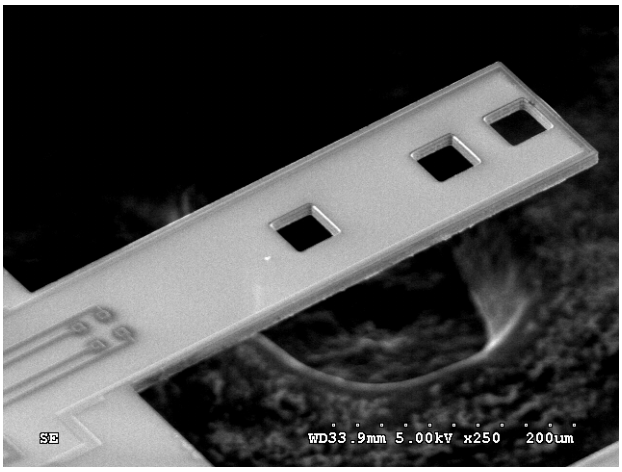

(b)

Figure 10.2. Characterized perforated cantilevers: (a) Optical micrograph of (clockwise from top-right) B2, C2, D2, and A2; (b) SEM picture of an E1 cantilever.

close as possible to the tip, hence, the vibration amplitude at the perforation site and thus the effective removed mass are largest in the fundamental flexural mode (see Figure 10.1(a) and (b)).

In Class B, single or double openings are formed at 215 μm from the clamped end (see Figure 10.1(c) and (d)): in this location, according to the results of finite element

simulation (COMSOL), shown in Figure 10.3, the perforated cantilevers exhibit an antinode (i.e., local deflection maximum) in the second flexural mode. It must be noted that because of perforation, the flexural mode shape of the cantilever is not necessarily the same as the theoretical prediction presented by Eq. (2.26); instead the location of the antinode depends on the size and placement of the holes and may be determined by simulation.

In Class C, single or double openings are formed at 357 μm from the clamped end, centered at the node location of the second flexural mode (see Figure 10.1(e) and (f)).

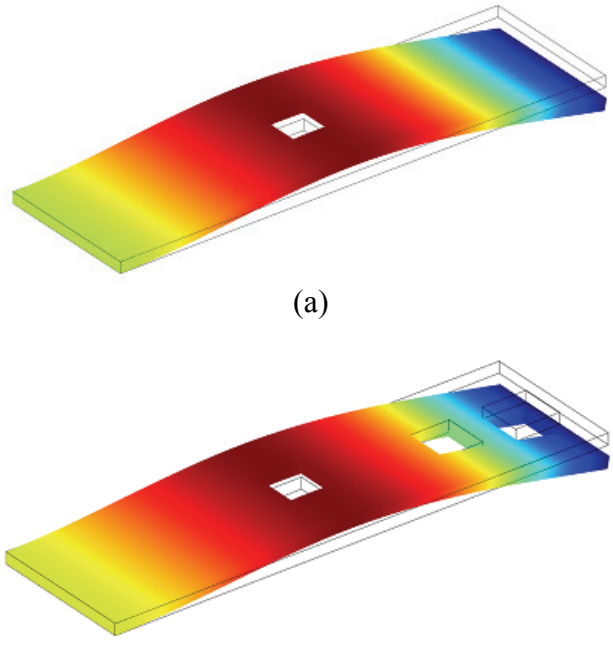

(a)

(b)

Figure 10.3. Finite element simulation results for perforated cantilevers resonating in the second flexural mode: (a) single hole Class B cantilever, in which the location of the hole coincides with the local deflection maximum (dark red region); (b) single hole Class E cantilever with the first hole on the local deflection maximum (dark region), the second hole at zero deflection region (yellow region), and a hole at the proximity of the tip.

Class D, the forth studied category, is a combination of the first two classes (see Figure 10.1(g) and (h)), while Class E is a combination of all pervious classes (see Figure 10.1(i) and (j)).

Table 10.1. Measured resonance frequency f and Q-factor of perforated and solid cantilevers in the first three flexural modes.

Cantilever type	1st flexural mode		2nd flexural mode		3rd flexural mode	
	f_1 (kHz)	Q	f_2 (kHz)	Q	f_3 (kHz)	Q
A1	75.89	742	467.5	360	1287	273
B1	71.63	752	441.4	464	1259	323
C1	74.98	709	444.4	516	1210	348
D1	75.21	669	450.9	594	1270	327
E1	78.03	621	454.1	854	1256	314
A2	78.68	685	481.8	616	1302	249
B2	68.70	811	412.2	990	1243	302
C2	76.21	679	431.8	811	‡	‡
D2	77.55	626	433.5	677	1262	322
E2	81.55	542	422.3	877	1158	316
Solid*	69.32	824	439.8	600	1234	320
Solid**	70.76	801	437.0	982	1218	584

* Solid cantilever's dimensions are the same as perforated cantilevers, i.e., L = 450 μm, H = 11 μm, W = 130 μm.
** Solid cantilever's dimensions are the same as perforated cantilevers with the exception of width: W = 82 μm.
‡ No detectable signal was measured for this particular device.

In Table 10.1 the measurement results for all studied perforated cantilevers resonating in the first three flexural modes are summarized and compared to solid cantilevers with the same length and thickness but widths of 130 and 82 μm. As expressed by Eqs. (2.6) and (7.13), the Q-factor of the n^{th} flexural mode is proportional to the effective mass m^*, the resonance frequency and the effective damping B^*:

$$Q = \frac{m^* \omega_n}{B^*}. \qquad (10.1)$$

On the other hand, the resonance frequency of the n^{th} flexural mode is proportional to the effective spring constant k^* and the effective mass m^* in that overtone:

$$\omega_n = 2\pi f_n = \sqrt{\frac{k^*}{m^*}} . \qquad (10.2)$$

Forming a hole in the cantilever, especially at locations where the cantilever has larger vibration amplitudes, results in a decrease in the effective mass, thus an increase in the resonance frequency is expected. Using Eq. (8.23), the effect of holes can be roughly approximated by the effect of an added negative mass, equal to the etched mass, distributed over the same locations on the solid (imperforated) cantilever where the holes are formed. This approximation is valid as long as the change in the stiffness of cantilever is negligible; in other words, as long as the flexural mode shapes of the perforated cantilever are approximately the same as those of a simple cantilever. However, for the studied cantilever designs (see Figure 10.1) such an assumption is hardly satisfied: Based on the measurement results, in most of the investigated arrangements the reduction in the potential energy of the system (i.e., the reduction in the effective spring constant) has cancelled the reduced mass effect in such a way that the resonance frequency is more and less equal to that of a solid cantilever.

As presented in Table 10.1, for all three flexural modes, the maximum increase of resonance frequency is observed for Class E, regardless of having single or double holes. However, because of the significant reduction of the effective mass, Class E cantilevers also exhibit the lowest Q-factors. Reviewing Table 10.1 reveals that in the fundamental flexural mode, all the proposed perforation arrangements, with an exception of type B2, result in reduced Q-factors compared to the solid cantilevers. In the second overtone, the

cantilevers with a single hole perforation, excluding type E1, exhibit Q-factors smaller than the Q-factor of the similar solid cantilever (i.e., the one with W = 130 μm). On the other hand, the Q-factors of cantilevers with double holes are generally larger than the Q-factor of the similar solid cantilever, to such an extent that they can be even compared to the Q-factor of the narrower solid cantilever (W = 82 μm) – here, it must be noted that in the second flexural mode, as mentioned in Chapter 7 (e.g., see Figure 7.5), the Q-factors of the presented solid cantilevers are inversely proportional to the cantilever width. Finally, in the third overtone, the Q-factor of the perforated cantilevers is almost the same as the similar solid cantilever, except for Class A cantilevers which exhibit smaller Q-factors.

Based on the data presented in Table 10.1, the type B2 cantilever deserves special recognition: In the fundamental mode, the type B2 cantilever resonates at slightly smaller resonance frequencies than the solid cantilevers, while both cantilever types have approximately equal Q-factors. Since the effective mass of the type B2 cantilever is smaller than that of the similar solid cantilever, the equivalence of the Q-factors and resonance frequencies implies via Eq. (10.1) that the effective damping of the perforated cantilever system is smaller than the effective damping of the solid cantilever system. The main advantage of the type B2 cantilever, however, appears in the second overtone, where at the price of only about 6% reduction in the resonance frequency, the Q-factor of the perforated cantilever is 65% larger than the Q-factor of the similar solid cantilever (W = 130 μm).

10.2 Quality Factor of SC Cantilevers

In Chapter 3 the fundamental flexural resonance characteristics of two SC cantilevers were compared with the resonance characteristics of a corresponding solid cantilever. Both types of cantilevers had the same length, width and thickness of 450, 82 and 12 μm, while the SC beam lengths were 3 and 9 μm and had a sidewall thickness of 1.0 μm. The average notch depth in the SC cantilevers was 6 μm and it was located 8.5 μm from the cantilever clamped edge. The total number of SC beams on each SC cantilever was 23. The presented measurement results indicated that the resonance frequencies of both types of cantilevers are approximately equal, and the difference in their Q-factors is less than 6%. In this chapter, again, the resonance characteristics of SC cantilevers with the same specifications are compared with the corresponding solid cantilevers with respect to the cantilever length and flexural overtone. To this end, the measurements are performed using the same setup as mentioned in Chapter 5.

The variation of the Q-factor with the length of both SC and solid cantilevers for the fundamental flexural resonance mode is shown in Figure 10.4. The specifications of the cantilevers are as mentioned before, except that in most cases the SC beam length is L_b = 6 μm, whereas for cantilevers with lengths of 175, 450, 750 and 1050 μm the results of SC cantilevers with SC beam lengths of 3 and 9 μm are included as well (although not differentiated on the graph). As observed in Figure 10.4, the Q-factors of both cantilever types closely follow each other, although the Q-factors of solid cantilevers for most lengths are larger. In two special cases, namely the solid cantilevers with lengths of 100 and 175 μm, coupling of resonance modes is observed around the fundamental flexural

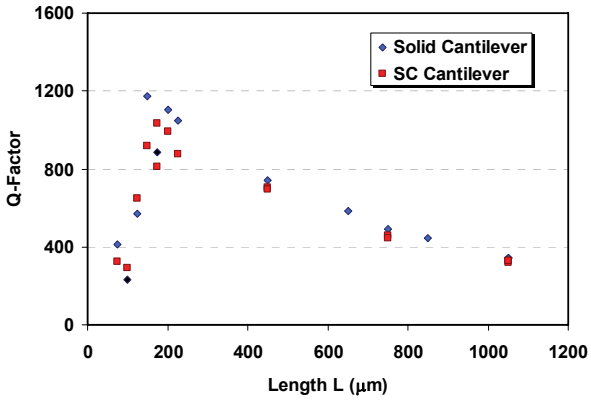

Figure 10.4. Measured Q-factor as a function of length for stress concentrating cantilevers (rectangles) and solid cantilevers (diamonds) which resonate in the fundamental flexural mode. The cantilevers width and thickness are 82 and 12 μm, respectively.

resonance frequency, therefore, the Q-factors are reduced. For the same lengths, the Q-factors of SC cantilevers with L_b = 6 μm are reduced as well, yet they stay larger than the Q-factors of similar solid cantilevers. However, no significant coupling is observed for the SC cantilever with the length of 175 μm and L_b = 9 μm. In other words, forming a notch on the clamped end can cause the coupled resonance modes to separate.

In Figure 10.5 the Q-factors of SC and solid cantilevers are plotted versus the resonance frequency of the first 7 flexural modes. The cantilever specifications are the same as before, except that all have a length of 1050 μm. The only difference among the represented SC cantilevers is in the length of SC beams L_b, which is equal to 3, 6, or 9 μm. For the SC cantilever with L_b = 9 μm, no meaningful data have been obtained beyond the 5th flexural mode. The same happens after the 6th flexural mode for the SC cantilever with L_b = 6 μm, while the SC cantilever with L_b = 3 μm has provided data up

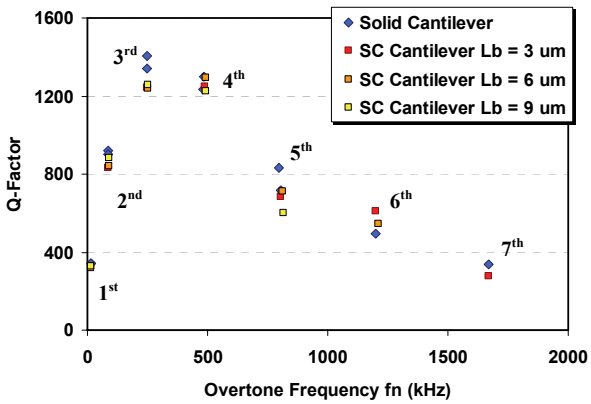

Figure 10.5. Measured Q-factor as a function of flexural resonance frequency (7 modes) for stress concentrating cantilevers (rectangles) and solid cantilevers (diamonds). The cantilevers length, width and thickness are 1050, 82 and 12 μm, respectively. The lengths of stress concentrating beams in the SC cantilevers are 3, 6, and 9 μm.

to the 7th overtone. This observation supports the earlier finding that the force sensitivity of SC cantilevers decreases with increasing L_b, as discussed in Chapter 3. On the other hand, since the implemented Wheatstone bridge in the solid cantilever is balanced, unlike in the SC cantilevers, this cantilever has been able to provide meaningful data even up to the 7th overtone. Regardless of this issue, the Q-factors of both cantilever types follow each other very closely; hence, adopting the aforementioned SC cantilever schemes (with an average notch depth equal to half of the cantilever thickness) will not noticeably change the damping mechanisms in the cantilevers. This observation can be explained by the fact that the difference in the effective masses of solid and SC cantilevers is virtually nothing: because the location of the notch in the adopted schemes (i.e., the proximity of the clamped edge) experiences insignificant vibration amplitudes in the flexural mode shapes; therefore, given the fact that both SC and solid cantilevers resonate at almost

equal frequencies, the removed mass at the trenches results in a negligible change in the kinetic energy of the systems, thus the effective masses of both cantilever types are equal.

***

It can be concluded from the measurement results presented in this chapter that the effort in improving the Q-factor of simple rectangular cantilevers by introducing holes has been successful only for the second flexural resonance mode and mainly for the cantilevers perforated with double holes at the center (i.e., at the antinode location). In general, it seems that in the second flexural mode the Q-factor of the cantilever improves by moving the double-hole perforation from the tip toward the middle of the cantilever. On the other hand, the experimental results presented in this chapter indicate that the SC and solid cantilevers exhibit almost equal Q-factors, regardless of the cantilever geometrical dimensions or flexural resonance overtone.

CHAPTER 11

CONCLUSION AND FUTURE TREND

The objectives of this thesis has been to optimize cantilevers in the static sensing mode, specifically to enhance the force sensitivity of piezoresistive cantilevers, as well as in the dynamic mode, with improving the performance of resonant cantilever mass sensors as a prime target.

In the first part of this thesis, i.e., the static optimization part, a new technique in utilizing the stress concentration in piezoresistive cantilever force sensors is introduced and verified through simulation and experiment. Introducing a new fabrication process module, embedded stress concentrating (SC) silicon wires and beams are implemented in cantilevers. By using these elements as piezoresistors and concentrating stress through them, the force sensitivity of the cantilever is increased without noticeably sacrificing the cantilever stiffness, resonance frequency, and quality factor. The experiment data confirm the performed finite element simulation results, indicating that in an SC cantilever the force sensitivity not only follows the same relationship with geometrical dimensions as in a solid (conventional) cantilever, but also the sensitivity increases by decreasing the thickness of stress concentrating elements. This advantage comes at the expense of a small decrease in the spring constant in comparison to solid cantilevers with the same dimensions. As an example, the measurement results of SC cantilevers with embedded stress concentrating wires show an up to 8.0 times increase in force sensitivity at the price of only a 15% reduction in stiffness. Nevertheless, in designing SC cantilevers, special

attention must be paid to the noise characteristic of the device. While the thermomechanical noise of both solid and SC cantilever types are very similar, to reduce the Johnson noise in SC cantilevers it is required to use less resistive stress concentrating elements, e.g., shorter SC elements.

As a future trend, the stress concentrating elements in SC beams can be further scaled down by utilizing either bottom-up approaches (e.g., nanotubes fabrication) or top-down approaches (e.g., nanolithography). This way, not only the width and thickness of the SC beams can be decreased, but also they can be fabricated in shorter length; hence, both sensitivity and resolution can be increased.

The focus of the second part of this thesis has been on optimization of resonant cantilevers, which potentially can be used in mass detection applications such as chemical and biological sensors. The objectives of this optimization include increasing the quality factor of the resonator as well as cancellation of the effect of environmental parameters on the frequency detection in resonant mass sensors. Although the presented results were obtained for magnetically excited piezoresistive cantilevers, these results can be generalized to any type of cantilever sensors.

For the flexural resonance of cantilevers, by combining analytical derivations and experimental results, two models are developed to estimate the optimum dimensions of resonant rectangular cantilever beams for achieving maximum quality factor in air. For silicon cantilevers with thicknesses between 5 to 17 μm, it has been calculated that the

reciprocal of the Q-factor is linearly proportional to $\chi = L/H^{1.5}$ if this ratio is larger than 15 $\mu m^{-0.5}$. This behavior is the result of the dominance of air damping for cantilevers with such length to thickness ratios; however, a close examination of the measured quality factors of these cantilevers shows that the air damping seems to be proportional to an empirical ratio of $L/H^{1.25}$ rather than $L/H^{1.5}$. Also, it has been shown that the effect of cantilever width may be neglected for cantilevers with large ratios of $L/H^{1.5}$. In contrast, with the support loss being a significant contributor to the damping, in short cantilevers (i.e., $\chi < 15\ \mu m^{-0.5}$), the Q-factor becomes a strong function of the cantilever width. Also, it was observed that the equation expressing support loss must be adjusted to include the effect of imperfectness on the cantilever clamped boundary. Combining the empirically corrected equations of air damping and support loss with the well-known Zener approximation for TED has made it possible to calculate the optimum lengths of resonant cantilevers for a given thickness to achieve the maximum quality factor for the fundamental flexural resonance mode in air.

In this thesis, the cantilever flexural resonance in any overtone is modeled with a set of coupled lumped mass resonators. Based on this model, the effective damping coefficients in the flexural modes of interest are calculated. The measurement results show that in higher flexural modes, similar to the fundamental mode, the dependence of the Q-factor on the cantilever geometry can be described by $\chi = L/H^{1.5}$; however, the critical transition region, where the dominant damping mechanisms have equal influence, occurs for a larger χ in a higher overtone. In other words, the Q-factors of cantilevers, which have the air damping as the dominant loss mechanism in the fundamental flexural mode, initially

increases in the second or third flexural modes (i.e., lower overtones), but eventually drops in higher overtones. An interesting observation is that for all the measured cantilevers, the maximum Q-factors are found in a small frequency span of 200 to 400 kHz, regardless of the overtone number. This observation indicates that, at least for the first three flexural modes of the investigated resonant cantilevers, the maximum achievable Q-factor is bound to an upper limit in frequency (i.e., $f < 400$ kHz).

From the measurement results it is observed that a temperature variation not only can influence the Q-factor, but also introduces a shift in the resonance frequency. In this thesis, a novel technique is introduced to cancel the effect of environmental parameters (e.g., temperature and relative humidity) on the resonance frequency of resonant mass sensors (e.g., resonant cantilevers). After applying this technique in a resonant cantilever, the undesired resonance frequency shifts caused by environmental parameters, namely temperature and humidity, are suppressed by up to 2 orders of magnitude. To detect a change in mass and meanwhile cancel the effect of environmental parameters, the presented technique needs only 4 frequency measurements; i.e., measuring the frequency of a pair of resonance overtones and comparing them with another pair measured before the potential variation in the mass. Hence, utilizing a single sensor, this technique eliminates any need for look-up tables, or the need for numerically adjusting the measurement results. The requirement for applying the presented technique are 1) the mass change must affect the examined overtone frequencies with different ratios, and 2) the mass change must not change the potential energy of the resonant system, i.e., it must have a minimal effect on the resonator stiffness. To fulfill the former requirement, the

surface of the resonant mass sensor, e.g., a mass-sensitive (bio-) chemical sensor, must be partially covered with the sensing layer. To address the latter requirement, either the sorption (binding) induced changes in the modulus of elasticity of the sensing layer must be negligible, or the sensing layer must be deposited on a portion of the resonator that has minimal contribution to the potential (strain) energy of the resonator.

To selectively tune to a desired overtone, e.g., for the presented temperature cancellation technique or for closed-loop oscillation in higher flexural modes, the piezoresistive cantilever is modified as an overtone filter. To this end, the magnetic excitation and piezoresistive detection schemes on a regular rectangular cantilever are modified to make the cantilever more (or less) sensitive to desired flexural modes. This objective is achieved by optimizing the location of the piezoresistive Wheatstone bridge, by modification of the excitation line pattern, or by a combination of both approaches. The presented measurement results indicate that a design with an excitation line based on the twisted loop topology has the best tuning selectivity in the second flexural mode, while the results from hybrid approaches in all investigated overtones were promising too.

APPENDIX A

PROCESS FLOW FOR CANTILEVER FABRICATION

Table A.1. Complete process flow for fabrication of piezoresistive silicon cantilevers.

Step	Description	Process Details
1	Thermal oxidation	Equipment: Tystar Furnace Temperature: 1050 ˚C (wet oxidation) Duration: 185 min Measured thickness: ~ 8600 Å
2	Lithography (defining doping area)	Photoresist: SC1813 Spin: 4000, 1000, 40 [rpm, rpm/sec, sec] Soft-bake (SB): 3 min at 100 ˚C on hotplate (HP) Exposure: λ = 405 nm, UV density = 172 mJ/cm^2 Developer: MF-319 Hard-bake (HB): 10 min at 110 ˚C – HP
3	Silicon oxide etch (defining doping area)	Equipment: Plasma Therm ICP with C_4F_6 Plasma Note: the entire thickness of the oxide layer (~ 8600 Å) in the opening must be etched.
4	Cleaning	Rinse the sample in acetone, methanol, and DI water. Use oxygen plasma to remove the remaining residues.
5	CMOS grade cleaning	Piranha solution: 10 min Rinse with DI water RCA clean: 10 min Rinse with DI water BOE dip: 15 sec Rinse and dry
6	Diffusion doping	Equipment: Tystar Furnace Solid boron source Temperature: 950 ˚C Duration: 60 min
7	Backside oxide protection	On the backside of the wafer: Photoresist: SC1827 Spin: 4000, 1000, 40 [rpm, rpm/sec, sec] SB: 3 min at 100 ˚C – HP No exposure HB: 10 min at 110 ˚C – HP
8	Boron oxide removal	BOE immersion: 20 min
9	CMOS grade cleaning	Same as step #5
10	Thermal oxidation (diffusion drive-in)	Equipment: Tystar Furnace Temperature: 950 ˚C (wet oxidation) Duration: 240 min Measured thickness: ~ 5650 Å
11	Rinse and dry	Rinse the sample with DI water and dry it by blowing nitrogen.

Table A.1. *Continued*.

Step	Description	Process Details
12	Isolation layer	Isolation layer : PECVD silicon oxide Equipment: Unaxis PECVD Deposited SiO_2 thickness: 2500 Å
13	Lithography (contact opening)	Photoresist: SC1827 Spin: 2 steps 1) 500, 100, 10 [rpm, rpm/sec, sec] 2) 4000, 1000, 40 [rpm, rpm/sec, sec] SB: 3 min at 100 ˚C – HP Exposure: λ = 405 nm, UV density = 374 mJ/cm^2 Developer: MF-319 HB: 10 min at 110 ˚C – HP
14	Silicon oxide etch (contact opening)	Equipment: Plasma Therm ICP with C_4F_6 Plasma Note: the entire thickness of the oxide layer (2500 Å) in the opening must be etched.
15	Cleaning	Same as step #4
16	Lithography (lift-off for contact metal)	Photoresist: SPR-220 7.0 Spin: 2 steps 1) 500, 100, 10 [rpm, rpm/sec, sec] 2) 4000, 1000, 33 [rpm, rpm/sec, sec] SB: 3 min at 110 ˚C – HP Exposure: λ = 405 nm, UV density = 365 mJ/cm^2 Developer: MF-319 No hard-bake
17	Aluminum deposition (lift-off for contact metal)	Equipment: Electron beam evaporator Deposition pressure: 1.3e-6 Aluminum thickness: 667 Å
18	Lift-off	The sample must be immersed in acetone for 45 min, until the aluminum layer completely get separated from the substrate. Next, sample needs to be rinsed with methanol and DI water and dried with nitrogen blow.
19	Sintering	Equipment: Lindberg furnace Forming gas: 98% N_2, 2% H_2 Temperature: 450 ˚C Duration: 65 min
20	Rinse and dry	Rinse the sample with DI water and dry it by blowing nitrogen.
21	Cavity filling (for SC cantilevers only)	Photoresist: SC1813 Spin: 2 steps 1) 500, 100, 10 [rpm, rpm/sec, sec] 2) 2500, 1000, 40 [rpm, rpm/sec, sec] SB: 3 min at 100 ˚C – HP Exposure: flood exposure λ = 405 nm, UV density = 108 mJ/cm^2 Developer: MF-319 for 45 sec (until the sample surface becomes clean) No hard-bake

Table A.1. *Continued*.

Step	Description	Process Details
22	Descum	Equipment: Plasma Therm RIE with oxygen plasma Duration : 40 sec
23	Metal line deposition	Equipment: Electron beam evaporator Deposition pressure: 1.5e-6 Aluminum thickness: 3000 Å
24	Lithography (metal line)	Same as step #2
25	Metal line patterning	Wet etchant: Al etch type A Temperature: 50 ˚C
26	Cleaning	Same as step #4
27	Passivation layer	Isolation layer : PECVD silicon oxide Equipment: Unaxis PECVD Deposited SiO_2 thickness: 4500 Å (for SC cantilevers: 2500 Å)
28	Backside mask deposition	On the back surface, in addition to the existing thermal SiO_2 layer: 1) PECVD silicon oxide Equipment: Unaxis PECVD Deposited SiO_2 thickness: 8400 Å The sample should be rinsed in DI water and dried. 2) PECVD silicon nitride Deposited SiN_x thickness: ~1.00 μm Note: it is better to partially pattern the sample between the two steps.
29	Lithography (Backside mask)	Photoresist: SPR-220 7.0 Spin: 2 steps 1) 500, 100, 10 [rpm, rpm/sec, sec] 2) 4000, 1000, 40 [rpm, rpm/sec, sec] SB: 3 min at 110 ˚C – HP Exposure: λ = 365 nm, UV density = 400 mJ/cm^2 Developer: MF-319 HB: 20 min at 120 ˚C – HP
30	Backside mask patterning	1) For etching SiN_x: Equipment: Plasma Therm RIE with SF_6 plasma Duration: ~ 25 min (until SiN_x layer is completely gone) 2) For etching SiO_2: Equipment: Plasma Therm ICP with C_4F_6 plasma Duration: ~ 15 min (until SiO_2 layer is completely gone)
31	Lithography (via)	Same as step #13
32	Silicon oxide etch (via opening)	Equipment: Plasma Therm RIE with CF_4 plasma (Until SiO_2 layer is completely etched in the openings)
33	KOH etch	KOH solution: 6 molar Temperature: 75 ˚C Electrochemical etch stop reverse bias: 1.500 V Duration: ~ 10 hours Note: only the back surface is exposed to the solution.

Table A.1. *Continued*.

Step	Description	Process Details
34	Rinse and dry	Thoroughly rinse the sample with DI water and dry it by blowing nitrogen.
35	Cleaning	Same as step #4
36	Lithography (cantilever release)	First, attach the sample to a carrier wafer using cool grease. Cool grease should not be applied under the etched cavities, but only at the edge of wafer. Photoresist: SPR-220 7.0 Spin: 2 steps 1) 500, 100, 10 [rpm, rpm/sec, sec] 2) 4000, 1000, 33 [rpm, rpm/sec, sec] SB: 6 min at 115 ˚C – HP Exposure: λ = 405 nm, UV density = 600 mJ/cm^2 Developer: MF-319 HB: 15 min at 120 ˚C – HP
37	Silicon oxide etch (cantilever release)	Equipment: Plasma Therm ICP with C_4F_6 Plasma Note: the entire thickness of the exposed silicon oxide layer must be etched.
38	Silicon etch (cantilever release)	Equipment: Plasma Therm ICP Recipe: Bosch process Note: the entire thickness of the exposed silicon membrane must be etched.
39	Cleaning	Same as step #4
40	Dicing	Dicing speed: 7.62 mm/sec Blade type: 01776-2501-040-CHO (Nickel) Dicing cut width: ~ 150 μm

APPENDIX B

FABRICATION OF SC ELEMENTS

Table B.1. Process module for fabrication of SC beams and wires.

Step	Description	Process Details
0	Thermal oxidation (diffusion drive-in)	Start after step #10 in Table A.1.
1	Rinse and dry	Rinse the sample with DI water and dry it by blowing nitrogen
2	Lithography (trench)	Photoresist: SC1813 Spin: 4000, 1000, 40 [rpm, rpm/sec, sec] SB: 3 min at 100 ˚C – HP Exposure: λ = 365 nm, UV density = 30 mJ/cm^2 Developer: MF-319 – immersed for 8 sec HB: 10 min at 110 ˚C – HP
3	Silicon oxide etch (trench window)	Equipment: Plasma Therm ICP with C_4F_6 Plasma Note: the entire thickness of the oxide layer (~ 5650 Å) in the opening must be etched.
4	Silicon etch (shallow trench, d_1)	Equipment: Plasma Therm ICP Recipe: Bosch process Silicon etch depth: d_1 (please refer to Chapter 3)
5	Cleaning	Rinse the sample in acetone, methanol, and DI water. Use oxygen plasma to remove the remaining residues.
6	CMOS grade cleaning	Piranha solution: 10 min Rinse with DI water RCA clean: 10 min Rinse with DI water BOE dip: 15 sec Rinse and dry
7	Thermal Oxidation	Equipment: Tystar Furnace Temperature: 950 ˚C (wet oxidation) Duration: 60 min Measured thickness: ~ 2200 Å
8	Silicon oxide etch (trench foot opening)	Equipment: Plasma Therm ICP with C_4F_6 Plasma Note: the entire thickness of the silicon oxide layer at the bottom of the trench must be etched.
9	Silicon etch (deep trench, d_2)	Equipment: Plasma Therm ICP Recipe: Bosch process Silicon etch depth: d_2 (please refer to Chapter 3)
10	KOH etch (front-side release)	KOH solution: 6 molar Temperature: 30 ˚C Etch rate: ~ 0.1 μm/min Duration: depends on G (please refer to Chapter 3) Note: only the front surface is exposed to the solution.

Table B.1. *Continued*.

Step	Description	Process Details
11	Rinse and dry	Thoroughly rinse the sample with DI water and dry it by blowing nitrogen.
12	Cleaning	Same as step #5
13	Isolation layer	Continue from step #12 in Table A.1

APPENDIX C

INTEGRAL VALUE OF EQUATION (6.8)

Transversal vibration amplitude of a simple cantilever beam is given by Eq. (2.26):

$$y(x) = c_1(\cos\frac{\lambda_n}{L}x - \cosh\frac{\lambda_n}{L}x) + c_2(\sin\frac{\lambda_n}{L}x - \sinh\frac{\lambda_n}{L}x),$$

where the coefficients c_1 and c_2 can be calculated based on the first boundary condition at the clamped end, which is described by Eq. (2.25b):

$$\left.\frac{\partial^2 y}{\partial x^2}\right|_{x=L} = 0,$$

and based on $y(L)$, the vibration amplitude at the free end (i.e., $x = L$). The result is presented by Eq. (2.26b):

$$c_1 = \frac{y(L)}{2},$$

$$c_2 = -\frac{\cos(\lambda_n) + \cosh(\lambda_n)}{\sin(\lambda_n) + \sinh(\lambda_n)} \times c_1 .$$

The integral of Eq. (6.8), I, is calculated as follows:

$$I = \int_0^L y^2(x)dx$$
$$= \int_0^L [\frac{y(L)}{2}(\cos\frac{\lambda_n}{L}x - \cosh\frac{\lambda_n}{L}x) - (\frac{\cos\lambda_n + \cosh\lambda_n}{\sin\lambda_n + \sinh\lambda_n})\frac{y(L)}{2}(\sin\frac{\lambda_n}{L}x - \sinh\frac{\lambda_n}{L}x)]^2 dx.$$

Hence,

$$\frac{4(\sin\lambda_n + \sinh\lambda_n)^2}{y^2(L)} I$$
$$= \int_0^L [(\sin\lambda_n + \sinh\lambda_n)(\cos\frac{\lambda_n}{L}x - \cosh\frac{\lambda_n}{L}x) - (\cos\lambda_n + \cosh\lambda_n)(\sin\frac{\lambda_n}{L}x - \sinh\frac{\lambda_n}{L}x)]^2 dx.$$

Multiplying and integrating each of the ten resulting terms leads to

$$I = \frac{Ly^2(L)}{4\lambda_n(\sin\lambda_n + \sinh\lambda_n)^2}\Big[(\sin\lambda_n + \sinh\lambda_n)^2$$
$$\times(\lambda_n + \frac{\sin 2\lambda_n}{4} + \frac{\sinh\lambda_n\cosh\lambda_n}{2} + \cos\lambda_n\sinh\lambda_n + \sin\lambda_n\cosh\lambda_n)$$
$$-(\sin\lambda_n\cos\lambda_n + \sinh\lambda_n\cosh\lambda_n + \sin\lambda_n\cosh\lambda_n + \sinh\lambda_n\cos\lambda_n)$$
$$\times(\sin^2\lambda_n + \cosh^2\lambda_n + 2\sin\lambda_n\sinh\lambda_n - 1)$$
$$+(\cos\lambda_n + \cosh\lambda_n)^2(-\frac{\sin 2\lambda_n}{4} + \frac{\sinh\lambda_n\cosh\lambda_n}{2} - \cos\lambda_n\sinh\lambda_n + \sin\lambda_n\cosh\lambda_n)\Big].$$

Considering that

$$\cosh^2\lambda_n = \sinh^2\lambda_n + 1,$$
$$\cos^2\lambda_n = 1 - \sin^2\lambda_n,$$

and

$$\sin 2\lambda_n = 2\sin\lambda_n\cos\lambda_n,$$

the integral I could be simplified to

$$I = \frac{Ly^2(L)}{4\lambda_n(\sin\lambda_n + \sinh\lambda_n)^2}\Big[(\sin\lambda_n + \sinh\lambda_n)^2(\lambda_n - \frac{\sin\lambda_n\cos\lambda_n}{2} - \frac{\sinh\lambda_n\cosh\lambda_n}{2})$$
$$+(\cos\lambda_n + \cosh\lambda_n)^2(-\frac{\sin\lambda_n\cos\lambda_n}{2} + \frac{\sinh\lambda_n\cosh\lambda_n}{2} - \cos\lambda_n\sinh\lambda_n + \sin\lambda_n\cosh\lambda_n)\Big].$$

By expanding the terms, the integral expression can be further simplified:

$$I = \frac{Ly^2(L)}{4\lambda_n(\sin\lambda_n + \sinh\lambda_n)^2}\Big[\lambda_n(\sin\lambda_n + \sinh\lambda_n)^2 - \cos\lambda_n\sinh\lambda_n + \sin\lambda_n\cosh\lambda_n$$
$$+\sin\lambda_n\cos\lambda_n\cosh^2\lambda_n - \cos^2\lambda_n\sinh\lambda_n\cosh\lambda_n\Big].$$

As expressed by Eq. (2.26a), for a resonant cantilever the boundary conditions requires

$$\cos\lambda_n\cosh\lambda_n = -1.$$

Hence, integral I can be even further simplified:

$$I = \frac{Ly^2(L)}{4\lambda_n(\sin\lambda_n + \sinh\lambda_n)^2}\left[\lambda_n(\sin\lambda_n + \sinh\lambda_n)^2 - \cos\lambda_n \sinh\lambda_n + \sin\lambda_n \cosh\lambda_n \right.$$
$$\left. - \sin\lambda_n \cosh\lambda_n + \cos\lambda_n \sinh\lambda_n\right]$$
$$= \frac{Ly^2(L)}{4\lambda_n(\sin\lambda_n + \sinh\lambda_n)^2}\left[\lambda_n(\sin\lambda_n + \sinh\lambda_n)^2\right] = \frac{y^2(L)}{4}.$$

In other words, the integral of Eq. (6.8) is calculated as

$$\int_0^L y^2(x)dx = \tfrac{1}{4}Ly^2(L).$$

REFERENCES

[1] J. Gere, *Mechanics of materials*, 6 ed. Pacific Grove: Brooks/Cole, 2004.

[2] W. Weaver, Jr., S.P. Timoshenko, D.H. Young, *Vibration Problems in Engineering*, 5 ed. New York: Wiley, 1990.

[3] N. V. Lavrik, M. J. Sepaniak, and P. G. Datskos, "Cantilever transducers as a platform for chemical and biological sensors," *Review of Scientific Instruments*, vol. 75, pp. 2229-2253, 2004.

[4] C. Ziegler, "Cantilever-based biosensors," *Analytical and Bioanalytical Chemistry*, vol. 379, pp. 946-959, 2004.

[5] R. Raiteri, G. Nelles, H. J. Butt, W. Knoll, and P. Skladal, "Sensing of biological substances based on the bending of microfabricated cantilevers," *Sensors and Actuators B (Chemical)*, vol. B61, pp. 213-17, 1999.

[6] D. Lange, C. Hagleitner, A. Hierlemann, O. Brand, and H. Baltes, "Complementary metal oxide semiconductor cantilever arrays on a single chip: mass-sensitive detection of volatile organic compounds," *Analytical Chemistry*, vol. 74, pp. 3084-3095, 2002.

[7] K. M. Goeders, J. S. Colton, and L. A. Bottomley, "Microcantilevers: Sensing chemical interactions via mechanical motion," *Chemical Reviews*, vol. 108, pp. 522-542, 2008.

[8] P. E. Nokes and E. G. Carr, "The use of electric gauging equipment in machine design," *Mechanical Engineering*, vol. 69, pp. 117-119, 1947.

[9] R. M. McClintock, "Strain gauge calibration device for extreme temperatures," *Review of Scientific Instruments*, vol. 30, pp. 715-718, 1959.

[10] F. P. Burns, "Piezoresistive semiconductor microphone," *Journal of the Acoustical Society of America*, vol. 29, pp. 248-253, 1957.

[11] M. Traite, W. Welkowitz, and R. Downs, "Intracardiac catheter tip piezoresistive pressure gauge," *Review of Scientific Instruments*, vol. 31, pp. 987-991, 1960.

[12] L. M. Roylance and J. B. Angell, "A batch-fabricated silicon accelerometer," *IEEE Transactions on Electron Devices*, vol. ED-26, pp. 1911-17, 1979.

[13] P. L. Chen, R. S. Muller, R. D. Jolly, G. L. Halac, R. M. White, A. P. Andrews, T. C. Lim, and M. E. Motamedi, "Integrated silicon microbeam PI-FET

accelerometer," *IEEE Transactions on Electron Devices*, vol. ED-29, pp. 27-33, 1982.

[14] G. Binnig, C. F. Quate, and C. Gerber, "Atomic force microscope," *Physical Review Letters*, vol. 56, pp. 930-3, 1986.

[15] Y. Martin, C. C. Williams, and H. K. Wickramasinghe, "Atomic force microscope-force mapping and profiling on a sub 100-A scale," *Journal of Applied Physics*, vol. 61, pp. 4723-9, 1987.

[16] R. Erlandsson, G. M. McClelland, C. M. Mate, and S. Chiang, "Atomic force microscopy using optical interferometry," *Journal of Vacuum Science & Technology A (Vacuum, Surfaces, and Films)*, vol. 6, pp. 266-70, 1988.

[17] R. Garcia and R. Perez, "Dynamic atomic force microscopy methods," *Surface Science Reports*, vol. 47, pp. 197-301, 2002.

[18] G. Meyer and N. M. Amer, "Simultaneous measurement of lateral and normal forces with an optical-beam-deflection atomic force microscope," *Applied Physics Letters*, vol. 57, pp. 2089-91, 1990.

[19] J. K. Gimzewski, C. Gerber, E. Meyer, and R. R. Schlittler, "Observation of a Chemical-Reaction Using a Micromechanical Sensor," *Chemical Physics Letters*, vol. 217, pp. 589-594, 1994.

[20] S. J. O'Shea, M. E. Welland, T. A. Brunt, A. R. Ramadan, and T. Rayment, "Atomic force microscopy stress sensors for studies in liquids," *Journal of Vacuum Science & Technology B (Microelectronics and Nanometer Structures)*, vol. 14, pp. 1383-5, 1996.

[21] H. P. Lang, R. Berger, F. Battiston, J. P. Ramseyer, E. Meyer, C. Andreoli, J. Brugger, P. Vettiger, M. Despont, T. Mezzacasa, L. Scandella, H. J. Guentherodt, C. Gerber, and J. K. Gimzewski, "A chemical sensor based on a micromechanical cantilever array for the identification of gases and vapors," *Applied Physics A (Materials Science Processing)*, vol. 66, pp. 61-4, 1998.

[22] K. M. Hansen, H. F. Ji, G. Wu, R. Datar, R. Cote, A. Majumdar, and T. Thundat, "Cantilever-based optical deflection assay for discrimination of DNA single-nucleotide mismatches," *Analytical Chemistry*, vol. 73, pp. 1567-1571, 2001.

[23] F. Huber, M. Hegner, C. Gerber, H. J. Guntherodt, and H. P. Lang, "Label free analysis of transcription factors using microcantilever arrays," *Biosensors & Bioelectronics*, vol. 21, pp. 1599-605, 2006.

[24] G. Meyer and N. M. Amer, "Novel optical approach to atomic force microscopy," *Applied Physics Letters*, vol. 53, pp. 1045-7, 1988.

[25] S. Alexander, L. Hellemans, O. Marti, J. Schneir, V. Elings, P. K. Hansma, M. Longmire, and J. Gurley, "An atomic-resolution atomic-force microscope implemented using an optical lever," *Journal of Applied Physics*, vol. 65, pp. 164-7, 1989.

[26] H. J. Mamin, R. Budakian, B. W. Chui, and D. Rugar, "Detection and manipulation of statistical polarization in small spin ensembles," *Physical Review Letters*, vol. 91, pp. 207604-1, 2003.

[27] D. Rugar, R. Budakian, H. J. Mamin, and B. W. Chui, "Single spin detection by magnetic resonance force microscopy," *Nature*, vol. 430, pp. 329-332, 2004.

[28] L. C. Kong, B. G. Orr, and K. D. Wise, "A micromachined silicon scan tip for an atomic force microscope," presented at *IEEE Solid-State Sensor and Actuator Workshop*, Hilton Head Island, SC, USA, 1990.

[29] R. A. Buser, J. Brugger, C. Linder, and N. F. de Rooij, "Micromachined silicon cantilevers and tips for bidirectional force microscopy," in *International Conference on Solid-State Sensors and Actuators 1991; TRANSDUCERS '91*. San Francisco, CA, USA, 1991, pp. 249-52.

[30] N. Backmann, C. Zahnd, F. Huber, A. Bietsch, A. Pluckthun, H. P. Lang, H. J. Guntherodt, M. Hegner, and C. Gerber, "A label-free immunosensor array using single-chain antibody fragments," *Proceedings of the National Academy of Sciences of the United States of America*, vol. 102, pp. 14587-92, 2005.

[31] X. X. Li, T. Ono, Y. L. Wang, and M. Esashi, "Ultrathin single-crystalline-silicon cantilever resonators: Fabrication technology and significant specimen size effect on Young's modulus," *Applied Physics Letters*, vol. 83, pp. 3081-3083, 2003.

[32] T. R. Albrecht, S. Akamine, T. E. Carver, and C. F. Quate, "Microfabrication of cantilever styli for the atomic force microscope," *Journal of Vacuum Science & Technology A (Vacuum, Surfaces, and Films)*, vol. 8, pp. 3386-96, 1990.

[33] N. F. Vanhulst, M. H. P. Moers, O. F. J. Noordman, R. G. Tack, F. B. Segerink, and B. Bolger, "Near-Field Optical Microscope Using a Silicon-Nitride Probe," *Applied Physics Letters*, vol. 62, pp. 461-463, 1993.

[34] B. Ilic, D. Czaplewski, H. G. Craighead, P. Neuzil, C. Campagnolo, and C. Batt, "Mechanical resonant immunospecific biological detector," *Applied Physics Letters*, vol. 77, pp. 450-452, 2000.

[35] M. Calleja, M. Nordstrom, M. Alvarez, J. Tamayo, L. M. Lechuga, and A. Boisen, "Highly sensitive polymer-based cantilever-sensors for DNA detection," *Ultramicroscopy*, vol. 105, pp. 215-222, 2005.

[36] J. H. T. Ransley, M. Watari, D. Sukumaran, R. A. McKendry, and A. A. Seshia, "SU8 bio-chemical sensor microarrays," *Microelectronic Engineering*, vol. 83, pp. 1621-1625, 2006.

[37] A. W. McFarland and J. S. Colton, "Chemical sensing with micromolded plastic microcantilevers," *Journal of Microelectromechanical Systems*, vol. 14, pp. 1375-1385, 2005.

[38] P. W. Bridgman, "Effect of homogeneous mechanical stress on the electrical resistance of crystals," *Physical Review*, vol. 42, pp. 858-863, 1932.

[39] G. C. Kuczynski, "Effect of elastic strain on the electrical resistance of metals," *Physical Review*, vol. 94, pp. 61-64, 1954.

[40] C. S. Smith, "Piezoresistance effect in germanium and silicon," *Physical Review*, vol. 94, pp. 42-49, 1954.

[41] S. U. Jen, C. C. Yu, C. H. Liu, and G. Y. Lee, "Piezoresistance and electrical resistivity of Pd, Au, and Cu films," *Thin Solid Films*, vol. 434, pp. 316-322, 2003.

[42] Y. Kanda, "Piezoresistance effect of silicon," *Sensors and Actuators, A: Physical*, vol. 28, pp. 83-91, 1991.

[43] A. Nathan and H. Baltes, *Microtransducer CAD : physical and computational aspects*. Wien: Springer, 1999.

[44] M. Tortonese, H. Yamada, R. C. Barrett, and C. F. Quate, "Atomic force microscopy using a piezoresistive cantilever," in *International Conference on Solid-State Sensors and Actuators; TRANSDUCERS '91*. San Francisco, CA, USA, 1991, pp. 448-451.

[45] M. Tortonese, R. C. Barrett, and C. F. Quate, "Atomic resolution with an atomic force microscope using piezoresistive detection," *Applied Physics Letters*, vol. 62, pp. 834-6, 1993.

[46] B. W. Chui, T. W. Kenny, H. J. Mamin, B. D. Terris, and D. Rugar, "Independent detection of vertical and lateral forces with a sidewall-implanted dual-axis piezoresistive cantilever," *Applied Physics Letters*, vol. 72, pp. 1388-90, 1998.

[47] A. Hierlemann, O. Brand, C. Hagleitner, and H. Baltes, "Microfabrication techniques for chemical/biosensors," *Proceedings of the IEEE*, vol. 91, pp. 839-863, 2003.

[48] M. Lutwyche, C. Andreoli, G. Binnig, J. Brugger, U. Drechsler, W. Haberle, H. Rohrer, H. Rothuizen, P. Vettiger, G. Yaralioglu, and C. Quate, "5x5 2D AFM

cantilever arrays a first step towards a Terabit storage device," *Sensors and Actuators, A: Physical*, vol. 73, pp. 89-94, 1999.

[49] I. W. Rangelow, T. Ivanov, K. Ivanova, B. E. Volland, P. Grabiec, Y. Sarov, A. Persaud, T. Gotszalk, P. Zawierucha, M. Zielony, D. Dontzov, B. Schmidt, M. Zier, N. Nikolov, I. Kostic, W. Engl, T. Sulzbach, J. Mielczarski, S. Kolb, D. P. Latimier, R. Pedreau, V. Djakov, S. E. Huq, K. Edinger, O. Fortagne, A. Almansa, and H. O. Blom, "Piezoresistive and self-actuated 128-cantilever arrays for nanotechnology applications," *Microelectronic Engineering*, vol. 84, pp. 1260-1264, 2007.

[50] J. A. Harley and T. W. Kenny, "1/f noise considerations for the design and process optimization of piezoresistive cantilevers," *Journal of Microelectromechanical Systems*, vol. 9, pp. 226-235, 2000.

[51] D. L. DeVoe and A. P. Pisano, "Surface micromachined piezoelectric accelerometers (PiXLs)," *Journal of Microelectromechanical Systems*, vol. 10, pp. 180-6, 2001.

[52] V. Ferrari, D. Marioli, A. Taroni, E. Ranucci, and P. Ferruti, "Development and application of mass sensors based on flexural resonances in alumina beams," *IEEE Transactions on Ultrasonics, Ferroelectrics and Frequency Control*, vol. 43, pp. 601-8, 1996.

[53] J. W. Yi, W. Y. Shih, R. Mutharasan, and W. H. Shih, "In situ cell detection using piezoelectric lead zirconate titanate-stainless steel cantilevers," *Journal of Applied Physics*, vol. 93, pp. 619-625, 2003.

[54] S. Zuyan, W. Y. Shih, and S. Wei-Heng, "Self-exciting, self-sensing $PbZr_{0.53}Ti_{0.47}O_3/SiO_2$ piezoelectric microcantilevers with femtogram/hertz sensitivity," *Applied Physics Letters*, vol. 89, pp. 23506-1, 2006.

[55] R. E. Hetrick, "Acoustically-driven cantilever for gas sensing," *Sensors and Actuators*, vol. 18, pp. 131-147, 1989.

[56] R. E. Hetrick, "Vibrating cantilever mass flow sensor," *Sensors and Actuators A (Physical)*, vol. A21, pp. 373-6, 1990.

[57] L. A. Pinnaduwage, A. Gehl, D. L. Hedden, G. Muralidharan, T. Thundat, R. T. Lareau, T. Sulchek, L. Manning, B. Rogers, M. Jones, and J. D. Adams, "Explosives: A microsensor for trinitrotoluene vapour," *Nature*, vol. 425, pp. 474-474, 2003.

[58] S. Akamine, T. R. Albrecht, M. J. Zdeblick, and C. F. Quate, "A planar process for microfabrication of a scanning tunneling microscope," *Sensors and Actuators A (Physical)*, vol. A23, pp. 964-70, 1990.

[59] T. Itoh and T. Suga, "Development of a force sensor for atomic force microscopy using piezoelectric thin films," *Nanotechnology*, vol. 4, pp. 218-224, 1993.

[60] P. F. Indermuhle, G. Schurmann, G. A. Racine, and N. F. de Rooij, "Atomic force microscopy using cantilevers with integrated tips and piezoelectric layers for actuation and detection," *Journal of Micromechanics and Microengineering*, vol. 7, pp. 218-220, 1997.

[61] S. C. Minne, S. R. Manalis, A. Atalar, and C. F. Quate, "Contact imaging in the atomic force microscope using a higher order flexural mode combined with a new sensor," *Applied Physics Letters*, vol. 68, pp. 1427-9, 1996.

[62] A. J. M. Draper and E. C. Dolton, "Continuous weighing and measurement of low tensile strengths -- Design and performance of suitable basic instrument," *Paper Technology*, vol. 5, pp. 265-268, 1964.

[63] J. Brugger, R. A. Buser, and N. F. de Rooij, "Micromachined atomic force microprobe with integrated capacitive read-out," *Journal of Micromechanics and Microengineering*, vol. 2, pp. 218-20, 1992.

[64] C. L. Britton, R. L. Jones, P. I. Oden, Z. Hu, R. J. Warmack, S. F. Smith, W. L. Bryan, and J. M. Rochelle, "Multiple-input microcantilever sensors," *Ultramicroscopy*, vol. 82, pp. 17-21, 2000.

[65] J. R. Matey and J. Blanc, "Scanning capacitance microscopy," *Journal of Applied Physics*, vol. 57, pp. 1437-44, 1985.

[66] S.-J. Kim, T. Ono, and M. Esashi, "Capacitive resonant mass sensor with frequency demodulation detection based on resonant circuit," *Applied Physics Letters*, vol. 88, pp. 053116, 2006.

[67] T. W. Kenny, S. B. Waltman, J. K. Reynolds, and W. J. Kaiser, "Micromachined silicon tunnel sensor for motion detection," *Applied Physics Letters*, vol. 58, pp. 100-2, 1991.

[68] G. Binnig and H. Rohrer, "Scanning Tunneling Microscopy," *IBM Journal of Research and Development*, vol. 30, pp. 355-369, 1986.

[69] T. W. Kenny, W. J. Kaiser, J. K. Reynolds, J. A. Podosek, H. K. Rockstad, E. C. Vote, and S. B. Waltman, "Electron tunnel sensors," *Journal of Vacuum Science & Technology A (Vacuum, Surfaces, and Films)*, vol. 10, pp. 2114-18, 1992.

[70] A. Majumdar, "Scanning thermal microscopy," vol. 29, *Annual Review of Materials Science*: Annual Reviews Inc., Palo Alto, CA, USA, 1999, pp. 505-585.

[71] G. Binnig, M. Despont, U. Drechsler, W. Haberle, M. Lutwyche, P. Vettiger, H. J. Mamin, B. W. Chui, and T. W. Kenny, "Ultrahigh-density atomic force microscopy data storage with erase capability," *Applied Physics Letters*, vol. 74, pp. 1329-31, 1999.

[72] A. Majumdar, J. Lai, M. Chandrachood, O. Nakabeppu, Y. Wu, and Z. Shi, "Thermal imaging by atomic force microscopy using thermocouple cantilever probes," *Review of Scientific Instruments*, vol. 66, pp. 3584, 1995.

[73] P. Vettiger, G. Cross, M. Despont, U. Drechsler, U. Durig, B. Gotsmann, W. Haberle, M. A. Lantz, H. E. Rothuizen, R. Stutz, and G. K. Binnig, "The 'millipede' - nanotechnology entering data storage," *IEEE Transactions on Nanotechnology*, vol. 1, pp. 39-55, 2002.

[74] W. P. King, T. W. Kenny, K. E. Goodson, G. Cross, M. Despont, U. Durig, H. Rothuizen, G. K. Binnig, and P. Vettiger, "Atomic force microscope cantilevers for combined thermomechanical data writing and reading," *Applied Physics Letters*, vol. 78, pp. 1300-1302, 2001.

[75] W. P. King, T. W. Kenny, and K. E. Goodson, "Comparison of thermal and piezoresistive sensing approaches for atomic force microscopy topography measurements," *Applied Physics Letters*, vol. 85, pp. 2086-2088, 2004.

[76] K. J. Kim, K. Park, J. Lee, Z. M. Zhang, and W. P. King, "Nanotopographical imaging using a heated atomic force microscope cantilever probe," *Sensors and Actuators A (Physical)*, vol. 136, pp. 95-103, 2007.

[77] C. M. Harris, *Harris's shock and vibration handbook*, 5 ed. New York: McGraw-Hill, 2002.

[78] C. A. Desoer and E. S. Kuh, *Basic circuit theory*. New York: McGraw-Hill, 1969.

[79] L. E. Kinsler, *Fundamentals of acoustics*, 3rd ed. New York: Wiley, 1982.

[80] S. D. Senturia, *Microsystem Design*. Boston: Kluwer Academic 2001.

[81] R. R. Archer, N. H. Cook, S. H. Crandall, N. C. Dahl, F. A. McClintock, E. Rabinowicz, and G. S. Reichenbach, *An introduction to the mechanics of solids*. New York: McGraw-Hill, 1959.

[82] J. L. Arlett, J. R. Maloney, B. Gudlewski, M. Muluneh, and M. L. Roukes, "Self-Sensing Micro- and Nanocantilevers with Attonewton-Scale Force Resolution," *Nano Lett.*, vol. 6, pp. 1000-1006, 2006.

[83] N. E. Jenkins, L. P. DeFlores, J. Allen, T. N. Ng, S. R. Garner, S. Kuehn, J. M. Dawlaty, and J. A. Marohn, "Batch fabrication and characterization of

ultrasensitive cantilevers with submicron magnetic tips," *Journal of Vacuum Science & Technology B*, vol. 22, pp. 909-915, 2004.

[84] K. Y. Yasumura, T. D. Stowe, E. M. Chow, T. Pfafman, T. W. Kenny, B. C. Stipe, and D. Rugar, "Quality factors in micron- and submicron-thick cantilevers," *Journal of Microelectromechanical Systems*, vol. 9, pp. 117-25, 2000.

[85] A. N. Cleland and M. L. Roukes, "Noise processes in nanomechanical resonators," *Journal of Applied Physics*, vol. 92, pp. 2758-2769, 2002.

[86] P. M. Morse and K. U. Ingard, *Theoretical acoustics*. Princeton, N.J: Princeton University Press, 1986.

[87] W. Thomson, "The Bakerian Lecture: -- On the Electro-Dynamic Properties of Metals," *Proceedings of the Royal Society of London*, vol. 8, pp. 50-55, 1856.

[88] H. Tomlinson, "The Influence of Stress and Strain on the Action of Physical Forces," *Philosophical Transactions of the Royal Society of London*, vol. 174, pp. 1-172, 1883.

[89] P. W. Bridgman, "The effect of tension on the transverse and longitudinal resistance of metals," *American Society of Art and Science -- Proceedings*, vol. 60, pp. 423-449, 1925.

[90] G. E. Kimball, "Electronic structure of diamond," *Journal of Chemical Physics*, vol. 3, pp. 560-564, 1935.

[91] J. F. Mullaney, "Optical properties and electronic structure of solid silicon," *Physical Review*, vol. 66, pp. 326-339, 1944.

[92] H. H. Hall, J. Bardeen, and G. L. Pearson, "The effects of pressure and temperature on the resistance of p - n junctions in germanium," *Physical Review*, vol. 84, pp. 129-132, 1951.

[93] Y. Kanda, "A graphical representation of the piezoresistance coefficients in silicon," *IEEE Transactions on Electron Devices*, vol. ED-29, pp. 64-70, 1982.

[94] K. Matsuda, K. Suzuki, K. Yamamura, and Y. Kanda, "Nonlinear piezoresistance effects in silicon," *Journal of Applied Physics*, vol. 73, pp. 1838-47, 1993.

[95] T. Toriyama and S. Sugiyama, "Analysis of piezoresistance in p-type silicon for mechanical sensors," *Journal of Microelectromechanical Systems*, vol. 11, pp. 598-604, 2002.

[96] T. Toriyama, D. Funai, and S. Sugiyama, "Piezoresistance measurement on single crystal silicon nanowires," *Journal of Applied Physics*, vol. 93, pp. 561-565, 2003.

[97] V. Mosser, J. Suski, J. Goss, and E. Obermeier, "Piezoresistive pressure sensors based on polycrystalline silicon," *Sensors and Actuators A (Physical)*, vol. 28, pp. 113-132, 1991.

[98] E. Obermeier and P. Kopystynski, "Polysilicon as a material for microsensor applications," *Sensors and Actuators A (Physical)*, vol. 30, pp. 149-155, 1992.

[99] D. E. Aspnes and M. Cardona, "Piezoresistance and the conduction-band minima of GaAs," *Physical Review B*, vol. 17, pp. 741, 1978.

[100] A. Dehe, K. Fricke, K. Mutamba, and H. L. Hartnagel, "A piezoresistive GaAs pressure sensor with GaAs/AlGaAs membrane technology," *Journal of Micromechanics and Microengineering*, vol. 5, pp. 139-42, 1995.

[101] H. Yamaguchi, S. Miyashita, and Y. Hirayama, "Giant magnetopiezoresistance at the localized-extended electronic state transition in a high-mobility 2DEG system," *Physica Status Solidi (C)*, vol. 3, pp. 663-666, 2006.

[102] A. D. Bykhovski, V. V. Kaminski, M. S. Shur, Q. C. Chen, and M. A. Khan, "Piezoresistive effect in wurtzite n-type GaN," *Applied Physics Letters*, vol. 68, pp. 818-819, 1996.

[103] J. S. Shor, D. Goldstein, and A. D. Kurtz, "Characterization of n-type β-SiC as a piezoresistor," *IEEE Transactions on Electron Devices*, vol. 40, pp. 1093-1099, 1993.

[104] M. Aslam, I. Taher, A. Masood, M. A. Tamor, and T. J. Potter, "Piezoresistivity in vapor-deposited diamond films," *Applied Physics Letters*, vol. 60, pp. 2923-5, 1992.

[105] A. Yamamoto and T. Tsutsumoto, "Piezoresistive effect of CVD polycrystalline diamond films," *Diamond and Related Materials*, vol. 13, pp. 863-866, 2004.

[106] S. Nishida, M. Konagai, and K. Takahashi, "Seebeck and piezoresistance effects in amorphous-microcrystalline mixed-phase silicon films and applications to power sensors and strain gauges," *Thin Solid Films*, vol. 112, pp. 7-16, 1984.

[107] E. Peiner, A. Tibrewala, R. Bandorf, S. Biehl, H. Luthje, and L. Doering, "Micro force sensor with piezoresistive amorphous carbon strain gauge," *Sensors and Actuators A (Physical)*, vol. 130-131, pp. 75-82, 2006.

[108] J. Cao, Q. Wang, and H. Dai, "Electromechanical Properties of Metallic, Quasimetallic, and Semiconducting Carbon Nanotubes under Stretching," *Physical Review Letters*, vol. 90, pp. 157601, 2003.

[109] J. Thaysen, A. D. Yalcinkaya, P. Vettiger, and A. Menon, "Polymer-based stress sensor with integrated readout," *Journal of Physics D: Applied Physics*, vol. 35, pp. 2698-2703, 2002.

[110] A. Johansson, M. Calleja, P. A. Rasmussen, and A. Boisen, "SU-8 cantilever sensor system with integrated readout," *Sensors and Actuators A (Physical)*, vol. 123-124, pp. 111-15, 2005.

[111] M. Li, H. X. Tang, and M. L. Roukes, "Ultra-sensitive NEMS-based cantilevers for sensing, scanned probe and very high-frequency applications," *Nat Nano*, vol. 2, pp. 114-120, 2007.

[112] G. R. Witt, "The electromechanical properties of thin films and the thin film strain gauge," *Thin Solid Films*, vol. 22, pp. 133-156, 1974.

[113] W. P. Mason and R. N. Thurston, "Use of piezoresistive materials in measurement of displacement, force, and torque," *Journal of Acoustical Society of America* vol. 29, pp. 1096-1101, 1957.

[114] W. G. Pfann and R. N. Thurston, "Semiconducting stress transducers utilizing the transverse and shear piezoresistance effects," *Journal of Applied Physics*, vol. 32, pp. 2008-2019, 1961.

[115] O. N. Tufte and D. Long, "Recent developments in semiconductor piezoresistive devices," *Solid-State Electronics*, vol. 6, pp. 323-338, 1963.

[116] H.-J. Timme, "CMOS-baed pressure sensors," in *CMOS-MEMS*, vol. 2, *Advanced micro and nanosystems*, O. Brand and G. K. Fedder, Eds. Weinheim: Wiley-VCH, 2005.

[117] K. Scott and A. Owens, "Instrumentation," in *Strain gauge technology*, A. L. Window and G. S. Holister, Eds. London: Applied Science Publishers, 1982, pp. 139.

[118] J. Thaysen, A. Boisen, O. Hansen, and S. Bouwstra, "Atomic force microscopy probe with piezoresistive read-out and a highly symmetrical Wheatstone bridge arrangement," *Sensors and Actuators, A: Physical*, vol. 83, pp. 47-53, 2000.

[119] P. Ohlckers and H. Jakobsen, "High volume production of silicon sensor microsystems for automotive applications," presented at *IEE Colloquium on Assembly and Connections in Microsystems*, London, UK, 1997.

[120] J. T. Suminto, "Wide frequency range, rugged silicon micro accelerometer with overrange stops," in *IEEE Micro Electro Mechanical Systems (MEMS'96)*. San Diego, CA, USA, 1996, pp. 180-185.

[121] F. J. Giessibl, "Atomic resolution of the silicon (111)-(7 x 7) surface by atomic force microscopy," *Science*, vol. 267, pp. 68-71, 1995.

[122] R. Berger, H. P. Lang, C. Gerber, J. K. Gimzewski, J. H. Fabian, L. Scandella, E. Meyer, and H. J. Guntherodt, "Micromechanical thermogravimetry," *Chemical Physics Letters*, vol. 294, pp. 363-369, 1998.

[123] J. Thaysen, M. H. Jacobsen, and L. K. Nielsen, "Nanomechanical sensor platform based on piezo-resistive cantilevers," in *2005 NSTI Nanotechnology Conference and Trade Show*, vol. vol.2. Anaheim, CA, USA, 2005, pp. 262-5.

[124] L. E. Hollander, G. L. Vick, and T. J. Diesel, "The piezoresistive effect and its applications," *Review of Scientific Instruments*, vol. 31, pp. 323-327, 1960.

[125] D. R. Kerr and A. G. Milnes, "Piezoresistive strain gages and transducer elements," *IEEE Transactions on Instrumentation and Measurement*, vol. IM-12, pp. 73-80, 1963.

[126] B. W. Chui, T. D. Stowe, T. W. Kenny, H. J. Mamin, B. D. Terris, and D. Rugar, "Low-stiffness silicon cantilevers for thermal writing and piezoresistive readback with the atomic force microscope," *Applied Physics Letters*, vol. 69, pp. 2767-9, 1996.

[127] R. P. Ried, H. J. Mamin, B. D. Terris, F. Long-Sheng, and D. Rugar, "6-MHz 2-N/m piezoresistive atomic-force microscope cantilevers with INCISIVE tips," *Journal of Microelectromechanical Systems*, vol. 6, pp. 294-302, 1997.

[128] J. A. Harley and T. W. Kenny, "High-sensitivity piezoresistive cantilevers under 1000 angstrom thick," *Applied Physics Letters*, vol. 75, pp. 289-291, 1999.

[129] L. F. Houlet, H. Yamaguchi, S. Miyashita, and Y. Hirayama, "InAs/AlGaSb piezoresistive cantilever for sub-angstrom scale displacement detection," *Japanese Journal of Applied Physics Part 2-Letters*, vol. 43, pp. L424-L426, 2004.

[130] H. Yamaguchi, S. Miyashita, and Y. Hirayama, "Microelectromechanical displacement sensing using InAs/AlGaSb heterostructures," *Applied Physics Letters*, vol. 82, pp. 394-396, 2003.

[131] T. Toriyama, Y. Tanimoto, and S. Sugiyama, "Single crystal silicon nano-wire piezoresistors for mechanical sensors," *Microelectromechanical Systems, Journal of*, vol. 11, pp. 605-611, 2002.

[132] W. H. Legat and L. K. Russell, "A silicon p-n junction transducer," *Solid-State Electronics*, vol. 8, pp. 709-714, 1965.

[133] R. Bashir, A. Gupta, G. W. Neudeck, M. McElfresh, and R. Gomez, "On the design of piezoresistive silicon cantilevers with stress concentration regions for scanning probe microscopy applications," *Journal of Micromechanics and Microengineering*, vol. 10, pp. 483-491, 2000.

[134] K. Naeli and O. Brand, "Cantilever sensor with stress-concentrating piezoresistor design," in *IEEE Sensors 2005*. Irvine, CA, USA, 2005, pp. 592-595.

[135] H. A. C. Tilmans, M. Elwenspoek, and J. H. J. Fluitman, "Micro resonant force gauges," *Sensors and Actuators A: Physical*, vol. 30, pp. 35-53, 1992.

[136] D. Rugar, H. J. Mamin, P. Guethner, S. E. Lambert, J. E. Stern, I. McFadyen, and T. Yogi, "Magnetic force microscopy: general principles and application to longitudinal recording media," *Journal of Applied Physics*, vol. 68, pp. 1169-83, 1990.

[137] G. G. Stoney, "The Tension of Metallic Films Deposited by Electrolysis," *Proceedings of the Royal Society of London. Series A, Containing Papers of a Mathematical and Physical Character*, vol. 82, pp. 172-175, 1909.

[138] J. W. Cahn and R. E. Hanneman, "(111) Surface tensions of III-V compounds and their relationship to spontaneous bending of thin crystals," *Surface Science*, vol. 1, pp. 387-398, 1964.

[139] G. Y. Chen, T. Thundat, E. A. Wachter, and R. J. Warmack, "Adsorption-induced surface stress and its effects on resonance frequency of microcantilevers," *Journal of Applied Physics*, vol. 77, pp. 3618-22, 1995.

[140] A. Boisen, J. Thaysen, H. Jensenius, and O. Hansen, "Environmental sensors based on micromachined cantilevers with integrated read-out," *Ultramicroscopy*, vol. 82, pp. 11-16, 2000.

[141] A. M. Moulin, S. J. O'Shea, and M. E. Welland, "Microcantilever-based biosensors," *Ultramicroscopy*, vol. 82, pp. 23-31, 2000.

[142] J. Thaysen, R. Marie, and A. Boisen, "Cantilever-based bio-chemical sensor integrated in a microliquid handling system," in *14th IEEE International Conference on Micro Electro Mechanical Systems (MEMS'01)*. Interlaken, Switzerland: IEEE, 2001, pp. 401-404.

[143] V. Dauksaite, M. Lorentzen, F. Besenbacher, and J. Kjems, "Antibody-based protein detection using piezoresistive cantilever arrays," *Nanotechnology*, vol. 18, 2007.

[144] A. Choudhury, P. J. Hesketh, T. Thundat, and Z. Y. Hu, "A piezoresistive microcantilever array for surface stress measurement: curvature model and

fabrication," *Journal of Micromechanics and Microengineering*, vol. 17, pp. 2065-2076, 2007.

[145] F. T. Goericke and W. P. King, "Modeling piezoresistive microcantilever sensor response to surface stress for biochemical sensors," *IEEE Sensors Journal*, vol. 8, pp. 1404-1410, 2008.

[146] W. H. King, "Piezoelectric Sorption Detector," *Analytical Chemistry*, vol. 36, pp. 1735-1739, 1964.

[147] J. P. Cleveland, S. Manne, D. Bocek, and P. K. Hansma, "A Nondestructive Method for Determining the Spring Constant of Cantilevers for Scanning Force Microscopy," *Review of Scientific Instruments*, vol. 64, pp. 403-405, 1993.

[148] T. Thundat, G. Y. Chen, R. J. Warmack, D. P. Allison, and E. A. Wachter, "Vapor Detection Using Resonating Microcantilevers," *Analytical Chemistry*, vol. 67, pp. 519-521, 1995.

[149] T. Thundat, E. A. Wachter, S. L. Sharp, and R. J. Warmack, "Detection of Mercury-Vapor Using Resonating Microcantilevers," *Applied Physics Letters*, vol. 66, pp. 1695-1697, 1995.

[150] M. Su, S. Li, and V. P. Dravid, "Microcantilever resonance-based DNA detection with nanoparticle probes," *Applied Physics Letters*, vol. 82, pp. 3562-3564, 2003.

[151] A. Hierlemann, D. Lange, C. Hagleitner, N. Kerness, A. Koll, O. Brand, and H. Baltes, "Application-specific sensor systems based on CMOS chemical microsensors," *Sensors and Actuators B-Chemical*, vol. 70, pp. 2-11, 2000.

[152] C. Hagleitner, A. Hierlemann, D. Lange, A. Kummer, N. Kerness, O. Brand, and H. Baltes, "Smart single-chip gas sensor microsystem," *Nature*, vol. 414, pp. 293-296, 2001.

[153] X. Yang, J. T. Lin, B. W. Alphenaar, and R. S. Keynton, "Viscous damping of microresonators for gas composition analysis," *Applied Physics Letters*, vol. 88, pp. 143513-1, 2006.

[154] J. W. Grate, S. J. Martin, and R. M. White, "Acoustic wave microsensors," *Analytical Chemistry*, vol. 65, pp. 940-948, 1993.

[155] J. W. Grate, S. J. Martin, and R. M. White, "Acoustic wave microsensors. Part II," *Analytical Chemistry*, vol. 65, pp. 987-996, 1993.

[156] Y. T. Yang, C. Callegari, X. L. Feng, K. L. Ekinci, and M. L. Roukes, "Zeptogram-scale nanomechanical mass sensing," *Nano Letters*, vol. 6, pp. 4 pp., 2006.

[157] K. L. Ekinci, Y. T. Yang, and M. L. Roukes, "Ultimate limits to inertial mass sensing based upon nanoelectromechanical systems," *Journal of Applied Physics*, vol. 95, pp. 2682-9, 2004.

[158] B. Ilic, H. G. Craighead, S. Krylov, W. Senaratne, C. Ober, and P. Neuzil, "Attogram detection using nanoelectromechanical oscillators," *Journal of Applied Physics*, vol. 95, pp. 3694-3703, 2004.

[159] H. Sone, A. Ikeuchi, T. Izumi, H. Okano, and S. Hosaka, "Femtogram mass biosensor using self-sensing cantilever for allergy check," *Japanese Journal of Applied Physics, Part 1 (Regular Papers, Short Notes & Review Papers)*, vol. 45, pp. 2301-4, 2006.

[160] A. Melling, "Tracer particles and seeding for particle image velocimetry," *Measurement Science & Technology*, vol. 8, pp. 1406-16, 1997.

[161] H. Royer, "Holography and particle image velocity," *Measurement Science & Technology*, vol. 8, pp. 1562-72, 1997.

[162] C. D. Meinhart, S. T. Wereley, and J. G. Santiago, "PIV measurements of a microchannel flow," *Experiments in Fluids*, vol. 27, pp. 414-419, 1999.

[163] L. V. King, "On the convection of heat from small cylinders in a stream of fluid: Determination of the convection constants of small platinum wires with applications to hot-wire anemometry," *Philosophical Transactions of the Royal Society of London Series a-Containing Papers of a Mathematical or Physical Character*, vol. 214, pp. 373-U44, 1914.

[164] J. Chen and C. Liu, "Development and characterization of surface micromachined, out-of-plane hot-wire anemometer," *Journal of Microelectromechanical Systems*, vol. 12, pp. 979-88, 2003.

[165] T. Nishimoto, S. Shoji, and M. Esashi, "Buried piezoresistive sensors by means of MeV ion implantation," *Sensors and Actuators A (Physical)*, vol. 43, pp. 249-253, 1994.

[166] N. Svedin, E. Kalvesten, E. Stemme, and G. Stemme, "A new silicon gas-flow sensor based on lift force," *Journal of Microelectromechanical Systems*, vol. 7, pp. 303-308, 1998.

[167] Y. Su, A. G. R. Evans, A. Brunnschweiler, and G. Ensell, "Characterization of a highly sensitive ultra-thin piezoresistive silicon cantilever probe and its application in gas flow velocity sensing," *Journal of Micromechanics and Microengineering*, vol. 12, pp. 780-785, 2002.

[168] J. Lee, K. Naeli, H. Hunter, J. Berg, T. Wright, C. Courcimault, N. Naik, M. Allen, O. Brand, A. Glezer, and W. P. King, "Characterization of liquid and gaseous micro- and nanojets using microcantilever sensors," *Sensors and Actuators a-Physical*, vol. 134, pp. 128-139, 2007.

[169] B. R. Munson, D. F. Young, and T. H. Okiishi, *Fundamentals of fluid mechanics*, 4 ed. New York: Wiley, 2002.

[170] J. Lee, K. Naeli, H. Hunter, J. Berg, T. Wright, C. Courcimault, N. Naik, M. Allen, O. Brand, A. Glezer, and W. P. King, "Characterization of liquid and gaseous micro- and nanojets using microcantilever sensors," *Sensors and Actuators A (Physical)*, vol. 134, pp. 128-139, 2007.

[171] Y. Xiaomei, T. Yaquan, Z. Haitao, L. Ting, and W. Wei, "Design of high-sensitivity cantilever and its monolithic integration with CMOS circuits," *IEEE Sensors Journal*, vol. 7, pp. 489-95, 2007.

[172] T. Muller, M. Brandl, O. Brand, and H. Baltes, "An industrial CMOS process family adapted for the fabrication of smart silicon sensors," *Sensors and Actuators A: Physical*, vol. 84, pp. 126-133, 2000.

[173] B. Kloeck, S. D. Collins, N. F. Derooij, and R. L. Smith, "Study of Electrochemical Etch-Stop for High-Precision Thickness Control of Silicon Membranes," *IEEE Transactions on Electron Devices*, vol. 36, pp. 663-669, 1989.

[174] O. Hansen and A. Boisen, "Noise in piezoresistive atomic force microscopy," *Nanotechnology*, vol. 10, pp. 51-60, 1999.

[175] H. J. Butt and M. Jaschke, "Calculation of thermal noise in atomic force microscopy," *Nanotechnology*, vol. 6, pp. 1-7, 1995.

[176] P. R. Gray and R. G. Meyer, *Analysis and design of analog integrated circuits*, 3rd ed. New York: Wiley, 1993.

[177] B. Razavi, *Design of analog CMOS integrated circuits*. Boston: McGraw-Hill, 2001.

[178] B. G. Streetman, *Solid state electronic devices*, 3rd ed. Englewood Cliffs, N.J.: Prentice-Hall, 1990.

[179] V. B. Braginsky, *Systems with small dissipation*. Chicago: University of Chicago Press, 1985.

[180] J. Yang, T. Ono, and M. Esashi, "Energy dissipation in submicrometer thick single-crystal silicon cantilevers," *Journal of Microelectromechanical Systems*, vol. 11, pp. 775-83, 2002.

[181] R. Abdolvand, H. Johari, G. K. Ho, A. Erbil, and F. Ayazi, "Quality factor in trench-refilled polysilicon beam resonators," *Journal of Microelectromechanical Systems*, vol. 15, pp. 471-478, 2006.

[182] B. Razavi, *RF microelectronics*. Upper Saddle River, NJ: Prentice Hall, 1998.

[183] W. E. Courtney, "Analysis and Evaluation of a Method of Measuring Complex Permittivity and Permeability of Microwave Insulators," *IEEE Transactions on Microwave Theory and Techniques*, vol. MT18, pp. 476-&, 1970.

[184] Y. Kobayashi and M. Katoh, "Microwave Measurement of Dielectric-Properties of Low-Loss Materials by the Dielectric Rod Resonator Method," *IEEE Transactions on Microwave Theory and Techniques*, vol. 33, pp. 586-592, 1985.

[185] T. M. Hirvonen, P. Vainikainen, A. Lozowski, and A. V. Raisanen, "Measurement of dielectrics at 100 GHz with an open resonator connected to a network analyzer," *IEEE Transactions on Instrumentation and Measurement*, vol. 45, pp. 780-786, 1996.

[186] L. F. Chen, C. K. Ong, and B. T. G. Tan, "Amendment of cavity perturbation method for permittivity measurement of extremely low-loss dielectrics," *IEEE Transactions on Instrumentation and Measurement*, vol. 48, pp. 1031-1037, 1999.

[187] Y. Kobayashi, T. Imai, and H. Kayano, "Microwave Measurement of Temperature and Current Dependences of Surface Impedance for High-Tc Superconductors," *IEEE Transactions on Microwave Theory and Techniques*, vol. 39, pp. 1530-1538, 1991.

[188] S. Timoshenko, D. H. Young, and W. Weaver, *Vibration problems in engineering*, 4th ed. New York,: Wiley, 1974.

[189] P. J. Petersan and S. M. Anlage, "Measurement of resonant frequency and quality factor of microwave resonators: Comparison of methods," *Journal of Applied Physics*, vol. 84, pp. 3392-3402, 1998.

[190] B. Nebendahl, D. N. Peligrad, M. Pozek, A. Dulcic, and M. Mehring, "An ac method for the precise measurement of Q-factor and resonance frequency of a microwave cavity," *Review of Scientific Instruments*, vol. 72, pp. 1876-1881, 2001.

[191] K. Leong and J. Mazierska, "Precise measurements of the Q factor of dielectric resonators in the transmission mode - Accounting for noise, crosstalk, delay of uncalibrated lines, coupling loss, and coupling reactance," *IEEE Transactions on Microwave Theory and Techniques*, vol. 50, pp. 2115-2127, 2002.

[192] K. J. Coakley, J. D. Splett, M. D. Janezic, and R. F. Kaiser, "Estimation of Q-factors and resonant frequencies," *IEEE Transactions on Microwave Theory and Techniques*, vol. 51, pp. 862-868, 2003.

[193] M. P. Robinson and J. Clegg, "Improved determination of Q-factor and resonant frequency by a quadratic curve-fitting method," *IEEE Transactions on Electromagnetic Compatibility*, vol. 47, pp. 399-402, 2005.

[194] P. R. Bevington and D. K. Robinson, *Data reduction and error analysis for the physical sciences*, 2nd ed. New York: McGraw-Hill, 1992.

[195] S. Rast, C. Wattinger, U. Gysin, and E. Meyer, "The noise of cantilevers," *Nanotechnology*, vol. 11, pp. 169-172, 2000.

[196] A. B. Carlson, *Communication systems : an introduction to signals and noise in electrical communication*, 3rd ed. New York: McGraw-Hill, 1986.

[197] J. R. Vig and F. L. Walls, "A review of sensor sensitivity and stability," in *Proceedings of the 2000 IEEE/EIA International Frequency Control Symposium and Exhibition*. Kansas City, MO, USA, 2000, pp. 30-3.

[198] L. Rodriguez-Pardo, J. F. Rodriguez, C. Gabrielli, and R. Brendel, "Sensitivity, noise, and resolution in QCM sensors in liquid media," *IEEE Sensors Journal*, vol. 5, pp. 1251-1257, 2005.

[199] M. B. Viani, T. E. Schaffer, A. Chand, M. Rief, H. E. Gaub, and P. K. Hansma, "Small cantilevers for force spectroscopy of single molecules," *Journal of Applied Physics*, vol. 86, pp. 2258-2262, 1999.

[200] J. A. Sidles and D. Rugar, "Signal-to-noise ratios in inductive and mechanical detection of magnetic resonance," *Physical Review Letters*, vol. 70, pp. 3506, 1993.

[201] W. Jing, J. E. Butler, D. S. Y. Hsu, and T. C. Nguyen, "CVD polycrystalline diamond high-Q micromechanical resonators," in *Technical Digest. of 2002 IEEE International Conference on Microelectromechanical Systems (MEMS 2002)*. Las Vegas, NV, USA, 2002, pp. 657-60.

[202] F. R. Blom, S. Bouwstra, M. Elwenspoek, and J. H. J. Fluitman, "Dependence of the quality factor of micromachined silicon beam resonators on pressure and geometry," *Journal of Vacuum Science & Technology B: Microelectronics Processing and Phenomena*, vol. 10, pp. 19, 1992.

[203] J. W. M. Chon, P. Mulvaney, and J. E. Sader, "Experimental validation of theoretical models for the frequency response of atomic force microscope

cantilever beams immersed in fluids," *Journal of Applied Physics*, vol. 87, pp. 3978-88, 2000.

[204] W. E. Baker, W. E. Woolam, and D. Young, "Air and internal damping of thin cantilever beams," *International Journal of Mechanical Sciences*, vol. 9, pp. 743-746, 1967.

[205] S. A. L. Glegg, "Sound radiation from beams at low frequencies," *Journal of Sound and Vibration*, vol. 87, pp. 637-642, 1983.

[206] G. R. Torr, "The acoustic radiation force," *American Journal of Physics*, vol. 52, pp. 402-8, 1984.

[207] M. C. Cross and R. Lifshitz, "Elastic wave transmission at an abrupt junction in a thin plate with application to heat transport and vibrations in mesoscopic systems," *Physical Review B (Condensed Matter and Materials Physics)*, vol. 64, pp. 085324-1, 2001.

[208] C. Zener, "Internal friction in solids. II. General theory of thermoelastic internal friction," *Physical Review*, vol. 53, pp. 90-99, 1938.

[209] R. Lifshitz and M. L. Roukes, "Thermoelastic damping in micro- and nanomechanical systems," *Physical Review B*, vol. 61, pp. 5600-5609, 2000.

[210] S. Reid, G. Cagnoli, D. R. M. Crooks, J. Hough, P. Murray, S. Rowan, M. M. Fejer, R. Route, and S. Zappe, "Mechanical dissipation in silicon flexures," *Physics Letters A*, vol. 351, pp. 205-11, 2006.

[211] Z. L. Hao, A. Erbil, and F. Ayazi, "An analytical model for support loss in micromachined beam resonators with in-plane flexural vibrations," *Sensors and Actuators a-Physical*, vol. 109, pp. 156-164, 2003.

[212] W. E. Newell, "Miniaturization of tuning forks," *Science*, vol. 161, pp. 1320-6, 1968.

[213] K. Kokubun, M. Hirata, H. Murakami, Y. Toda, and M. Ono, "A bending and stretching mode crystal oscillator as a friction vacuum gauge," *Vacuum*, vol. 34, pp. 731-735, 1984.

[214] J. E. Sader, "Frequency response of cantilever beams immersed in viscous fluids with applications to the atomic force microscope," *Journal of Applied Physics*, vol. 84, pp. 64-76, 1998.

[215] L. D. Landau and E. M. Lifshitz, *Fluid mechanics*, 2 ed. Oxford: Elsevier, 2004.

[216] K. Yum, Z. Wang, A. P. Suryavanshi, and M.-F. Yu, "Experimental measurement and model analysis of damping effect in nanoscale mechanical beam resonators in air," *Journal of Applied Physics*, vol. 96, pp. 3933-3938, 2004.

[217] K. Kokubun, M. Hirata, M. Ono, H. Murakami, and Y. Toda, "Unified Formula Describing the Impedance Dependence of a Quartz Oscillator on Gas-Pressure," *Journal of Vacuum Science & Technology A-Vacuum Surfaces and Films*, vol. 5, pp. 2450-2453, 1987.

[218] G. Y. Chen, R. J. Warmack, T. Thundat, D. P. Allison, and A. Huang, "Resonance response of scanning force microscopy cantilevers," *Review of Scientific Instruments*, vol. 65, pp. 2532-7, 1994.

[219] H. Hosaka, K. Itao, and S. Kuroda, "Damping characteristics of beam-shaped micro-oscillators," *Sensors and Actuators, A (Physical)*, vol. 49, pp. 87-95, 1995.

[220] D. A. Walters, J. P. Cleveland, N. H. Thomson, P. K. Hansma, M. A. Wendman, G. Gurley, and V. Elings, "Short cantilevers for atomic force microscopy," *Review of Scientific Instruments*, vol. 67, pp. 3583-90, 1996.

[221] P. I. Oden, G. Y. Chen, R. A. Steele, R. J. Warmack, and T. Thundat, "Viscous drag measurements utilizing microfabricated cantilevers," *Applied Physics Letters*, vol. 68, pp. 3814-3816, 1996.

[222] D. W. Stauff and D. J. Montgomery, "Effect of air damping on transverse vibrations of stretched filaments," *Journal of Applied Physics*, vol. 26, pp. 540-544, 1955.

[223] S. Kirstein, M. Mertesdorf, and M. Schonhoff, "The influence of a viscous fluid on the vibration dynamics of scanning near-field optical microscopy fiber probes and atomic force microscopy cantilevers," *Journal of Applied Physics*, vol. 84, pp. 1782-90, 1998.

[224] M. Alvarez, J. Tamayo, J. A. Plaza, K. Zinoviev, C. Dominguez, and L. M. Lechuga, "Dimension dependence of the thermomechanical noise of microcantilevers," *Journal of Applied Physics*, vol. 99, pp. 024910-7, 2006.

[225] T. Ikehara, J. Lu, M. Konno, R. Maeda, and T. Mihara, "A high quality-factor silicon cantilever for a low detection-limit resonant mass sensor operated in air," *Journal of Micromechanics and Microengineering*, vol. 17, pp. 2491-2494, 2007.

[226] L. Rosenhead, *Laminar boundary layers; an account of the development, structure, and stability of laminar boundary layers in incompressible fluids, together with a description of the associated experimental techniques*. Oxford: Clarendon Press, 1963.

[227] D. M. Photiadis and J. A. Judge, "Attachment losses of high Q oscillators," *Applied Physics Letters*, vol. 85, pp. 482-4, 2004.

[228] A. Duwel, R. N. Candler, T. W. Kenny, and M. Varghese, "Engineering MEMS resonators with low thermoelastic damping," *Journal of Microelectromechanical Systems*, vol. 15, pp. 1437-45, 2006.

[229] P. M. Morse, *Vibration and sound*, 2d ed. New York,: McGraw-Hill Book Co., 1948.

[230] R. P. Feynman, R. B. Leighton, and M. L. Sands, *The Feynman lectures on physics*. Reading, Mass.,: Addison-Wesley, 1963.

[231] R. A. Johnson, *Mechanical filters in electronics*. New York: Wiley, 1983.

[232] J. W. S. Rayleigh and R. B. Lindsay, *The theory of sound*, 2nd ed. New York,: Dover, 1945.

[233] A. V. Oppenheim, A. S. Willsky, and S. H. Nawab, *Signals & systems*, 2nd ed. Upper Saddle River, N.J.: Prentice Hall, 1997.

[234] Z. L. Hao, A. Erbil, and F. Ayazi, "An analytical model for support loss in micromachined beam resonators with in-plane flexural vibrations," *Sensors and Actuators A (Physical)*, vol. 109, pp. 156-164, 2003.

[235] V. M. Mecea, "Loaded vibrating quartz sensors," *Sensors and Actuators A: Physical*, vol. 40, pp. 1-27, 1994.

[236] H. Zhang and E. S. Kim, "Micromachined acoustic resonant mass sensor," *Journal of Microelectromechanical Systems*, vol. 14, pp. 699-706, 2005.

[237] H. Wohltjen, "Mechanism of Operation and Design Considerations for Surface Acoustic-Wave Device Vapor Sensors," *Sensors and Actuators*, vol. 5, pp. 307-325, 1984.

[238] F. M. Battiston, J. P. Ramseyer, H. P. Lang, M. K. Baller, C. Gerber, J. K. Gimzewski, E. Meyer, and H. J. Güntherodt, "A chemical sensor based on a microfabricated cantilever array with simultaneous resonance-frequency and bending readout," *Sensors and Actuators B (Chemical)*, vol. 77, pp. 122-131, 2001.

[239] T. Thundat, P. I. Oden, and R. J. Warmack, "Microcantilever sensors," *Nanoscale and Microscale Thermophysical Engineering*, vol. 1, pp. 185 - 199, 1997.

[240] M. Li, H. X. Tang, and M. L. Roukes, "Ultra-sensitive NEMS-based cantilevers for sensing, scanned probe and very high-frequency applications," *Nature Nanotechnology*, vol. 2, pp. 114-120, 2007.

[241] F. L. Walls and J. J. Gagnepain, "Environmental sensitivities of quartz oscillators," *IEEE Transactions on Ultrasonics, Ferroelectrics and Frequency Control*, vol. 39, pp. 241-9, 1992.

[242] E. P. Quevy and R. T. Howe, "Redundant MEMS resonators for precise reference oscillators," in *2005 IEEE Radio Frequency Integrated Circuits (RFIC) Symposium*. Long Beach, CA, USA, 2005, pp. 113-116.

[243] J. J. Caron, R. B. Haskell, P. Benoit, and J. F. Vetelino, "Surface acoustic wave mercury vapor sensor," *IEEE Transactions on Ultrasonics Ferroelectrics and Frequency Control*, vol. 45, pp. 1393-1398, 1998.

[244] T. Ono, D. F. Wang, and M. Esashi, "Mass sensing with resonating ultrathin double beams," in *IEEE Sensors Conference 2003*, vol. 2. Toronto, Ont., Canada, 2003, pp. 825-829.

[245] K. Sundaresan, G. K. Ho, S. Pourkamali, and F. Ayaji, "Electronically temperature compensated silicon bulk acoustic resonator reference oscillators," *IEEE Journal of Solid-State Circuits*, vol. 42, pp. 1425-1434, 2007.

[246] J. H. Seo, K. S. Demirci, A. Byun, S. Truax, and O. Brand, "Temperature compensation method for resonant microsensors based on a controlled stiffness modulation," *Journal of Applied Physics*, vol. 104, pp. 014911, 2008.

[247] R. Melamud, K. Bongsang, S. A. Chandorkar, M. A. Hopcroft, M. Agarwal, C. M. Jha, and T. W. Kenny, "Temperature-compensated high-stability silicon resonators," *Applied Physics Letters*, vol. 90, pp. 244107-1, 2007.

[248] P. Wei, R. C. Ruby, R. Parker, P. W. Fisher, M. A. Unkrich, and J. D. Larson, III, "A temperature-stable film bulk acoustic wave oscillator," *IEEE Electron Device Letters*, vol. 29, pp. 315-18, 2008.

[249] J. Bjurstrom, G. Wingqvist, V. Yantchev, and I. Katardjiev, "Temperature compensation of liquid FBAR sensors," *Journal of Micromechanics and Microengineering*, vol. 17, pp. 651-8, 2007.

[250] H. Wan-Thai, J. R. Clark, and C. T. C. Nguyen, "Mechanically temperature-compensated flexural-mode micromechanical resonators," in *International Electron Devices Meeting (IEDM)* San Francisco, CA, USA, 2000, pp. 399-402.

[251] J. Veris, "Temperature compensation of silicon resonant pressure sensor," *Sensors and Actuators A (Physical)*, vol. 57, pp. 179-182, 1996.

[252] R. G. Azevedo, W. Huang, O. M. O'Reilly, and A. P. Pisano, "Dual-mode temperature compensation for a comb-driven MEMS resonant strain gauge," *Sensors and Actuators A (Physical)*, vol. 144, pp. 374-380, 2008.

[253] M. Koskenvuori, V. Kaajakari, T. Mattila, and I. Tittonen, "Temperature measurement and compensation based on two vibrating modes of a bulk acoustic mode microresonator," in *21st IEEE International Conference on Micro Electro Mechanical Systems - MEMS '08*. Tucson, AZ, USA, 2008, pp. 78-81.

[254] D. E. Pierce, Y. Kim, and J. R. Vig, "A temperature insensitive quartz microbalance," *IEEE Transactions on Ultrasonics Ferroelectrics and Frequency Control*, vol. 45, pp. 1238-1245, 1998.

[255] N. Lobontiu, *Dynamics of microelectromechanical systems*. New York: Springer, 2007.

[256] S. Dohn, R. Sandberg, W. Svendsen, and A. Boisen, "Enhanced functionality of cantilever based mass sensors using higher modes," *Applied Physics Letters*, vol. 86, pp. 233501-1, 2005.

[257] S. Dohn, W. Svendsen, A. Boisen, and O. Hansen, "Mass and position determination of attached particles on cantilever based mass sensors," *Review of Scientific Instruments*, vol. 78, pp. 103303-3, 2007.

[258] D. Lange, O. Brand, and H. Baltes, *CMOS cantilever sensor systems : atomic force microscopy and gas sensing applications*. Berlin ; New York: Springer, 2002.

[259] C. Vancura, M. Ruegg, Y. Li, C. Hagleitner, and A. Hierlemann, "Magnetically actuated complementary metal oxide semiconductor resonant cantilever gas sensor systems," *Analytical Chemistry*, vol. 77, pp. 2690-2699, 2005.

[260] D. K. Cheng, *Field and wave electromagnetics*. Reading, Mass: Addison-Wesley, 1989.

Kianoush Naeli was bron in 1976 in Tehran, Iran. After an intensive high school education with National Organization for Development of Exceptional Talents (NODET; SAMPAD in Farsi), he was admitted to Sharif University of Technology, Iran, and received a Bachelor's degree in Electrical Engineering in 1999. He continued with his graduate study at the University of Tehran, Iran, with a Master's degree in Microelectronics being awarded to him in 2001. To further pursue the research in the field of Microelectromechanical Systems (MEMS), Kianoush entered the PhD program at Georgia Institute of Technology in 2002. He joined Prof. Oliver Brand's research group in 2004, and started his thesis research from the summer of that year.